2128 nm Laser and Squeezed-Light Platform
Technologies for Future
Gravitational-Wave Observatories

Dissertation
zur Erlangung des Doktorgrades
an der Fakultät für Mathematik, Informatik und Naturwissenschaften
Fachbereich Physik
der Universität Hamburg

vorgelegt von

Julian Tobias Gurs

Hamburg
2026

Gutachter/innen der Dissertation:	Prof. Dr. Roman Schnabel Assoc. Prof. Dr. Sebastian Steinlechner
Zusammensetzung der Prüfungskommission:	Prof. Dr. Ludwig Mathey Prof. Dr. Roman Schnabel Assoc. Prof. Dr. Sebastian Steinlechner Prof. Dr. Oliver Gerberding Prof. Dr. Peter Schauß
Vorsitzende/r der Prüfungskommission:	Prof. Dr. Ludwig Mathey
Datum der Disputation:	20. Juli 2026
Vorsitzender Fach-Promotionsausschusses PHYSIK:	Prof. Dr. Johannes Haller
Leiter des Fachbereichs PHYSIK:	Prof. Dr. Markus Drescher
Dekan der Fakultät MIN:	Prof. Dr.-Ing. Norbert Ritter

Conceive. Believe. Achieve.
by Napoleon Hill

Kurzfassung

Seit der ersten Messung von Gravitationswellen im Jahr 2015 haben sich die Technologien der Gravitationswellen-Observatorien (GWO) erheblich verbessert, was höhere Sensitivität und die Analyse weiter entfernter Quellen ermöglicht. Eine wesentliche Limitierung bleibt jedoch das thermische Beschichtungsrauschen der Testmassen, das im Frequenzbereich um 100 Hz dominiert. Das Kühlen der Testmassen bis auf kryogene Temperaturen würde dieses Limit signifikant reduzieren; dennoch sind aktuelle Beschichtungen, die für Zimmertemperatur und die Betriebswellenlänge von 1064 nm optimiert sind, nicht für diese Bedingungen geeignet. Daher werden neuartige Materialien wie amorphes Silizium in Kombination mit Betriebswellenlängen von 1550 nm oder im Bereich von 2 µm erforscht. Der Betrieb im 2-µm-Bereich erfordert jedoch ausgereifte Laser- und Quantentechnologien, die derzeit noch nicht verfügbar sind. Aus diesem Grund konzentrieren sich aktuelle Entwürfe für kryogene GWOs überwiegend auf 1550 nm als primäre Wellenlänge.

Ziel dieser Arbeit ist es, die Reife der 2-µm-Technologie für zukünftige kryogene GWOs voranzutreiben, indem drei zentrale Technologieplattformen untersucht werden, wobei der Schwerpunkt insbesondere auf einer Betriebswellenlänge von 2128 nm liegt. Erstens die Entwicklung eines Hochleistungslasers mit 20 W konvertierter Leistung bei einer Konversionseffizienz von 68 %. Zudem wurde das technische Rauschen dieses Lasers untersucht und gezeigt, dass der gewählte nichtlineare Prozess eine Unterdrückung des Relativintensitätsrauschens von bis zu 50 % im Vergleich zum 1064 nm-Licht ermöglichte. Zweitens wurde die Entwicklung einer Quantenrauschunterdrückung bei niedrigen Messfrequenzen unter Verwendung gequetschten Lichts demonstriert. Es wurde eine Rauschunterdrückung von bis zu 3,3 dB bei einer Messfrequenz von 15 kHz erreicht. Für diesen Prozess wurde auch ein optischer Isolator zur Vermeidung störender Rückreflexionen entwickelt sowie Photodioden charakterisiert und optimiert. Drittens wurde die Kopplung zwischen fundamentalen und höheren Moden des von einem Resonator mit unzureichender Modenanpassung reflektierten gequetschten Lichts untersucht. Zwei Koppelregime der Moden wurden dabei gefunden: Erstens der vollständige Verlust der Quanteneigenschaften mit einem Übergang in einen thermisch ähnlichen Zustand. Zweitens ließ sich der durch unzureichende Modenanpassung entstehende zusätzliche Verlust durch eine optimierte Phase zwischen der fundamentalen und höheren Moden deutlich verringern.

Diese Arbeit demonstriert zum ersten Mal einen rauscharmen Hochleistungslaser, die Unterdrückung des Schrotrauschens bei niedrigen Messfrequenzen sowie die Kopplung zwischen fundamentalen und höheren Moden gequetschten Lichts in Resonatoren mit unzureichender Modenanpassung. Zusammengefasst stellen diese Ergebnisse wichtige Schritte auf dem Weg zur Etablierung von Technologien im 2-µm-Bereich und damit zur Verbesserung der Empfindlichkeit künftiger gekühlter Gravitationswellenobservatorien dar.

Abstract

Since the first detection of gravitational waves in 2015, the technology of gravitational-wave observatories (GWOs) has advanced significantly, enabling higher sensitivity and the observation of increasingly distant astrophysical sources. A major limitation remains the coating thermal noise of the test masses, which dominates the detector sensitivity around 100 Hz. Cooling the test masses to cryogenic temperatures can reduce this contribution; however, current optical coatings, optimized for room-temperature operation at 1064 nm, are not compatible with cryogenic conditions. This motivates the search for novel coating materials, such as amorphous silicon, as well as a shift toward longer operating wavelengths around 1550 nm or 2 µm. Operation in the 2 µm regime offers particularly promising performance but requires laser and quantum technologies that are less mature. For this reason, current designs for cryogenic GWOs predominantly focus on 1550 nm as a primary wavelength.

The aim of this thesis is to advance the maturity of 2 µm technology for future cryogenic GWOs by investigating three key technology platforms, with a particular focus on an operating wavelength of 2128 nm. First, a high-power laser with 20 W of converted power and a conversion efficiency of 68 % was developed. Its technical noise was characterized, revealing that the utilized nonlinear process reduced relative intensity noise by up to 50 % compared to 1064 nm light. Second, low-frequency quantum-noise suppression using squeezed light was demonstrated, achieving up to 3.3 dB of quantum noise reduction at a measurement frequency of 15 kHz. For this purpose, an optical isolator was developed to suppress detrimental back-reflections, and photodiodes for 2128 nm were characterized and optimized. Third, the coupling between higher-order and fundamental spatial modes of squeezed light reflected from a resonator under imperfect mode-matching conditions was investigated. Two coupling regimes were identified: one in which the quantum properties were completely lost and transformed into a thermal-like state, and another in which the additional loss from imperfect mode overlap could be significantly reduced by optimizing the relative phase between the fundamental and higher-order modes.

This work demonstrates for the first time a low-noise high-power laser system, low-frequency shot-noise suppression using squeezed light, and the controlled coupling of squeezed-light modes in resonators under imperfect mode-matching conditions. Together, these results represent important steps toward the realization of mature 2 µm technologies and enhanced sensitivity in future gravitational-wave observatories.

Contents

Introduction

Nearly a century passed between Albert Einstein's prediction of gravitational waves and their first direct detection from a binary black-hole merger, by the LIGO observatories, a milestone that was recognized with the Nobel Prize in Physics [1]. This significantly advanced our understanding of compact astrophysical objects, including black holes and neutron stars, and marked the beginning of gravitational-wave astronomy. Such progress illustrates the remarkable technological development from early optical equipment to today's highly advanced systems and highlights the pace at which further advances may be expected in the coming decades.

Detecting a gravitational-wave signal was the first major milestone in gravitational-wave astronomy. The next essential step was the operation of a global network of at least three detectors, which enabled the triangulation of source positions and allowed electromagnetic observatories to be directed toward the corresponding region in the sky to search for EM counterparts. Today, this network consists of LIGO Hanford and Livingston in the United States, Virgo in Italy, KAGRA in Japan, and GEO600 in Germany. A simplified schematic of a future GWO is illustrated in Figure 1. Its basic layout is a Michelson interferometer pumped by a high-power laser, with each arm containing a Fabry–Pérot optical cavity to enhance the circulating power. To suppress quantum noise, which limits the detector sensitivity over a broad frequency band, frequency-dependent squeezed light is employed. The squeezed field is generated by a squeezer and injected into the interferometer's dark port. Its frequency dependence is shaped using a filter cavity to suppress quantum noise across the full sensitivity band. Additional cavities formed by the power recycling mirror (PRM) and the signal recycling mirror (SRM) increase the circulating power and enhance the detection bandwidth, respectively. At the interferometer's dark port, the high-power field is suppressed by destructive interference, leaving only the gravitational-wave-induced signal sidebands together with the injected squeezed field. The combined field is then directed to the detection system, which consists of a homodyne detector.

Despite the technological progress in gravitational-wave detection over the past decades, many key questions remain. Future GWOs will require significantly improved sensitivities in order to detect weaker sources, probe larger volumes of the universe, and ultimately provide a more complete picture of cosmic structure and evolution. In this thesis, I focus on the current limitations of the LIGO detectors, the most sensitive instruments in the network, and on technologies relevant for future third-generation observatories such as the Einstein Telescope, which is a European collaboration project, and Cosmic Explorer, which is planned to be built in the USA.

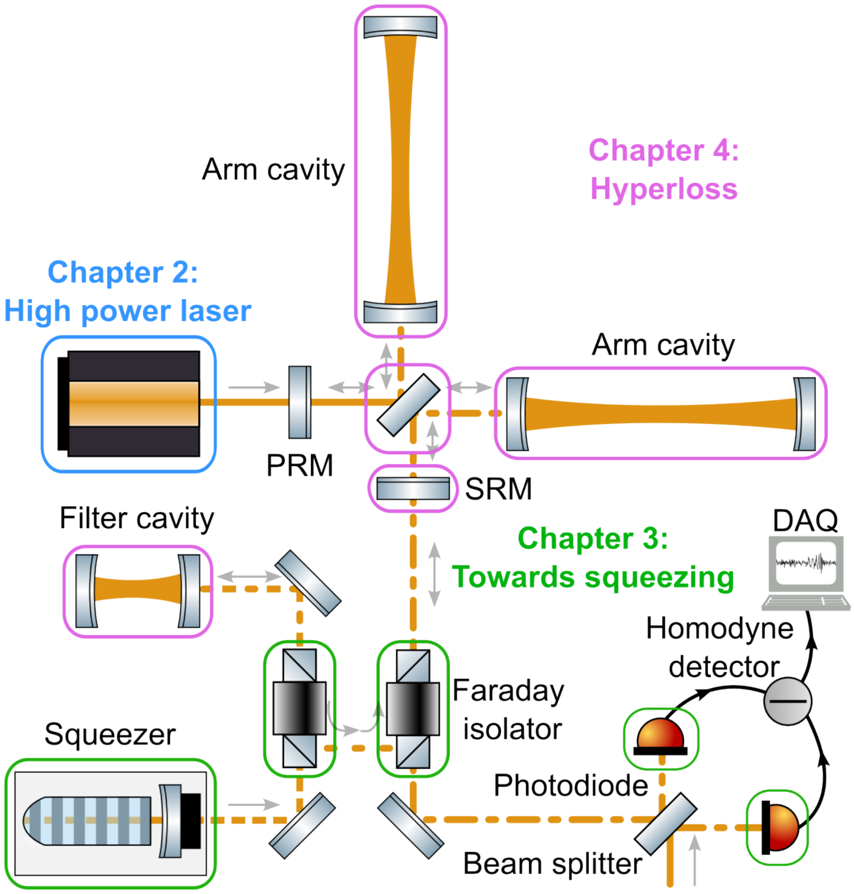

Figure 1: *Schematic representation of a gravitational-wave detector employing squeezing technology. A high-power laser injects light into a Michelson interferometer with two arm cavities, while additional cavities are formed by the PRM (power recycling mirror) to further amplify the power and the SRM (signal recycling mirror) to enhance detection bandwidth. Frequency-dependent squeezed light is injected into the interferometer's output port, and the signal is read out at the dark port using a homodyne detector and a data acquisition system (DAQ). The figure also highlights the structure of the thesis. At the beginning of each chapter, the figure is reused to highlight the specific subsystem or physical concept discussed in that chapter. In this way, the GWO serves as a structural guide throughout the thesis, linking the detailed topics of each chapter to their functional role within a full interferometric gravitational-wave detector.*

Current GWOs are affected by various noise sources, including instrumental contributions such as control noise and scattered light, quantum noise such as radiation pressure noise and shot noise, and thermal noise [2]. Thermal noise is a collective term for several contributions including suspension thermal noise, thermoelastic and thermorefractive noise, and, most relevant for this work, coating Brownian noise, which arises from thermally driven mechanical fluctuations in the mirror coatings. Radiation-pressure noise is the displacement noise of the test masses induced by quantum fluctuations of the photon momentum flux of the high-power beam in the interferometer. Shot noise is caused by quantum fluctuations in the number of detected photons. A total noise budget for the advanced LIGO (aLIGO) configuration was simulated using the Python package `pygwinc` [3], as shown on the left-hand side of Figure 2. The motivation for this work is the sensitivity limitation imposed by thermal noise. Mitigating this limitation requires a new operating wavelength, which is illustrated as a block diagram on the right-hand side of the figure and is discussed in detail in the following paragraph.

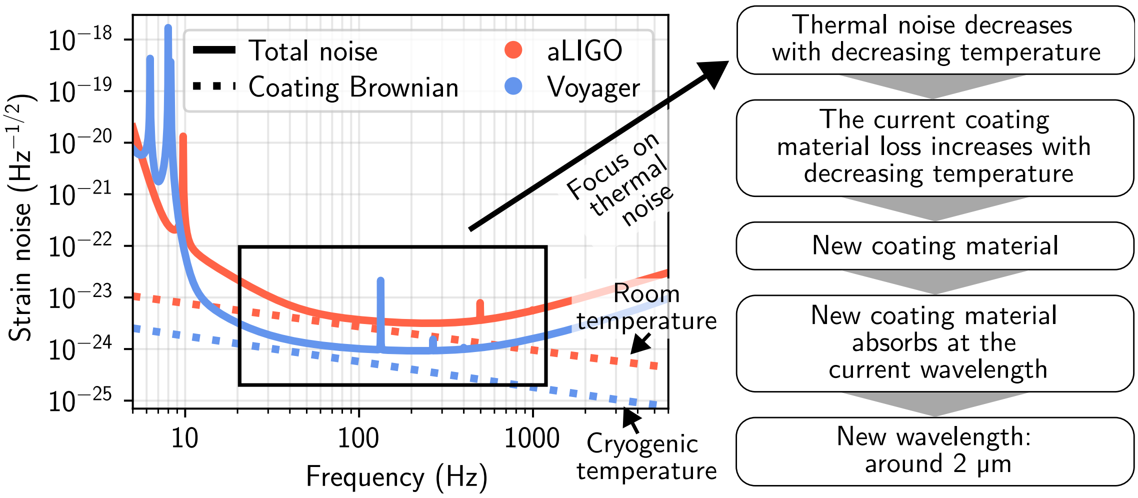

Figure 2: *The left-hand side shows the noise budget of the aLIGO detector (red), with thermal noise as the dominant noise source motivating this work. The right-hand side shows a block diagram illustrating the motivation for a new operating wavelength. Following this approach leads to the proposed upgrade LIGO Voyager, shown as the blue curve in the noise budget.*

Thermal noise is determined by the mechanical loss of the mirror substrates and coatings and by their temperature. Coating Brownian noise can be reduced by cooling the test masses to cryogenic temperatures and by increasing the beam diameter on the test masses, which allows to average out the coupling of thermal vibrations to the light field. Current room-temperature coating technologies are already operating close to their practical limits in terms of mechanical loss, which prevents further significant reductions of coating Brownian noise. To lower thermal noise beyond this point, cryogenic operation becomes necessary. This, in turn, requires coating materials with low mechanical loss at cryogenic temperatures, such as amorphous silicon and silicon nitride [4]. The best performance of these coating materials is achieved at longer operating wavelengths, making the adoption of such wavelengths essential to avoid excess optical loss. These changes propagate through the entire system and require a comprehensive update.

Shot noise can be reduced by injecting squeezed light. However, radiation-pressure noise and shot noise exhibit opposing scalings with respect to key system parameters: increasing the circulating power reduces shot noise but enhances radiation-pressure noise, because on the one hand, more photons are detected, which makes the random photon-count fluctuations smaller relative to the signal (lower shot noise); on the other hand, more photons deliver radiation pressure to the test masses, causing larger quantum fluctuations in their motion (higher radiation-pressure noise). Likewise, operating at longer wavelengths reduces radiation-pressure noise but increases shot noise, because at a given circulating power the photon number increases, strengthening the relative impact of photon-counting statistics while the radiation-pressure coupling to the test masses becomes weaker. Due to this trade-off, frequency-dependent squeezing provides a more advanced approach, enabling radiation-pressure noise suppression at low frequencies and shot-noise reduction at high frequencies. Radiation-pressure noise can be further mitigated by increasing the test-mass mass, thereby reducing its susceptibility to radiation-pressure fluctuations. The adaptation of all system components to a new operating wavelength, including system-wide optimization, results in the proposed Voyager design [5], which is shown as the blue curve in the noise budget in Figure 2.

The gravitational-wave community has converged on operating wavelengths near either 1.5 μm or 2 μm, where optical coating designs exist that perform well both optically and at cryogenic temperatures [6, 7]. In particular, a wavelength of 1550 nm has been chosen for planned detectors as a compromise between reduced thermal noise and the maturity of available photonic technologies. Although operating at 2 μm offers further potential for low thermal noise when appropriate cryogenic coating designs are used, the required technology platforms are not yet fully developed. In particular, this concerns auxiliary components [5, 8, 9], beam quality at high power operation [5], and squeezed-light generation [8, 10, 11, 5].

Current high-power laser and amplifier systems at 2 μm suffer from limited beam quality and suboptimal intensity- and phase-noise performance, typically delivering optical powers of up to 100 W with an M^2 between 3 and 15 (see Chapter 2.5). In contrast, third-generation gravitational-wave observatories such as the Einstein Telescope (ET) require laser systems with optical powers on the order of several hundred watts and a diffraction-limited, single-mode TEM_{00} beam profile, together with extremely low intensity and phase noise [12], in order to achieve the required circulating arm powers and sensitivity. However, no existing 2 μm laser meets these combined requirements.

In this thesis, I present an approach based on using the well-established 1064 nm non-planar ring-oscillator (NPRO) laser as a seed source and amplifying it with a neoVAN-4S-HP laser amplifier, providing power levels of up to 75 W, as used in the O3 run of LIGO [13]. Through the nonlinear process of degenerate optical-parametric oscillation, the pump light was converted to 2128 nm with a high-quality spatial mode and the potential for high conversion efficiency. The first objective of this work was to construct and characterize a 2128 nm laser source and to demonstrate more than 20 W of output power, thereby exceeding the input power requirements of the low-frequency interferometer of the ET while representing a significant step toward the higher power levels required for the high-frequency interferometer, and establishing a basis for future implementation within existing LIGO infrastructure. This approach addresses limitations in beam quality, provides sufficient converted power, and offers favorable intensity-noise characteristics.

Squeezed-light generation at 2 μm is similarly constrained. At audio frequencies, squeezing levels are limited primarily by the dark-noise characteristics of available photodiodes. To date, squeezing levels of up to 3.9 dB at 2 kHz and 7.2 dB at 2 MHz have been demonstrated [10, 11]. This limitation motivates the work presented in this thesis, in which an audio-band squeezed-light source at 2128 nm was developed and investigated how photodiode dark noise affects low-frequency measurements.

The second aim of this thesis is therefore to investigate commercially available photodiodes with respect to several performance criteria and to explore methods for optimizing their operation for low-frequency squeezing measurements. In addition, an audio-band squeezed-light source at 2128 nm was constructed and characterized. Furthermore, commercially available injection components such as Faraday isolators were examined and improved with respect to their transmission and suppression ratio to meet the requirements for strong squeezed-light injection.

Optical losses constitute the main limitation to the achievable quantum enhancement at any wavelength. In addition to losses arising from the generation and injection of squeezed light, it has been theorized that coupling between the fundamental and higher-order spatial modes of squeezed light can represent a significant and previously underappreciated source of excess optical loss in gravitational-wave observatories [14]. This effect arises when higher-order spatial modes generated by imperfect mode matching are reflected from an optical cavity and subsequently couple into the fundamental mode. The third objective of this thesis is to investigate this phenomenon using a well controlled tabletop quantum-optics setup. In this context, it was demonstrated that the underlying mechanism can completely suppress the quantum enhancement of the squeezed state by effectively transforming it into a thermal-like state. Possible mitigation strategies were subsequently analyzed.

Together, these results provide a foundation for developing 2128 nm technology and offer guidance for critical improvements and risk mitigation in the design of next-generation cryogenic gravitational-wave detectors.

The structure of this thesis is illustrated using a simplified diagram of a gravitational-wave observatory, as shown in Figure 1. It begins with a brief theoretical overview in Chapter 1, followed by the first set of experimental results in Chapter 2, which focus on the development of a high-power laser at 2128 nm and the improvement of its relative-intensity noise characteristics. Next, Chapter 3 discusses the development of an audio-band squeezer operating at 2128 nm, together with supporting optical components such as Faraday isolators and photodiodes. Finally, Chapter 4 investigates a critical loss mechanism that is common to all quantum networks and gravitational-wave observatories in particular, namely, the coupling of higher-order spatial modes into the fundamental mode due to imperfect mode matching to optical resonators.

Chapter 1

Quantum Optical Systems and Their Auxiliary Components

A simplified representation of a gravitational-wave observatory is shown in Figure 1.1. At the heart of the system lies a Michelson interferometer, which is illuminated by two light sources. The first is a high-power laser serving as the carrier field; the second is a non-classical quantum state generator, referred to as the squeezer, which injects a state that reduces quantum noise. Auxiliary components, such as optical cavities and Faraday isolators, are essential for operating both the interferometer and its light sources.

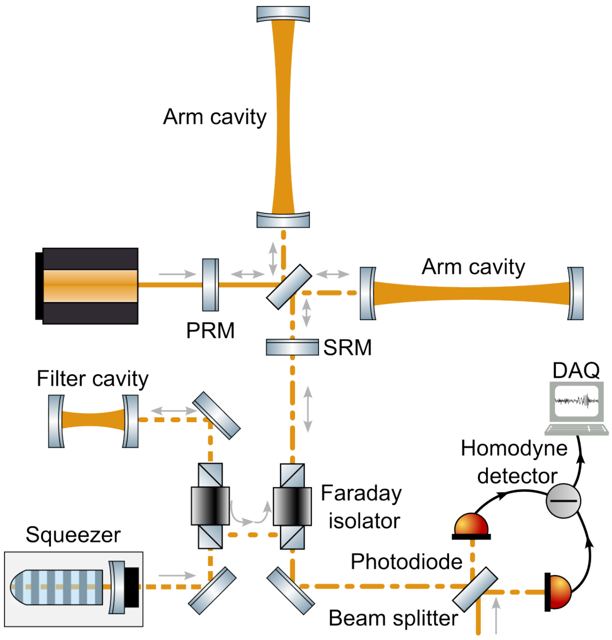

Figure 1.1: *Schematic illustration of a GWO.*

Since this thesis investigates various aspects of a gravitational-wave observatory (GWO) operating at 2128 nm, this chapter summarizes the fundamental concepts and techniques required for this work. It begins with an overview of essential optical components, such as Faraday isolators and cavities, followed by a discussion of nonlinear optical processes used to generate and manipulate light. Finally, it introduces the description of non-classical light, focusing on squeezed states and their properties.

1.1 Auxiliary Components and Their Role in Quantum Setups

1.1.1 Cavity Design and Functionality

Optical cavities are fundamental tools in quantum optical experiments and serve a variety of purposes. There are many possible designs and applications; here, we focus on two configurations that are particularly relevant for this work: a standing-wave cavity in a linear configuration, also referred to as a linear cavity, and a travelling-wave cavity in a triangular configuration, also referred to as a triangular cavity. The naming of these cavities originates from whether the light field forms a standing wave or propagates in a travelling-wave manner. Both cavity types are illustrated in Figure 1.2.

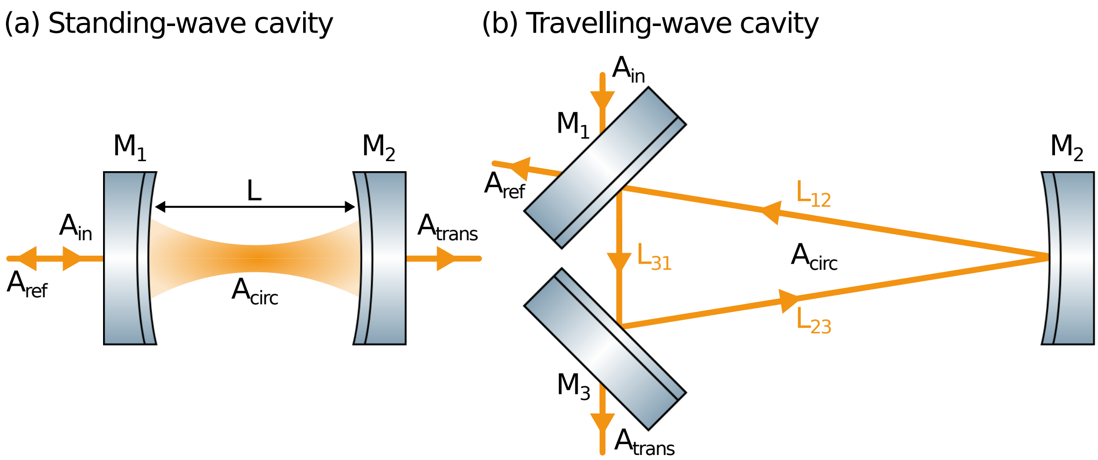

Figure 1.2: *Schematic representation of (a) a standing-wave cavity in a linear configuration and (b) a travelling-wave cavity in a triangular configuration.*

Fabry–Pérot Cavity

A Fabry–Pérot optical cavity, alias linear cavity, consists of two mirrors, M_1 and M_2, separated by a distance L. Each mirror is characterized by an optical field reflectivity r_i and transmissivity t_i, corresponding to intensity reflectivities $R_\mathrm{i} = |r_\mathrm{i}|^2$ and transmissions $T_\mathrm{i} = |t_\mathrm{i}|^2$, respectively.The presentation closely follows the notation and formalism introduced by Nur Ismail *et al.* [15].

Optical resonators inherently experience propagation losses, here assumed to arise primarily from finite mirror reflectivity. Other loss contributions, such as absorption, scattering in the mirror coatings, or losses introduced by additional intracavity elements, are neglected, as they mainly modify effective loss rates (e.g., the cavity linewidth) without changing the generic functional Airy response discussed here. Under these assumptions, the round-trip loss parameter associated with each mirror is defined as

$$\delta_{\mathrm{out},i} = \frac{2L}{c\,\tau_{\mathrm{out},i}}. \tag{1.1}$$

The quantity $\tau_{\mathrm{out},i}$ represents the photon decay time associated with outcoupling at the corresponding mirror. Accordingly, the total round-trip loss can be expressed as $\delta_{\mathrm{total}} = -\ln(R_1 R_2)$.

In the limit of high reflectivities ($R_i \approx 1$), this definition is consistent with the linear loss approximation $1 - R_1 R_2$ used in the Airy formalism.

Resonant enhancement of the optical field inside the cavity is described by the circulating Airy function $A_{\text{circ}}(\phi)$. Normalized to the incident intensity, it is given by

$$A_{\text{circ}}(\phi) = \frac{|E_{\text{circ}}|^2}{|E_{\text{inc}}|^2} = \frac{1 - R_1}{(1 - \sqrt{R_1 R_2})^2 + 4\sqrt{R_1 R_2}\,\sin^2(\phi)}, \tag{1.2}$$

where $\phi = 2\omega L/c$ is the round-trip phase of the cavity. E_{circ} and E_{inc} denote the circulating and incident electric field amplitudes, respectively. The expression can be extended to describe the transmitted Airy function $A_{\text{trans}}(\phi)$ as

$$A_{\text{trans}}(\phi) = (1 - R_2)\, A_{\text{circ}}(\phi). \tag{1.3}$$

The reflected Airy function $A_{\text{refl}}(\phi)$ is defined via the reflected electric field E_{refl} and is given by

$$A_{\text{refl}}(\phi) = \frac{|E_{\text{refl}}|^2}{|E_{\text{inc}}|^2} = \frac{\left(\sqrt{R_1} - \sqrt{R_2}\right)^2 + 4\sqrt{R_1 R_2}\,\sin^2(\phi)}{\left(1 - \sqrt{R_1 R_2}\right)^2 + 4\sqrt{R_1 R_2}\,\sin^2(\phi)}. \tag{1.4}$$

This expression follows from the coherent interference of the directly reflected and cavity-leaked fields. Together, these three Airy functions characterize the cavity response resulting from the resonant enhancement of light injected into the resonator.

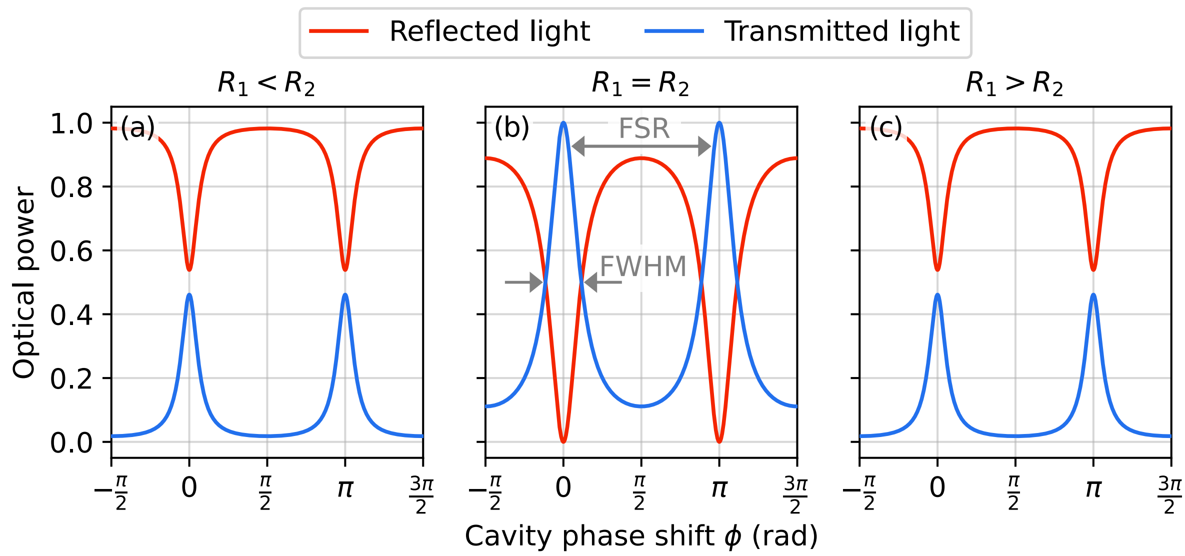

Figure 1.3: *Transmitted and reflected Airy functions as a function of the cavity phase shift for three different coupling regimes: (a) under-coupled cavity ($R_1 < R_2$), (b) impedance-matched cavity ($R_1 = R_2$), and (c) over-coupled cavity ($R_1 > R_2$). Panel (b) also indicates the free spectral range (FSR) and the full width at half maximum (FWHM), which quantify the spectral properties and quality of the cavity.*

Figure 1.3 illustrates the transmitted and reflected responses as a function of the cavity phase shift, which can be experimentally varied by tuning the cavity length. The circulating Airy function is not shown, as its strong amplification would reduce the clarity of the illustration. Three coupling regimes are distinguished: (a) an under-coupled cavity ($R_1 < R_2$), (b) an impedance-matched cavity ($R_1 = R_2$), and (c) an over-coupled cavity ($R_1 > R_2$). These cases correspond to the reflectivity pairs $R_1 = [0.5, 0.5, 0.9]$ and $R_2 = [0.9, 0.5, 0.5]$, respectively.

Optical cavities are typically optimized for a specific transverse mode. In the simplest case, this is the fundamental transverse electromagnetic mode, denoted TEM_{00}. Using the TEM_{mn} notation, the indices m and n describe the horizontal and vertical transverse mode order, respectively. In subsequent experiments, higher-order transverse modes, non-resonant with the cavity, are mostly reflected. This behavior arises because higher-order modes (HOM) experience an additional Gouy phase shift. As a result, their resonance condition is modified according to

$$\phi_{mn} = (1 + m + n)\,\phi_{\text{cavity}}, \quad (1.5)$$

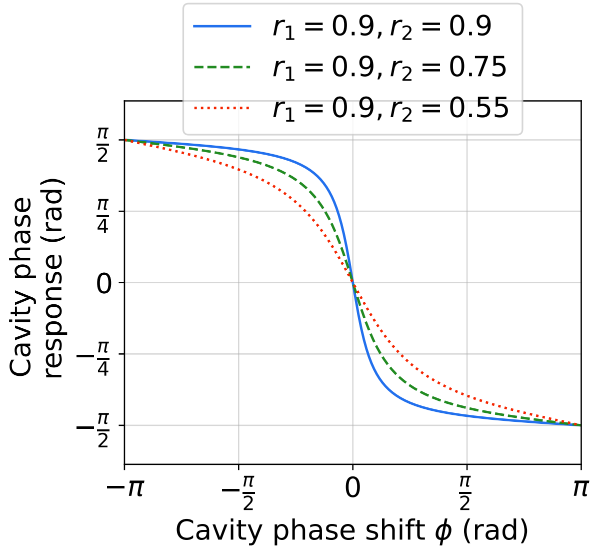

Figure 1.4: *Theoretical simulation of the cavity phase response of the transmitted light field as a function of the cavity phase shift.*

where ϕ_{cavity} denotes the cavity phase shift for the fundamental TEM_{00} mode. Consequently, higher-order modes resonate at different cavity lengths and no longer fulfill the resonance condition simultaneously with the fundamental mode (FM). The cavity-induced phase response of the transmitted field is given by

$$\Phi(\phi) = \arg\left(\frac{t_1 t_2 e^{-i\phi/2}}{1 - r_1 r_2 e^{-i\phi/2}}\right), \quad (1.6)$$

and is shown in Figure 1.4 for three different reflectivity configurations.

The spectral quality of the cavity is quantified by the finesse F, defined as

$$F = \frac{\text{FSR}}{\text{FWHM}} \approx \frac{\pi\sqrt{R_1 R_2}}{1 - R_1 R_2}, \quad (1.7)$$

where the free spectral range is given by $\text{FSR} = c/(2n(\lambda)L)$, with $n(\lambda)$ denoting the refractive index of the medium inside the cavity at wavelength λ (for an air-filled cavity, $n(\lambda) \approx 1$). The FWHM denotes the cavity linewidth (full width at half maximum), as illustrated in Figure 1.3(b).

Another important parameter is the intracavity power build-up B, obtained from Equation 1.2 evaluated at $\phi = 0$. It is given by

$$B = A_{\text{circ}}(\phi = 0) = \frac{1 - R_1}{(1 - \sqrt{R_1 R_2})^2}. \quad (1.8)$$

The dependence of the intracavity power build-up on the mirror reflectivities is illustrated in Figure 1.5.

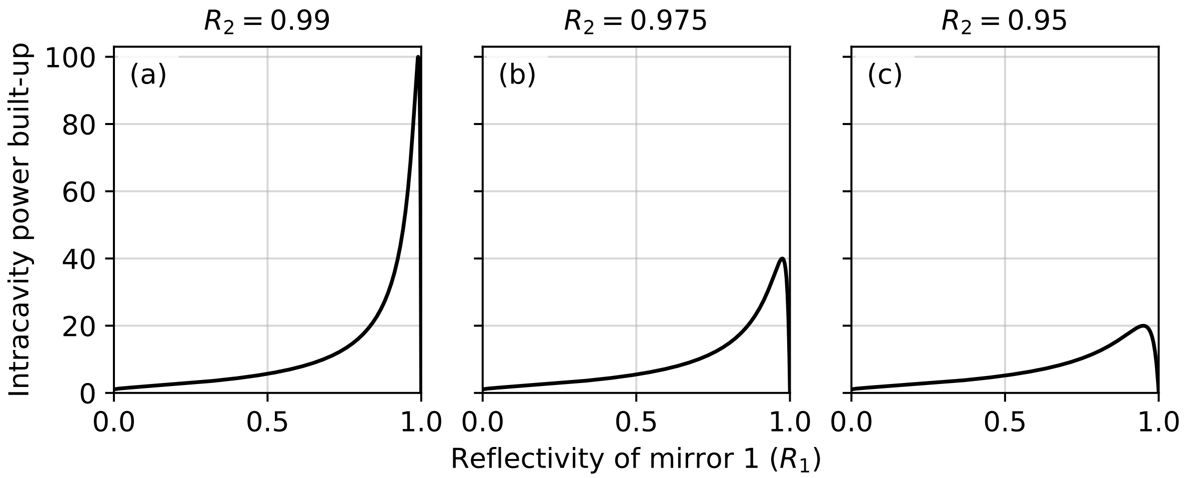

Figure 1.5: *Intracavity power build-up (Airy peak at $\phi = 0$) as a function of input mirror reflectivity R_1 for different end-mirror reflectivities R_2: (a) $R_2 = 0.9$, (b) $R_2 = 0.75$, and (c) $R_2 = 0.3$.*

The intracavity power build-up exhibits a maximum at $R_1 = R_2$, corresponding to the impedance-matched condition. For $R_1 \neq R_2$, the cavity is not impedance matched, resulting in a reduced steady-state intracavity field due to the mismatch between input coupling and effective round-trip losses.

In the context of this work, linear cavities serve multiple purposes. First, they enhance nonlinear optical processes when a nonlinear medium is placed inside the cavity. Second, they act as frequency-selective elements for laser stabilization and finally, they function as spatial mode filters.

Triangular Cavity

A triangular cavity consists of three mirrors, each characterized by a field amplitude reflectivity r_i and transmissivity t_i. Mathematically, it behaves similarly to a linear cavity, with the main difference being that three mirrors are involved instead of two. The generalized expressions for the finesse F and the FSR are then given by

$$F \approx \frac{\pi\sqrt{r_1 r_2 r_3}}{1 - r_1 r_2 r_3}, \tag{1.9}$$

$$\mathrm{FSR} = \frac{c}{L_{12} + L_{23} + L_{31}}, \tag{1.10}$$

where L_{ij} denotes the distance between mirrors i and j.

In this work, the primary application of the triangular cavity is the superposition of two beams via mode matching. Transverse cavity modes can be described in terms of Hermite–Gaussian (HG) or Laguerre–Gaussian (LG) modes, depending on the chosen coordinate system. Mode mismatch or misalignment couples optical power into higher-order modes (HOM), which are typically undesired in precision measurements. Consequently, mode matching aims to maximize the overlap with the fundamental mode, typically the TEM_{00} mode, while minimizing power in HOMs.

One advantage of a non-confocal cavity (for example, a triangular cavity) is that the accumulated Gouy phase lifts the degeneracy of transverse modes, improving spatial mode discrimination. In particular, this allows a clearer distinction between horizontal and vertical mismatch. The confocal linear case is special, where transverse modes can become degenerate. A second advantage is that the cavity can also act as a spatial filter, separating the fundamental mode from higher-order transverse modes.

1.1.2 The Role of the Faraday Isolator

Faraday isolators (FIs) are essential components of GWOs, as illustrated in Figure 1.1. They provide optical isolation by suppressing back-reflected light while allowing forward transmission, thereby effectively acting as optical diodes. Such isolators are commonly used in front of the squeezer or the high-power laser system. Furthermore, they enable the injection of squeezed light into the filter cavity for the implementation of frequency-dependent squeezing and its subsequent injection into the interferometer dark port. To fulfill their respective functions effectively, FIs must satisfy two key requirements: high transmission efficiency (i.e., minimal optical losses) and strong suppression of back-reflected light. Likewise, the FR-based injection stage must also exhibit low optical losses.

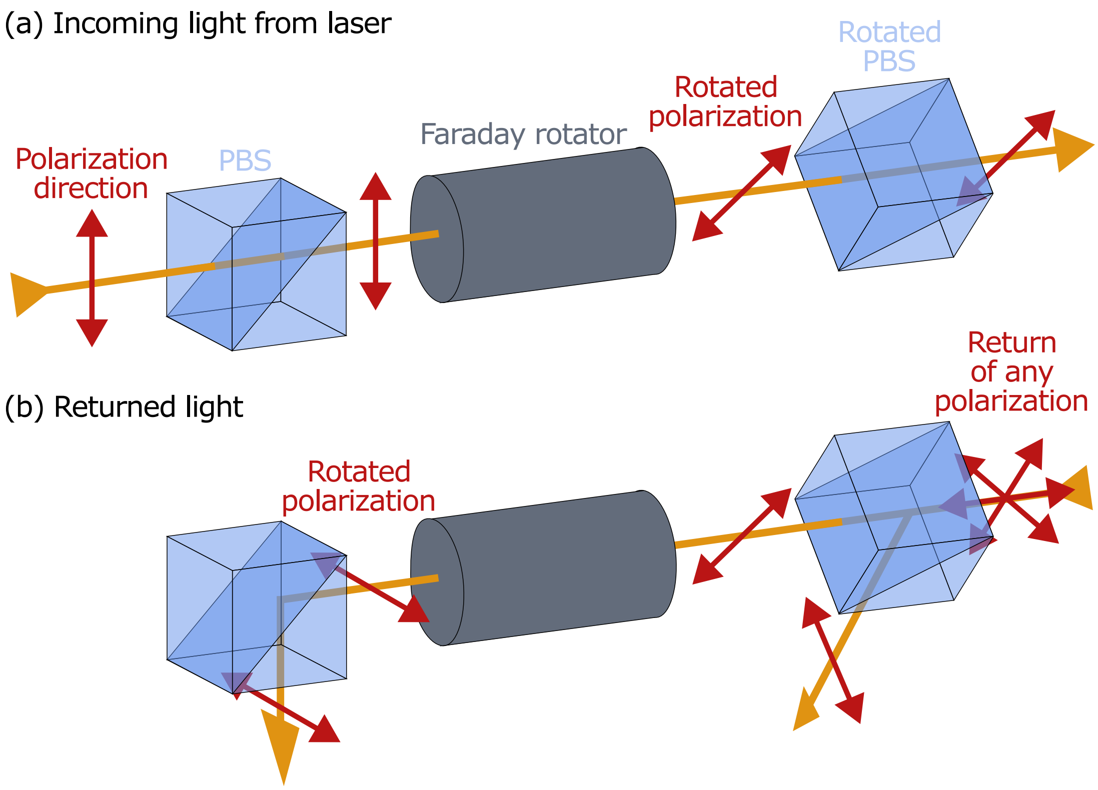

Figure 1.6: *Schematic representation of a Faraday isolator consisting of two polarization beam splitter (PBS) and a Faraday rotator, which contains a magneto-optical crystal that ideally rotates the polarization by 45°. (a) shows the forward direction, as seen from the laser, while (b) shows the return direction.*

Figure 1.6 illustrates the working principle of a Faraday isolator. In the forward direction (upper part of the figure), vertically polarized light enters the first polarizing beam splitter (PBS), which is aligned to transmit this polarization. The light then passes through the Faraday rotator, which contains a magneto-optical material of thickness d and Verdet constant V. A permanent magnet encloses the magneto-optical material with the magnetic field B. This combination produces a polarization rotation

$$\alpha = VBd. \tag{1.11}$$

Ideally, the Faraday rotator rotates the polarization by 45° clockwise, allowing full transmission through the second PBS, which is likewise rotated by 45° clockwise. Rotating the PBS simply means that its transmission axis is aligned with the rotated polarization of the light, ensuring that the light passes through without further attenuation. Any light returning toward the laser is reflected at one of the PBSs, preventing it from reaching the light source, as shown in the lower panel in Figure 1.6. Losses in this configuration arise only from component imperfections, such as absorption.

If the rotation of the Faraday rotator deviates from the ideal angle, light is partially blocked by the second PBS. The intensity transmission $I_{\text{tran.}}$ as a function of the angular offset θ_{offset} is given by the law of Malus [16] as

$$I_{\text{tran}} = I_0 \cos^2(\underbrace{|\theta_{\text{perfect}} - \theta_{\text{measured}}|}_{\theta_{\text{offset}}}), \tag{1.12}$$

where I_0 denotes the initial intensity. In GWOs, squeezed light passes through the FI twice. A 3° deviation from the ideal Faraday-rotator angle corresponds to a loss of approximately 1.1 % after two passes, assuming unit initial intensity.

In GWOs, a subsystem of the FI is also used to inject a secondary optical field (e.g., squeezed light) into the interferometer, typically consisting of a first PBS and a Faraday rotator (FR). In this configuration, the injected field is coupled into the system via the second input port of the first PBS, which corresponds to the reflected output path of the isolator. The injected field is prepared in a defined linear polarization state and co-propagates with the main optical field through the isolator. In the forward direction, the polarization state is rotated by the FR, and the second PBS directs both optical fields into the interferometer input path. In the reverse direction, however, light returning from the interferometer experiences the same non-reciprocal polarization rotation and is therefore projected onto a polarization state that is not aligned with the transmission axis of the second PBS. Consequently, it is reflected and routed toward the reflection port of the first PBS. To prevent this back-propagating light from reaching the secondary light source, an additional FI is placed in the injection path. In principle, a single PBS would already be sufficient for this injection scheme; however, in practical implementations the additional PBS in the FI configuration is often used as a monitoring channel.

1.2 Fundamentals of Second-Order Nonlinear Parametric Processes

In the regime of weak optical fields, the material response can be approximated as linear, such that the induced polarization scales proportionally with the applied electric field.

$$\mathbf{P}(t) = \varepsilon_0 \cdot \chi^{(1)}\mathbf{E}(t) \tag{1.13}$$

This linear relationship accounts for fundamental optical phenomena such as refraction and absorption. However, when the electric field strength reaches sufficiently high values, as achievable with modern laser sources, this linear approximation breaks down and higher-order contributions to the material polarization become significant.

In nonlinear media, the material polarization can be expressed as a power series in the electric field, giving rise to higher-order interaction terms. These effects are governed by the second-order nonlinear susceptibility, $\chi^{(2)}$, and give rise to phenomena such as second-harmonic generation, sum- and difference-frequency generation, and optical parametric amplification.

In this chapter I describe, the fundamental principles of second-order nonlinear parametric processes, including the nonlinear polarization, energy and momentum conservation (phase matching), and the basic equations governing frequency conversion in $\chi^{(2)}$ media. I follow closely the mathematical description by R. W. Boyd [17] and H. A. Bachor [18].

1.2.1 Nonlinear Polarization and Classification of Second-Order Parametric Processes

In second-order nonlinear processes, an optical field interacts with a nonlinear medium that can produce new optical fields at various frequencies ω. A defining characteristic of these interactions is that they are parametric: energy and momentum are exchanged between the interacting fields, while the medium remains in its ground state. This can be expressed as

$$\omega_1 = \omega_2 + \omega_3, \tag{1.14}$$

$$\mathbf{k}_1 = \mathbf{k}_2 + \mathbf{k}_3, \tag{1.15}$$

where $\mathbf{k}_{1,2,3} = \frac{2\pi n(\lambda)}{\lambda_{1,2,3}}\mathbf{u}_{1,2,3}$ is the wavevector of the field, $\lambda_{1,2,3}$ its wavelength, $\mathbf{u}_{1,2,3}$ a unit vector along the direction of propagation, and the indices 1, 2, and 3 correspond to the pump, signal, and idler fields, respectively.

An illustration of this process is shown in Figure 1.7 (left). As discussed above, the linear approximation for the material polarization is no longer sufficient at high field intensities. The nonlinear polarization can be obtained by a Taylor expansion of the material response:

$$\mathbf{P}(t) = \varepsilon_0\Big(\underbrace{\chi^{(1)}\mathbf{E}(t)}_{\text{linear}} + \underbrace{\chi^{(2)}\mathbf{E}^2(t) + \chi^{(3)}\mathbf{E}^3(t) + \dots}_{\text{nonlinear}}\Big). \tag{1.16}$$

Correspondingly, the time-dependent electric field can be expressed as

$$\mathbf{E}(t) = \mathbf{E}_1 e^{-i\omega_1 t} + \mathbf{E}_2 e^{-i\omega_2 t} + \text{c.c.} \tag{1.17}$$

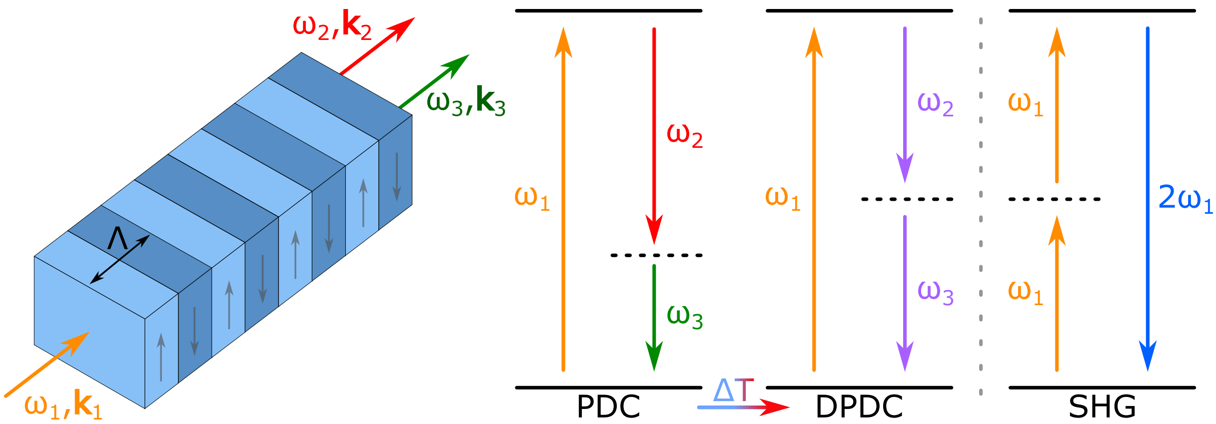

Figure 1.7: *Schematic illustration: the left panel shows energy and momentum conservation in a nonlinear process occurring in a periodically poled nonlinear crystal with poling period Λ. The right panel depicts an energy-level diagram illustrating common second-order nonlinear processes. It starts with basic PDC, which can be temperature-tuned by ΔT to achieve DPDC, and includes the reverse process, SHG.*

In this thesis, only second-order nonlinear effects are considered. Substituting the expressions above and retaining only the $\chi^{(2)}$ terms yields

$$\mathbf{P}^{(2)}(t) = \varepsilon_0 \chi^{(2)} \mathbf{E}^2(t) = \sum_n \mathbf{P}(\omega_n) e^{i\omega_n t}, \tag{1.18}$$

where ω_n represents the generated frequency components, e.g $\omega_1 \pm \omega_2$, and ε is the vacuum permittivity. By substituting the expressions for the electric fields and expanding the squares, we obtain the following general second-order polarization terms:

$$\mathbf{P}(2\omega_{1,2}) = \varepsilon_0 \chi^{(2)} \mathbf{E}_{1,2}^2 \qquad \text{SHG} \tag{1.19}$$

$$\mathbf{P}(\omega_1 + \omega_2) = 2\varepsilon_0 \chi^{(2)} \mathbf{E}_1 \mathbf{E}_2 \qquad \text{SFG} \tag{1.20}$$

$$\mathbf{P}(\omega_1 - \omega_2) = 2\varepsilon_0 \chi^{(2)} \mathbf{E}_1 \mathbf{E}_2^* \qquad \text{DFG} \tag{1.21}$$

Second-Harmonic Generation (SHG) generates a new field at twice the frequency of a single input field, i.e., $\omega_1 = \omega_2$.

Sum-Frequency Generation (SFG) generates a new field from the sum of two different input fields, i.e., $\omega_3 = \omega_1 + \omega_2$.

Difference-Frequency Generation (DFG) generates a new field from the difference of two input fields, i.e., $\omega_3 = \omega_1 - \omega_2$.

The right panel in Figure 1.7 shows a visualization of these processes using virtual energy levels. As an example, parametric down-conversion (PDC) is illustrated, where a pump photon at frequency ω_1 is converted into two lower-frequency photons, ω_2 and ω_3, such that $\omega_1 = \omega_2 + \omega_3$. SFG corresponds to the reverse process, i.e., the combination of two fields to generate a higher-frequency field, while DFG corresponds to the difference process. On the far right side of the panel, SHG is displayed.

Heating the nonlinear crystal modifies effective refractive indices, enabling output wavelength tuning. When both generated fields reach the same frequency, i.e. $\omega_2 = \omega_3$, the process is called degenerate parametric down-conversion (DPDC). A detailed discussion of temperature tuning and quasi phase matching is given in the following section.

I would like to highlight a special sub-case that plays a major role in this work, namely optical parametric oscillation (OPO) and its cavity-enhanced implementation. By placing a nonlinear medium inside an optical cavity and pumping it with a pump field at frequency ω_1, the process generates two output frequencies, ω_2 and ω_3, fulfilling the energy conservation $\omega_1 = \omega_2 + \omega_3$. Although formally identical to cavity-enhanced PDC, the cavity provides feedback, enhances the nonlinear interaction, and enables coherent oscillation of the generated fields.

The threshold pump power P_{thr} is defined as the point at which the number of generated photons becomes sufficiently large that the output fields can be described as bright classical light sources and is given by [19] as

$$P_{\text{thr}} = \frac{\pi^2}{4F_{\omega_{2,3}}^2\, B_{\omega_1}\, \eta_{\text{NL}}}, \tag{1.22}$$

where $F_{\omega_{2,3}}$ denotes the cavity finesse at the converted modes, B_{ω_1} the intracavity build-up factor of the pump field, and the nonlinear conversion efficiency factor η_{NL} given by the material. Two critical operational regimes of the OPO must be distinguished:

Above-threshold operation: The non-degenerate OPO is commonly used as a bright and widely tunable laser source [20, 21, 22]. In most cases, one of the generated fields is not utilized, which limits the maximum conversion efficiency to approximately 50 %. This limitation can be overcome by using a temperature-tuned nonlinear medium, mostly a crystal, which shifts both output fields together, enabling a degenerate operation, alias the degenerate optical parametric oscillation (DOPO), and reaching significantly higher conversion efficiencies [23].

Below-threshold operation: In this regime, the output fields are weak and occupied with very few photons, giving rise to nonclassical states of light. In particular, the OPO generates a so-called squeezed state. A detailed explanation of this state can be found in Section 1.3.3.

As mentioned above, the OPO process can be optimized by adjusting the crystal temperature. In the next chapter, we will examine in detail how temperature tuning can be used to optimize nonlinear interactions, a concept known as quasi-phase matching.

1.2.2 Principles of Phase Matching

For a nonlinear process to occur, both energy and momentum conservation must be satisfied. Momentum conservation, in particular, requires a specific phase relation, meaning that the interacting optical waves must maintain a fixed phase while propagating through the nonlinear medium, thereby enabling efficient energy transfer between the fields. The following discussion is based on the analysis presented in R. W. Boyd [17].

In one dimension, the phase matching condition is given by

$$\Delta k = k_1 - k_2 - k_3 \equiv 0, \tag{1.23}$$

where k_1, k_2, and k_3 denote the wave vectors of the interacting waves of the pump, signal, and idler fields along the propagation direction. If this condition is fulfilled, the generated nonlinear polarization remains in phase with the generated field, leading to a monotonic increase of the conversion efficiency along the propagation direction. Achieving this condition requires careful control of the refractive indices for each interacting wave. A widely used and well-established method is temperature tuning of the nonlinear crystal, which exploits the birefringence of the optical material. However, this approach has limitations, since in some materials the birefringence is nearly constant or insufficient to fully compensate the wave-vector mismatch.

When conventional phase matching reaches its limits, an alternative technique known as quasi-phase matching (QPM) can be applied. In this approach, a periodically poled nonlinear crystal is used, in which the sign of the effective nonlinear coefficient d_{eff} alternates between positive and negative values. One period of this modulation is defined as the poling period Λ, as illustrated in the left panel of Figure 1.7.

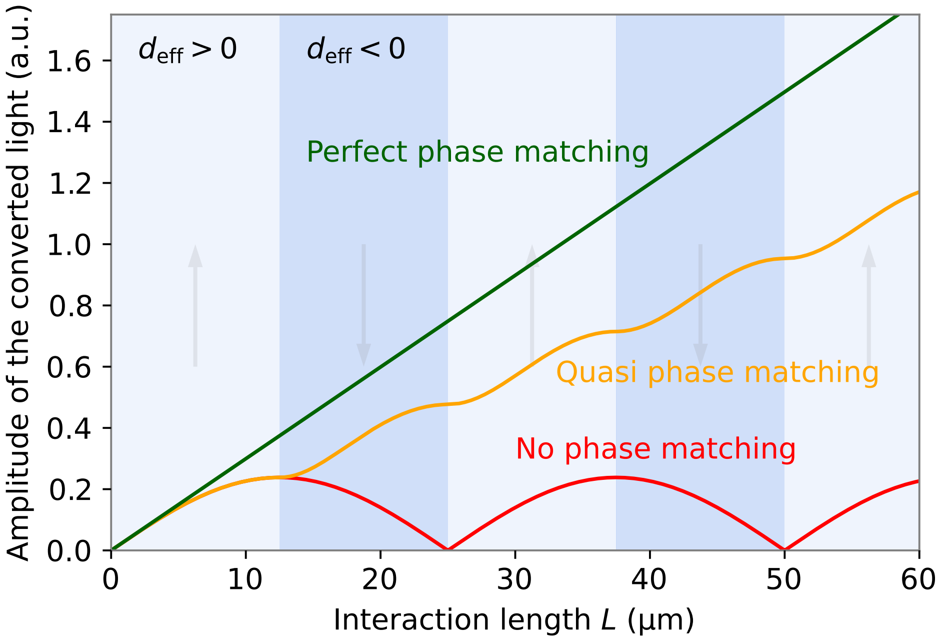

Figure 1.8: *Simulation of three different phase matching conditions in a periodically poled nonlinear crystal. For perfect phase matching, the generated field amplitude increases linearly with propagation length. Without phase matching (no phase matching case), a nonzero wave-vector mismatch causes the amplitude to oscillate along the propagation direction. Finally, the quasi phase matching case uses a periodic modulation of the nonlinear coefficient to compensate for the phase mismatch, resulting in a monotonic increase of the field amplitude with interaction length. Simulation taken from [24].*

Figure 1.8 illustrates the generated field amplitude as a function of interaction length for three different phase matching scenarios: the *no phase matching* case, the *perfect phase matching* case, and the *quasi phase matching* case. These three cases are described in the following. Without phase matching, a nonzero wave-vector mismatch $\Delta k = k_1 - k_2 - k_3 \neq 0$ causes the generated field to oscillate in amplitude, reducing the net conversion efficiency. Critical phase matching corresponds to perfect phase matching, where the amplitude increases monotonically along the propagation direction. In QPM, the periodic inversion of d_{eff} effectively resets the phase of the nonlinear polarization after each coherence length L_{coh}, i.e., the buildup length over which the accumulated phase mismatch reaches π (so that the contributions add constructively), allowing a monotonic increase of the generated field along the crystal. For first-order QPM, the optimal poling period is given by $\Lambda = 2L_{\mathrm{coh}}$ as shown in Figure 1.7 (left). Mathematically, the first-order effective phase-matching condition can be written as

$$\Delta k_{\mathrm{m}} = k_1 - k_2 - k_3 - \frac{2\pi}{\Lambda}, \tag{1.24}$$

and it is fulfilled when $\Delta k_{\mathrm{m}} = 0$. This effective phase-matching condition can be optimized by adjusting the temperature, since the temperature dependence of the refractive indices changes the effective phase accumulation.

1.3 From Classical Fields to Quantum States: Coherent and Squeezed Light

Quantum optical experiments rely on highly coherent laser sources, which serve as carriers for both control fields and non-classical states. In this thesis, I focus in particular on squeezed light, which exhibits reduced quantum fluctuations in a chosen quadrature. To provide the theoretical background, this chapter first introduces coherent states, which serve as the closest quantum analogue of classical laser light, following the formalism of Gerry and Knight [25]. Building on this, squeezed states are then introduced by the formalism of Gerry and Knight [25] and R. Schnabel [26], highlighting their distinct quantum properties and relevance for the experiments discussed in this work.

1.3.1 Light Field Quantization

We begin by considering a classical harmonic oscillator as a model for a single mode of the electromagnetic field in a one-dimensional cavity along the z-axis, with the electric field polarized along the x-direction. The classical Hamiltonian of this oscillator is given by

$$H = \frac{1}{2}(p^2 + \omega^2 q^2), \tag{1.25}$$

where q and p are the canonical position and momentum variables. To describe the system quantum mechanically, we replace these variables with operators $\hat{q}$ and $\hat{p}$, which satisfy the canonical commutation relation $[\hat{q}, \hat{p}] = i\hbar$, where the identity operator $\hat{I}$ has been omitted for brevity. With this, the quantum Hamiltonian becomes

$$\hat{H} = \frac{1}{2}(\hat{p}^2 + \omega^2 \hat{q}^2). \tag{1.26}$$

Introducing the annihilation operator $\hat{a}$ and the creation operator $\hat{a}^\dagger$ as

$$\hat{a} = \frac{1}{\sqrt{2\hbar\omega}}(\omega\hat{q} + i\hat{p}), \tag{1.27}$$

$$\hat{a}^\dagger = \frac{1}{\sqrt{2\hbar\omega}}(\omega\hat{q} - i\hat{p}), \tag{1.28}$$

which satisfy the commutation relation $[\hat{a}, \hat{a}^\dagger] = 1$, the Hamiltonian can be rewritten as

$$\hat{H} = \hbar\omega\left(\hat{a}^\dagger\hat{a} + \frac{1}{2}\right). \tag{1.29}$$

The number operator $\hat{n}$ is given as $\hat{a}^\dagger\hat{a}$. Following the standard formalism [25], the field quadratures are defined with the annihilation and creation operators as

$$\hat{X} = \frac{1}{2}(\hat{a} + \hat{a}^\dagger), \tag{1.30}$$

$$\hat{Y} = \frac{1}{2i}(\hat{a} - \hat{a}^\dagger), \tag{1.31}$$

which can equivalently be expressed in terms of position $\hat{X} = \sqrt{\frac{\omega}{2\hbar}}\hat{q}$ and momentum $\hat{Y} = \frac{1}{\sqrt{2\hbar\omega}}\hat{p}$. These operators satisfy the commutator relation $[\hat{X}, \hat{Y}] = \frac{i}{2}$. The Hamiltonian operator can be rewritten as

$$\hat{H} = \hbar\omega(\hat{X}^2 + \hat{Y}^2), \tag{1.32}$$

and the Heisenberg uncertainty relation is given by

$$\langle(\Delta\hat{X})^2\rangle\langle(\Delta\hat{Y})^2\rangle \geq \frac{1}{16}. \tag{1.33}$$

A quadrature operator for an arbitrary phase angle θ is defined as

$$\hat{X}_\theta = \cos(\theta)\hat{X} + \sin(\theta)\hat{Y}. \tag{1.34}$$

1.3.2 Coherent State of Light

Coherent states $|\alpha\rangle$, eigenstates of the annihilation operator, represent the closest quantum analogue to classical light fields. A coherent state is defined as the eigenstate of the annihilation operator,

$$\hat{a}\,|\alpha\rangle = \alpha\,|\alpha\rangle\,, \tag{1.35}$$

where α is a complex number. The coherent state can be written as

$$|\alpha\rangle = \hat{D}(\alpha)\,|0\rangle \tag{1.36}$$

$$= \exp\left(-\frac{1}{2}|\alpha|^2\right)\sum_{n=0}^{\infty}\frac{\alpha^n}{\sqrt{n!}}\,|n\rangle\,. \tag{1.37}$$

$\hat{D}(\alpha) = \exp(\alpha\hat{a}^\dagger - \alpha^*\hat{a})$ describes the displacement operator acting on a vacuum field $|0\rangle$. For the coherent state, the expectation value of an arbitrary quadrature operator is

$$\langle\alpha|\,\hat{X}_\theta\,|\alpha\rangle = \langle\hat{X}_\theta\rangle_\alpha = \cos(\theta)\langle\hat{X}\rangle_\alpha + \sin(\theta)\langle\hat{Y}\rangle_\alpha, \tag{1.38}$$

with $\langle\hat{X}\rangle_\alpha = \Re(\alpha)$ and $\langle\hat{Y}\rangle_\alpha = \Im(\alpha)$. The coherent state saturates the Heisenberg uncertainty relation

$$\langle(\Delta\hat{X})^2\rangle\,\langle(\Delta\hat{Y})^2\rangle = \frac{1}{4}\cdot\frac{1}{4} = \frac{1}{16}, \tag{1.39}$$

and therefore is also referred to as a minimum-uncertainty state.

Figure 1.9 illustrates coherent states in the so-called phasor diagram. Panel (a) shows a quantum vacuum state, while panel (b) shows a coherent state with amplitude $|\alpha|$. In both cases, the size and shading indicate the identical quantum uncertainties of the $\hat{X}$- and $\hat{Y}$-quadratures.

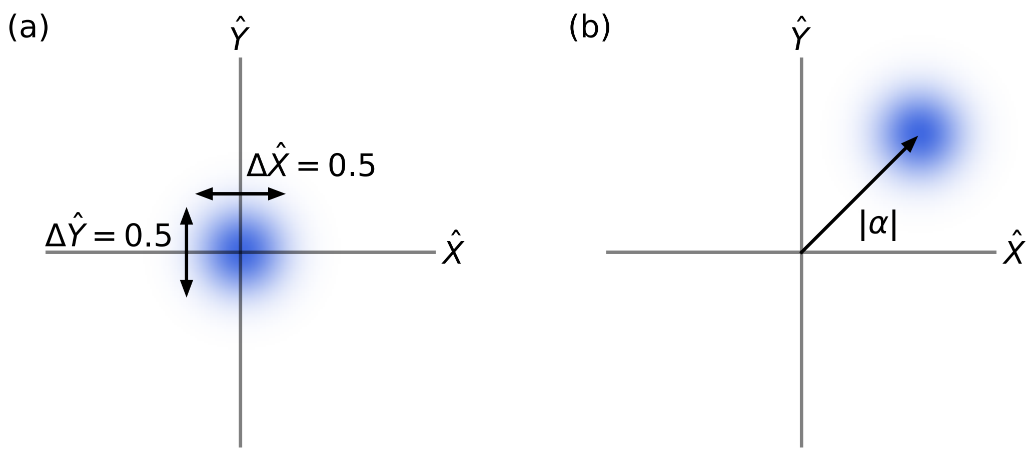

Figure 1.9: *Phase-space simulation of (a) a quantum vacuum state and (b) a coherent state with amplitude $|\alpha|$. The size of the circle and the shading illustrate the equal uncertainty in both quadratures.*

1.3.3 Squeezed State of Light

A special type of quantum light is the so-called squeezed light, which plays a central role in this thesis as well as in a variety of quantum experiments, including quantum metrology. Squeezed states reduce quantum uncertainty in one quadrature while increasing it in the conjugate quadrature, known as the squeezed and anti-squeezed quadratures:

$$\langle(\Delta\hat{X})^2\rangle < \frac{1}{4},$$
$$\langle(\Delta\hat{Y})^2\rangle > \frac{1}{4},$$

or vice versa, while the Heisenberg uncertainty of $\langle(\Delta\hat{X})^2\rangle\langle(\Delta\hat{Y})^2\rangle = \frac{1}{16}$ remains satisfied. This transforms the circular uncertainty region of the coherent state into an ellipse, as shown in Figure 1.10. Panel (a) shows a squeezed vacuum state whereas (b) depicts a displaced squeezed state with amplitude $|\alpha|$.

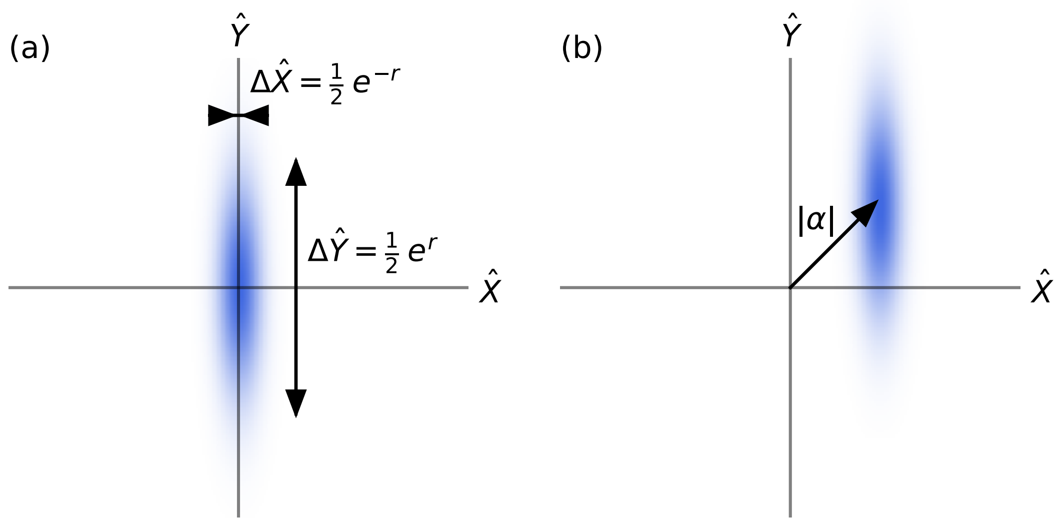

Figure 1.10: *Phase-space simulation of (a) a quantum vacuum squeezed state and (b) a displaced squeezed state with amplitude $|\alpha|$. The size and shading of the ellipse illustrate the quantum uncertainty in both quadratures. In both panels, the squeezing occurs along the $\hat{X}$ quadrature, while the anti-squeezing is along the $\hat{Y}$ quadrature.*

A generic quadrature operator can be written as

$$\hat{X}_\theta = \frac{1}{2}(\hat{a}e^{-i\theta} + \hat{a}^\dagger e^{i\theta}) \tag{1.40}$$

with $\hat{X}_{\theta=0} = \hat{X}$ and $\hat{X}_{\theta=\frac{\pi}{2}} = \hat{Y}$.

The squeeze operator is defined as

$$\hat{S}(\xi) = \exp\left[\frac{1}{2}(\xi^*\hat{a}^2 - \xi\hat{a}^{\dagger 2})\right], \tag{1.41}$$

where $\xi = re^{i\theta}$ and r is the squeeze parameter. Applying the squeeze operator to an arbitrary state $|\Psi\rangle$ yields the squeezed state $|\Psi_S\rangle = \hat{S}(\xi)|\Psi\rangle$. In the special case where $|\Psi\rangle$ is a vacuum state $|0\rangle$, the quadrature variances are given by

$$\langle(\Delta\hat{X})^2\rangle = \frac{1}{4}\left[\cosh(r)^2 + \sinh(r)^2 - 2\sinh(r)\cosh(r)\cos(\theta)\right], \tag{1.42}$$

$$\langle(\Delta\hat{Y})^2\rangle = \frac{1}{4}\left[\cosh(r)^2 + \sinh(r)^2 + 2\sinh(r)\cosh(r)\cos(\theta)\right]. \tag{1.43}$$

For $\theta = 0$, these reduce to

$$\langle(\Delta\hat{X})^2\rangle = \frac{1}{4}e^{-2r}, \tag{1.44}$$

$$\langle(\Delta\hat{Y})^2\rangle = \frac{1}{4}e^{+2r}. \tag{1.45}$$

Because squeezing depends on the phase, the variance along a rotated quadrature $\hat{X}_\theta$ is the projection of the squeezed ellipse onto the measurement axis,

$$\Delta^2\hat{X}_\theta = \Delta^2\hat{X}\cos(\theta)^2 + \Delta^2\hat{Y}\sin(\theta)^2. \tag{1.46}$$

Squeezed states of lights play a crucial role in modern quantum technologies, as they reduce the noise in a specific quadrature and thus enhance the sensitivity of measurement along that quadrature.

Squeezing in a Degenerate Optical Parametric Oscillator

This section presents squeezing in a degenerate optical parametric oscillator. The analysis follows the treatment by Ling-An Wu, Min Xiao, and H. J. Kimble [19].

In a DOPO, the quadrature variances are represented by the squeezing functions: $\langle(\Delta\hat{X})^2\rangle \propto S_-$ (phase quadrature) and $\langle(\Delta\hat{Y})^2\rangle \propto S_+$ (amplitude quadrature). To facilitate the description of different noise regimes in later chapters (see Chapter 4), I also introduce two reference variances. The vacuum (shot-noise) variance is denoted by S_v, corresponding to the quadrature noise of the quantum vacuum state. A thermal-like state with increased and approximately isotropic quadrature noise is denoted by S_t. Together with the squeezed and anti-squeezed variances S_- and S_+, these definitions provide a consistent notation for all noise levels discussed in this thesis. Squeezing dynamics in and around the threshold regime are described by

$$S_\pm(\nu) = 1 \pm \frac{4\Gamma_1|\epsilon_2|(\Gamma_2^2+\nu^2)}{[\Gamma_2(\Gamma_1 \mp |\epsilon_2|) + |\epsilon_1|^2 - \nu^2] + \nu^2(\Gamma_1 \mp |\epsilon_2| + \Gamma_2)^2}, \tag{1.47}$$

where $\Gamma_{1/2}$ are the amplitude decay rates of the cavity modes and ν is the Fourier frequency. The quantities $\epsilon_{1/2} = \kappa\alpha_{1/2}$ are defined in terms of the intracavity amplitudes α_1 (subharmonic field) and α_2 (fundamental field), with κ denoting the nonlinear coupling coefficient.

Equation 1.47 describes the general squeezing spectrum in terms of the intracavity amplitudes $\epsilon_{1,2}$. In order to connect this expression to experimentally accessible parameters, the pump amplitude is related to the pump power via $|\epsilon_2| \propto \sqrt{P}$. The threshold pump power P^thr is defined by the condition $|\epsilon_2| = |\epsilon_2^\mathrm{thr}|$ at the onset of parametric oscillation. This allows the squeezing spectrum to be expressed in terms of the dimensionless ratio P/P^thr in the below-threshold regime. The corresponding equation is

$$S_\pm = 1 \pm \eta\frac{4\sqrt{P/P^\mathrm{thr}}}{4(\nu/\Gamma_1)^2 + (1 \mp \sqrt{P/P^\mathrm{thr}})^2}. \tag{1.48}$$

Squeezed states of light are highly sensitive to optical losses, which represent the main limiting factor for achieving high squeezing levels. To quantify this effect, we introduce the overall detection efficiency of the system as η.

Figure 1.11 shows a simulation based on Equation 1.48, where anti-squeezing (S_+) and squeezing (S_-) are shown relative to the shot-noise level. This simulation considers realistic parameters reported in the paper [27], while neglecting optical losses. In particular, the cavity decay rate is $\Gamma_1 \approx 110\,\mathrm{MHz}$ at a Fourier frequency of $\nu \approx 5\,\mathrm{MHz}$. Maximum squeezing is achieved for $P/P^{\mathrm{thr}} \rightarrow 1$. In other words, operation close to the threshold ($P \lesssim P^{\mathrm{thr}}$) yields maximum squeezing. The achievable squeezing and anti-squeezing levels are limited by the ratio of the chosen Fourier frequency and the cavity decay rate.

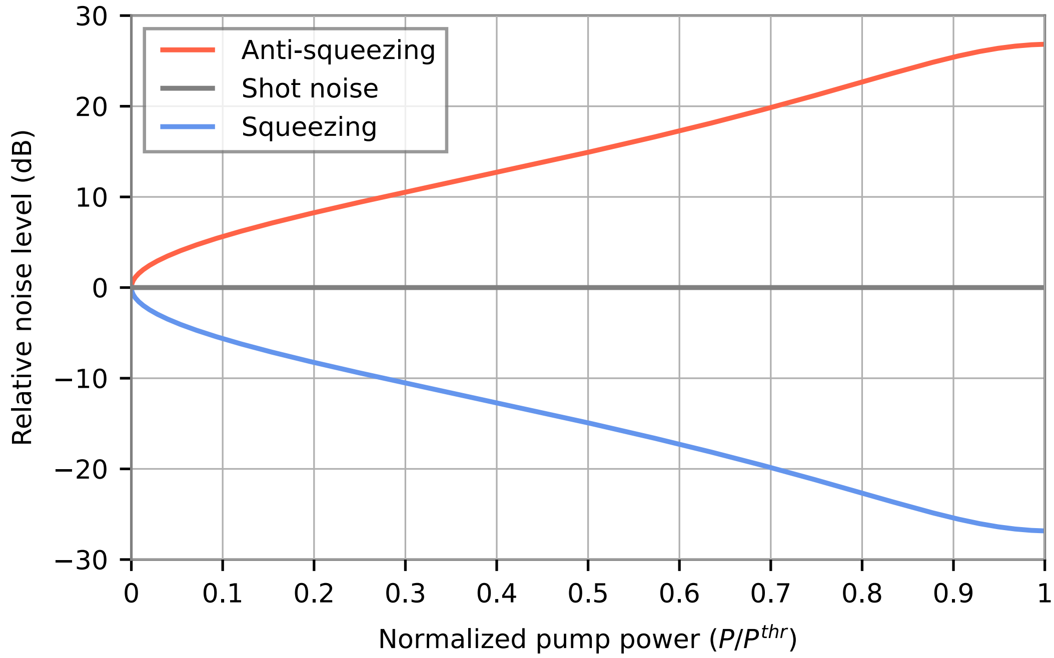

Figure 1.11: *Phase- and amplitude-quadrature squeezing $S_\pm$ as a function of the normalized pump power P/P^{thr}. The red line corresponds to anti-squeezing, the blue line to squeezing, and the grey line to shot noise.*

Impact of Optical Losses on Squeezing

Losses are modeled as a beam splitter with transmission η, mixing the ideal squeezed state with a vacuum state and increasing the squeezed quadrature variance. In contrast, the variance of the anti-squeezing quadrature is already large, making it less sensitive to losses. This mixing is ultimately limited by the total loss of a quantum state, which can transform a squeezed state towards a coherent like state.

Figure 1.12 shows an analytical plot of this formula, displaying the observed (anti-)squeezing as a function of optical loss (1-η) in percent, for different pump-to-threshold power ratios and $\nu/\Gamma_1 = 0.005$. Squeezing is shown as the blue trace, while anti-squeezing is shown in red.

This demonstrates that losses have a much stronger impact on squeezing than on anti-squeezing, highlighting the importance of minimizing optical losses in experiments aiming for high squeezing levels.

The achievable squeezing in a DOPO is primarily determined by the normalized pump power P/P^{thr} and the overall detection efficiency η, as seen in Equation 1.48. In realistic setups, this intrinsic squeezing is limited by optical losses that reduce the overall efficiency. These losses include, for example, imperfect quantum efficiency (QE) of photodiodes, absorption and scattering in optical components, and other technical imperfections, which together constitute the dominant loss channels in the system. This highlights that high pump power alone is insufficient to achieve strong squeezing; instead, minimizing optical losses is essential. Moreover, phase-matching conditions further limit the achievable squeezing by reducing the effective nonlinear gain.

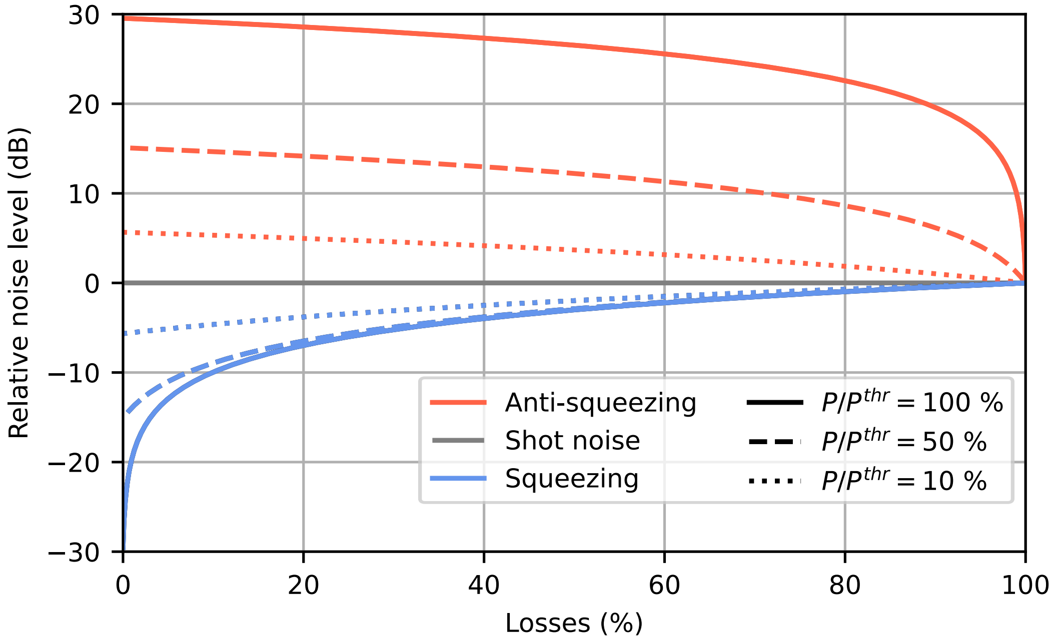

Figure 1.12: *Simulation of (anti-)squeezing relative to the shot-noise level as a function of optical loss for different pump-to-threshold power ratios. Two main observations emerge: first, squeezing is significantly more sensitive to losses; second, anti-squeezing is strongly affected only at very high losses.*

1.4 Detection Strategy for Squeezed Light

Accurate detection of squeezed states requires photodetectors with high efficiency, as optical loss directly degrades the observable squeezing. Various photodetector technologies exist for this purpose, including PIN photodiodes and avalanche-based systems. In this thesis, I focus on PIN photodiodes, as they were used in all experiments. In addition to the detector itself, the detection strategy plays an equally important role. A widely used approach is balanced homodyne detection, which employs two photodiodes and allows measurement of arbitrary quadratures through control of the local oscillator (LO) phase. As photodiodes form the core of this technique, we first review their fundamental properties before discussing the homodyne detection scheme applied in this work.

1.4.1 Basics of Photodiodes for Quantum Optical Detection

Squeezed states are highly sensitive to optical loss, meaning that any inefficiency in the detection chain directly reduces the observable squeezing and increases decoherence. Photodiodes are the last element in the detection chain, and their performance is of central importance for quantum-noise–limited measurements. For this reason, it is essential to understand the key properties of the photodiodes used in this work. Photodiodes operating at 1064 nm are widely used in the gravitational-wave community, which has driven the development of highly efficient and low-noise devices [28]. In contrast, photodiode technologies for the proposed 2 μm wavelength regime are less mature. Since detection of squeezed states places stringent requirements on both quantum efficiency (QE) and dark noise, we briefly summarize these two properties in the following. The theoretical considerations presented here follow the analysis by Abdelhakim Boudkhil, Asmaâ Ouzzani, and Belabbes Soudini [29].

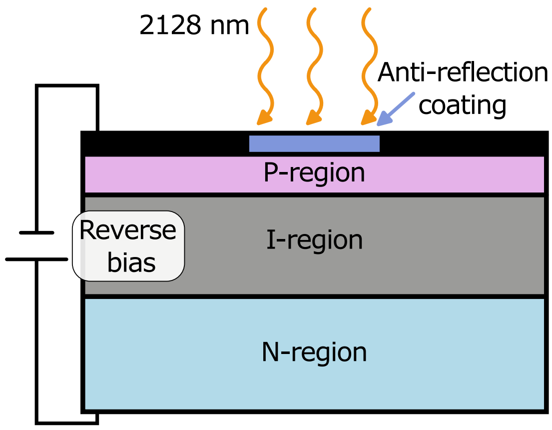

Figure 1.13: *Schematic representation of a PIN photodiode, illustrating the P-, I-, and N-regions.*

A schematic of a PIN photodiode is shown in Figure 1.13. The P-region provides an excess of holes, while the N-region provides an excess of electrons. The intrinsic (I) region serves as the photon absorption layer, and its performance can be tuned by adjusting the reverse bias voltage applied to the diode.

Photodiode Noise

Photodiode detection is affected by several noise sources, which can be broadly divided into two categories:

Fundamental noise: The first is thermal noise, originating from the random motion of electrons due to thermal energy. This can be described by

$$\bar{i}^2_{\text{thermal}} = \frac{4k_B T \Delta f}{R}, \tag{1.49}$$

where k_B is Boltzmann's constant, T is the temperature in Kelvin, R is the photodiode resistance, and Δf is the measurement bandwidth. A second fundamental source is quantum noise, commonly referred to as shot noise. It describes the stochastic fluctuation of the photocurrent due to the discrete nature of photons:

$$\bar{i}^2_{\text{shot}} = 2e(I_{\text{dark}} + I_{\text{light}})\Delta f, \tag{1.50}$$

where I_{dark} is the photodiode dark current, representing the current contribution arising from intrinsic (mainly thermal) charge-carrier processes in the absence of incident light, and I_{light} is the photocurrent due to incident light.

Excess noise: Includes pink noise, also known as 1/f noise, which arises from defects and barrier effects in the semiconductor:

$$\bar{i}^2_{\text{pink}} = \frac{A}{f^\alpha}, \tag{1.51}$$

where f is the measurement frequency, A is a proportionality constant, and α is the power-law exponent characterizing the spectral frequency dependence. The generation–recombination (G-R) noise, caused by the random generation and recombination of carriers, is defined as

$$\bar{i}^2_{\text{G-R}} = \frac{A}{1 + (2\pi f \tau)^2}, \tag{1.52}$$

where τ is the average carrier lifetime and A is a proportionality constant.

The total noise of the photodiode is then given by

$$\bar{i}^2_{\text{total}} = \bar{i}^2_{\text{thermal}} + \bar{i}^2_{\text{shot}} + \bar{i}^2_{\text{pink}} + \bar{i}^2_{\text{G-R}}. \tag{1.53}$$

Figure 1.14 illustrates the different noise contributions of a photodiode, compiled from a variety of realistic photodiode parameters. The parameters used for the thermal noise calculation are $T = 293\,\text{K}$ and $R = 4\,\text{k}\Omega$, corresponding to realistic operating conditions of the FDG50 model from THORLABS [30]. For shot noise, values of $I_{\text{light}} = 1\,\text{mA}$ and $I_{\text{dark}} = 60\,\mu\text{A}$ are assumed, representing typical experimental operating conditions [30]. Pink noise is modeled using $A^2 = 2.4 \cdot 10^{-10}$ and $\alpha = 1$, based on the self-measured experiment described in Section 3.2.1. For the G–R noise model, the parameters $\tau = 3\,\text{ms}$ and $A^2 = 1 \cdot 10^{-10}$ are used, based on the model described in [31]. In practical experiments, the dominant noise contribution is typically either shot noise or pink noise, depending on the frequency and wavelength. For squeezed light measurements, the system is optimized to operate in the shot-noise-limited regime.

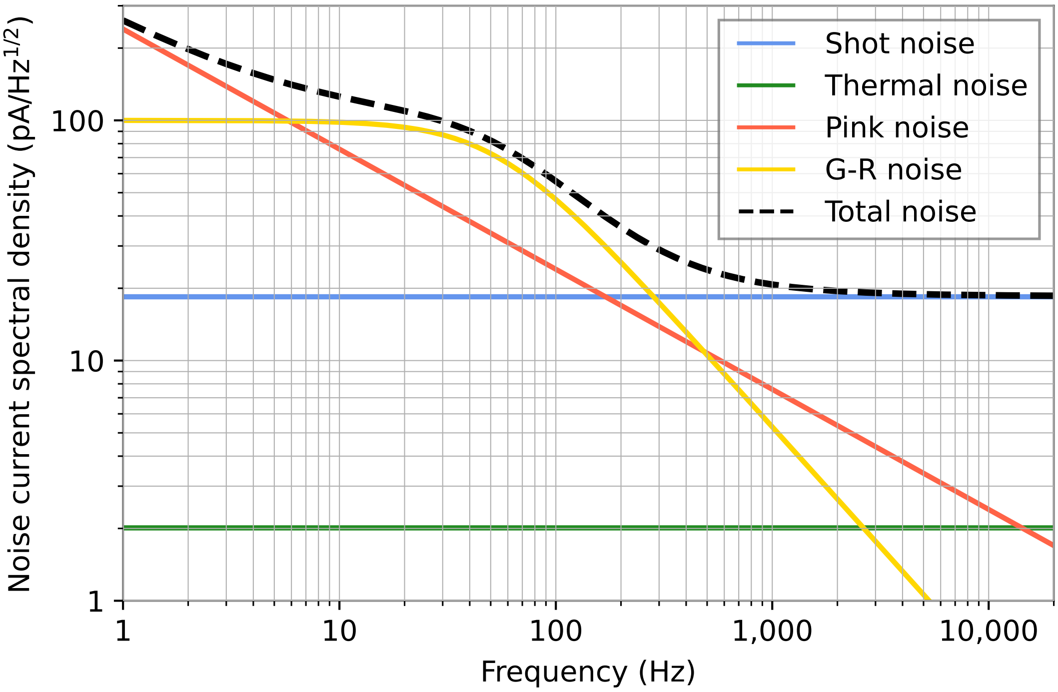

Figure 1.14: *Illustration of the various individual and total noise contributions in a photodiode. In typical experiments, the measurement is dominated by shot or pink noise, while generation–recombination and thermal noise play a minor role.*

Photodiode Efficiency

For squeezing experiments, the most important photodiode parameter is the quantum efficiency, η_{QE}. This quantity describes the probability of generating an electron–hole pair for each absorbed photon. Intuitively, any photon that is not absorbed represents a loss in the system, which should generally be minimized.

Here, QE is defined to include contributions from the dark current or, equivalently, the dark voltage after transimpedance amplification. The detection efficiency (DE), η_{DE}, refers to the photodiode's response excluding dark contributions. In the following, we express both quantities in terms of voltage, since this is directly relevant for later experiments. These definitions lead to:

$$\eta_{\mathrm{DE}} = \frac{U_{\mathrm{tot}} - U_{\mathrm{dark}}}{U_{\mathrm{perf}}}, \tag{1.54}$$

$$\eta_{\mathrm{QE}} = \frac{U_{\mathrm{tot}} - U_{\mathrm{dark}}}{U_{\mathrm{perf}} + U_{\mathrm{dark}}}, \tag{1.55}$$

where U_{tot} is the total measured voltage, U_{dark} is the contribution when no light is impinging on the PD, and U_{perf} denotes the idealized voltage that would be produced if every photon incident on the photodiode were converted into exactly one electron–hole pair and the dark voltage were zero.

1.4.2 Balanced Homodyne Detection

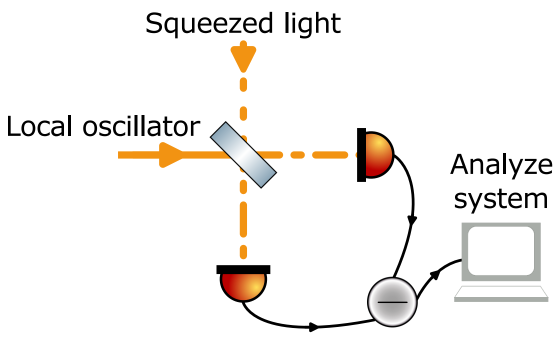

Figure 1.15: *Schematic setup of a homodyne detection system for the measurement of squeezed light.*

Figure 1.15 shows a typical experimental setup for homodyne detection. A strong coherent beam, referred to as the LO, is spatially overlapped with the squeezed beam at a beam splitter. The quality of this overlap is crucial for an accurate quadrature measurement and can be quantified using two common methods. The first method employs a reference cavity to match the spatial modes of both beams and to quantify the mode-matching of each beam to this cavity, which determines the quality of their overlap. The second method uses an interference measurement, where the mode overlap is determined from the visibility V, defined as

$$V = \frac{I_{\text{max}} - I_{\text{min}}}{I_{\text{max}} + I_{\text{min}}}. \tag{1.56}$$

Here, I_{max} and I_{min} denote the maximum and minimum intensities of the interference pattern on the PD, respectively. For both measurement methods, the squeezed field must be accompanied by a coherent carrier. After optimal alignment, the two output ports of the beam splitter are detected by identical photodiodes, and the corresponding photocurrents are subtracted electronically. This balanced detection scheme suppresses classical amplitude noise of the LO and enables a direct measurement of the quantum noise of the squeezed field. To gain a deeper understanding of this process, the mathematical description of homodyne detection is reviewed in the following, based on the treatment given in [17].

The interference outputs after the beam splitter are given by

$$\hat{a}_1 = \frac{1}{\sqrt{2}}(\hat{a}_{\text{LO}} + \hat{a}_{\text{sqz}}), \tag{1.57}$$

$$\hat{a}_2 = \frac{1}{\sqrt{2}}(\hat{a}_{\text{LO}} - \hat{a}_{\text{sqz}}). \tag{1.58}$$

Detection of these outputs with photodiodes, followed by subtraction of the photocurrents, yields a difference current I_-. In the ideal case, this current is proportional to the difference of the photon number operators,

$$I_- \propto \hat{a}_1^\dagger \hat{a}_1 - \hat{a}_2^\dagger \hat{a}_2. \tag{1.59}$$

By substituting the general field quadrature operator (Equation 1.40), assuming that the local oscillator dominates over the squeezed field, and replacing the LO amplitude operator with its classical amplitude $\hat{\alpha}_{\text{LO}} \rightarrow \alpha_{\text{LO}} = |\alpha_{\text{LO}}|e^{i\phi_{\text{LO}}}$, the variance of the measured photocurrent becomes

$$\langle(\Delta I_-)^2\rangle \approx 4 I_{\text{LO}} \left(\langle(\Delta\hat{X})^2\rangle \cos^2(\phi_{\text{LO}}) + \langle(\Delta\hat{Y})^2\rangle \sin^2(\phi_{\text{LO}})\right). \tag{1.60}$$

Here, I_{LO} denotes the photocurrent contribution generated by the local oscillator, which is proportional to its optical power. The measured field quadrature is selected by the phase of the local oscillator ϕ_{LO} and can be scanned in order to reconstruct the full quadrature noise distribution.

In a realistic squeezing experiment, several additional effects must be taken into account. First, the overall detection efficiency η reduces the observable squeezing and leads to

$$\langle(\Delta I_{-})^2\rangle_{\mathrm{meas}} = 4I_{\mathrm{LO}}\eta\left(\langle(\Delta\hat{X})^2\rangle\cos^2(\phi_{\mathrm{LO}}) + \langle(\Delta\hat{Y})^2\rangle\sin^2(\phi_{\mathrm{LO}})\right) + \frac{1}{4}I_{\mathrm{LO}}(1-\eta). \tag{1.61}$$

Second, technical noise contributions originating from the laser source, photodiodes, and electronic amplifiers add to the measured variance. For reliable squeezing measurements, these noise sources must be suppressed such that the detector operates in the shot-noise-limited regime.

Chapter 2

Conversion of 30 W Laser Light at 1064 nm to 20 W at 2128 nm

Figure 2.1 highlights the subsystem addressed in this section. The high-power light source delivers the stable optical power required by the interferometer. A central goal of this work is to generate at least 20 W of stable, high-quality light at 2128 nm. This corresponds to roughly one-fifth of the pump power required for future GWOs [5, 6, 7].

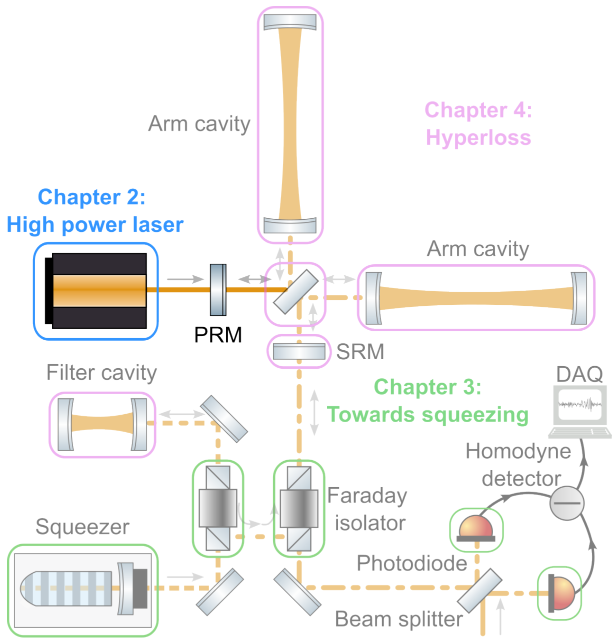

Figure 2.1: *A schematic representation of the GWO highlighting the focus of this chapter, the high-power pump laser.*

At the core of this experiment lies wavelength doubling of the pump laser through degenerate optical-parametric oscillation. This technique is known to transfer the noise characteristics of the pump source to the converted light [32, 33]. We demonstrate that this process can even reduce the noise of the converted light, as reported in the journal Optics & Laser Technology [34].

A 1064 nm seed laser from Mephisto was used to produce the pump light, which was then amplified to 75 W by a neoLASE model neoVAN-4S-HP and converted to 2128 nm. The same amplification stage was used in the Advanced LIGOs during the fourth observation run [13]. Results were published in the journal Classical and Quantum Gravity [35].

This chapter is structured into two parts: the generation of a 2128 nm high-power laser and the observation of noise reduction in a degenerate optical-parametric down-conversion.

The high-power experiment was carried out in collaboration with the group of Apl. Prof. Dr. Benno Willke, who provided the 1064 nm laser and its amplification stages. I set up the nonlinear cavity and characterization system and delivered them to Hannover. Dr. Christian Darsow-Fromm assisted me in doing the experimental demonstration and characterization. This section is structured into three parts: first, preliminary considerations with a closer look at the nonlinear cavity; second, the experimental setup; and third, the results (including conversion efficiency and relative power noise).

In Hamburg, a low power setup was used to carry out and evaluate the noise suppression experiment. To identify and study this behavior, I used the setup that I built during my master thesis. The classical theory was done with help from Asst. Prof. Sebastian Steinlechner and the quantum theory was done fully by Dr. Mikhail Korobko and can be found in the paper [34] or the Appendix A.2 for the sake of completeness. In this section, I give an overview of the classical theory, followed by the experimental setup and main results.

Technical challenges must be overcome in order to operate the system reliably at both high and low power. These include stabilizing the nonlinear cavity on resonance via Pound–Drever–Hall locking, ensuring simultaneous resonance of both wavelengths, achieving sufficient mode separation in the cavity, and maintaining the degenerate state of the signal and idler fields through precise temperature control. Especially at high pump powers, thermal effects such as changes in the refractive index and thermal lensing become increasingly relevant and impact both the achievable conversion efficiency and the cavity-length stabilization system. These aspects are discussed in detail in the following sections.

2.1 Preliminary Considerations About the Project

To achieve the required high-power light at 2128 nm, we rely on the well-understood, established, and highly optimized NPRO 1064 nm laser source and convert its wavelength via the nonlinear process of degenerate optical parametric oscillation. This approach makes it possible to retain the excellent technical properties of the NPRO system instead of developing an entirely new laser source. Previous low-power experiments in our group had already demonstrated this concept, and components such as the nonlinear crystal were reused for the high-power setup.

With this motivation in mind, this section discusses the design and parameters of the nonlinear cavity, focusing on the optimization of the coupling-mirror reflectivity. The crystal, with fixed dimensions of $(9 \times 2 \times 1)$ mm, was installed in an existing mount, which only allowed minor optimization of the air gap by repositioning the crystal. Due to the limited mechanical space of this mount, more substantial modifications would have required a complete redesign of the mount. The resulting configuration aims to balance threshold power and maximum conversion efficiency.

2.1.1 Detailed Examination of the Parametric Cavity

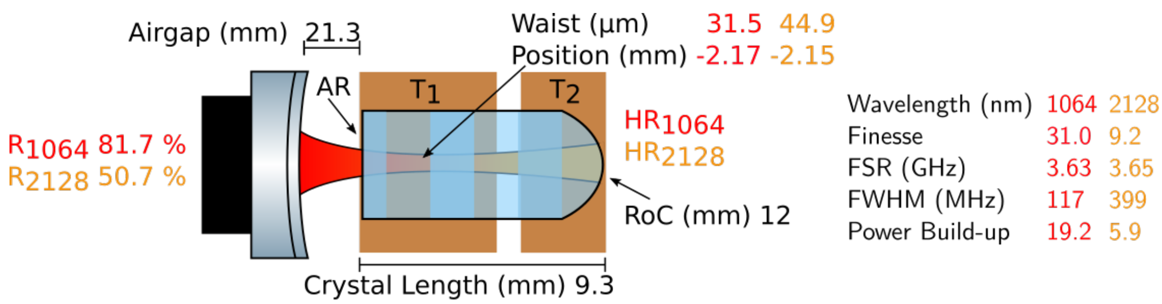

Figure 2.2: *Simplified parametric cavity design for high-power frequency conversion. resonator scheme. The resonator is defined by the coupling mirror and the end surface of the crystal. Its length is controlled by a ring piezo attached to the coupling mirror and actively stabilized through a feedback loop. Phase matching is achieved by tuning the effective optical length of the periodically poled domains via the temperature T_1. Simultaneous resonance of both wavelengths is obtained by tuning T_2 together with the piezo position*

The parametric cavity, also referred to as a nonlinear cavity, was pumped at 1064 nm, and through the (degenerate) optical-parametric oscillation process it generated bright light at half the pump frequency, i.e., at 2128 nm. An overview of its layout is shown in Figure 2.2, whose design was based on the work of Dr. Axel Schönbeck [36] and was optimized for my purpose. The cavity began with the coupling mirror, mounted on a piezo actuator for length control. This allowed the resonator to be actively stabilized to the pump frequency using the Pound–Drever–Hall technique [37, 38]. It was followed by an air gap and the periodically poled potassium titanyl phosphate (PPKTP) crystal with a curved end face. The flat side of the crystal had an anti-reflection (AR) coating, while the curved side carried a high-reflectivity (HR) coating for both wavelengths. In other words, the coupling mirror and the HR-coated curved end face of the crystal together formed the cavity. The nonlinear crystal therefore acted simultaneously as the intracavity medium and as one of the mirrors, thereby minimizing intracavity losses since the light passed only a single AR-coated surface. There was ongoing research about a monolithic cavity, which further reduced internal losses but posed other challenges [39]. Two temperature regions, T_1 and T_2, were applied to the crystal. Temperature T_1 was used to stabilize the cavity length by primarily changing the refractive index of the crystal and, to a lesser extent, its physical length due to thermal expansion. Temperature T_2 was used to optimize the phase matching by compensating for the poor overlap of the periodic poling at the crystal's end face, which would otherwise have reduced the conversion efficiency. A more detailed explanation can be found in Chapter 1.2.

2.1.2 Air-Gap Optimization Between the Coupling Mirror and the Crystal

A central design parameter of the nonlinear cavity is the air gap between the coupling mirror and the crystal, as it determines the cavity geometry, the mode structure, and the achievable mode matching. Since the physical dimensions of the crystal and its mount were fixed, the air-gap length was one of the few degrees of freedom available for optimization.

I used the simulation Dr. Christian Darsow-Fromm wrote with Finesse/PyKat [40] for his cavity analyses and modified it for my purpose. Pump and converted fields were treated separately and without the nonlinearity coefficient, since Finesse cannot perform nonlinear calculations but is well suited for cavity analysis. Stability was achieved for cavity lengths between 20.8 mm and 27.5 mm. The optimal mode separation at 21.3 mm matched the existing crystal-holder design, so no redesign was required.

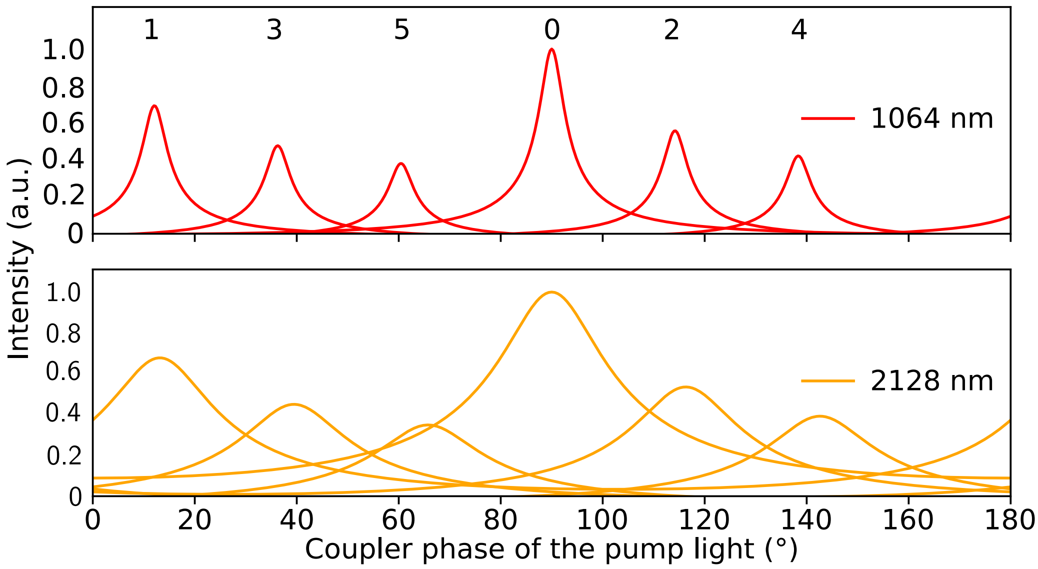

Figure 2.3: *Here a simulation of the optimized air gap with 21.3 mm and the corresponding order $m+n$ of the Gaussian TEM_{mn} modes up to fifth order for both wavelengths is presented. I chose an equal mode distribution over the coupling mirror phase to make the cavity work as a mode cleaner. For this simulation, anisotropic mode separation in the crystal was not considered. The amplitudes of the modes were chosen to be* $1/\sqrt{m+n+1}$ *to highlight the decreasing influence of higher modes. For completeness, the y-axis is plotted on a linear scale.*

All TEM_{mn} modes up to order five, with $m+n \leq 5$ are shown in Figure 2.3. Higher-order modes are omitted because their narrow linewidths overlap strongly and cannot be displayed unambiguously. A further simplification is that any permutations of the same order of $m+n$ are degenerate and indistinguishable. This is not true for real crystals since their refractive indices vary in the vertical and horizontal axes, resulting in a slight separation of the modes. The effect can be used for mode matching, as it helps identify which higher-order mode corresponds to which axis and can therefore be optimized. To highlight the diminishing contribution of higher-order modes, the Gaussian mode amplitudes were set to $1/\sqrt{m+n+1}$. They were assigned different amplitudes because the occurrence of higher-order modes becomes increasingly unlikely with rising mode order, as the cavity was optimized for the TEM_{00} mode. Experimental cavity scans later verified this behavior through linewidth measurements, as illustrated in Figure 2.6.

2.1.3 Coupling-Mirror Reflectivities

In a (D)OPO, the converted power I_{out} depends on the initial power I_{in} and the threshold power I_{th}, where $I_{\mathrm{in}} \geq I_{\mathrm{th}}$ [41, 42]:

$$I_{\mathrm{out}} = 4\eta_{\mathrm{max}} I_{\mathrm{th}} \left(\sqrt{\frac{I_{\mathrm{in}}}{I_{\mathrm{th}}}} - 1 \right), \tag{2.1}$$

with η_{max} as the maximum achievable conversion efficiency. For convenience, this was set to 100 % in the simulation, which is not the case in a real experiment. It depends on several factors, such as the mode matching to the cavity, the internal cavity losses, and the intrinsic non-linearity of the crystal. Conversion efficiency can therefore be defined either as "external", meaning it is not corrected for losses, or as "internal", meaning it is corrected for losses. I always assume external conversion efficiency in this dissertation. I_{th} is defined as the threshold power which is proportional to the reflectivities of the light fields at the coupling mirror [43, 44] and its effective nonlinear coefficient.

In Figure 2.4, the behavior of three different coupling mirror reflectivities is investigated. These examples include, for instance, points of low, medium, and high pump power corresponding to perfect conversion efficiency, demonstrating the range of possible system responses. I chose an effective nonlinearity d_{eff} of 5.07 pmV^{-1} as measured in our previous 2128 nm experiments [45]. Potential crystal damage from absorption was considered. The absorption at 1064 nm is below 20 ppm/cm [46], while the value at 2128 nm is unknown. I did not want to risk damaging the crystal, which led me to operate at lower power levels. The main criterion was a moderate threshold power, combined with the ability to reach the target output power of 20 W at a suitable conversion efficiency. To explore suitable operating points, I considered the following combinations of coupling-mirror reflectivities:

Case one: With reflectivities of $R_{1\,\mu\mathrm{m}} = 80\,\%$ and $R_{2\,\mu\mathrm{m}} = 75\,\%$, the threshold power would be reached at around 1 W input power, allowing us to verify cavity operation and identify potential thermal-lensing effects using our laser without an external power-amplification stage. Such thermal lenses were expected, as they had already been observed in our previous low-power experiment at similar pump powers [45]. The peak conversion efficiency would occur at approximately 2 W, but with these reflectivities the target converted power would not be achievable.

Case two: Reflectivities of $R_{1\,\mu\mathrm{m}} = 80\,\%$ and $R_{2\,\mu\mathrm{m}} = 50\,\%$ resulted in a threshold power of approximately 3 W, with maximum conversion efficiency reached at a pump power of about 13 W. The target converted power therefore fell within a favorable pump-power range without significant loss in efficiency. In addition, there was sufficient headroom to investigate thermal-lensing effects at lower powers while still enabling higher-power operation.

Case three: Using reflectivities of $R_{1\,\mu m} = 70\,\%$ and $R_{2\,\mu m} = 50\,\%$, a threshold power of about 6 W was obtained, and the best conversion efficiency occurred at a pump power of roughly 29 W. At these higher pump powers, the increased thermal load made the cavity behavior more difficult to assess, as thermal effects tended to distort the resonance conditions. Understanding thermal lensing was essential, as it could impair mode matching, damage the crystal, or lower the conversion efficiency. Increasing the output power while preserving high efficiency was therefore an important step toward meeting the requirements of future GWOs.

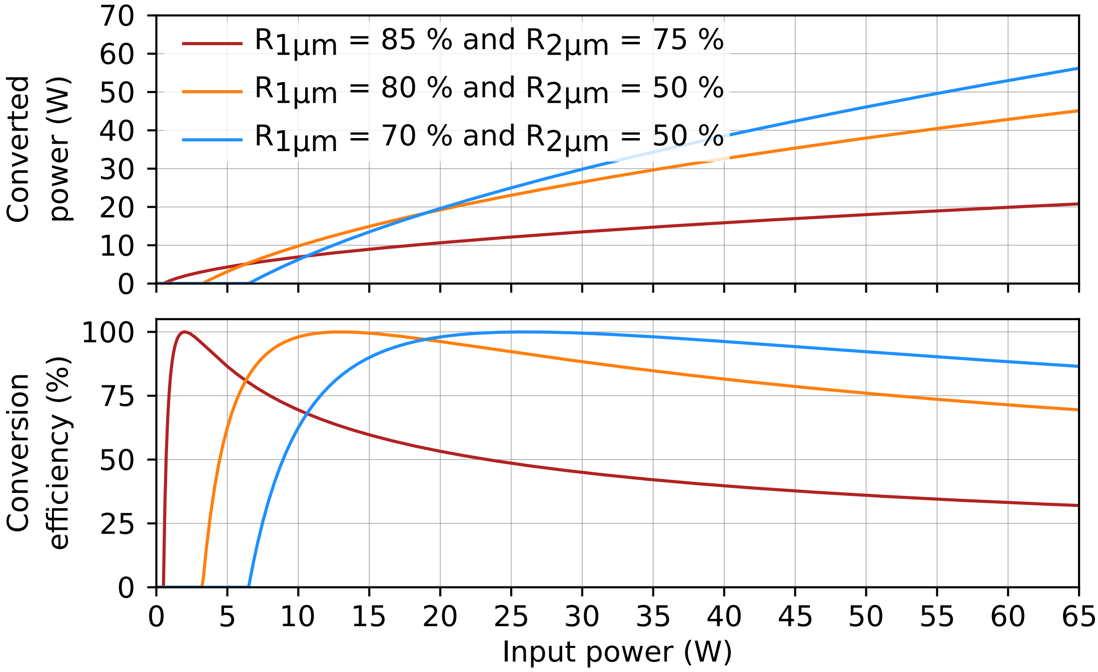

__Figure 2.4:__ Simulating the converted power behavior for three coupling mirror reflectivities; end mirror is always highly reflective. Chosen was the second case with $R_{1\,\mu m} = 80\,\%$ and $R_{2\,\mu m} = 50\,\%$, resulting in $P_{thr} = 3.25$ W with the point of best conversion efficiencies at 13.1 W (see main text for more detail).

After evaluating the three presented cases, I selected the second case with $R_{1\,\mu m} = 80\,\%$ and $R_{2\,\mu m} = 50\,\%$. This case is advantageous because the threshold power falls within a moderate pump power range, making it a suitable starting point for investigating thermal lensing effects. Furthermore, it allows for the possibility of exceeding the target output power of 20 W.

Reflectivities of the coupling mirror were measured with an Agilent Cary 5000 spectrophotometer. This resulted in slightly different values than simulated, the measured values can be seen in the picture 2.2 (more explanation in Section 2.2 and 2.3.1).

2.2 Experimental Setup

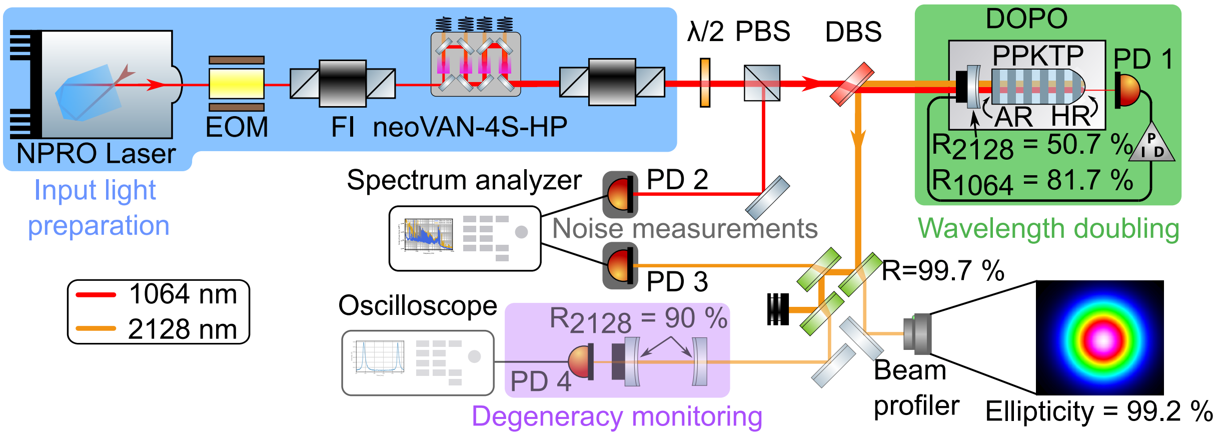

Figure 2.5: *Schematics of the high power 2 μm experiment. The NPRO laser and the* NEOVAN-4S-HP *amplifier provided up to 70 W pump power at the wavelength of 1064 nm (coloured blue: input light preparation) for the degenerate optical-parametric oscillator for wavelength doubling (coloured green: wavelength doubling). To monitor the degeneracy (single frequency), a small portion of the converted light was adapted to a concentric resonator whose length was continuously altered (coloured purple: degeneracy monitoring). The relative power noises were detected with photodiodes PD 2 and PD 3 and spectrally analyzed (coloured silver: noise measurements). A beam profiler was used to measure a (99.2 ± 7.0) % ellipticity of the converted beam.*

The experimental setup is shown in Figure 2.5. Depicted in the blue box "input light preparation" is a first amplification stage that follows the same design as the laser system employed in Advanced LIGO during the fourth observation run O4 [13]. A 2 W non-planar ring oscillator at 1064 nm, provided by MEPHISTO, served as the seed laser. Its light was sent through an electro-optical modulator, which produced a phase modulation at 28 MHz required for Pound-Drever-Hall locking of the resonator length. A Faraday isolator protected the seed laser from back-reflections and back-scattering. The light was then amplified by a NEOLASE model neoVAN-4S-HP laser amplifier up to power levels between 5 and 75 watts [47]. A second Faraday isolator shielded the amplifier from back-reflections. From the high-power beam, a small fraction was detected on a photodiode (PD 2) for relative power-noise analysis, while the remaining light was used to pump the non-linear cavity.

Table 2.1: *Main parameters of the degenerate optical parametric oscillator cavity.*

	1064 nm	2128 nm	
Waist radius	31.5	44.9	μm
Finesse	31.0	9.2	
Free spectral range	3.63	3.65	GHz
Linewidth (FWHM)	117	399	MHz
Coupler reflectivity	81.7	50.7	%
Power built-up	19.2	5.9	

In principle, the spatial mode quality of the pump beam can limit the mode matching to the nonlinear cavity. However, the beam profile in this setup was sufficiently clean and did not limit the coupling. If the beam quality is insufficient, a triangular cavity can be used as a mode cleaner.

As described in Section 2.1.1, a self-built nonlinear degenerate optical parametric oscillator was used, containing a planoconcave, periodically poled (type 0) potassium titanyl phosphate PPKTP crystal. One end of the resonator was formed by the highly reflective, curved end face of the crystal, while the opposite end was AR-coated for both wavelengths. The resonator's coupling mirror had reflectivities of 81.7 % at 1064 nm and 50.7 % at 2128 nm. A detailed discussion of these values is provided in Section 2.1.3. According to the performance-data manuscript, the associated uncertainties are negligible [48]. An overview of the cavity parameters is given in Table 2.1, while Figure 2.2 shows them in more detail.

To stabilize the length of the cavity on resonance, a Pound-Drever-Hall control scheme with the sensor placed in cavity transmission was used (PD 1). A digital controller [45] produced the actuator feedback signal for the piezo-mounted coupling mirror. The parametric process converted the pump field into the idler and signal fields. Here, we achieved degeneracy of these two fields by adjusting the temperatures of two separate regions of the nonlinear crystal [36]. We continuously monitored (PD 4) the degeneracy with a length-varied confocal cavity (length: 25 mm; mirror reflectivities: 90 %). As observed in our earlier 2128 nm experiment [23], the degeneracy was an intrinsically stable operating point. Temperature drifts in the laboratory prevented long-term stable operation at degeneracy. A gentle mechanical impulse, however, consistently returned the system to degeneracy, most likely by causing a slight repositioning of the piezo. Separation of the 1064 nm and 2128 nm light was achieved with a dichroic beam-splitter. A small portion of the light was sent to a beam profiler (BP209-IR2/M by Thorlabs) for measuring the ellipticity (min diameter divided by the max diameter) of the converted beam, resulting in $(99.2 \pm 7.0)\,\%$, limited by the beam profilers beam diameter uncertainty [49]. The relative power noise of the generated 2128 nm output field was measured with an extended InGaAs photo diode (PD 3; Thorlabs model FD05D) with custom transimpedance amplifier, and evaluated with a signal analyzer by Stanford Research Systems model SR785.

2.2.1 Pump-Laser to Nonlinear-Cavity Coupling-Efficiency Measurement

An important parameter is the overlap between the Gaussian mode of the pump field and the resonator. Insufficient mode coupling (which we refer to as mode matching) causes scattered light to be coupled into the laser path, potentially affecting measurements and damaging components, especially at these high powers. In Figure 2.6 the best achieved mode matching of the pump field to the nonlinear cavity is shown. A full scan over one free-spectral range is shown, including the fundamental TEM_{00} mode. The oscilloscope (Tektronix TDS 3014B) limited the resolution, restricting the zoom between the two main modes. An automated mode matching and finesse evaluation program has been used for evaluation. This tool was presented in [40] and is called OpenQlab (`openqlab.analysis.cavity.modematching`) [50].

Measured values for the finesse are (25 ± 0.5) for the left peak and (35 ± 0.7) for the right peak. The discrepancy is attributed to nonlinearities of the piezo actuator. Good agreement is observed between the measured finesse and the simulations presented in Section 2.1. A coupling efficiency of $(90 \pm 2)\,\%$ for the pump field into the cavity was achieved. Due to the relatively low finesse of the cavity, modes can be obscured within the linewidth of the dominant mode, and modes with significant amplitude may be concealed by background noise. These two artifacts lead to an overestimation of the measured parameters. Furthermore, thermal lensing effects can contribute to the limitation of coupling efficiency.

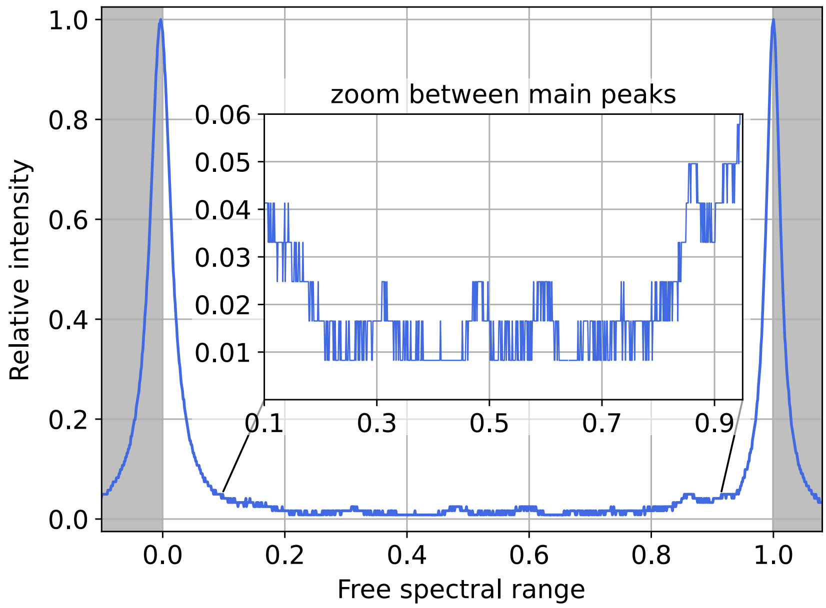

Figure 2.6: *Mode matching of the pumped field to the nonlinear cavity is essential for efficient generation of the converted field. The figure shows a scan over one full free spectral range, including the fundamental* TEM_{00} *resonance peaks on the left and right. A zoom into the region between the two main resonances reveals several smaller higher-order mode contributions, which limits the achieved mode-matching efficiency of* $(90 \pm 2)\,\%$*. A finesse of* (25 ± 0.5) *is obtained for the left peak and* (35 ± 0.7) *for the right peak, yielding a mean value of approximately 30. The discrepancy between the two finesse values arises from non-linearities in the piezo actuator during the scan.*

2.2.2 Nonlinear-Cavity Length-Stabilization System

The cavity was actively stabilized on resonance using a Pound–Drever–Hall locking technique [37]. Figure 2.7 left panel shows a schematic of the stabilization system. An electro-optic modulator generates sidebands at a frequency of 28 MHz on the laser beam. In transmission of the cavity, a photodiode with an integrated demodulation circuit extracts the error signal. The digital controller [45] then sends a high-voltage feedback signal to the piezo actuator of the coupling mirror. A variety of digital filters can be applied to optimize the lock for high bandwidth and low noise.

Figure 2.7 right panel shows the transfer function of the low-power nonlinear cavity. Note that a different coupling mirror was used for this measurement, while the same electronic components were employed. The control bandwidth is limited by a piezo resonance at approximately 10 kHz.

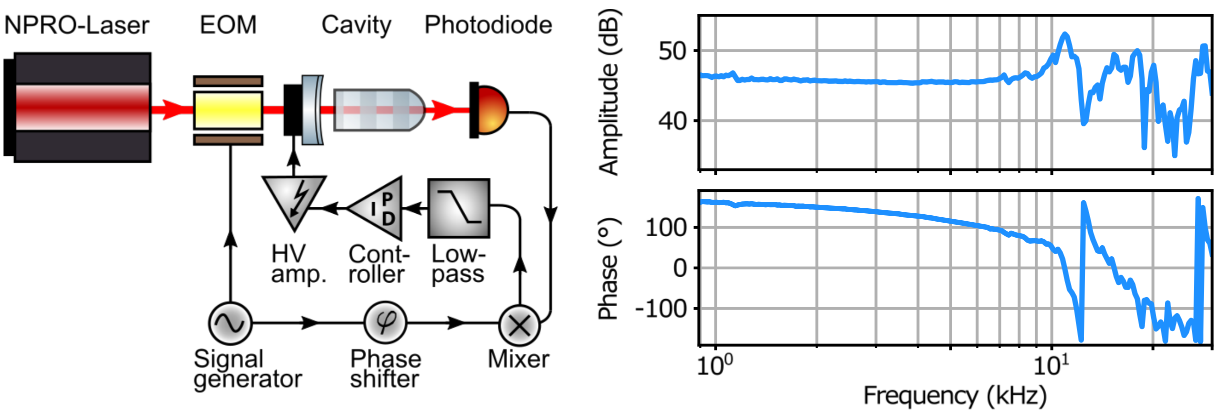

Figure 2.7: *Left: Schematic stabilization setup. Right: Transfer function of the frequency-stabilization system of the high-power cavity. The top panel shows the amplitude response versus frequency, and the bottom panel shows the corresponding phase response.*

I optimized the system for low-noise performance, as shown in Figure 2.8. Therefore, the converted light was sent to a photodiode, and the corresponding signal was recorded for different filter configurations. The spectrum was recorded using a Stanford Research Systems SR785 spectrum analyzer for both the unoptimized and optimized filter configurations, with an average of 100 repetitions and a resolution bandwidth of 128 Hz. In the range between 0.5 kHz and 10 kHz, the main optimization was carried out, resulting in an improvement of up to 5 dBV. Table 2.2.2 lists the filters employed in this configuration. The aim of this optimization step was to reduce the technical noise of the cavity-length stabilization system, as I intended to compare the amplitude noise of the converted and pump light. Since the performance of the length-stabilization loop can influence the noise properties of the converted field, improving the controller reduces technical noise contributions. However, the optimized filter configuration made the stabilization system more sensitive to external disturbances.

Table 2.2: *Comparison of unoptimized and optimized filters.*

Case	*Filters*
Unoptimized	*Integrator 1 kHz* *Integrator 500 Hz* *Differentiator 200 Hz* *Lowpass 3 kHz* *Gain 0.002*
Optimized	*Integrator 1 kHz* *Integrator 30 kHz* *Integrator 250 Hz* *Lowpass 50 kHz* *Gain 0.0005*

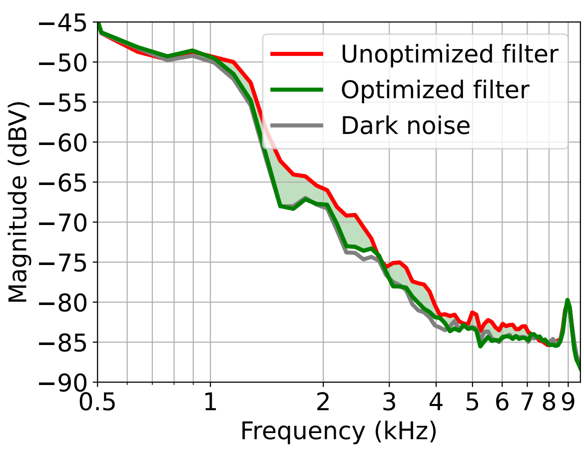

Figure 2.8: *2128 nm light spectrum for optimized and unoptimized filters.*

Intracavity intensities reach the gigawatt-per-centimeter range, producing strong thermal effects that modify the effective optical path length. This effect can destabilize the length-control loop and ultimately cause the cavity to fall out of resonance. Therefore, the cavity temperature is monitored and stabilized to within $\pm$ 10 mK by a Peltier element. Despite this stabilization, internally induced thermal effects still exceed this control range and degrade the length-stabilization performance of the high-power setup, as discussed in Section 2.3.1.

2.2.3 Controlling the Degenerate State of the Nonlinear Cavity

Optical parametric oscillation produces a signal and idler wave field ($\lambda_{\mathrm{pump}} \rightarrow \lambda_{\mathrm{signal}} + \lambda_{\mathrm{idler}}$). The frequency of these produced light fields can be tuned by controlling the length of the cavity. If both fields reach the same frequency we call them degenerate ($\lambda_{\mathrm{pump}} \rightarrow 2 \cdot \lambda_{\mathrm{signal/idler}}$). For this experiment, it was important to demonstrate that this state can be generated, as interaction with other light fields, such as squeezed light, becomes easier when both fields have exactly the same wavelength. We use a linear cavity to monitor degeneracy. Several techniques to maintain or generate the degenerate state have been developed, and these are explained in Appendix A.1.

Tuning the Degenerate State with Temperature

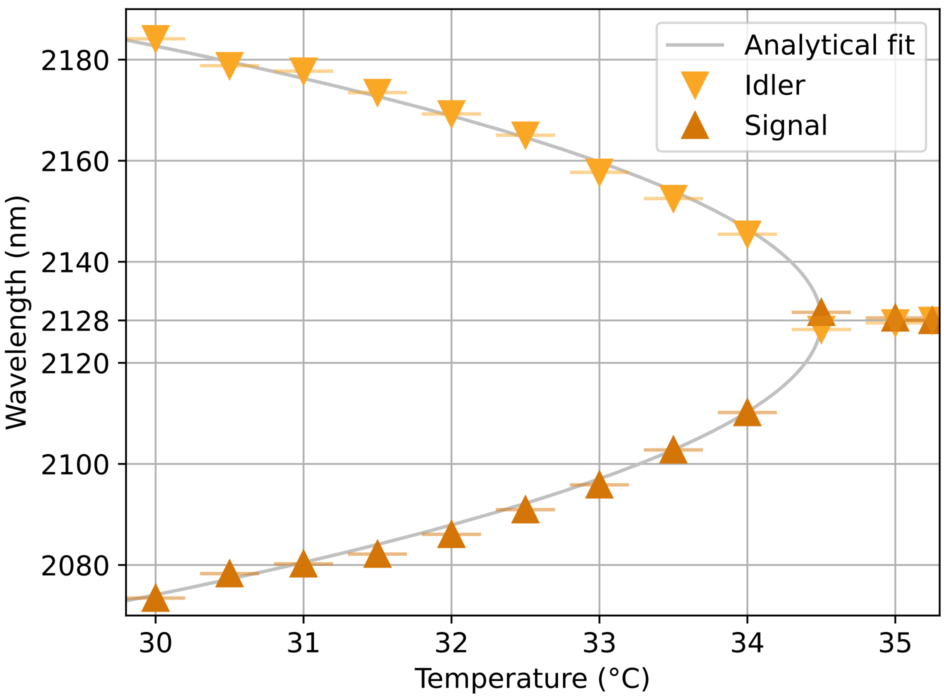

Figure 2.9: *The measured signal and idler wavelengths at different phase-matching temperatures of the crystal are shown. At approximately (34.5 $\pm$ 0.35) °C, the degenerate state is reached, while below this temperature the two fields remain spectrally distinct. Agreement with the theoretical prediction is confirmed by an analytical fit.*

Figure 2.9 shows the change from a non-degenerate state to a degenerate state as a function of temperature (with, $T_1 = T_2$ see Figure 2.2 for explanation). This indicates that by tuning the temperature, the output wavelength of the signal and idler fields can be varied, as measured with a BRUKER Equinox 55 spectrometer with a resolution of 0.2 nm [51]. The wavelength shift is mainly caused by changes in the effective optical path length arising from the temperature-dependent refractive index of the crystal. In contrast, thermal expansion effects are considered negligible [52]. My measurement follows the theoretical behavior of the temperature dependency near degeneracy, as evidenced by an analytical fit, $\Delta\omega = \eta\sqrt{\mathrm{T}-\mathrm{T}_0}$, where $\Delta\omega$ is the frequency difference between both light fields and η is the system's calibration constant [53]. A degenerate state is reached at a temperature of $(34.5 \pm 0.35)\,°\mathrm{C}$, where the temperature uncertainty is determined by the 1 % tolerance of the NTC thermistor [54].

Monitoring the Degenerate State During the Experiment

A confocal cavity with a reflectivity of $R = 90\,\%$, as shown in Figure 2.10(a), was used for this purpose. The cavity was originally developed by Dr. Axel Schoenbeck [36], and I adapted it for the present experiment. As displayed in Figure 2.10(b), the degenerate state exhibits a characteristic mode pattern. The offset along the y-axis is determined by the photodiode's dark voltage. In a confocal cavity, the even and odd higher-order modes each overlap into their respective resonance. Consequently, for one full free spectral range, two peaks appear: one corresponding to the odd modes and one corresponding to the even modes.

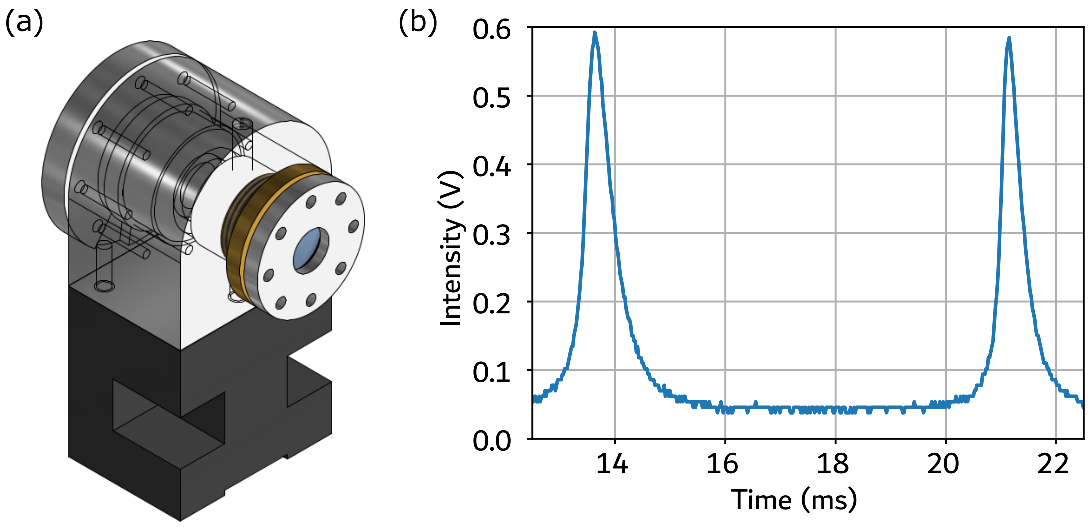

Figure 2.10: *Left panel, Schematic drawing of a confocal cavity for monitoring the degenerate state of the nonlinear cavity. Right panel, Degenerate operation of the OPO cavity is revealed by mode matching observed with a length-tuned confocal monitoring cavity.*

Another advantage of this cavity is that monitoring the degeneracy does not require perfect mode matching to the TEM_{00} Gaussian mode, which allows the confocal cavity to be positioned at a slight angle. This configuration prevents back-reflections from the cavity without the need for a Faraday isolator. In previous setups, such back-reflections caused instabilities in the nonlinear cavity.

2.3 Results

The key findings are divided into two sections. Section 2.3.1 addresses the conversion efficiency and its experimental results, while Section 2.3.2 examines the noise properties between the pump and the converted laser light.

2.3.1 Conversion Efficiency

The conversion efficiency and the generated 2128 nm power as functions of the 1064 nm input power are depicted in Figure 2.11. Measurements did not account for any losses, including imperfect mode matching, reflection losses from the crystal's anti-reflection coating, internal absorption, or residual transmission through the crystal's end surface coating. An analytical fit was performed using Equation 2.1, yielding a threshold power of $I_{\mathrm{th}} = (9.73 \pm 0.12)\,\mathrm{W}$ and a maximum conversion efficiency of $(64.8 \pm 0.5)\,\%$. At this point, approximately $(32.5 \pm 0.12)\,\mathrm{W}$ of pump power was converted into $(22.0 \pm 0.8)\,\mathrm{W}$ of output power. The highest measured converted power was $(29.0 \pm 0.9)\,\mathrm{W}$ at an input pump power of $(50.6 \pm 0.15)\,\mathrm{W}$. The uncertainties in these measurements are primarily related to the 3 % relative measurement error of our thermal power meter, as specified by the manufacturer OPHIR (model 3A-QUAD) [55].

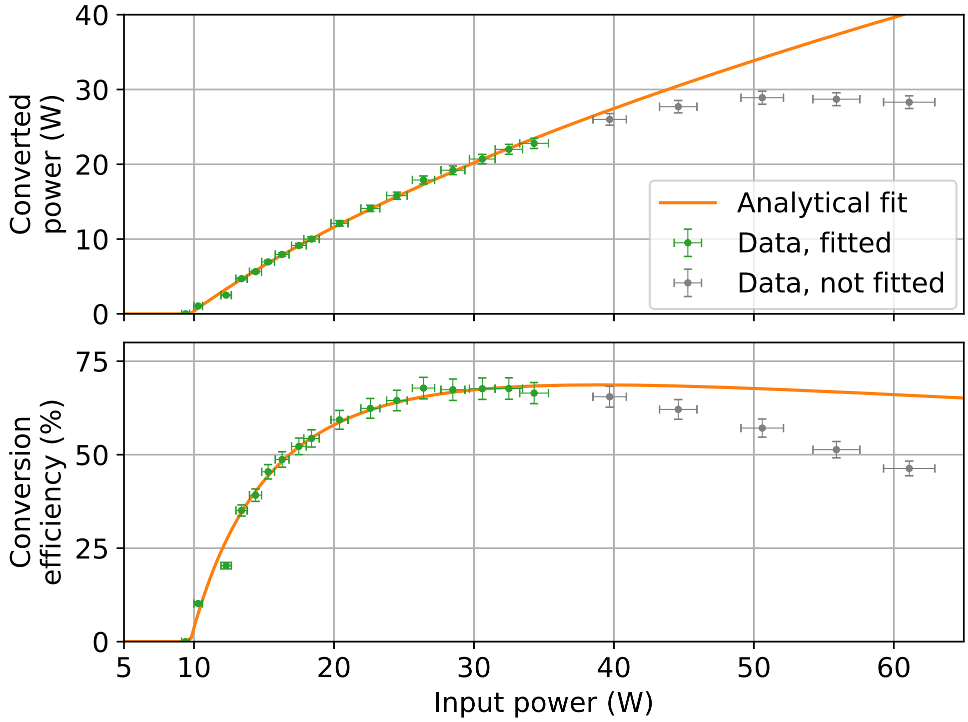

Figure 2.11: *The top image shows the power of the converted light, while the bottom figure depicts the conversion efficiency, both as functions of the input power. An analytical fit is represented by the orange line. Data points above 34 W input power were omitted from the fit due to distortion of the error signal used for DOPO length control (see main text for explanation).*

Although the cavity was designed for a threshold of approximately 3 W, the measured value was about 10 W. Two factors mainly contribute to this discrepancy: variations in the coupling-mirror coatings and thermal effects. The latter include changes in the refractive index and thermal lensing, which lead to variations in the effective nonlinearity. Both contributions, namely variations in the coupling-mirror coatings and thermal effects, influence the cavity properties, either directly or indirectly, leading to deviations from the original design.

I examined the coating of the coupling mirror using an AGILENT Cary 5000 spectrophotometer and measured reflectivities of 81.7 % at 1064 nm and 50.7 % at 2128 nm. According to the data sheet, the uncertainties of the spectrophotometer are very small and therefore negligible [48]. This minor discrepancy of 1.7 % at 1064 nm and 0.7 % at 2128 nm between the simulated and measured reflectivities does not account for the observed variation.

Simulating the measured scenario while using the effective nonlinearity d_{eff} as the only free parameter, and applying the boundary conditions given by the measured reflectivities together with the fitted threshold power, yields a value of 1.94 pm/V. This deviates significantly from the value used to simulate the cavity, where 5.07 pm/V was assumed based on earlier experiments. The discrepancy can be attributed to thermal changes in the cavity properties induced by the higher pump power. Table 2.3 provides an overview of other reported effective nonlinear coefficients.

Table 2.3: *Effective nonlinear optical coefficient of PPKTP at around 2 µm.*

Wavelength (nm)	Threshold power (W)	$\lvert d_{\text{eff}} \rvert$ (pm/V)	Crystal	Cavity	Source
1984	0.35	6.43	PPKTP	Bow-tie	[8]
2128	0.15	5.07	PPKTP	DOPO	[11]
	9.7	1.94	PPKTP	DOPO	this work

During the experiment, two effects were observed: First, as shown in Figure 2.12, the DOPO error signal became more distorted as the pump power increased. This effect began at approximately 30 W and made it impossible to stabilize the resonator length using our automated length control system. Instead, we manually adjusted the feedback voltage to bring the DOPO resonator into resonance. Second, the conversion efficiency declined more rapidly after the point of maximum conversion than predicted by theory (see the gray data points in Figure 2.11). This behavior is likely caused by imperfect length control of the resonator, combined with increased thermal load in the cavity. This could have led to the onset of thermal lensing, resulting in decreased mode matching.

The influence of thermal effects is illustrated in Figure 2.12. By distinguishing between low and high pump power levels, we compare these two cases in terms of the transmitted 1064 nm power, the converted 2128 nm power, and the error signal.

Transmitted power: It can be observed that the resonator in ramp mode converts light once the optimal length is reached, as indicated by a plateau of peaks. Depending on the pump power, this occurs earlier at higher powers, since increased thermal load due to absorption effects causes variations in the effective optical path length. These variations are due to changes in the refractive index caused by temperature heating. Two lines are drawn to highlight and compare the peaks within the plateau.

Converted power: In both cases, a gradient from left to right is observable. This effect can be attributed to two phenomena, both of thermal origin. The first arises from absorption effects caused by high pump power, while the second results from external temperature control used to adjust the cavity length. Both factors influence the resonator's size and, consequently, the ramping time of the external piezo actuator, leading to a deformed shape of the resonator. More specifically, as the crystal expands due to thermal effects, shifting the mirror in the direction of the crystal results in a shorter ramping time, and vice versa. This phenomenon impacts the maximum monitored converted power because the PHD technology is designed to stabilize in the error signal center, typically at the middle of the converted peak. While this deformed shape has minimal effect at low power levels, it becomes significant at higher powers. This effect, namely the thermal Kerr effect, can be used to measure the absorption of materials as shown in [56, 57].

Error signal: The stabilization performance depends on the error signal, which is generated through a demodulation stage in the photodiode; in other words, it corresponds to the derivative of the intensity. The intensity is determined by the transmitted power through the crystal, which is affected by thermal effects. These thermal effects can lead to an insufficient or distorted error signal, thereby impacting the stability of the system.

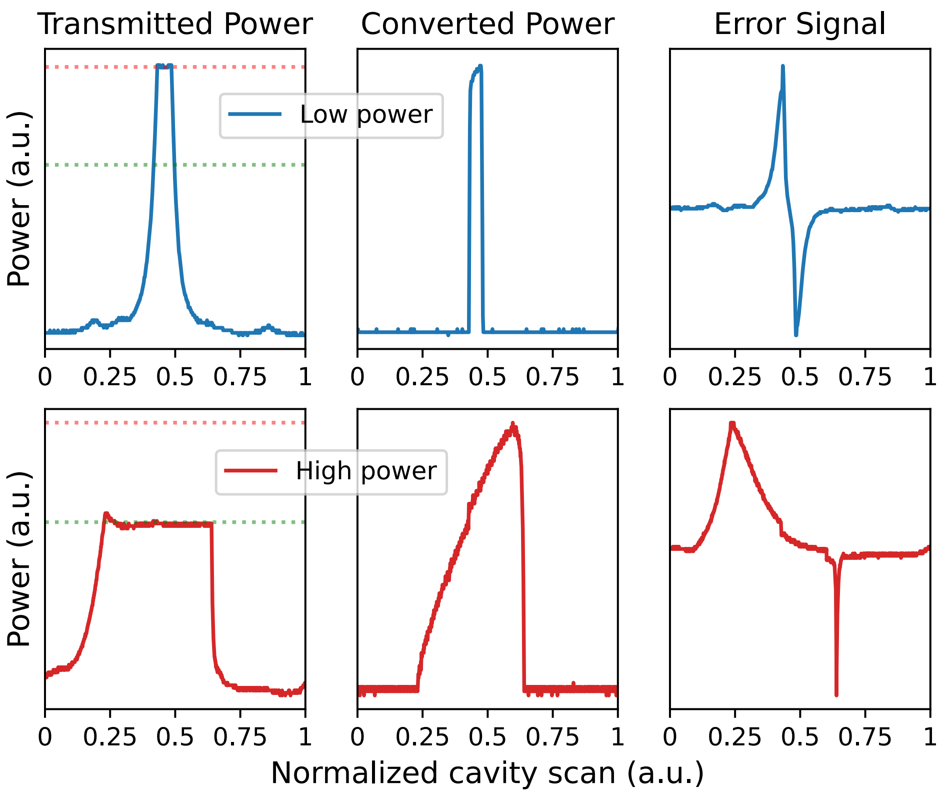

Figure 2.12: *The transmitted cavity peak of the pump power, the converted cavity peak, and the error signal at low and high pump powers are presented. Pump depletion is evident at low power, indicating effective frequency stabilization. At higher powers, degradation of the cavity peaks is observed, along with broadening of the error signal, leading to insufficient length stabilization. No saturation is observed on PD 1. The x-axis represents the normalized scan position corresponding to cavity detuning, obtained by rescaling each scan to the interval [0,1] and the y-axis shows the measured power.*

2.3.2 Relative Intensity Noise

In Figure 2.13, two (extended) InGaAs photodiodes (PD 2 for 1064 nm and PD 3 for 2128 nm) simultaneously measure the relative intensity noise (RIN) of the input and output light beams using a signal analyzer from Stanford Research Systems (model SR785). Electronic dark noise was negligible and was not subtracted. Ground loops are responsible for the noise peaks observed in the 1064 nm light, which we were unable to eliminate during our measurement campaign. Below 100 Hz, the RIN of the converted light is significantly higher. This increase is primarily due to electronic artifacts of the extended InGaAs photodiode [8] and mechanical resonances, such as those from the mirror mounts, which couple into the RIN of the DOPO via pointing fluctuations [58]. Above 100 Hz, the RIN are comparable between the input and output, and above 3 kHz, it can be observed that the RIN of the converted light is about 50 % higher. For the measurement shown, a pump power close to the maximum conversion efficiency was used.

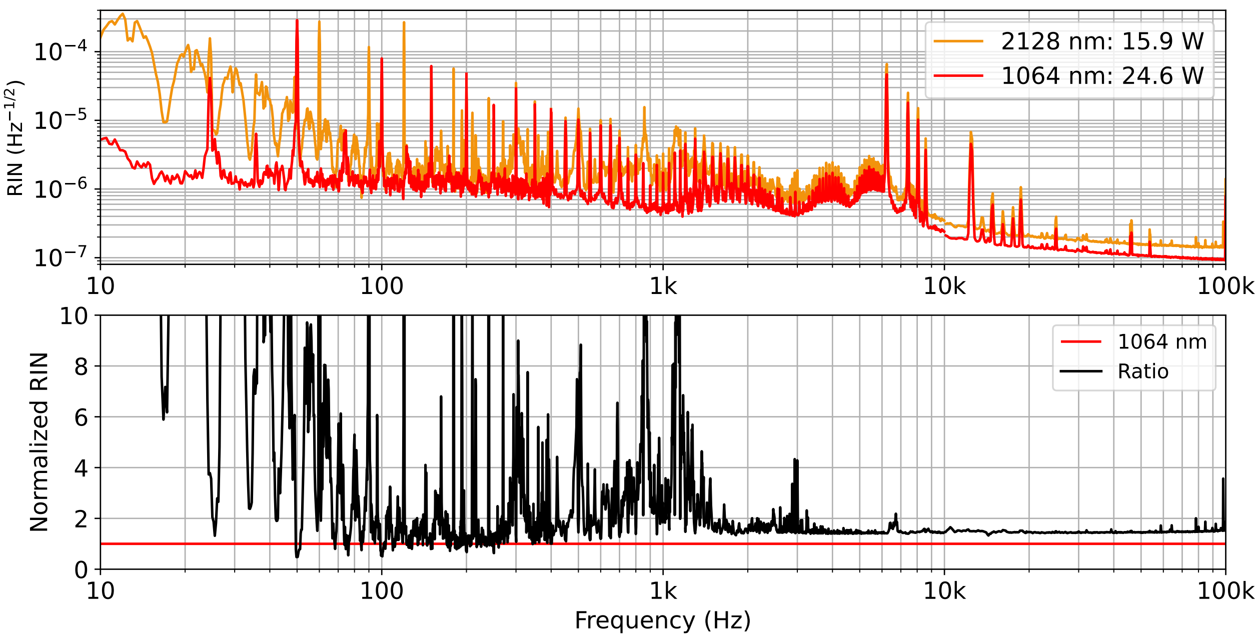

Figure 2.13: *(Top) RIN measurements of the pump laser beam (red) and the converted laser beam (orange). The relative power noise at 2128 nm was generally slightly higher than that of the input beam. Below 100 Hz this was due to detection noise from the extended InGaAs photo diode (*Thorlabs *FD05D). At higher frequencies, we measured only slightly increased relative noise (see Section 2.4 for explanation). (Bottom) RIN level of the converted beam (black) normalized to the RIN of the input (blue).*

As described in the next section, the noise level of the converted light depends on the power of the input light field. Increasing the pump power would result in a similar or even reduced noise level. Measuring a spectrum at high powers was not feasible due to difficulties with cavity stabilization, as explained in Section 2.3.1.

2.4 Coherent Noise Suppression in a High-Efficiency Wavelength-Doubling Experiment

We realized a nearly 30 W laser at 2128 nm with noise characteristics similar to its pump source, as discussed in Section 2.3.2. Importantly, we introduce a novel noise reduction technique achieving up to 50 % attenuation of technical noise without additional equipment. This method involves pumping above the optimal point of conversion, exploiting a previously unutilized regime to intrinsically suppress noise. An experimental demonstration of this method, along with the corresponding theoretical background, is described in this chapter.

2.4.1 Theoretical Model

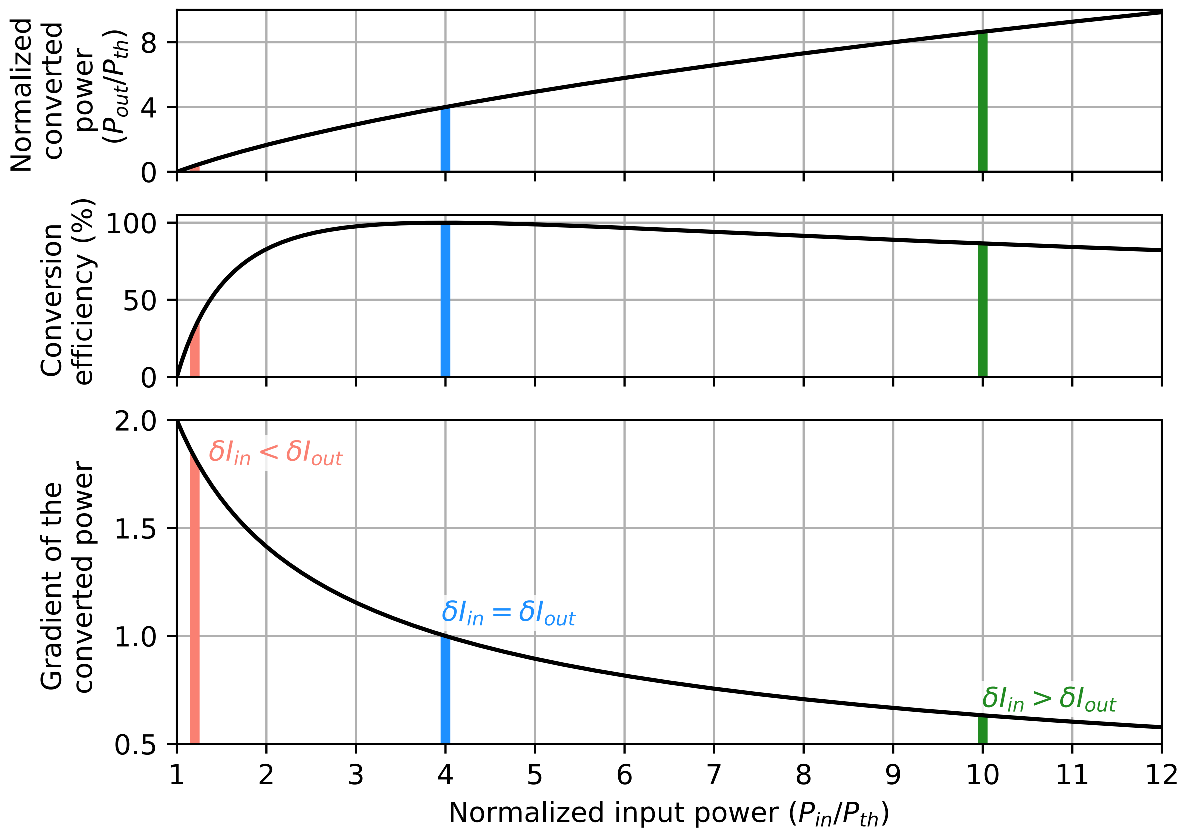

Figure 2.14: *The top figure illustrates the classical degenerate optical-parametric oscillator cavity conversion curve based on Equation 2.1. The middle figure shows the conversion efficiency as a function of the pump laser power, while the bottom figure depicts the derivative of Equation 2.1, i.e., the slope. In other words, it represents the response δI_{out} to fluctuations in the pump laser power, δI_{in}.*

A simplified schematic representation of the observed effect is shown in Figure 2.14. The purpose of this figure is to graphically relate the classical conversion theory to the three regimes of intensity-fluctuation transfer discussed below. The first two images summarize the classical theory, while the bottom image highlights the derivation of the conversion process according to the formula

$$\mathfrak{F}(I_{\text{in}}) = {}^{2\eta_{\text{max}}}\!/\!\sqrt{\tfrac{I_{\text{in}}}{I_{\text{th}}}}.$$

In this context, the derivative represents the response of the converted light as a function of the pump light. It therefore quantifies the transfer of small pump-intensity fluctuations to converted-light intensity fluctuations. Accordingly, three distinct regimes can be identified:

Weakly pumped: Amplification of the pump field fluctuations, such that $\delta I_{in} < \delta I_{out}$.

Optimally pumped: An identical transfer of the fluctuations.

Strongly pumped: Reduction of intensity fluctuations, such that $\delta I_{in} > \delta I_{out}$.

Referring to the three regions of the conversion efficiency, *optimally pumped* corresponds to the point of highest conversion efficiency, *weakly pumped* lies below this point, and *strongly pumped* is above it.

To understand the origin of laser noise suppression in a DOPO cavity at pump powers significantly above the optical parametric oscillation threshold, we present a simple theoretical model. A rigorous Hamiltonian treatment is provided in the published paper [34] and the Appendix A.2. The average output power, I_{out}, of a DOPO for $I_{\text{in}} \geq I_{\text{th}}$ is given by [41, 42] (which is Equation 2.1):

$$I_{\text{out}} = \eta I_{\text{in}} = 4\eta_{\text{max}} I_{\text{th}} \left(\sqrt{\frac{I_{\text{in}}}{I_{\text{th}}}} - 1 \right).$$

We then consider a slight fluctuation δI_{in} in the pump power, such that $I_{\text{in}} = \overline{I_{\text{in}}} + \delta I_{\text{in}}$, where $\overline{I_{\text{in}}} \gg \delta I_{\text{in}}$ represents the average power. These fluctuations are transformed into variations δI_{out} of the converted signal power, given by $I_{\text{out}} = \overline{I_{\text{out}}} + \delta I_{\text{out}}$. By substituting this expression into Equation 2.1, we can analyze the output power in terms of its average value and the noise components:

$$\overline{I_{\text{out}}} + \delta I_{\text{out}} = 4\eta_{\text{max}} I_{\text{th}} \left(\sqrt{\frac{\overline{I_{\text{in}}} + \delta I_{\text{in}}}{I_{\text{th}}}} - 1 \right). \tag{2.2}$$

Since the fluctuations are much smaller than the average power, i.e., $\delta I \ll I$, we can linearize Equation 2.2 by retaining only the terms linear in $\delta I_{\text{in,out}}$,

$$\delta I_{\text{out}} = 2\delta I_{\text{in}} \eta_{\text{max}} \sqrt{\frac{I_{\text{th}}}{\overline{I_{\text{in}}}}}. \tag{2.3}$$

Equation 2.3 shows that, as the pump power increases, the converted noise δI_{out} decreases relative to the pump noise δI_{in}. At very high input powers, the suppression of these fluctuations becomes so pronounced that the influence of quantum uncertainty becomes noticeable, saturating at the shot noise level, as demonstrated in Appendix A.2. However, increasing noise suppression according to Equation 2.3 leads to a decrease in the conversion efficiency, as described by Equation 2.1, which in turn does not impacts the relative noise level. Since the RIN is independent of the absolute power level in the field, this metric allows us to compare noise levels across different systems with varying powers.

$$\mathrm{RIN}_{\mathrm{out}} \equiv \frac{\delta I_{\mathrm{out}}}{\overline{I_{\mathrm{out}}}} = \frac{\delta I_{\mathrm{in}}}{2\overline{I_{\mathrm{in}}}} \left(1 - \sqrt{\frac{\overline{I_{\mathrm{th}}}}{\overline{I_{\mathrm{in}}}}}\right)^{-1} = \mathrm{RIN}_{\mathrm{in}} \cdot \mathcal{N} \,. \tag{2.4}$$

We introduced the noise transfer factor $\mathcal{N}$, which quantifies how noise is transferred from the pump to the converted signal,

$$\mathcal{N} = \frac{1}{2} \left(1 - \sqrt{\frac{\overline{I_{\mathrm{th}}}}{\overline{I_{\mathrm{in}}}}}\right)^{-1} . \tag{2.5}$$

The equations above enable the expansion of the definition of the three operating regimes:

Weakly pumped oscillation, $\overline{I_{\mathrm{in}}} \geq \overline{I_{\mathrm{th}}}$, where the noise transfer factor $\mathcal{N}$ increases significantly above 1 as the threshold is approached (see Equation 2.5), resulting in a strong amplification of the RIN on the converted field.

Optimally pumped oscillation, $\overline{I_{\mathrm{in}}} \approx 4\overline{I_{\mathrm{th}}}$, where the conversion efficiency reaches its maximum (see Equation 2.1) and $\mathcal{N} \approx 1$; thus, the RIN of the pump and the converted field are approximately identical.

Strongly pumped oscillation, $\overline{I_{\mathrm{in}}} > 4\overline{I_{\mathrm{th}}}$, where $\mathcal{N} < 1$, leading to the suppression of the RIN of the converted field. At very high pump powers, $\overline{I_{\mathrm{in}}} \gg \overline{I_{\mathrm{th}}}$, the noise transfer factor approaches $\mathcal{N} \to 0.5$, allowing for a maximum RIN suppression by a factor of 2. However, in this regime the conversion efficiency progressively decreases to very low levels.

2.4.2 Experimental Setup

I experimentally tested our theoretical predictions in a DOPO setup, shown in Figure 2.15. The continuous-wave pump laser was a 1064 nm NPRO. Its output beam passed through an electro-optical modulator (EOM) for sideband generation at 28 MHz, facilitating PDH length stabilization of the nonlinear resonator. A FI protected the NPRO from back reflections and back scattering. A small portion of the pump light was tapped off and measured by a photodiode (PD 2) for RIN analysis, while the remaining light was directed into the DOPO. The degenerate optical-parametric oscillator cavity featured a half-monolithic (hemilithic) design and was composed of a PPKTP crystal along with a separate coupling mirror, as detailed in the schematic diagram 2.2, with different cavity parameters, optimized for low power operation. A high-reflectivity coating for both the pump and converted light fields was deposited on the crystal's curved end face, whereas the flat front face received an anti-reflective coating for both fields. As specified in the manufacturer's data sheet, the coupling mirror had reflectivities of 96 % at 1064 nm and 90 % at 2128 nm. Table 2.4 lists the detailed resonator parameters for both wavelengths. To stabilize the length of the DOPO at resonance, we employed a modified PDH control scheme in transmission (PD 1), with feedback applied to the piezo-mounted coupling mirror with the help of a digital control circuit [45]. The wavelength-doubling process involved a type 0 optical-parametric amplification in the nonlinear crystal, converting the pump field into signal and idler fields. A degenerate state of the signal and idler was achieved by controlling the temperature of two regions of the nonlinear crystal [36, 59] and was monitored

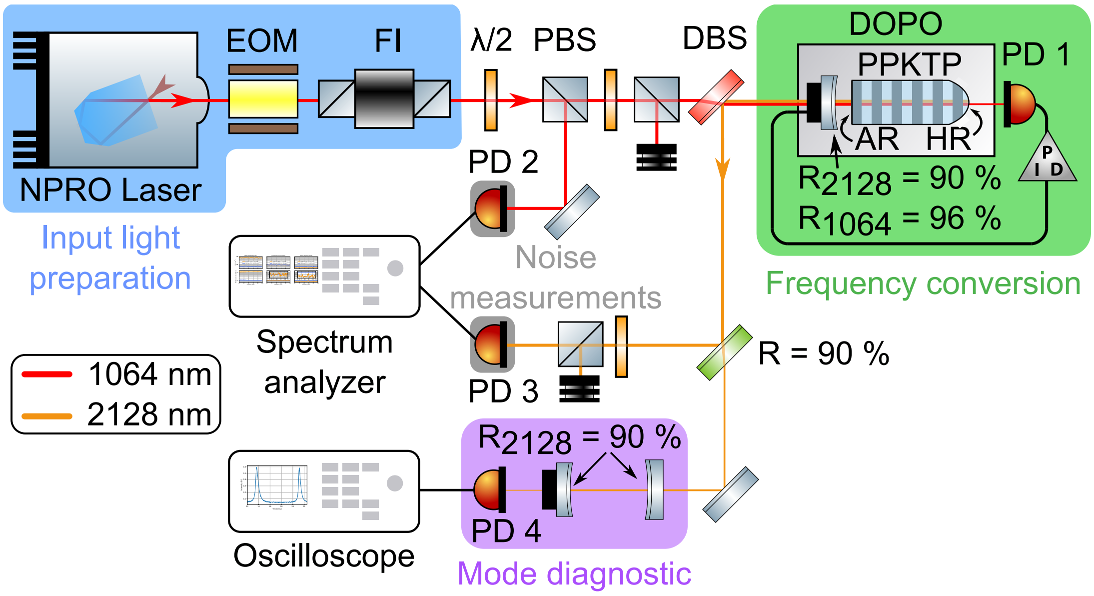

Figure 2.15: *A 1064 nm NPRO laser (blue box: input light preparation) pumped a degenerate optical parametric oscillator to double the input wavelength to 2128 nm (green box: frequency conversion). The relative intensity noise of both wavelengths was detected using amplified photodiodes (InGaAs PD 2 and Ext-InGaAs PD 3, respectively) and measured with a signal analyzer (gray boxes: noise measurement). To ensure operation in a degenerate state, the light's frequency mode content was monitored with a confocal cavity (violet box: mode diagnostic).*

Table 2.4: *Overview of the DOPO cavity parameters.*

	1064	2128	nm
waist radius	33.5	47.4	µm
finesse	153	59.5	
free spectral range	3.80	3.83	GHz
linewidth (FWHM)	24.9	64.3	MHz
coupler reflectivity	96	90	%

with a linear confocal cavity (reflectivities of 90 %, PD 4). Using this setup, the DOPO reached its threshold at a pump power of $I_{\text{th}} = (23.6 \pm 0.7)$ mW. A dichroic beam splitter (DBS) separated the 1064 nm and 2128 nm beams after the cavity. The RIN of the converted light was measured with a photodiode (PD 3, extended InGaAs, Thorlabs FD05D) equipped with a custom transimpedance amplifier and analyzed using a signal analyzer from Stanford Research Systems (model SR785).

2.4.3 Results

The relative intensity noise measurements for various pump powers of both the pump and converted light are shown in Figure 2.16. A spectral range was chosen that was free of spurious lines and well above the photodiode dark noise for both wavelengths, spanning from 90 kHz to 100 kHz. However, noise transfer was observable across a broad frequency range determined by the cavity linewidths of 24.9 MHz for 1064 nm and 64.3 MHz for 2128 nm. In the left column, the pump power was reduced to just above threshold. Under these conditions, the RIN of the converted field was significantly higher, reaching nearly 14 times the RIN of the pump field. For the middle column, the pump power was chosen near the point of optimal conversion efficiency, where $I_{\mathrm{in}} \approx 4I_{\mathrm{th}} \approx 100\,\mathrm{mW}$. As expected, the RIN levels of the 1064 nm and 2128 nm fields matched closely in this regime. In the right column, the pump power was increased to more than ten times the threshold level. At these higher pump powers, the RIN of the converted light dropped below that of the pump light. In our setup, a maximum noise reduction of (25.1 $\pm$ 1.8) % was achieved at a pump power of (275 $\pm$ 8) mW. The available pump-laser power of 2 W was not fully utilized, as the experiment focused on the operational range around the maximum conversion efficiency and thus on the onset of noise suppression, as well as on the steep slope at the lower-power side. These features are the most critical for the analytical fit.

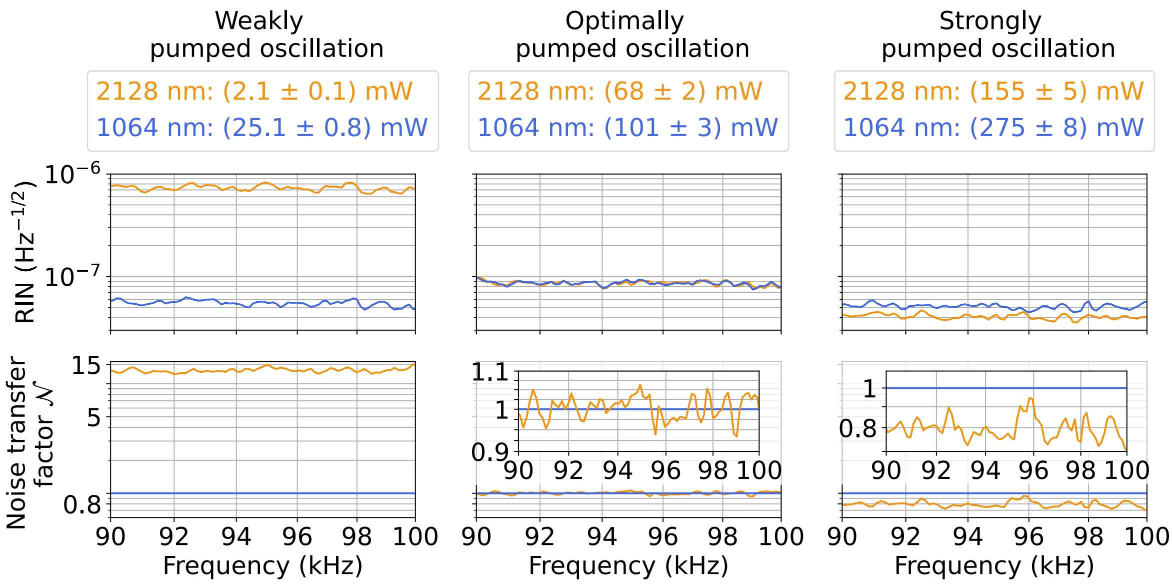

Figure 2.16: *Top row: RIN measurements of the pump and converted beam for three different pump powers (left, close to threshold $I_{in} \approx (25.1 \pm 0.8)$ mW; middle, at the point of highest conversion efficiency $I_{in} \approx (101 \pm 3)$ mW; right, strongly pumped $I_{in} \approx (275 \pm 8)$ mW). Bottom row: Showing the noise transfer factor $\mathcal{N}$ for the pump and converted light fields. All traces were root mean square averaged 40 times.*

To determine the ratio between the RIN of the pump and the converted light over a broad range of pump powers, the measurements were repeated, and the results are summarized in Figure 2.17. The data are well described by the theoretical model for the noise-transfer factor $\mathcal{N}$ from Equation 2.5. A red line indicates the theoretical limit of noise suppression, while a horizontal blue line represents the noise level of the 1064 nm pump source. Below is a direct comparison of the conversion efficiency in each region. The error bars of the measured values are primarily dominated by the 3 % measurement uncertainty of the thermal power meter head (Ophir model 3A-QUAD) [55] specified by the manufacturer.

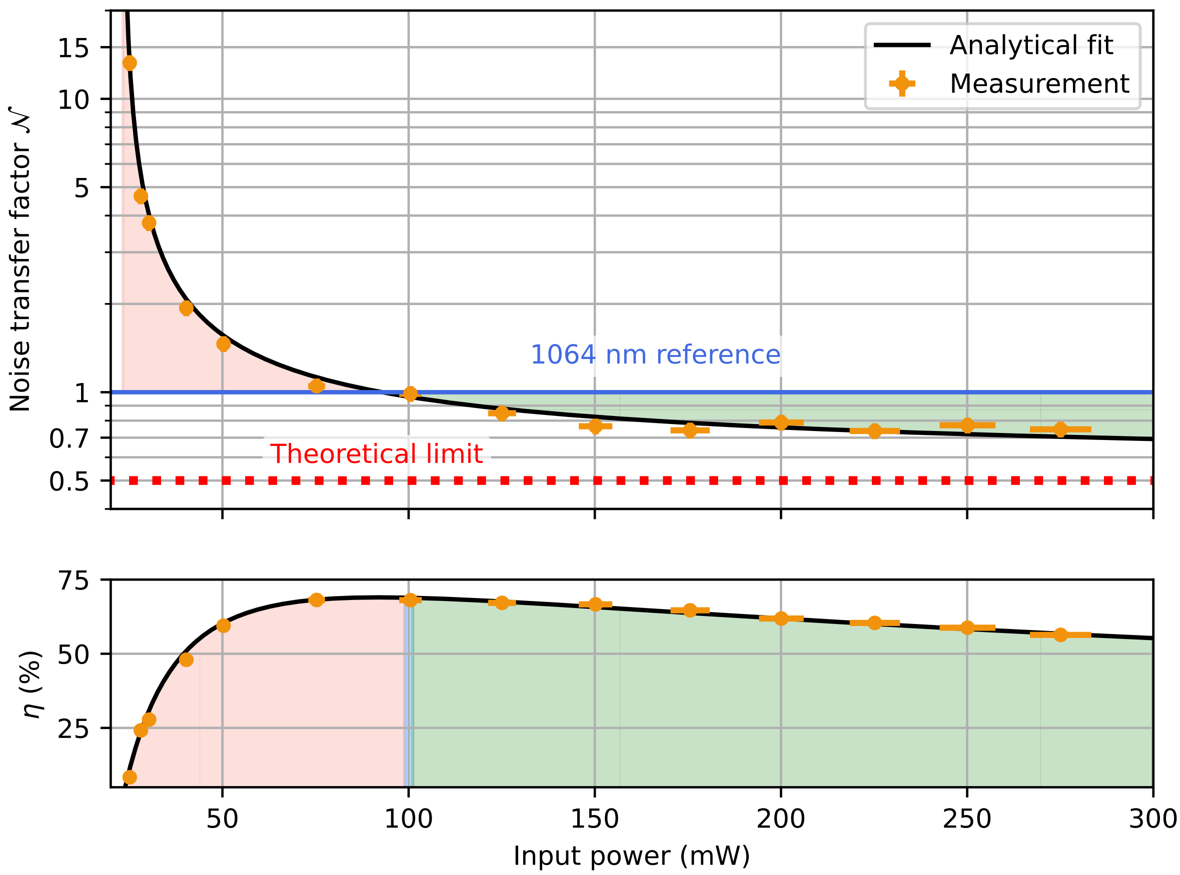

Figure 2.17: *Top image: Shown is the noise transmission factor at various pump powers (orange points) in comparison with the theoretical model (black). At high pump powers, the model approaches a suppression factor of two (red dotted line), with the experiment reaching (25.1 $\pm$ 1.8) % at a pump power of (275 $\pm$ 8) mW. For reference, the RIN of the pump field is also shown (blue). Bottom image: Displayed is the conversion efficiency η together with the analytical fit from Equation 2.1, using threshold power and maximal conversion efficiency as free fit parameters. The fit yields I_{th} = (23.6 $\pm$ 0.7) mW and η_{max} = (68.74 $\pm$ 0.4) %.*

2.5 Conclusion and Outlook

A high-power light source was developed and characterized, capable of producing up to 29 W of light at 2128 nm. This was achieved by utilizing an amplified 1064 nm MEPHISTO laser, which was injected into a nonlinear cavity and converted via optical parametric oscillation to 2128 nm. Additionally, it was demonstrated that the nonlinear process influences the transfer of coherent noise from the pump to the converted light field. This behavior can be exploited to suppress noise over a broad frequency range by a factor of up to two, resulting in a noise profile that is more coherent and cleaner than that of the pump source.

Using the scheme shown, the target of at least 20 W was successfully reached, along with the required power for low frequency ET of a few watts [7]. Higher powers may be attainable through optimization of the nonlinear cavity. One approach is to increase the beam waist within the crystal, as demonstrated in [60], though this is limited by potential clipping inside the resonator. Redesigning the cavity could offer further improvements but is constrained by the maximum crystal size available from the manufacturer. An alternative improvement involves reducing the cavity reflectivity further; however, this complicates mode separation and may result in inefficient conversion or undesired converted modes.

Beyond this approach, several alternative technologies may be considered to achieve higher output powers or improved performance at 2 µm. One possibility is to use laser systems based on active gain media, such as holmium- or thulium-doped crystalline materials, which are particularly suitable for emission wavelengths around 2090 nm due to their advantageous physical properties.

A further strategy involves coherently combining multiple beams, either within an optical ring resonator or at a beam splitter [61]. When implemented in conjunction with the presented and optimized method, beam combining could enable the generation of substantially higher power levels while retaining the advantages of well-established and reliable 1064 nm laser systems.

In addition, fiber-based systems offer another viable pathway toward high output powers, as they can efficiently scale power by combining the methods described above. These systems benefit from compactness and robust operation, although their intrinsic noise properties often require additional stabilization and improvement.

Figure 2.18 provides an overview of high-power laser systems operating in the 2 µm wavelength range. Appendix A.3 contains Table A.1, which presents the underlying data derived from this figure and includes additional information such as the M^2 parameter, with appropriate citations. The primary selection criteria for the systems displayed are continuous wave operation, emission near 2 µm, and high output power. Factors such as noise characteristics were not considered, as including them would exclude fiber-based systems or thin-disk lasers, which are inherently noisier and typically require post-stabilization. Intrinsically stable systems like the active gain medium and nonlinear conversion are particularly favored for future GWOs; other systems, such as thin-disk laser, are also under investigation. It is acknowledged that the figure may not be entirely comprehensive, and some sources may have been overlooked during the research; the author has endeavored to include all relevant data to the best of his knowledge.

The next step in this project involves characterizing a light source with an output power of approximately 50 W to 100 W, with a particular emphasis on long-term operation. This entails operating the laser continuously for several weeks to monitor potential crystal degradation, an effect not observed in our short-term experiments. Furthermore, comprehensive assessments of phase noise and beam quality (quantified by the M^2 parameter) are essential.

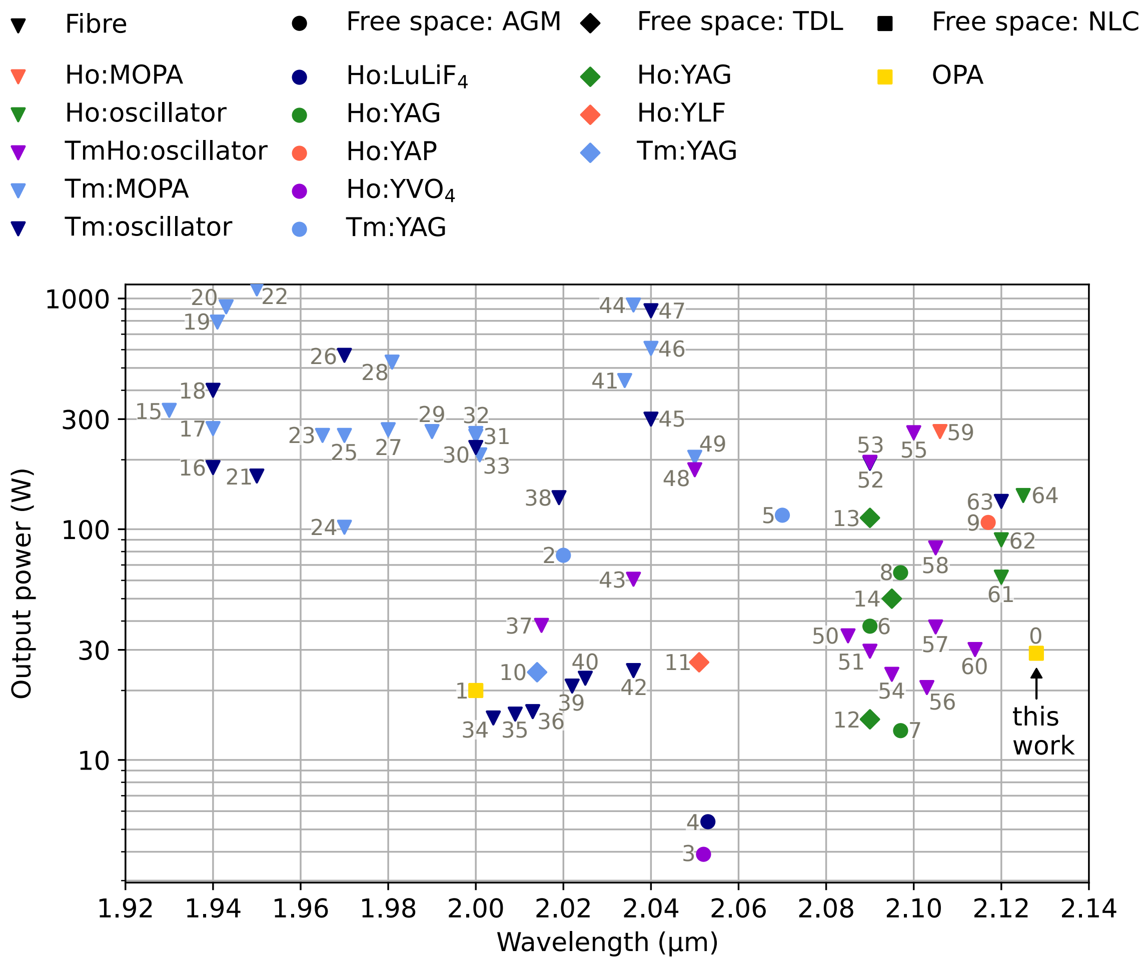

Figure 2.18: *This figure provides an overview of high-power laser systems operating around a wavelength of 2 μm. The primary selection criteria were continuous-wave operation, high output power, and emission near 2 μm. Noise characteristics were not considered. The figure distinguishes between fiber lasers (represented as triangles), and free-space lasers, which are further categorized into active gain medium (AGM, represented as circle), thin-disk lasers (TDL, represented as diamond), and nonlinear conversion (NLC, represented as square) systems. Appendix A.3, Table A.1 lists the underlying data, including the M^2 parameter and the source for each data point. The number at each data point serves as an index for easier identification in the table.*

Demonstrating that the RIN can be reduced by up to a factor of two through the nonlinear process of optical parametric oscillation opens a new pathway toward meeting the noise requirements of next-generation GWOs. In particular, further optimization of the well-established 1064 nm laser sources, as described in [62], together with their conversion to 2128 nm while preserving the intrinsic noise-reduction capability, provides a promising strategy for achieving these targets. This also highlights the next steps, in particular the development of even lower-noise 1064 nm laser systems and the combination of such ultra-low-noise sources with frequency conversion, demonstrating that exceptionally low noise levels can indeed be achieved.

Chapter 3

2128 nm Audio-Band Squeezing and Its Platforms

Squeezed states of light enhance the sensitivity of gravitational-wave observatories [63, 64, 65] and are therefore essential for their operation. As discussed in the previous chapters, detector concepts at 2 µm offer several advantages and has became a promising option for future observatories. Consequently, generating squeezed light at 2128 nm becomes a critical requirement if such detectors are to be operated at this wavelength. In this chapter, I demonstrate an audio-band squeezed-light source at 2128 nm.

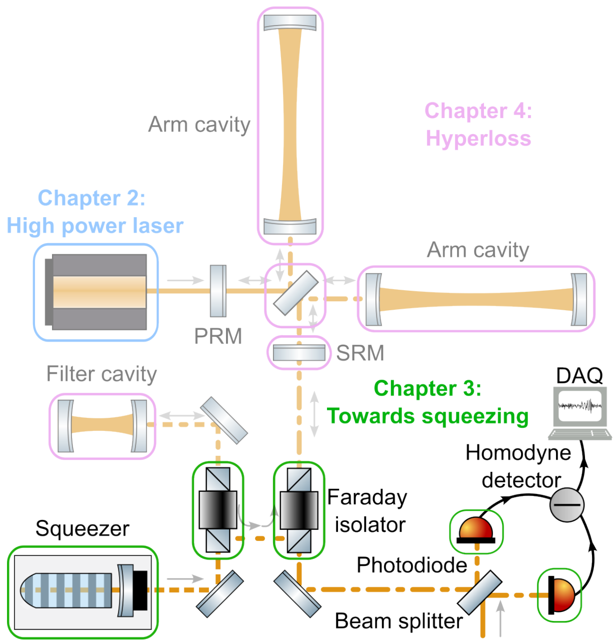

Figure 3.1: *Schematic illustration of a GWO.*

Several challenges had to be addressed along this path, as illustrated in the simplified diagram of a gravitational-wave observatory in Figure 3.1. Starting from the left, the demonstration of 7.2 dB squeezing in the high-frequency measurement regime at 2128 nm was achieved by Christian Darsow-Fromm and myself [11]. Georgia Mansell and Min Jet Yap previously demonstrated audio-band squeezing at a wavelength of around 2 µm. From 400 Hz up to approximately 1 kHz, they achieved about 2 dB of shot noise reduction. Beyond this range, up to approximately 80 kHz, the shot noise reduction increased to about 3.9 dB [8, 10]. These preliminary studies motivated this work to detect squeezing in the audio-band at 2128 nm.

However, achieving this goal presents two challenges. The first challenge concerns the photodetectors, whose quantum efficiency is currently insufficient [11, 8, 10], while their dark noise becomes limiting in the lower audio-band [8, 10]. The second challenge concerns commercially available auxiliary components required for squeezing experiments, such as Faraday isolators, which still exhibit too high optical loss. These devices are essential for suppressing back-reflections and preventing parasitic interference, both of which are critical for coupling squeezed light into gravitational-wave detectors.

This chapter addresses these two challenges in order to ultimately enable the measurement of squeezing, which forms the core of this chapter. The first section describes the investigation of a low-loss Faraday isolator constructed entirely from commercially available components. During this work, I supervised a master's student, M. Sc. Tobias Schoon, who assisted with the measurements. The second section focuses on the analysis and optimization of photodiodes, particularly regarding their quantum efficiency at lower frequencies; here, I was assisted by M. Sc. Nils Sültmann, with whom I share first authorship on a publication about cooling commercially available 2 μm photodiodes [66]. In the final section, I present the measurement of squeezed light in the frequency range of 10 kHz to 20 kHz, with assistance from M. Sc. Tobias Schoon.

3.1 Characterization of Commercially Available Faraday Isolator Components

Low-loss Faraday rotators are crucial components in GWOs, as they enable the coupling of squeezed light and help mitigate back-scattered light through Faraday isolators. The key requirements for these devices are low optical loss and a high isolation ratio.

Currently, there is limited knowledge about the performance of auxiliary optics operating at this wavelength. In this work, I present the characterization of commercially available Faraday isolators and the components required for their construction, as well as a self-assembled version using the best performing components identified.

The chapter is divided into three parts: first, focusing on the Faraday rotator manufactured by FARADAY PHOTONICS; second, on the characterization of a polarizing beam splitter produced by ARTIFEX; and finally, an analysis of a custom Faraday isolator assembled from components supplied by FARADAY PHOTONICS and ARTIFEX.

3.1.1 Faraday Rotator by Faraday Photonics

In this section, a low-loss Faraday Rotator (FR) from the company FARADAY PHOTONICS was evaluated for various properties at a wavelength of 2128 nm. The analysis includes the transmission characteristics, the crystal's absorption spectrum, broadband AR coating performance, and the polarization rotation.

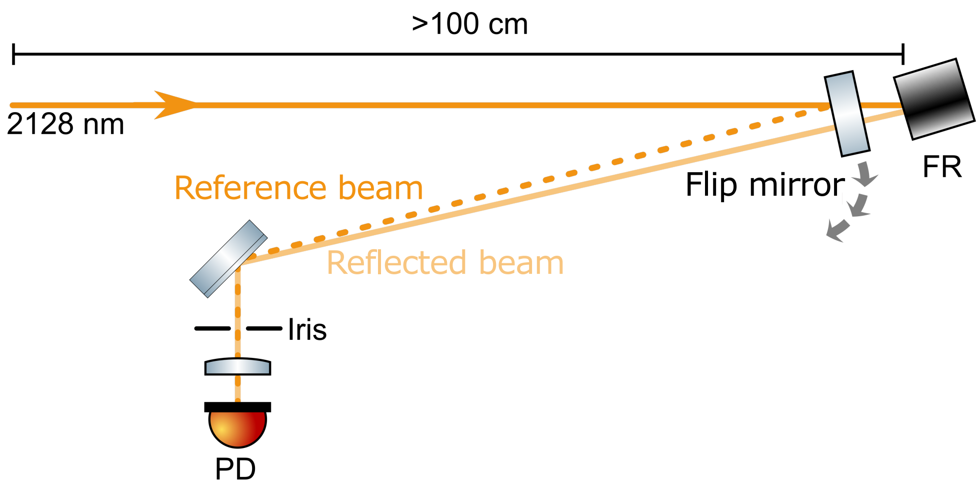

Figure 3.2: *Experimental setup to measure the back-reflected light from the FR crystal's broadband AR-coating. The 2128 nm beam was sent through the FR, and the reflected light was measured by a photodiode. Side reflections were suppressed using an iris.*

The transmission of the Faraday Rotator was measured with a PD, yielding a value of (97.6 ± 0.1) %. Laser-power drift constituted the main source of uncertainty.

To understand the remaining 2.4 %, the quality of the AR coating was further analyzed. Figure 3.2 illustrates the experimental setup, where 2128 nm light was directed onto the FR at a small angle of incidence (AOI). Reflected light from the AR coatings was detected by a photodiode. To ensure accurate results, the transmission through the Faraday Rotator was maintained at its optimal level throughout the measurements. Since the beam was transmitted through the crystal, it was reflected by both AR coatings; the main spot was identified and selected via an iris. A reference measurement was performed directly in front of the FR using a flip mirror. More precisely, flipping the high-reflectivity-coated mirror into the beam path directed the light directly onto the photodiode.

Figure 3.3 presents the results of the broadband AR-coating characterization, showing the reflectivity of the coatings as a function of the AOI. Both sides of the crystal were characterized individually. The brown dots represent the reflection from the front side (also called the first side), and the violet crosses correspond to the back side. Resulting in $(1.39 \pm 0.06)\,\%$ for the front and $(1.34 \pm 0.06)\,\%$ for the back, with no significant dependence on the AOI observed for either side. The primary sources of uncertainty in these measurements are the $0.06\,\%$ intensity fluctuations measured by the photodiode and the $0.25\,°$ adjustment of the angle.

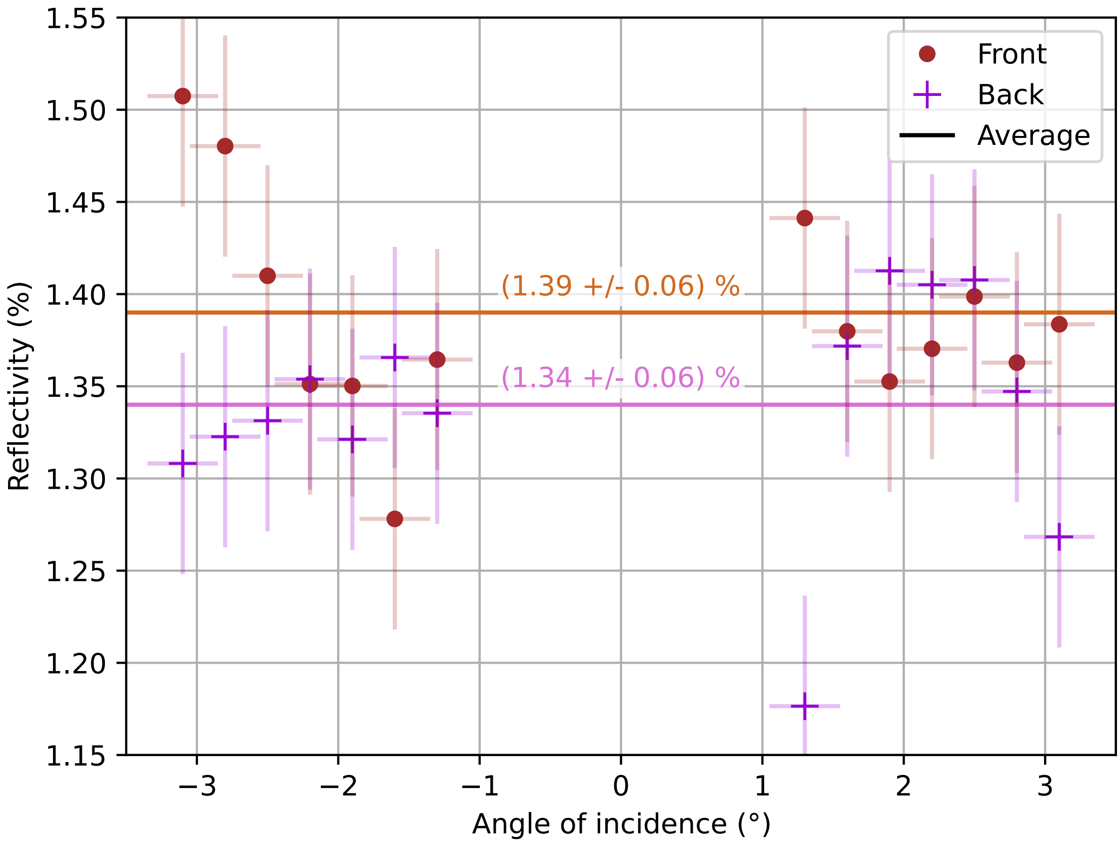

Figure 3.3: *Reflection of the AR-coatings as a function of the AOI. The violet crosses represent measurements of the front coating of the crystal, while the brown dots correspond to the back coating. Reflectivity values of $(1.39 \pm 0.06)\,\%$ and $(1.34 \pm 0.06)\,\%$ were obtained for the front and back sides, respectively. The lines show the average values derived from the measurements. Measurement inaccuracies are omitted to preserve the visualization clarity of the results.*

Combining these values indicates that the primary source of optical loss is the AR-coating, which is likely optimized for a broader wavelength band. Tailoring the coating specifically to the wavelength used can significantly improve transmission, potentially achieving a high-transmission Faraday Rotator with >99 % efficiency.

I investigated the polarization rotation of the light field as it passes through the Faraday Rotator. The optimal single-pass rotation angle is 45°. To verify this, we employed the experimental setup shown in Figure 3.4.

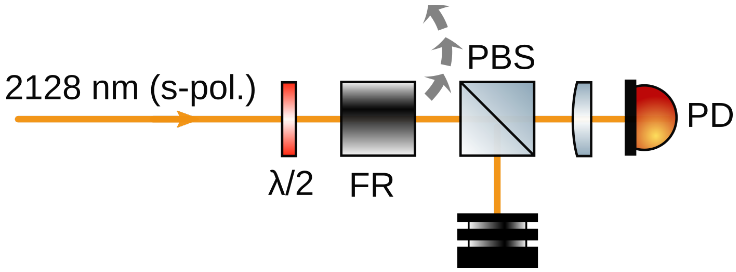

Figure 3.4: *Schematic setup for measuring the polarization rotation caused by the FR. The s-polarized light is divided into p- and s-polarization components by a PBS after passing through a λ/2-waveplate and the FR. A photodiode measures the transmitted light (p-polarization), while a beam dump absorbs the reflected light (s-polarization).*

S-polarized light was sent through a λ/2-waveplate and the FR before being split by the polarizing beam splitter. The intensity of the transmitted light was measured both with and without the FR, as a function of the polarization rotation introduced by the λ/2-waveplate. This measurement was performed at wavelengths of 2128 nm and 1550 nm to assess the rotation angle and examine how it varies across different wavelengths.

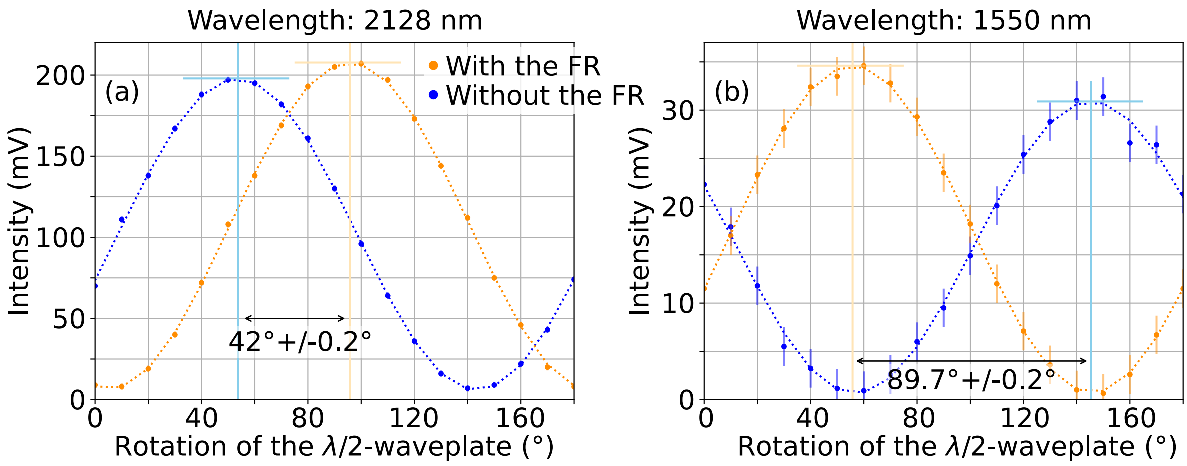

Figure 3.5: *Orange dots were recorded with the FR in the optical path, while the blue dots correspond to measurements without the FR. The maximum transmitted powers and rotation angles were determined by fitting a $\cos^2$ function. (a) shows the results at 2128 nm, and (b) at 1550 nm. For 2128 nm, the rotation angle diverges only slightly from the ideal 45° rotation. Measurement inaccuracies in the angle of ± 0.2° are too small to be visible in the image, while the intensity is dominated by the photodiode noise level, with an uncertainty of ± 2 mV.*

Figure 3.5 presents the results of the polarization measurement, where the measured intensity is plotted against the waveplate rotation angle. The maximum intensity I_0 was extracted by fitting the data with the theoretical model:

$$I(\theta) = I_0 \cdot \cos(\theta - \theta_0)^2 + I_{\text{offset}},$$

with θ denotes the waveplate angle, θ_0 is the rotation induced by the FR, and I_{offset} accounts for the photodiode's dark-voltage offset. At 2128 nm, the FR rotated the polarization of the light field by approximately $(42.0 \pm 0.2)\,^\circ$, and at 1550 nm by about $(89.7 \pm 0.2)\,^\circ$. In both measurements, the main source of uncertainty was the precision with which the waveplate angle could be set.

If a $42\,^\circ$ rotation is applied to the Faraday isolator used for coupling squeezed light into a gravitational-wave observatory, as shown in Figure 3.1, the light passes through the isolator twice. This results in an additional loss of 1.1 %, which can be reduced by carefully optimizing either the magnetic field B or the material thickness d, as described by the theoretical model [67]

$$\theta_0 = d \cdot B \cdot V. \tag{3.1}$$

The Verdet constant V could not be determined due to the difficulty in measuring the magnetic field, as the FR's metallic casing likely affects the magnetic flux.

Note that the material used for the Faraday Rotator is a company secret and was not disclosed to us.

3.1.2 Polarizing Beam Splitter by Artifex

In this chapter, I present my evaluation of various features of a PBS from the company Artifex Engineering at a wavelength of 2128 nm. A schematic drawing of the two experimental setups is shown in Figure 3.6.

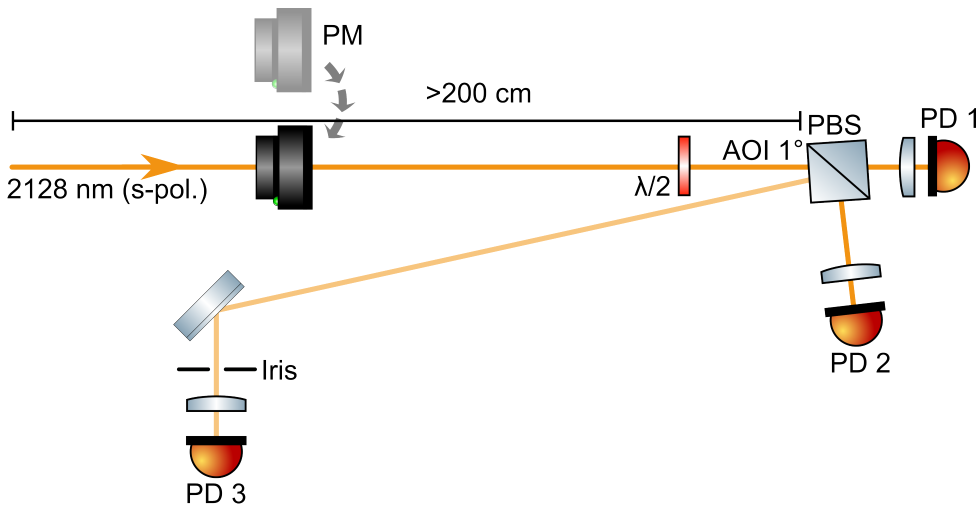

Figure 3.6: *A simplified schematic illustrating two experimental setups. The first investigates the PBS transitivity and internal reflectivity using PD 1 and PD 2 for analysis, with a $\lambda/2$ waveplate to separate the two signals. In the second setup, the AR coating was examined by reflecting light at a small incident angle onto the coating and detecting the back-reflected light at PD 3, with an iris used to filter out the strongest reflections. For both setups, a power meter (PM) recorded the reference intensity, calibrated to the corresponding photodiode.*

Initially, the splitting ratio was analyzed by passing light through a $\lambda/2$-waveplate and directing it onto the PBS. The transmitted light was detected with PD 1, as was the internal reflected light with PD 2. A power meter was used to measure the incident power, which was calibrated to PD 1. This measurement was performed for several PBS units. The results showed a transmission range of approximately $(95.0 \pm 0.5)\,\%$ to $(97.0 \pm 0.5)\,\%$, and a reflection range of about $(97.0 \pm 0.5)\,\%$ to $(99.0 \pm 0.5)\,\%$. Measurement uncertainties mainly stem from the calibration uncertainty of the power meter [55]. All tested PBS units satisfied the manufacturer's specifications. The minor absorption observed could be due to broadband AR coatings, material absorption, or the cement used between the layers in the MacNeille PBS design.

Characterizing the AR-coating was the focus of the second measurement. For this, the same setup as shown in Figure 3.6 was used, with the key difference being the increased distance between the light source and the PBS. This was done to achieve a separable back reflection at a very small angle. The transmission was maintained at its maximum by adjusting the waveplate in front of the PBS. Identifying the most intense back reflection as the main source, other reflections were blocked with an iris. Two brighter reflections were observed, one from the front surface and one from the back surface of the PBS, as well as several extremely suppressed reflections with poor beam profiles, likely originating from the cement layer. PD 3 was used to quantify the intensity of the back-scattered light, and a power meter measured the incident beam power to serve as a reference. Calibration with the photodiode allowed the power meter to translate power measurements into voltage readings.

The ratio of the transmitted and reflected beams was then calculated, resulting in approximately $(0.032 \pm 0.020)\,\%$ of the incident light being reflected by the AR-coating. According to the data sheet, the material used for the PBS is H-FK61, which has an absorption coefficient of approximately $0.10005\,\frac{\%}{\mathrm{cm}}$ [68]; based on this, the resulting absorption is estimated to be around $0.15\,\%$. Additionally, NOA 61, a commonly used cement material, has an estimated absorption of about $5\,\%$ per typical layer thickness at $2128\,\mathrm{nm}$ [69].

3.1.3 Composed Faraday Isolator

An analysis of the individual components of a Faraday Isolator was conducted. The next step is to assemble these components and evaluate the overall performance of the FI. Figure 3.7 illustrates the detailed design of the custom setup. The design consists of four main parts:

PBS holder: Contains the PBS housed within a cylindrical device made of polyvinyl chloride (PVC). The PBS is fixed with screws and features a hole for measuring the intensity at all output ports.

PBS holder adapter: A metal ring that connects the PBS holder to the FR holder. Screws allow the PBS holder to be freely rotated and secured in any desired position.

FR holder: A cylindrical tube into which the Faraday Rotator is inserted and fixed with a screw. Note: The FR does not have a preferred light direction.

Foot: Made of a plastic plate that can be clamped to a table. The FR is placed into a U-shaped recess and secured with a yoke, allowing independent adjustment of the FR and PBS positions.

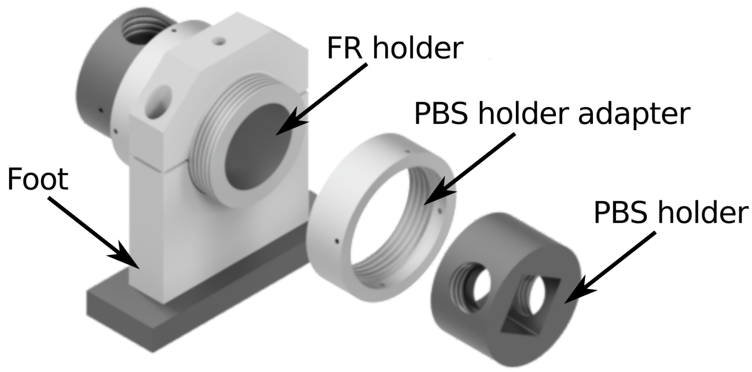

Figure 3.7: *CAD model of the FI optical design. The design is divided into four sections: the PBS holder, the PBS holder adapter, the FR holder, and the foot. Optimizing the setup is achieved by rotating the PBS and FR holders.*

Table 3.1 presents the measured transmission efficiencies of the handmade Faraday Isolator.

Table 3.1: *Transmission efficiencies of the custom FI, assembled with a Faraday Rotator from* FARADAY PHOTONICS *and PBS from* ARTIFEX. *Each component was characterized individually, selecting the best PBSs available. Subsequently, the overall transmission loss of the FI was measured. Discrepancies between the product of individual efficiencies and the total transmission were observed and can be attributed to coupling losses and possible internal clipping. Maximum transmission was prioritized during setup optimization, rather than suppression of back-reflections.*

Component	**Efficiency (%)**
Incoupling PBS	98.0 $\pm$ 0.5
Faraday Rotator	97.6 $\pm$ 0.5
Outcoupling PBS	96.2 $\pm$ 0.5
Total efficiency as product of components	**92.0 $\pm$ 0.8**
Measured total transmission	**88.9 $\pm$ 1.3**

The incoupling PBS exhibited an efficiency of (98.0 ± 0.5) % and the outcoupling PBS showed an efficiency of (96.2 ± 0.7) %. From our order batch, we selected the two best-performing PBS units. The Faraday Rotator achieved an efficiency of (97.6 ± 0.5) %, resulting in a total calculated efficiency of (92.0 ± 0.8) %. All uncertainties stem from measurement inaccuracies in the intensity readings.

After assembling and testing these components, the overall system efficiency was measured to be (88.9 ± 1.3) %, with losses likely due to coupling inefficiencies and possible internal clipping.

Back-reflected light coupling through the FI was suppressed to (0.053 ± 0.003) %, corresponding to approximately (32.8 ± 0.3) dB of isolation. Improving the polarization rotation of the FR could enhance the suppression further, but this would come at the cost of reduced transmission.

3.1.4 Conclusion and Outlook

Using squeezed light in gravitational-wave detectors makes the development of low-loss output Faraday isolators increasingly essential. Future detectors may operate at a wavelength of 2 µm, but optical components with excellent properties at this wavelength have seen limited development. In this context, commercially available Faraday rotators and polarizing beam splitters were examined for their performance at 2128 nm.

Faraday Photonics' Faraday rotator exhibits a transmission of $(97.6 \pm 0.1)\,\%$ in its current configuration. Losses are mainly attributed to a broadband anti-reflective coating, which could be nearly eliminated by optimizing it for the specific wavelength used. This device imparts a polarization rotation of $(42.0 \pm 0.2)^\circ$ on the incident light, which could introduce approximately 1.1 % additional losses in a gravitational-wave observatory. The rotation angle can be improved by modifying the magnetic field, thus reducing related losses.

Artifex Engineering's PBS features an exceptionally effective AR coating, resulting in minimal losses due to the low material absorption of H-FK61 at 2128 nm. Replacing the current cemented PBS with an optically contacted one is expected to achieve near-lossless performance.

A custom FI housing was designed and built using the characterized components. This configuration achieved a transmission of $(88.92 \pm 1.30)\,\%$ and an isolation of approximately (32.8 ± 0.3) dB against back-scattered light.

Table 3.2 compares this custom FI to available models from various manufacturers. The information was obtained from manufacturer websites and should be regarded as guidelines rather than confirmed performance values [70, 71, 72].

Table 3.2: *Comparison of performance between commercial and self-built Faraday isolators.*

	Wavelength (nm)	**Transmitted power (%)**	**Isolation (dB)**
Thorlabs	2000 - 2100	89	23
Agiltron	1310 - 2000	90	35
Coherent	1900 - 2100	94	33
This work	2128	88.92 ± 1.3	32.8 ± 0.3

As shown, the performance of the currently built FI falls within the mid-range of commercially available solutions. However, it can be readily optimized to outperform existing products.

For use in a gravitational-wave observatory, the total transmission loss must be minimized, with current versions achieving less than 1 % loss [73]. The issues discussed earlier can be addressed with current technologies, potentially leading to an almost lossless FI; making it suitable for application in a GWO.

3.2 Investigation of Photodiodes

In the field of quantum technologies, encompassing quantum sensing, quantum communication, and quantum computing, high-quality detectors are essential for the reliable operation of quantum networks. Two key limitations of such detectors are insufficient detection efficiency and excessive dark current, the latter arising from thermally generated electrons entering the conduction band and thereby producing spurious counts that mimic true photon detection events. To characterize these effects, we distinguish between the quantum efficiency, η_{QE}, which includes contributions from the photodiode's dark noise, and the detection efficiency, η_{DE}, which excludes dark noise contributions, as introduced in Equation 1.54 and 1.55. For convenience, they are also listed here:

$$\eta_{\text{DE}} = \frac{U_{\text{tot}} - U_{\text{dark}}}{U_{\text{perf}}},$$
$$\eta_{\text{QE}} = \frac{U_{\text{tot}} - U_{\text{dark}}}{U_{\text{perf}} + U_{\text{dark}}},$$

Photodiode manufacturers are primarily concerned with detection efficiency, since the impact of dark noise depends on external factors such as the optical power used and the noise characteristics of the transimpedance amplifier. For users of quantum technologies, however, the quantum efficiency of the entire detection system is more relevant. For example, if the dark current equals the photocurrent, even under perfect detection conditions the quantum efficiency is limited to 50 %. This parameter is irrelevant for standard applications such as monitoring photodiodes. In these cases, a lower QE is sufficient, as long as it stays within a moderate range.

Photodiode Room-Temperature Investigations

Investigating photodiode performance at 2 µm is particularly important, as the widely used detector material extended InGaAs typically exhibits lower detection efficiency and higher dark noise at this wavelength. We therefore begin by characterising multiple photodiode models at room temperature by measuring their quantum efficiency, using the setup shown in Figure 3.8.

Since both the photodiode response and, in particular, the dark current depend on the applied reverse bias, we set and continuously monitored this parameter throughout all measurements. The depletion region lies within the intrinsic layer (see Chapter 1.4.1) and depends on the applied voltage. This influences the photodiode's capacitance, resistance, and dark-current behaviour [74]. A schematic diagram of the setup is shown on the left-hand side. To set the photodiode to the desired bias voltage, an external voltage source (GPS-3303 by GW INSTEK) was used, and the applied voltage was verified with a voltmeter (UT804 by UNI-T). The corresponding photocurrent was measured with an ammeter (UT804 by UNI-T).

A photograph of the experimental setup is displayed on the right-hand side. Using a mirror and a focusing lens, the 2128 nm laser beam was directed onto each photodiode. The lens was subsequently adjusted to reach the photocurrent's saturation plateau, ensuring a reproducible operating condition for every device. In other words, the laser focus was always adjusted to ensure that the maximum amount of light was directed onto the photodiode. Optical power measurements were performed by redirecting the beam to a power meter (OPHIR model 3A-QUAD) via a flip mirror.

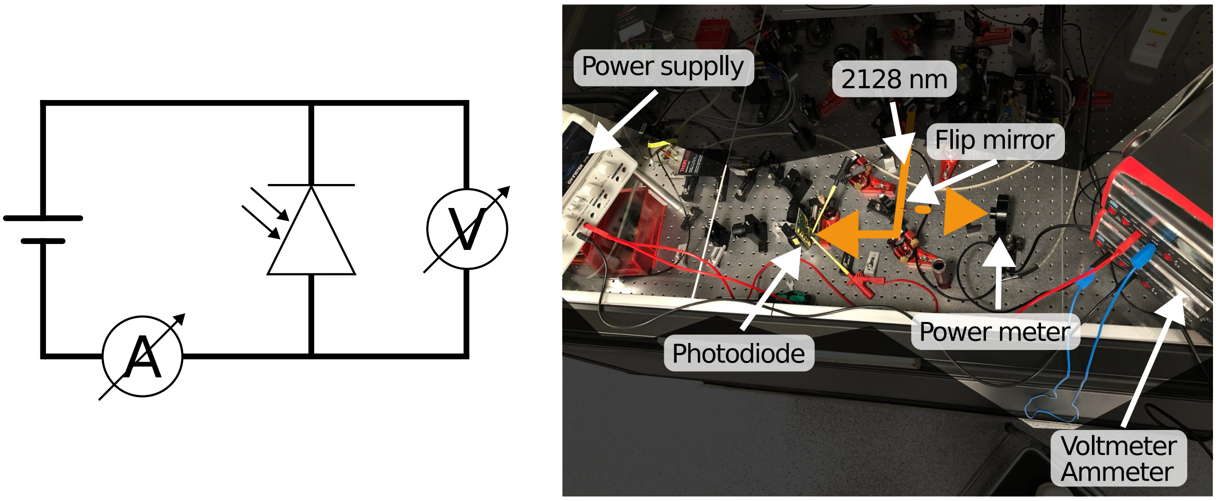

Figure 3.8: *Shown on the left is a schematic representation of the setup used for determining the quantum efficiency, while the right side displays a photograph of the actual arrangement. The reverse bias of the photodiode was adjusted with a power supply, verified using a voltmeter, and the resulting photocurrent was recorded with an ammeter.*

The maximum measurable number of photoelectrons was estimated by first measuring the input power and converting it into the corresponding photon flux N. Assuming a given quantum efficiency, this photon flux yields the number of electrons generated per second. The conversion was performed using

$$N = \frac{P\lambda}{hc},$$

where P denotes the measured optical power, λ the operation wavelength, h Planck's constant, and c the speed of light. The resulting value was then inserted into Equation 1.55, together with the measured photovoltage, in order to determine the quantum efficiency. Figure 3.9 shows the quantum efficiency as a function of bias voltage for multiple photodiode models intended for use at wavelengths close to 2128 nm. The investigated photodiode models include FD05D, shown as diamonds, and FD10D, shown as squares, both sold by THORLABS. G12183, represented by circles, is manufactured by HAMAMATSU, while IG26H and IG22X, indicated by downward- and upward-pointing triangles respectively, were produced by LASER COMPONENTS. Data points shown as stars correspond to an FD05D measured once with a protective window (light-blue stars) and once without it (dark-blue stars). This comparison allows the transmission of the window at 2128 nm to be quantified and reveals an additional loss of approximately 3 %.

Bias voltages were applied only up to the maximum values recommended in the respective datasheets [75]. All models employ extended InGaAs as the semiconductor material. A substantial variation in quantum efficiency appears both across different models and within the same model series, likely arising from manufacturer-specific doping processes and batch-to-batch variations inherent to semiconductor growth. Two photodiodes with particularly high performance, reaching quantum efficiencies of around 90 %, were identified. The accuracy of the data is limited by the 3 % uncertainty of the power meter measurement [55].

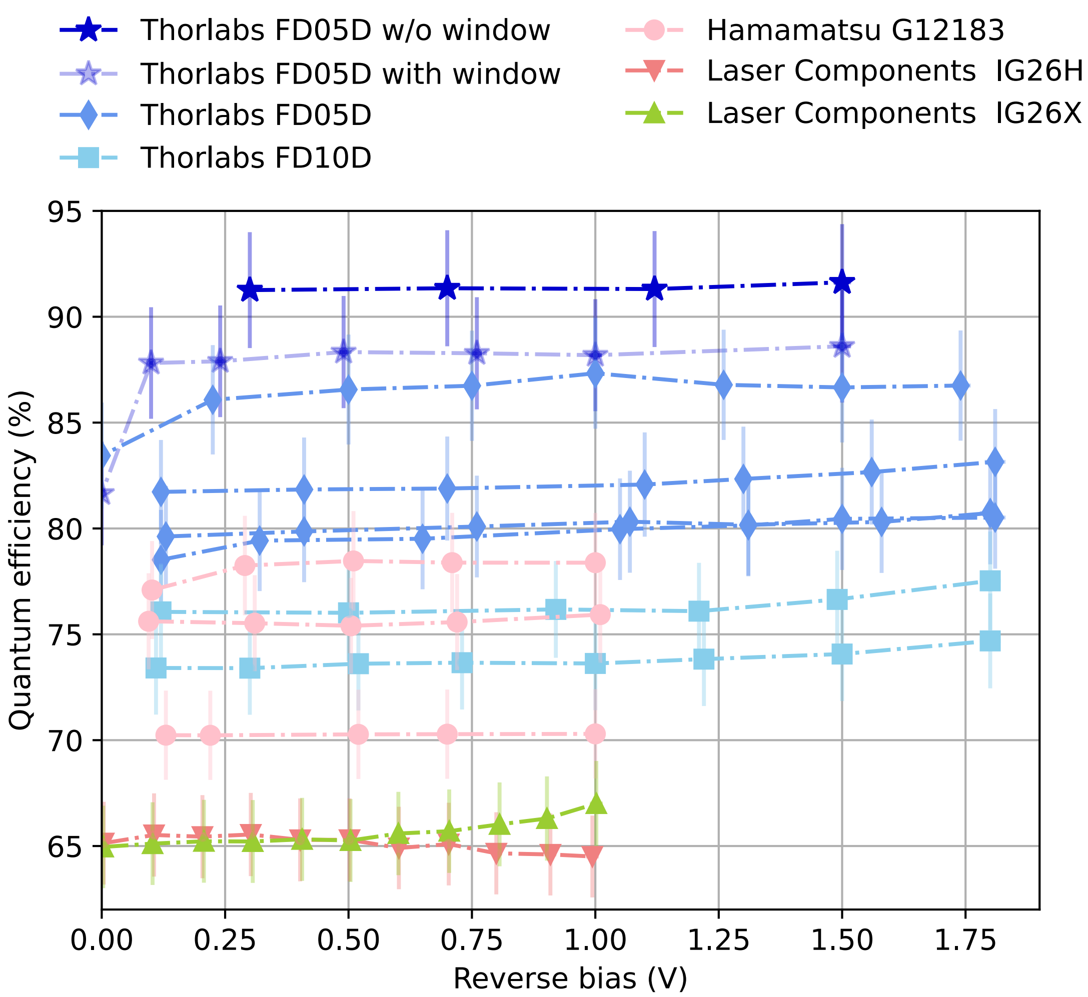

Figure 3.9: *This figure presents the quantum efficiency as a function of bias voltage for several photodiode models. Each model is represented by a distinct symbol: FD05D by a diamond, G12183 by a circle, FD10D by a square, IG26H by a downward-pointing triangle, and IG22X by an upward-pointing triangle. Particular attention should be given to the star symbol, which compares an FD05D with and without its protective window and indicates a loss of approximately 3 %. The quantum efficiency varies significantly across the different models and shows no clear dependence on the applied bias voltage. Two photodiodes with exceptionally good performance were identified; however, one of them broke during the course of the measurements. Data are displayed only within the bias-voltage range recommended by the manufacturer, as operation above this threshold led to an avalanche-like response, which was not investigated in greater detail.*

Two additional measurements were carried out to determine whether the quantum efficiency is limited by the semiconductor material itself or by the coating applied to it. The first measurement examined the QE as a function of the laser AOI, shown in Figure 3.10(a). The second measurement investigated the reflectivity of the semiconductor's anti-reflection (AR) coating as a function of AOI, shown in Figure 3.10(b). Both measurements were performed without the photodiode's protective window.

The QE was determined using the procedure described above, and its accuracy is primarily limited by the 3 % power-measurement uncertainty. For analytical and empirical fitting, a

Tschebyscheff-type function was used, as it provides a flexible peak-shaped profile with independently adjustable amplitude and width. This functional form offered a stable and accurate empirical fit to the measured data, without implying any physical model. The equation is given as

$$\mathfrak{F}(x) = \frac{a}{\sqrt{1 + b^2 \cdot ((x/c)^2 - 1)^2}},$$

where a controls the amplitude of the function and b characterizes its width, describing how quickly the QE decreases with the angle. In this expression, parameter c denotes the optimal angle of incidence and was determined to be $(35.9 \pm 0.2)\,°$. The reflected power exhibits substantial variation but shows a weak trend toward higher values at larger AOI. On average, approximately $(0.85 \pm 0.4)\,\%$ of the light is reflected.

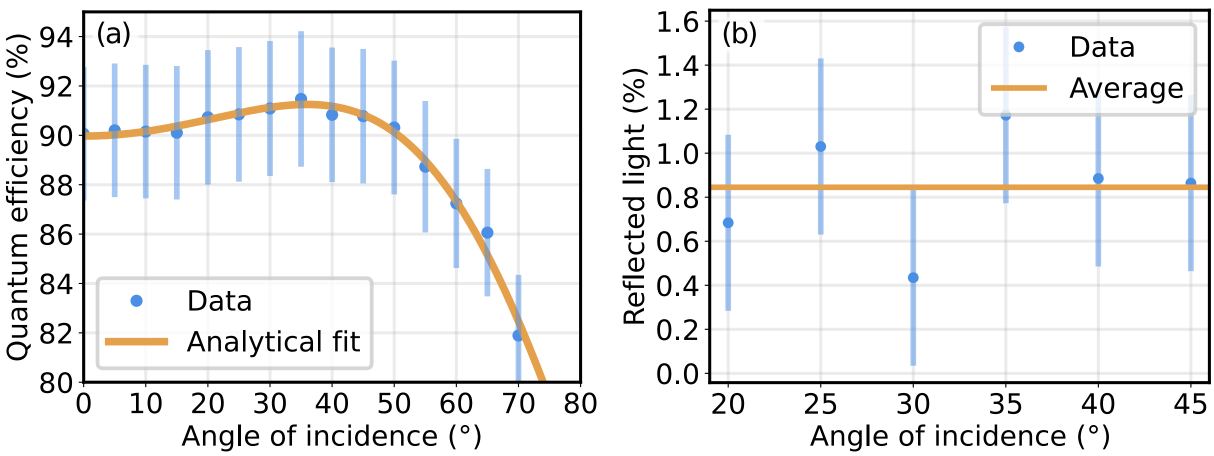

Figure 3.10: *This figure displays (a) the quantum efficiency and (b) the reflectivity of the semiconductor's anti-reflection coating as functions of the laser's angle of incidence. An optimal angle of approximately (35.9 ± 0.2) ° was identified and provides an increased QE while maintaining nearly constant reflected power. Note that the measurement was done without the photodiode window.*

This characterization shows that the model FD05D by THORLABS is the most suitable candidate, as it exhibits the highest measured QE over a wide range of reverse bias voltages. Two additional optimizations are the removal of the protective window and operating the photodiode at the optimal angle of incidence. One further approach is to reuse the light reflected from the photodiode at the chosen angle of incidence by placing a retroreflector behind the device. When positioned appropriately, the curved mirror redirects the reflected beam back onto the active area of the photodiode, allowing the previously lost light to be measured once more, as demonstrated in [76, 77].

3.2.1 Exploratory Study on Photodiode Cooling

Low-frequency shot-noise reduction measurements in the experiment conducted by G. Mansell and M. J. Yap were limited by the dark noise of the photodiodes [10, 8]. Cooling provides a promising approach to mitigating this limitation and is therefore examined in the following chapter. A reduction in dark noise with decreasing temperature is expected and well understood, as dark noise primarily originates from thermal excitation [78]. Thermal generation of charge carriers leads to a finite probability of overcoming the bandgap between the valence and conduction bands, even in the absence of incident light. For InGaAs photodiodes, an additional consideration is the temperature dependence of the bandgap; as the temperature decreases, the bandgap typically widens, which can lead to a substantial reduction in photoelectric response below a wavelength-dependent threshold temperature [74].

In light of these temperature-dependent effects, a preliminary study was carried out to obtain rapid insight into the behavior of the photodiodes under lower temperatures, followed by a more detailed and comprehensive investigation.

A schematic of the experiment is provided in Figure 3.11(a); a photograph of the setup, consisting of a THORLABS FD05D photodiode and a custom electronic evaluation board, is shown in Figure 3.11(b). The purpose of the experiment was to rapidly assess the dark-noise behavior of the photodiode as a function of frequency in two temperature regimes: room temperature and liquid-nitrogen temperatures, necessitating the use of a liquid-nitrogen tank. A reference measurement of the total noise of the photodiode was taken at room temperature before cooling (orange trace) and after cooling (violet trace). To cool the photodiode, it was immersed in liquid nitrogen for 10 minutes (blue trace). A shielded cable was used to connect the cold photodiode to the electronic evaluation board. This board, which was designed in-house by M. Sc. M. Schröder, includes a variable bias voltage set to 1.5 V and a transimpedance amplifier (AD797 with a 2 kΩ feedback resistor). Before analyzing the signal with a signal analyzer from STANFORD RESEARCH SYSTEMS (model SR785), the signal was amplified using an AD797 with a gain of 100 and high-pass filtered at 100 Hz. The overall design was optimized for low-frequency operation.

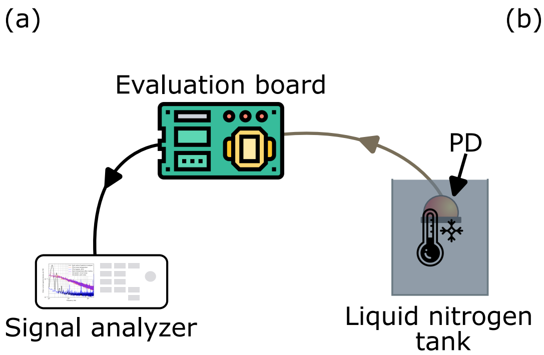

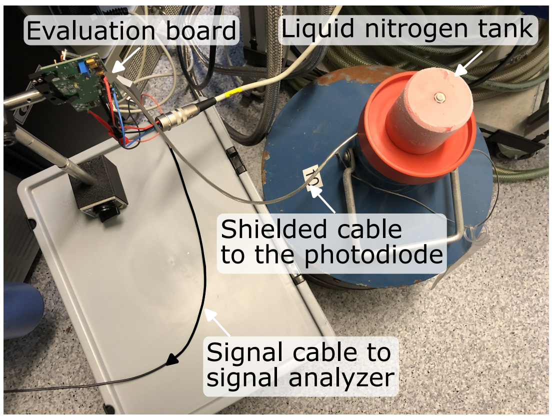

Figure 3.11: *(a) Schematic of the preliminary study investigating dark-noise reduction of the photodiode by cooling it with liquid nitrogen. (b) Photograph of the experimental setup using the FD05D photodiode (THORLABS). A custom electronic evaluation board converted the photodiode current into a voltage and forwarded it to the signal analyzer for spectral analysis.*

Figure 3.12 presents the results. Dark noise was measured from the electrical board without a photodiode, using a 10 pF capacitor to emulate the photodiode (black trace). This total circuit noise, N_{Circuit}, was then simulated (dashed gray trace) based on Equation 14.26 from "Photonic Devices" by Jia-Ming Liu [79], as illustrated by Equation 3.2. In this equation, h and k_B are the Planck and Boltzmann constants, respectively; B is the system bandwidth (set to 1, as the bandwidth is not a limiting factor); f is the frequency; and T is the temperature.

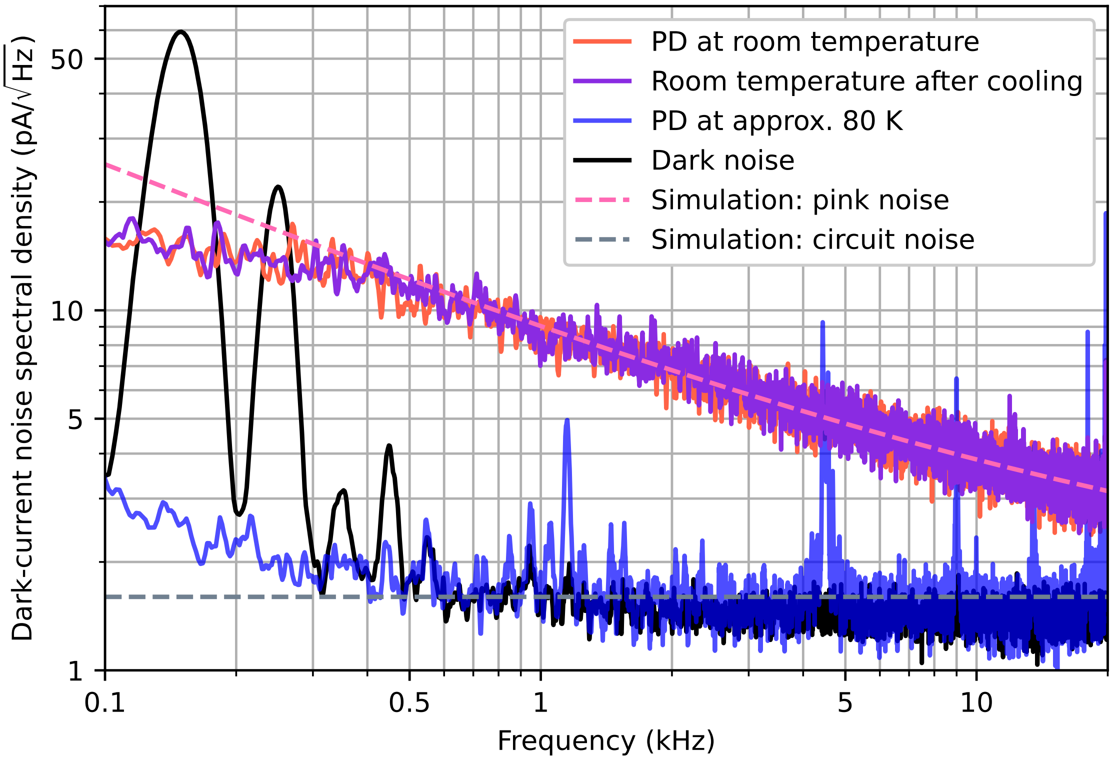

Figure 3.12: *Spectral density of the dark-current noise as a function of frequency, showing dark-noise measurements of the 2 µm photodiode FD05D from* THORLABS*. Room-temperature measurements are shown in orange and violet, taken before and after cooling with liquid nitrogen, respectively. In blue, the trace corresponds to the photodiode cooled to liquid-nitrogen temperature. The dark noise of the electronic evaluation board was recorded separately using a simulated photodiode input with 10 pF capacitance (black trace); see main text for a discussion of the low-frequency features. Comparison with theoretical models shows good agreement, with the pink dashed line representing pink noise and the gray dashed line indicating the circuit noise. Note that the RBW was set to 30 Hz and the VBW to 10 Hz, and the data were averaged.*

The corresponding noise terms are defined as

$$N_{\text{Resistor}} = \sqrt{B \cdot \frac{4 \cdot h \cdot f}{R \cdot \exp(\frac{h \cdot f}{k_B \cdot T}) - 1}}, \tag{3.2}$$

$$N_{\text{Circuit}} = \sqrt{N_{\text{Resistor}}^2 + N_{\text{Opamp}}^2}. \tag{3.3}$$

Based on the current-noise specifications given in the AD797 datasheet and considering the operating conditions of the circuit, the operational-amplifier noise contribution in the setup was estimated to be $N_{\text{Opamp}} = 1.6 \,\frac{\text{pA}}{\sqrt{\text{Hz}}}$ [80]. Since the measured noise at low frequencies exhibits a 1/f-like behavior, the photodiode noise was modeled using the basic expression for pink noise given in Equation 1.51. The corresponding power spectral density was converted into an amplitude spectral density and extended by additional fitting parameters to account for experimental deviations:

$$\mathfrak{F}(f) = \frac{a}{\sqrt{f}} + y_0, \tag{3.4}$$

where a represents a scaling factor determining the strength of the noise contribution and was found to be 0.24 nA, and y_0 accounts for a constant background noise floor, with a value of $1.5\,\frac{\mathrm{pA}}{\sqrt{\mathrm{Hz}}}$. The simulation confirms that the photodiode noise follows pink-noise behavior. Moreover, the results clearly show that cooling significantly reduces this noise contribution. Low-frequency oscillations in the dark noise can be attributed to the behavior of the operational amplifier. These oscillations could have been minimized by optimizing the capacitor across the feedback resistor; however, this was not implemented to preserve a direct comparison between the simulated dark noise and the cooled photodiode.

Reheating the photodiode revealed that it withstands cooling without damage, as evidenced by its return to initial noise levels. This suggests that operating outside the temperature range specified in the datasheet [75] does not necessarily harm the photodiode. Furthermore, the photodiode's response to 2128 nm wavelength was tested; it was integrated into a laser setup and exposed to light at this wavelength, resulting in a measurable response.

3.2.2 In-Depth Investigations into Photodiode Cooling

In the previous chapter, preliminary investigations into the cooling of photodiodes were conducted using a simplified experimental setup. The present chapter provides a more detailed analysis of the photodiode's performance under controlled cooling conditions, with particular emphasis on its detection efficiency. To this end, we employ a cryostat system capable of reaching significantly lower temperatures while allowing precise temperature monitoring.

Shown in Figure 3.13(a) is the experimental setup used for these measurements. A custom-built closed-cycle ^{3}He cryostat, equipped with a pulse-tube pre-cooling stage and an integrated dilution refrigeration unit (manufactured by ENTROPY), serves as the core cooling apparatus. The experimental chamber is mechanically decoupled from the cryostat and mounted on an optical table. This mechanical isolation substantially reduces the transfer of vibrational noise from the cooling system, thereby preventing disturbances of the optical alignment and ensuring stable measurement conditions.

Light from a 2128 nm laser source [23], located in another laboratory, was delivered via a 20 m fibre to the cryostat and directed onto a THORLABS FD05D photodiode. The photodiode window was removed since it introduces an additional approximately 3 % loss due to the broadband anti-reflective coating. Nonetheless, approximately 0.8 % reflectivity of the semiconductor surface remains, as discussed in the previous chapter. Long-term stability of the laser power was verified through long-duration measurements of the photodiode signal at room temperature, which remained stable over several days. The laser beam was coupled into the cryostat in free space through an optical viewport featuring anti-reflective-coated windows and a clear aperture of 10 mm. Three layers of thermal shielding, each with an anti-reflective coating window, provided protection from thermal radiation. The photodiode was mounted in a copper holder to ensure good thermal contact, as shown in the zoomed-in image in Figure 3.13(b).

A Cernox sensor from LAKESHORE was installed as close as possible to the photodiode and used to measure the temperature throughout a complete cooling cycle. This is shown in the lower left corner of Figure 3.13(a) (blue indicates cooling, and red indicates heating). During this measurement, the cryostat did not have an active heating system, which accounts for the extended heating period.

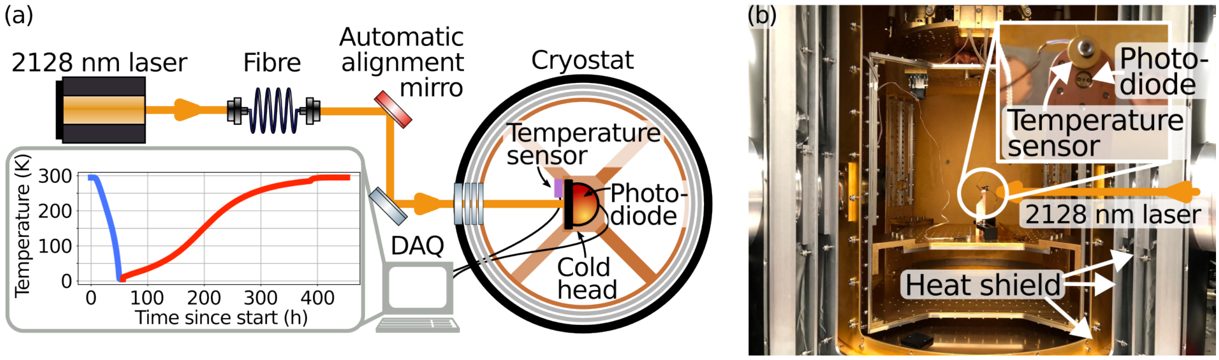

Figure 3.13: *(a) 2128 nm light was sent to a* THORLABS *FD05D photodiode, which was placed inside the cryostat. An automatic alignment system was implemented to ensure that the optical signal on the photodiode remained stable despite mechanical shifts caused by thermal expansion. The temperature sensor was installed as close as possible to the photodiode, i.e., directly on the mounting frame, as shown in the picture (b). DAQ: data acquisition system as data card by* ADVANTECH *model PCIe-1840L. Together with N. Södermann, this figure was produced for our publication.*

The custom transimpedance amplifier (gain of 300 $\frac{\text{kV}}{\text{A}}$) was housed outside the cryostat. Due to this high gain, the detector's dark noise was significantly higher than other noise sources. Consequently, the incident laser power was reduced to approximately $(100 \pm 20)\,\mu$W. To ensure that the laser's heat load did not influence the measurements, we monitored the system for heating effects by analyzing the time-resolved behavior at the wavelength cutoff point of the photodiode's response (where the gradient is highest). At this point, the photodiode becomes less sensitive to 2128 nm light because the band-gap increases with decreasing temperature, shifting the detectable wavelength range toward shorter wavelengths.

Photocurrent stability was strongly affected by misalignment, primarily caused by movement of the photodiode mount inside the cryostat due to thermal expansion. To counteract this, an automated alignment system was installed. It employed a feedback loop between the measured signal of the photodiode and a steered mirror. Alignment was optimized using a gradient descent algorithm with momentum [81]. The algorithm steered the mirror every five minutes during periods when no data was being collected, aiming to maximize the power on the photodiode. This was achieved by iteratively evaluating the change in the photodiode response and adjusting the mirror position based on the improvement relative to earlier measurements.

3.2.3 Results

Dark-Noise and Detection-Efficiency Investigations

Figure 3.14 shows the measured dark noise power spectral densities of the photodiode at room temperature and three progressively lower temperatures. The lowest noise levels were already achieved near 180 K, with a reduction of more than 15 dB. At temperatures below this, the dark noise did not decrease further, likely due to the dark noise of the room-temperature transimpedance amplifier stage. The noise power of our data acquisition system (dashed line) was approximately 5 dB below the lowest measured dark noise level of the system. Our dark noise spectra display several peaks, which we attribute to a ground loop in the mains and to the temperature data recording.

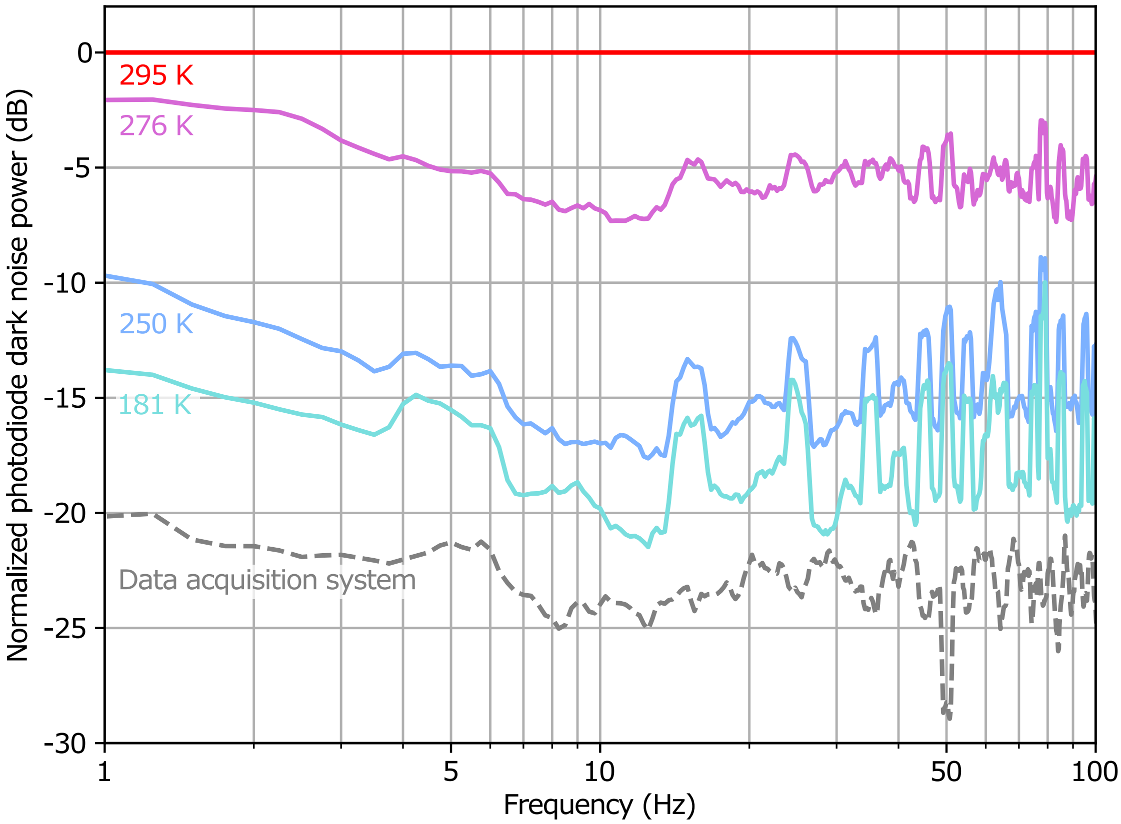

Figure 3.14: *Detector dark noise power spectral density in the frequency range of 1 Hz to 100 Hz at various temperatures, normalized to the value at room temperature. This frequency range was chosen because it is relevant for gravitational-wave detection; the effects at higher frequencies (100 Hz to 20 kHz) were discussed in the pilot studies (see Figure 3.11). As the temperature decreases, the detector dark noise significantly diminishes, reaching a minimum around 180 K. This limit is most likely imposed by the noise of the transimpedance amplifier stage.*

We calculated the relative detection efficiency $\Delta\eta_{\mathrm{DE}}$, for all temperatures during the full cycle and normalized them to the room temperature value according to Equation 1.54:

$$\Delta\eta_{\mathrm{DE}} = \frac{\eta(T)_{\mathrm{DE}}}{\eta(293\,\mathrm{K})_{\mathrm{DE}}} = \frac{U(T)_{\mathrm{tot}} - U_{\mathrm{dark}}(T)}{U(293\,\mathrm{K})_{\mathrm{tot}} - U_{\mathrm{dark}}(293\,\mathrm{K})},$$

assuming constant laser power. The data were split into cooling (blue dots) and warming (red dots) phases, as shown in Figure 3.15. Both phases exhibit similar patterns, with minor variations attributed to the measurement inaccuracy arising from light power fluctuations.

Below 10 K, the quantum efficiency drops to approximately 40 % compared to room temperature. A sharp decline below a characteristic temperature (around 50 K) is well-known and is generally attributed to an enlarged band gap [82, 83]. Additionally, cooling from room temperature down to 125 K results in a quasi-monotonic decrease in quantum efficiency of roughly 30 %. Below 125 K, the temperature dependence can be empirically described by an exponential decay ($\eta_{\mathrm{DE}} \approx \exp(-1/T)$), suggesting a thermally activated process.

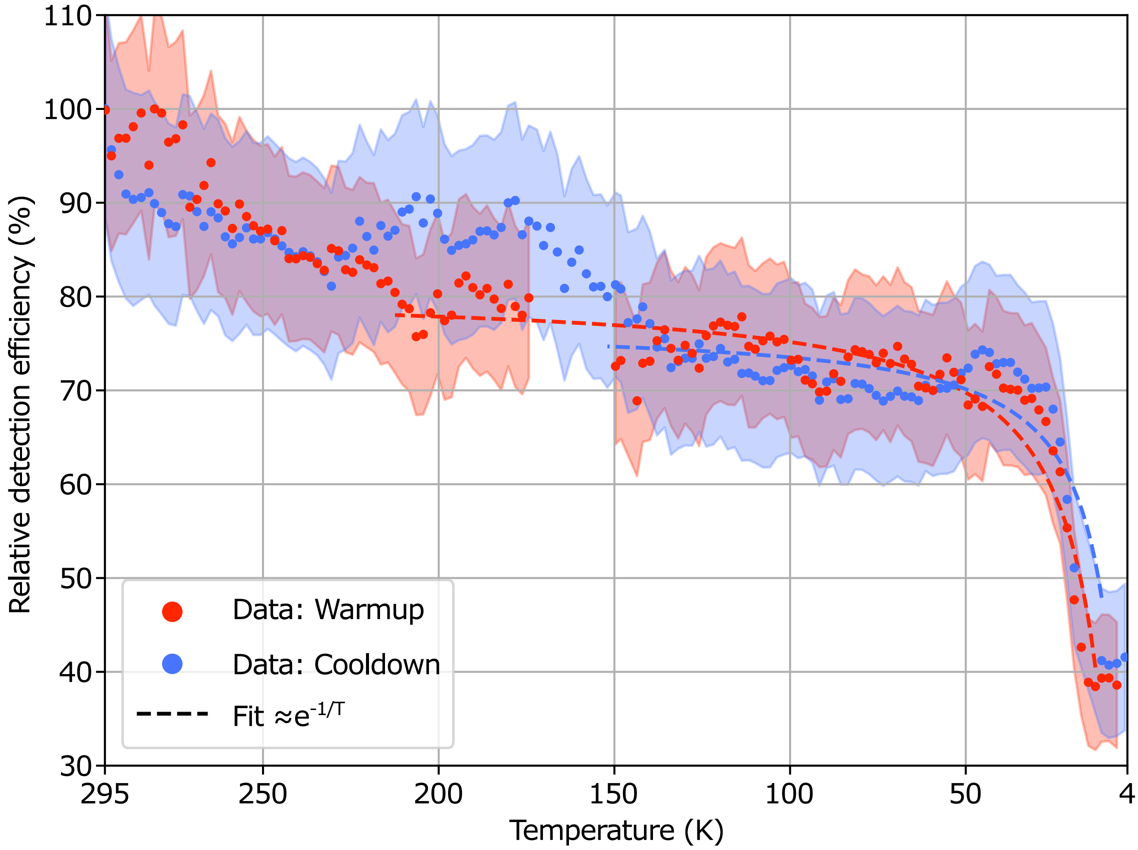

Figure 3.15: *Change in the relative detection efficiency of the photodiode FD05D by* THORLABS *as a function of temperature. The data were collected continuously over a full cycle (cooling down and heating up) of the cryostat. Blue points were recorded during the cooling phase over approximately 48 hours, while red points correspond to the warm-up phase over 16 days; the missing data during warm-up are due to a computer failure. A slight hysteresis was observed. At low temperatures, the data follow an exponential decay. All measurements were performed at a bias voltage of 0.39 V. The shaded area indicates the systematic uncertainty arising from light power fluctuations. This illustration was created by N. Sültmann and adapted for this work. Note, RBW: 0.25 Hz and averaged over 50 repetitions.*

Reverse Bias Investigations

As shown in the preliminary investigation, the detection efficiency exhibits a strong dependence on the applied reverse bias. In this section, we therefore investigate the dark current, the relative detection efficiency, and the noise power at different cooling temperatures for a range of reverse-bias voltages.

The Figure 3.16(a) depicts the dark current behavior as a function of increasing reverse bias at various temperatures. At room temperature (yellow dots), the current exhibits a roughly linear increase, modeled by the fit $m \cdot x + b$ and shown as a solid line. In contrast, cooling causes the dark current to rise exponentially, described by the fit $a \cdot \exp(b \cdot x) + c$. The underlying reason for this difference is that lowering the temperature increases the semiconductor's band gap, thereby requiring more energy to transfer an electron from the valence band to the conduction band. This energy increase is facilitated by applying higher reverse bias.

Moving to Figure 3.16(b), the graph displays the detection efficiency at 154 K, normalized to the detection efficiency at 0 V reverse bias, as a function of reverse bias. Two notable effects are observed: first, a small increase in detection efficiency at approximately 0.7 V, which is within the measurement uncertainties and influenced by laser power fluctuations, making it not reliably reproducible; second, an exponential decrease in detection efficiency at bias voltages above 1.5 V. This second effect can be explained by the rising dark current, which contributes to increased current and reduces the detection performance.

Figure 3.16(c) illustrates the total laser noise and photodiode dark noise over a frequency range of 1 Hz to 100 Hz at 144 K. The photodiode dark noise exhibits a slight increase with increasing reverse bias, while the total laser noise remains constant at higher frequencies but appears to increase at lower frequencies. This behavior indicates that, in this measurement regime, the total laser noise dominates, and variations in dark noise with reverse bias have only a minor impact on the overall noise performance.

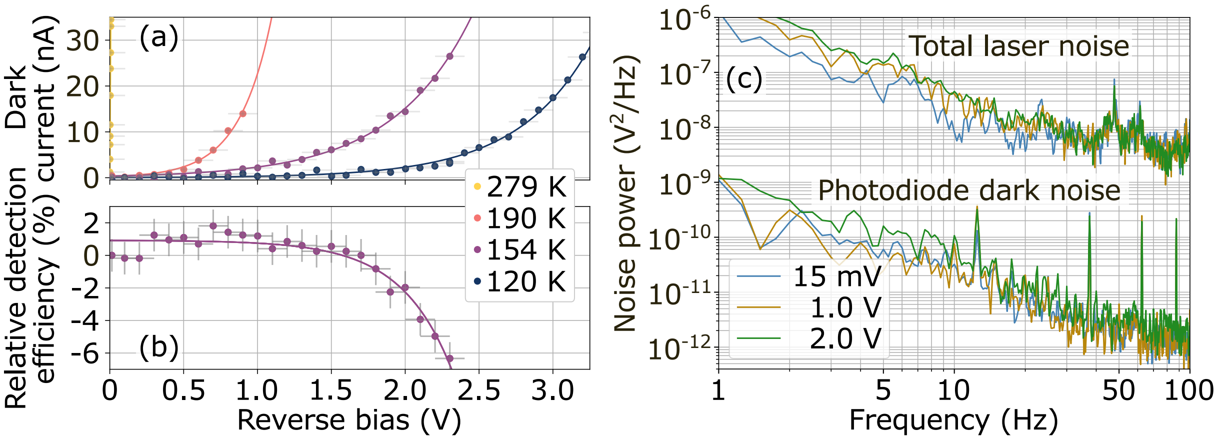

Figure 3.16: *(a) Top: Dark current at various reverse biases for different temperatures. Cooling alters the response of the photodiode to increasing bias voltage: at room temperature, the dark current increases linearly, while in the cooled state, it increases exponentially. (b) Bottom: Detection efficiency relative to 0 V reverse bias at 154 K. Two notable effects are observed: first, a small increase in DE around 0.7 V, most likely due to signal fluctuation; second, an exponential decrease in detection efficiency, which is attributed to increasing dark current. (c) Photodioden dark noise and total laser noise in the frequency range of 1 Hz to 100 Hz are shown at different bias voltages for the temperature of 144 K. As part of our publication, N. Sültmann and I collaborated on this illustration.*

In summary, the effect of reverse bias on the photodiode differs significantly between room-temperature and cooled operation. At room temperature, the dark current increases linearly with bias, whereas under cooling it exhibits an exponential rise. Although the detection efficiency decreases at higher reverse-bias voltages due to the increased dark current, the impact on the overall noise performance remains minor, as the total laser noise dominates in the relevant frequency band. Moreover, the photodiode withstands bias voltages well above the manufacturer's specification at low temperatures, suggesting that the maximum safe bias voltage increases as the device temperature decreases.

3.2.4 Conclusion and Outlook

The results showed that the THORLABS products performed best, with a maximum measured QE of around 88 % for the FD05D model, which can be increased to approximately 91 % by removing the broadband-coated window. An additional 1 % increase in QE, up to almost 92 %, is achieved when the photodiode is positioned at an angle of around 35 °. The anti-reflection coating on the substrate reflects approximately 0.8 %, which does not explain the remaining 8 % needed to reach 100 % QE. This indicates an internal semiconductor limitation that must be addressed by selecting the appropriate doping or material.

A promising option was demonstrated in Moseley et al. (1986), who used metalorganic vapor-phase epitaxy to create a GaInAs/AlInAs heterostructure (see Figure 3.17). This design achieved a broadband QE of 95 % over the wavelength range from 1.7 μm to 2.25 μm [84]. Dark voltage plays a significant role in quantum efficiency and therefore also in detection efficiency, which motivated a more detailed investigation. It was shown that a reduction of up to 15 dB is possible at a temperature of 200 K; however, this comes at the cost of a 15 % loss in DE. Semiconductor design improvements may be able to compensate for this, keeping DE/QE stable at lower temperatures while eliminating dark voltage. Moreover, no degradation in performance was observed when cooling the photodiode multiple times to 5 K, even though these temperatures exceed the manufacturer's recommended limits.

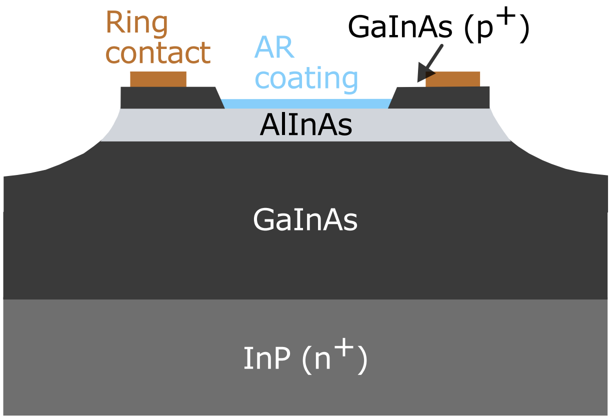

Figure 3.17: *Schematic representation of the GaInAs/AlInAs heterostructure achieving a QE of 95 % at 2.1 μm. The figure is based on the original layout but has been adapted for this thesis.*

Overall, the results indicate that current photodiodes can meet many of the requirements for small experimental setups when properly optimized. Based on these findings, it appears likely that future gravitational-wave observatories will benefit from semiconductor materials with intrinsically higher QE, lower dark current, and stable cryogenic performance. Advancing such materials and device architectures may therefore be essential for enabling the next generation of detector sensitivities.

3.3 Development of a Squeezed Light Source for Audio-Band Operation

The use of squeezed light reduces quantum noise and is therefore considered a key technology for current and future GWOs [7, 6, 28]. Initial squeezer prototypes in the 2 µm wavelength range have already been demonstrated. One approach follows the conventional scheme using a 2 µm laser that serves both as the LO for detection and as the fundamental field for SHG, which produces the pump field for an OPO in a bow-tie configuration. This system achieved approximately 4 dB of audio-band noise reduction, with the performance limited by photodiode dark noise [8, 10]. An alternative approach uses a 1064 nm pump laser to operate an OPO above threshold for LO generation and below threshold for squeezed-light generation at 2128 nm, reaching about 7 dB of noise reduction in the MHz regime [11].

In this work, the 2128 nm squeezer is extended from MHz sidebands to operation in the audio-band. This extension is challenged by several noise sources, including technical noise, phase noise, and photodiode dark noise. The initial investigations were carried out together with my former master student, Tobias Schoon.

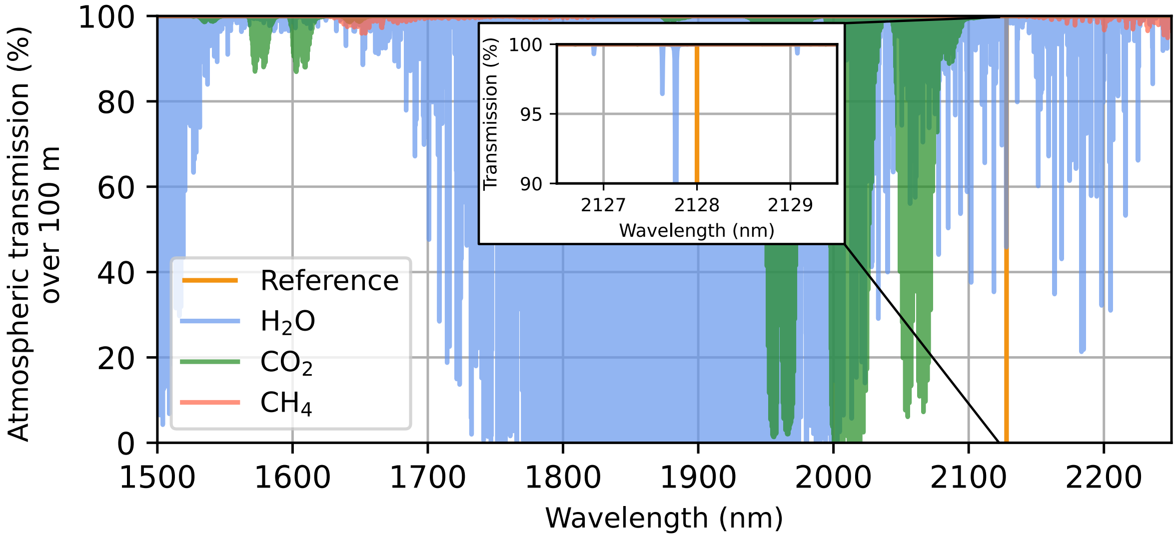

Figure 3.18: *Atmospheric transmission in the 1500 nm to 2250 nm range for a path length of 100 m, with a zoom around the operating wavelength of 2128 nm (orange line, labeled as reference). In this spectral region, gases such as N_2O and O_3 do not contribute significantly. The prominent absorption peak near the operating wavelength is due to H_2O. Data are based on the HITRAN 2016 database [85].*

Squeezed states of light are highly susceptible to optical losses. For example, an optical loss of only 5 % reduces an initial squeezing level of 20 dB to approximately 13 dB, as predicted by the theoretical model (Equation 1.48). For certain wavelength regimes, atmospheric absorption introduces an additional loss channel that must be taken into account. The atmospheric transmission spectrum is shown in Figure 3.18. Our operating wavelength of 2128 nm (orange line, labeled as reference) lies within a favorable transmission window, comparable to the potential window at 1550 nm. However, the surrounding 2 µm region is dominated by pronounced absorption features. In this simulation configuration, the transmission at the operating wavelength was 99.99 %. This further motivates the choice of 2128 nm as a future main wavelength in GWOs. Detailed investigations of the atmospheric transmission at this wavelength are ongoing [86]. The simulation assumes an optical path length of 100 m, which overestimates typical laboratory conditions. Adjusting the path length primarily affects the transmission amplitude, while the spectral structure remains unchanged. In real GWOs, most of the propagation occurs through vacuum, with a smaller fraction passing through the atmosphere and therefore subject to atmospheric absorption.

3.3.1 Experimental Setup

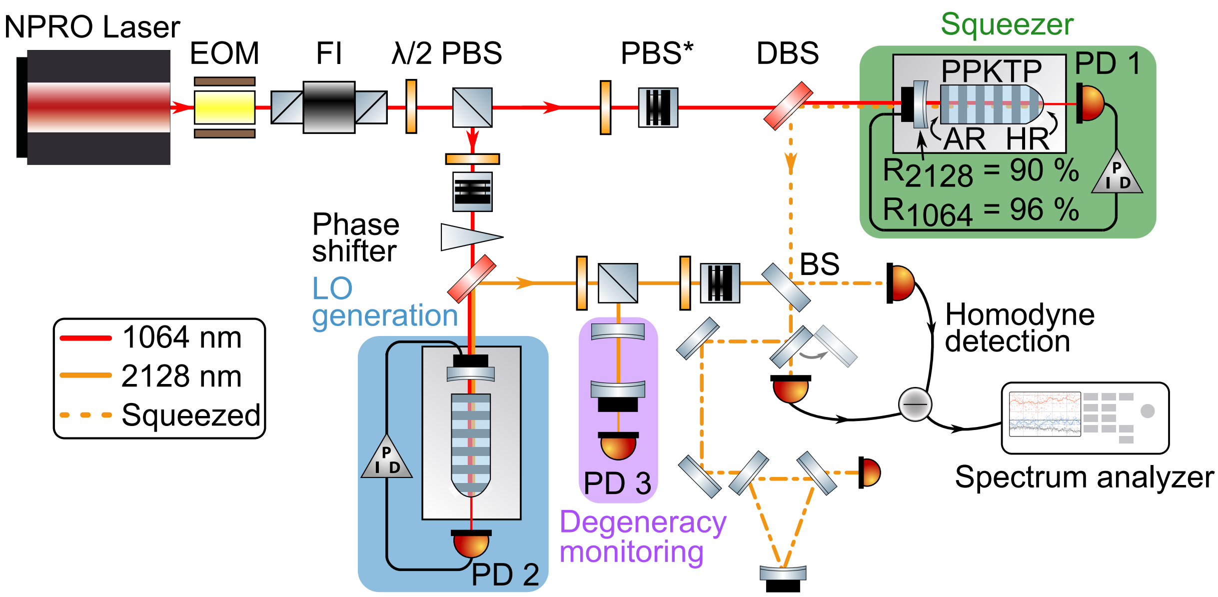

Figure 3.19: *Schematic of the experimental setup. An NPRO 1064 nm laser pumps two optical parametric oscillators that generate light at 2128 nm. One OPO operates above threshold as a degenerate source for the local oscillator, depicted in blue. The other operates below threshold as a squeezed-light source (squeezer) and is marked in green. Both fields are combined at a beam splitter (BS), spatially overlapped using a triangular cavity, and measured with a balanced homodyne detector. Part of the LO light is coupled into a confocal cavity to monitor the degenerate state, indicated in purple. Both cavities are frequency-stabilized using a modified Pound-Drever-Hall scheme, with 28 MHz sidebands impressed on the pump and detected at PD 1 and PD 2. Power adjustments are made using a half-wave plate and a PBS, which transmits s-polarized light. The reflected beam is directed to a beam dump. This PBS and beam dump arrangement is indicated as PBS* in the figure.*

Figure 3.19 shows the schematic setup used for generating and detecting 2128 nm squeezed light. A low-noise, single-frequency 1064 nm NPRO laser (manufactured by Mephisto) is used as the pump source. The beam passes through an EOM that imprints 28 MHz sidebands, followed by a FI to protect the laser from back-reflections. After passing through a half-wave plate and a PBS, the pump beam is split into two arms. Each arm is constructed identically and contains a power-adjustment stage comprising a half-wave plate followed by a PBS. In this configuration, the PBS is oriented to transmit s-polarized light, while the reflected beam is directed out of the optical plane and terminated with a beam dump. This component is labeled PBS* in Figure 3.19 to distinguish it from the main power-splitting PBS.

After splitting, the beams pass through a DBS, which is transmissive at 1064 nm and highly reflective at 2128 nm, and are then coupled into their respective nonlinear cavities. Each cavity consists of a coupling mirror with reflectivities of $R_{2128\,\mathrm{nm}} = 90\,\%$ and $R_{1064\,\mathrm{nm}} = 96\,\%$ and is mounted on a piezoelectric actuator. This is followed by a PPKTP crystal, whose right side is curved to act as the second cavity mirror and is high-reflectivity coated for both wavelengths. Cavity parameters are listed in Table 3.3. A modified PDH stabilization is applied using photodiode 1 or 2.

The two arms differ in their operating regimes: the squeezer, indicated in green, operates below threshold and produces a squeezed state, whereas the local oscillator generation cavity operates above threshold and produces a bright coherent field, depicted in blue. After being combined at a beam splitter (BS) and spatially overlapped in a triangular cavity, the two fields are measured with a balanced homodyne detector. LO phase is controlled using a piezo-actuated phase shifter. To reduce pointing instabilities caused by imperfections in the phase-shifter mount, the pump beam is aligned as close as possible to the cavity axis. A portion of the LO light is guided into a confocal cavity to monitor mode degeneracy.

The corresponding cavity design is shown in Figure 2.2. Compared to the high-power cavity, the only modification is the adjusted reflectivity of the coupling mirror. Low-noise operation of the PDH stabilization follows Section 2.2.2. Degeneracy in this cavity is again achieved by tuning the crystal temperature, as demonstrated in Figure 2.9.

Table 3.3: *Overview of the LO and Squeezer cavity parameters.*

	1064	2128	nm
waist radius	33.5	47.4	μm
finesse	153	59.5	
free spectral range	3.80	3.83	GHz
linewidth (FWHM)	24.9	64.3	MHz
coupler reflectivity	96	90	%

Monitoring of Mode Degeneracy

The signal and idler wave modes of the local oscillator can be tuned via the crystal temperature. When both fields reach the same wavelength, the system operates in the degenerate regime. Monitoring and maintaining this condition is essential for measuring squeezing, as the squeezed state is intrinsically degenerate and interference between unequal wave fields introduces loss. To verify degeneracy, the local oscillator output is monitored using a confocal cavity. The criterion for degeneracy is the appearance of the minimum number of transmission peaks with maximum intensity. Due to dispersion and wavelength-dependent mirror reflectivities, the confocal cavity exhibits different Finesse values for the different wavelengths, as shown in Equation 1.7. Therefore, if the OPO is not degenerate and produces more than one field, these fields can be distinguished using this method. For our setup, this typically appears as in the top-left panel of Figure 3.20. However, because the confocal cavity has a relatively low finesse of 30 ($R_1 = R_2 = 90\,\%$; FWHM $= 0.143$ GHz; FSR $= 4.283$ GHz), its limited spectral resolution may cause two closely spaced peaks to appear as a single one.

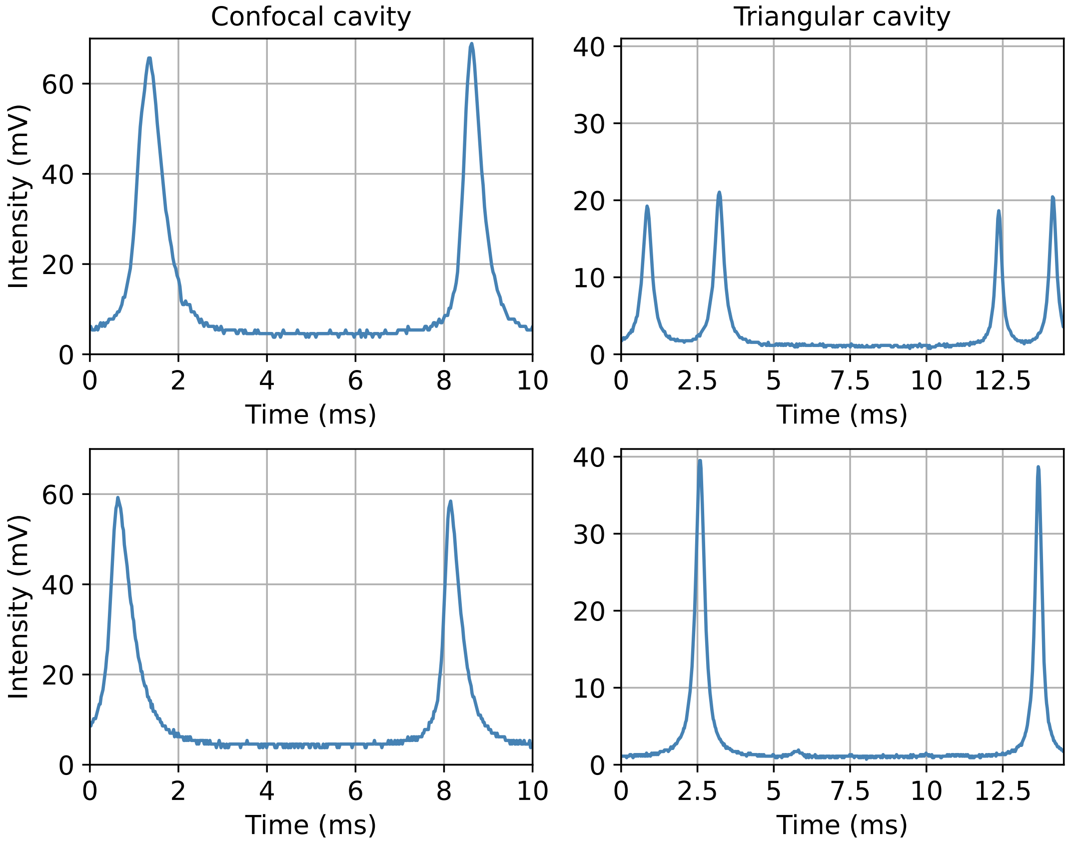

Figure 3.20: *This figure illustrates the challenge of identifying mode degeneracy in the squeezing experiment. The left column shows the mode pattern of the linear cavity, while the right column shows that of the triangular cavity. In the top row, a non-degenerate state is observed. Although this state appears degenerate in the confocal cavity, the triangular cavity clearly reveals its non-degenerate nature, as each mode appears as an individual fundamental-mode spot on the beam profiler. Pairs of these spots correspond to the signal and idler fields. In contrast, the bottom row shows the true degenerate state: for the same cavity-length tuning, only two fundamental-mode spots are visible, each with approximately twice the intensity of the non-degenerate modes. Note that the small peak in the bottom-right image is a higher-order mode due to non-perfect mode matching.*

Figure 3.20 illustrates this issue. The left column shows the transmission of the confocal cavity, while the right column shows that of a triangular cavity with a finesse of 27 ($R_1 = R_2 = 90\,\%$ and $R_3 = 98\,\%$; FWHM $= 0.026$ GHz; FSR $= 0.714$ GHz). In the top row, the confocal cavity suggests a degenerate state, yet the triangular cavity clearly reveals two separate fundamental modes, indicating a non-degenerate condition. In contrast, the bottom row displays the true degenerate state: within the same cavity-length-tuning range, only two fundamental-mode peaks are observed, each with approximately twice the intensity of the non-degenerate modes. A comparison of the measured cavity finesse of the non-degenerate state, the degenerate state, and a simulated response does not provide a reliable distinction. Because both the degenerate and non-degenerate cases exhibit nearly identical linewidths. The observed difference in the number of resolvable resonances between the two cavities arises from their different cavity parameters. In particular, the smaller FSR and narrower FWHM of the triangular cavity increase the density and spectral resolvability of cavity modes.

Audio-Band Homodyne Detector

Measuring squeezed light in the audio-band is challenging because electronic noise dominates at low frequencies. To overcome this limitation, a low-noise homodyne detector was developed, and its performance is analyzed in the following. The layout of the detector is shown in Appendix A.4. It was originally designed during my Master's thesis and has now been adapted for low-frequency operation.

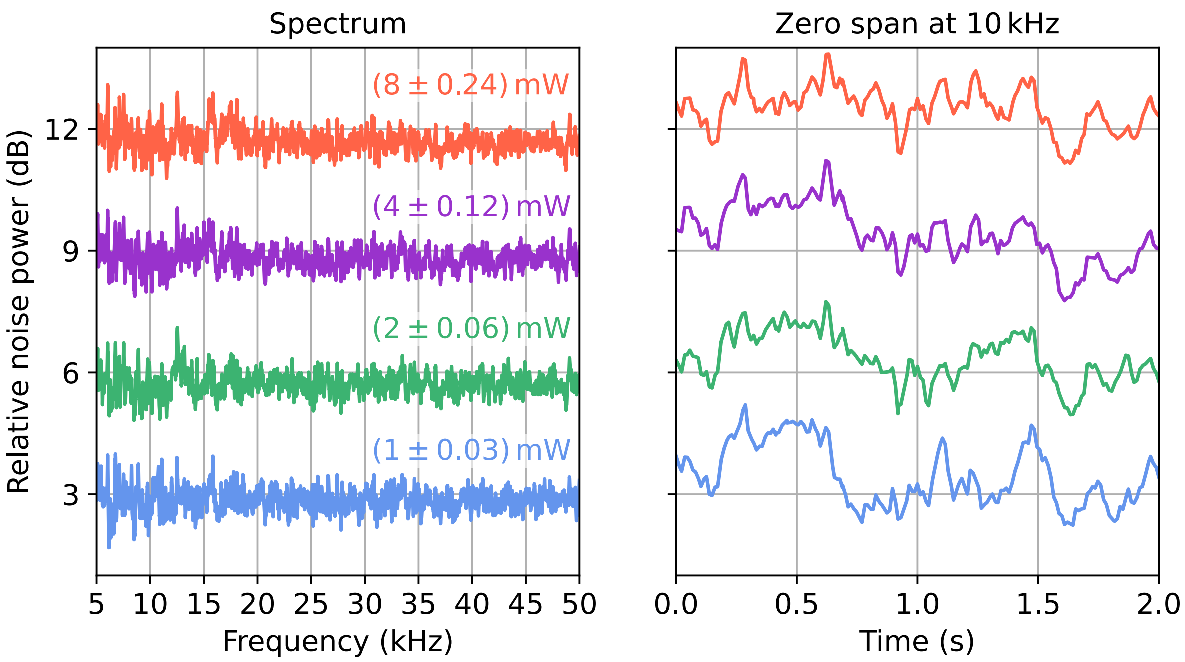

Figure 3.21: *Proof of linearity of the homodyne detector. Relative noise spectrum (5 kHz to 50 kHz, left) and zero-span at 10 kHz (right), normalized to (0.5 ± 0.015) mW LO power. Linearity up to (8 ± 0.24) mW is observed. Signal analyzer settings: video band width (VBW) = 1 Hz, resolution band width (RBW) = 100 Hz, averages (AVG) = 100.*

First, the linearity of the system is investigated. The results are shown in Figure 3.21: the left panel displays the noise spectrum, while the right panel presents a zero-span measurement at 10 kHz. Linearity is verified by doubling the LO power, which theoretically leads to a 3 dB increase in shot noise. For the procedure of homodyne measurement the differential current ($i_{\text{diff}} = i_1 - i_2$) of each individual photodiode ($i_{1,2}$) is measured. Since the shot-noise contributions of the two photodiodes arise from independent quantum processes, the corresponding noise currents are statistically uncorrelated. Therefore, the variance of the differential signal is given by the sum of the individual shot-noise variances (seen Equation 1.50):

$$\langle i_{\text{diff}}^2 \rangle = \langle i_1^2 \rangle + \langle i_2^2 \rangle = 2 \cdot \left(2e \frac{i_{\text{LO}}}{2} \Delta f \right) = 2e i_{\text{LO}} \Delta f , \tag{3.5}$$

where the photocurrents at the beam splitter output ports are each $i_1 = i_2 = {}^{i_{\text{LO}}}/_{2}$ assuming identical and ideal PDs. This implies that the differential shot-noise amplitude scales as $i_{\text{diff}} \propto$

$\sqrt{i_{\mathrm{LO}}}$. The conversion from photocurrent to voltage using the transimpedance amplifier is given by

$$V = Gi, \tag{3.6}$$

where G is the transimpedance gain and $I \propto i_{\mathrm{diff}}$, ideally without any residual DC offset. The electrical power measured by the signal analyzer (SA) is

$$P_{\mathrm{SA}} = \frac{V^2}{R} \propto i^2 \propto i_{\mathrm{diff}}^2, \tag{3.7}$$

with R being the input impedance. Consequently, doubling the LO power results in a doubling of the electrical noise power measured by the SA, i.e., $P_{\mathrm{SA}} \propto i_{\mathrm{LO}}$.

Linearity is observed up to (8 ± 0.24) mW. Imperfect power adjustment together with the 3 % powermeter uncertainty [55] accounts for the small deviations observed. The measurements were taken using a Rohde & Schwarz FSV signal analyzer (10 Hz to 4 GHz) with a VBW of 1 Hz, an RBW of 100 Hz, and an averaging factor of 100.

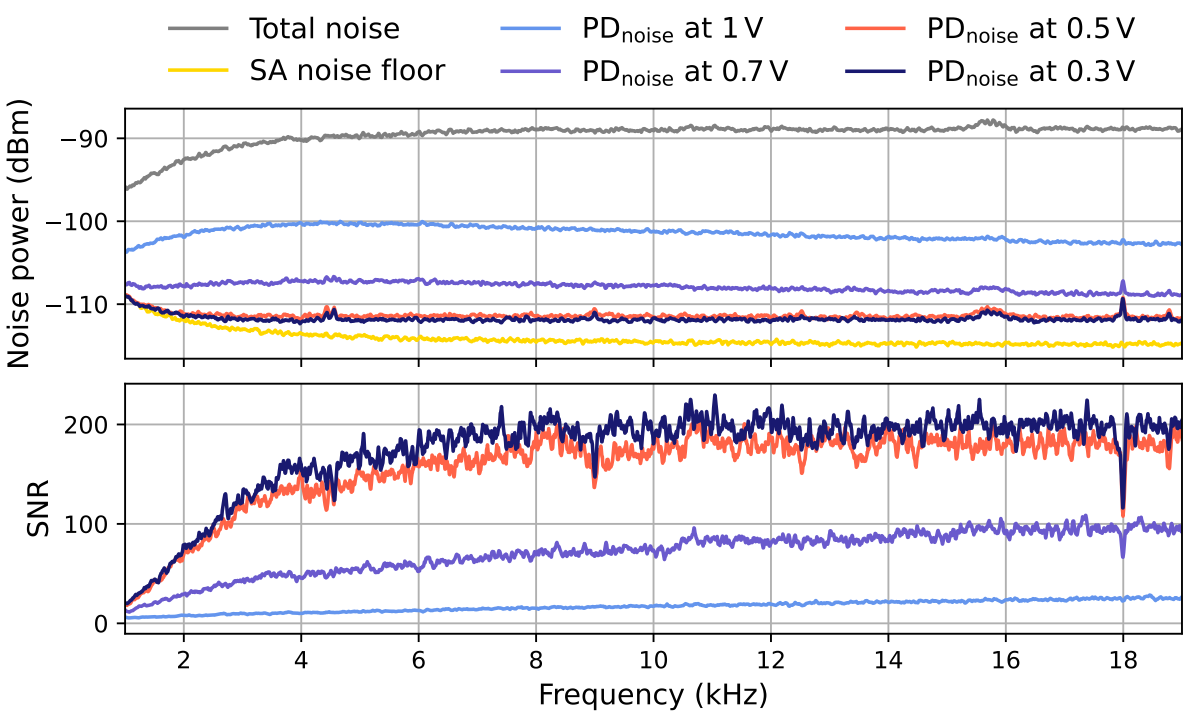

Figure 3.22: *Dark-noise optimization of the homodyne detector by adjusting the reverse bias. Top panel: noise spectra in the audio-band, showing the total detected noise, the signal analyzer noise floor, and the photodiode dark noise for several reverse-bias voltages. Bottom panel: corresponding signal-to-noise ratio obtained by comparing the total noise with the respective dark-noise levels. Data were taken with a signal analyzer using a VBW of 1 Hz, an RBW of 50 Hz, and an averaging factor of 100.*

Second, the reverse bias of the photodiodes is optimized to minimize their electrical dark noise. This is necessary to avoid limitations imposed by electronic dark noise. Figure 3.22 shows the results. The top panel displays the noise spectrum in the audio-band measurement range for several reverse-bias voltages, together with the total detected noise (photodiode noise plus laser noise) and the noise floor of the signal analyzer. Decreasing the reverse bias reduces the intrinsic noise of the photodiodes, but it does not alter the total detected noise, as the photodiode contribution is comparatively small. For example, the highest point of the total noise floor is about −88 dBm, while the maximum photodiode noise at a reverse bias of 1 V is approximately −100 dBm. This 12 dB difference corresponds to a factor of 16, meaning that the photodiode noise accounts for only about 6 % of the total detected noise, with the remaining contribution originating from laser noise. The bottom panel shows the corresponding signal-to-noise ratio (SNR) of the spectra. An SNR of up to 200 is obtained for a reverse bias of approximately 0.3 V, and reducing the bias further does not lead to any significant improvement. Therefore, a reverse bias of around 0.3 V provides the optimal dark-noise clearance. Lower reverse-bias voltages reduce the photodiode bandwidth, but this effect is negligible for measurements in the audio-band. A Rohde & Schwarz FSV signal analyzer (10 Hz to 4 GHz) with a VBW of 1 Hz, an RBW of 100 Hz, and an averaging factor of 100 was used for the experiments.

3.3.2 Observation of Audio-Band Squeezing

Left panel of Figure 3.23 shows the shot-noise-normalized squeezing spectrum in the upper audio-band between 10 kHz and 20 kHz, with anti-squeezing shown as red points and squeezing as blue points. The black line indicates the shot-noise level, and the grey points represent the electronic dark-noise floor of the measurement system, including the spectrum analyzer and the homodyne detector. Solid lines represent Savitzky–Golay-filtered traces (window size 5, polynomial order 3), as discussed in the next section. Across the full measurement band, more than 10 dB of anti-squeezing were observed, with a maximum of (13.9 ± 2.2) dB, while the squeezing reached approximately 1 dB, with a maximum of (3.6 ± 2.1) dB. The data clearly show that the dark-noise level limits the observable squeezing. Recording of the data was done with a Rohde & Schwarz FSV signal analyzer (10 Hz to 4 GHz) with an RBW of 300 Hz and a VBW of 30 Hz, and a local-oscillator power of 1.5 mW.

A zero-span measurement at 15 kHz is shown in the right panel of Figure 3.23. Squeezing is shown in blue, anti-squeezing in red, and the phase scan is plotted in grey. The horizontal lines indicate the mean values of (8.5 ± 2.0) dB of anti-squeezing and (3.3 ± 1.5) dB of squeezing, corresponding to an inferred initial squeezing S_{init} of about 10.5 dB. This value is calculated from the measured squeezing and anti-squeezing levels using the loss equation

$$L = \frac{1 - S_+ S_-}{2 - S_+ - S_-}, \tag{3.8}$$

and

$$S_{\text{init}} = 10 \log_{10}\left(\frac{S_+ - L}{1 - L}\right), \tag{3.9}$$

where S_+ and S_- denote the anti-squeezing and squeezing variances in linear units. Measurements were taken with the same signal analyzer using an RBW of 500 Hz and a VBW of 30 Hz. The uncertainties given are based on the standard deviation of the data.

Two artifacts are apparent in the data: (i) the squeezed trace occasionally rises above the shot-noise level and (ii) it drops below the dark-noise level. Both effects are non-physical and can be attributed to statistical noise fluctuations and interference from technical noise sources.

It should be noted that, due to time constraints, the measurement data presented here was taken under non-ideal conditions. These results represent a first test measurement, and significant improvements are expected, as discussed below.

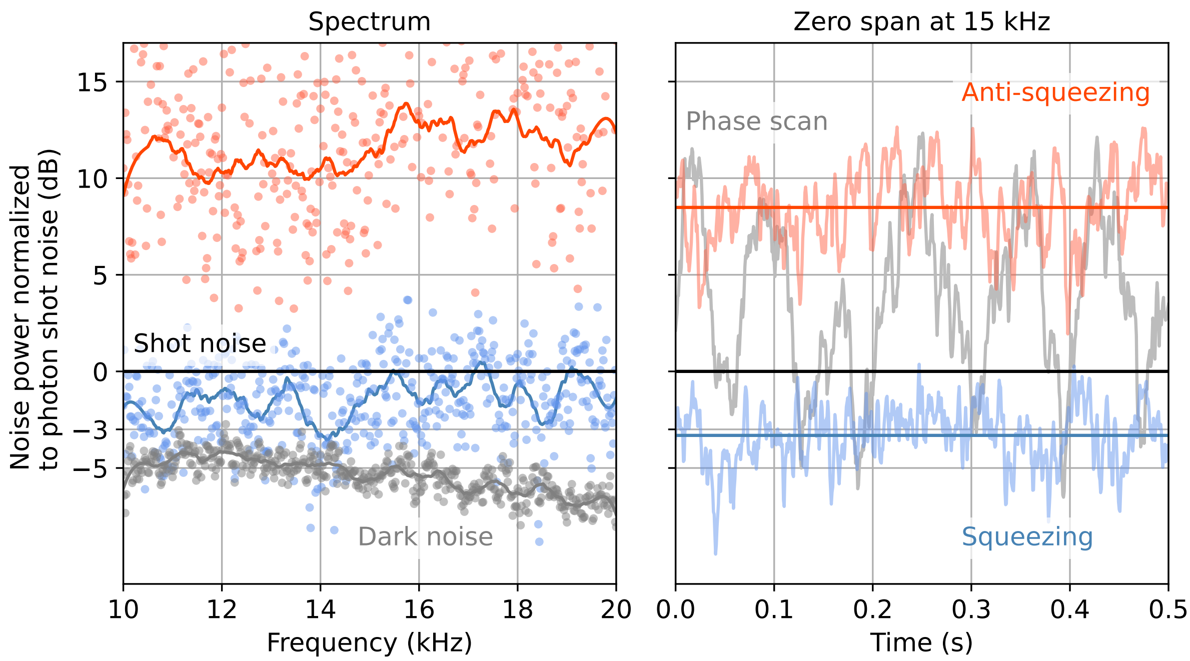

Figure 3.23: *Left panel: shot-noise-normalized squeezing spectrum in the upper audio-band from 10 kHz to 20 kHz. Red points indicate the anti-squeezed quadrature and blue points the squeezed quadrature. The black line marks the shot-noise level, and the grey points show the electronic dark-noise floor of the spectrum analyzer. Data were recorded with an RBW of 300 Hz and a VBW of 30 Hz. Solid lines show Savitzky–Golay-filtered traces (window size 5, polynomial order 3) for visualization. Right panel: zero-span measurement at 15 kHz. The phase scan is shown in light grey, while the horizontal lines indicate the mean values of the hand-locked squeezing (blue) and anti-squeezing (red). These data were recorded with an RBW of 500 Hz and a VBW of 30 Hz.*

Savitzky–Golay Filter

The Savitzky–Golay filter is a widely used method for smoothing noisy spectral data while preserving characteristic features such as peak height and width [87]. It operates by fitting a polynomial of order k to a local window of $2m + 1$ data points, where m denotes half the window width:

$$y_{\text{polynomial}}(x) \approx a_0 + a_1 x + a_2 x^2 + \cdots + a_k x^k, \tag{3.10}$$

with $x = 0$ corresponding to the central point of the window. The smoothed value at index i is obtained from the value of the fitted polynomial at the center:

$$y_i^{\text{smooth}} = y_{\text{polynomial}}(0) = a_0. \tag{3.11}$$

This procedure is applied to all data points. Because the central point of each window is used, the filter does not introduce any shift along the x-axis. For a window centered at position i, the contributing data points are

$$y_{i-m}, y_{i-m+1}, \ldots, y_i, \ldots, y_{i+m-1}, y_{i+m}. \tag{3.12}$$

At the boundaries of the dataset, where a full window is not available, the filter uses modified coefficients so that interpolation is performed using only the accessible neighboring points.

Loss Analyses

As discussed above, several aspects of the squeezing measurement can be optimized to improve the observed squeezing levels. These can be categorized into technical improvements of the detection hardware, improvements in data acquisition and averaging, and optical loss channels in the experimental setup.

Technical optimization:
The first area of improvement concerns the reduction of electronic dark noise. This could be achieved by further lowering the intrinsic noise floor of the homodyne detector, for example by selecting even lower-noise electronic components or by redesigning parts of the detection circuit. An even more promising approach is the use of a lower-noise signal analyzer. As shown in Figure 3.22, the current homodyne detector noise floor approaches the noise floor of the spectrum analyzer, meaning that the analyzer partly limits the achievable clearance. Improving linearity to allow operation at higher local-oscillator powers is possible but considerably more challenging. Overall, reducing the noise of both the homodyne detector and the signal analyzer would lower the effective background noise.

Data evaluation:
Another improvement concerns the statistical stability of the measurement. Increasing the total measurement time and the number of averages reduces the variance of individual data points.

Optical loss channels:
Table 3.4 summarizes the primary loss mechanisms in the current setting. The total efficiency includes escape efficiency from the resonator, propagation loss, photodiode quantum efficiency, and the calculated visibility between the squeezed field and the local oscillator. Additionally, the effective overall efficiency, calculated from the observed squeezing and anti-squeezing in the zero-span measurement, is shown in the table and defined in Equation 3.8. A detailed discussion of each individual loss channel is given below.

Table 3.4: *Overview of loss sources in the squeezing measurement.*

Source	Efficiency (%)
Escape from resonator	98 ± 1
Light propagation	>99
Photodiode	92 ± 3
Calculated visibility	65.5
Total value from squeezing and anti-squeezing	58.5 ± 0.5

Escape from resonator: The escape efficiency is defined as $^{T}/_{T+L}$, where T denotes the transmissivity of the output coupler and L the round-trip loss of the resonator. Losses arise from imperfect AR coatings at the nonlinear crystal, scattering and absorption in the crystal, and residual transmission of the high-reflectivity end face. The transmissivities are taken from the manufacturer (Layertec) [88], and scattering/absorption losses are estimated to be 1 % to 2 % based on prior experience.

Light propagation: Propagation efficiency is determined by the quality of each optical element, primarily governed by HR and AR coatings. High-quality optics from LASEROPTIK were used, and their specified coating losses [89] form the basis of the estimate.

Photodiodes: The photodiodes introduce loss through their quantum efficiency and dark-noise contribution. In this experiment, two photodiodes with a measured quantum efficiency of $(92 \pm 3)\,\%$ were used. A detailed characterization is provided in Section 3.2. Their dark-noise contribution becomes relevant primarily at low frequencies.

Visibility: Visibility quantifies the spatial and spectral mode overlap between the squeezed field and the local oscillator. It can be determined either from the interference contrast between the two beams (Equation 1.56) or from mode matching to a (triangular) cavity. Degeneracy of the involved fields plays a significant role because any wavelength mismatch introduces a time-dependent phase difference. If this phase varies significantly over the detector integration time, the interference term averages out and the visibility decreases toward zero [90]. Because the visibility measurement data were unavailable, only the calculated value of 65.5 % is available.

3.3.3 Conclusion and Outlook

In this chapter, a squeezed-light source operating in the frequency range of 10 kHz to 20 kHz was demonstrated. Squeezing of 3.3 dB and anti-squeezing of 8.5 dB were achieved at 15 kHz. The performance is primarily limited by electronic dark noise and optical losses, in particular imperfect mode overlap and incomplete degeneracy. By selecting a lower-noise signal analyzer, working at higher LO powers, and further optimizing the homodyne detector, the noise performance can be substantially improved. Improving the spatial mode matching and ensuring stable degeneracy will reduce the dominant optical loss channels.

The next major goal is to extend squeezing measurements toward very low frequencies. Achieving this will require corresponding improvements in the detector and signal analyzer. If thermal noise of the photodiodes becomes a limiting factor, cooling the devices may be necessary. In addition, further refinement of the mode-matching optics and a more reliable degeneracy-monitoring scheme will be important. To stabilise the squeezing measurement for a selected quadrature, implementing a control scheme is an important step. With these improvements implemented, we expect significantly higher squeezing levels at low frequencies.

A longer-term development step involves replacing the current photodiodes, which remain a major limitation. Ongoing efforts toward developing photodiodes with substantially higher quantum efficiency could enable squeezing levels well above 10 dB, providing a direct demonstration of the suitability of 2 µm squeezed-light sources for future gravitational-wave observatories.

In summary, this work represents an important milestone in the development of a 2128 nm squeezed-light source. The favourable optical properties at this wavelength and demonstrated performance strongly support 2128 nm as a promising candidate wavelength for next-generation GWOs.

Chapter 4

Hyperloss in Quantum-Correlated Networks

Quantum-enhanced GWOs rely on squeezed states to surpass classical sensitivity limits. However, their performance is fundamentally limited by decoherence mechanisms, in particular by optical losses. A well-known source of such losses is imperfect mode matching between interfering fields. In this chapter, I present the physical picture and experimental demonstration of the current understanding of this mechanism, which can result in an effective loss exceeding 100 %, manifesting as a thermal-like state and thereby motivating the term *hyperloss*. Unlike classical optical loss, where squeezed light interacts with a zero-temperature bath, hyperloss arises from the coupling of a discrete set of spatial modes in a pure state. These modes originate from the coherent coupling of the fundamental mode of the squeezed field at various interfaces, such as optical cavities or beam splitters. Such spatial-mode coupling is ubiquitous in gravitational-wave observatories, as illustrated in Figure 4.1.

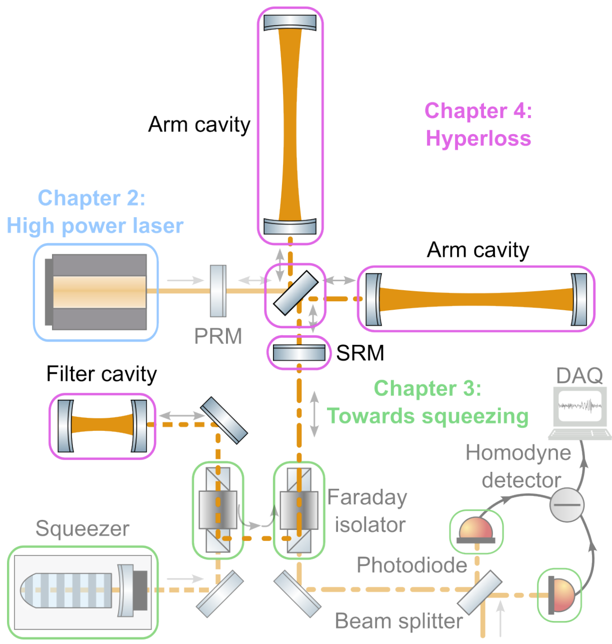

Figure 4.1: *Schematic illustration of a GWO.*

This effect is significant because it occurs in all quantum networks employing high levels of squeezing, including GWOs and photonic quantum computers. In future implementations, where higher degrees of squeezed states are planned [6, 7], the associated hyperloss is expected to increase substantially. Although this effect has not yet been critical in current quantum networks due to relatively low levels of squeezing, it remains an important consideration.

While mode-mismatch-induced decoherence has been theoretically discussed [14, 91, 92, 93], its full physical mechanism and experimental verification in highly squeezed regimes have remained incomplete. The aim of this chapter is to provide a complete physical picture and the first experimental demonstration of hyperloss. For a comprehensive and rigorous theoretical treatment of our findings, the interested reader is referred to our accompanying paper [94].

Squeezed light was generated and directed into a linear cavity, with intentional misalignment of the input beam to the resonator. This misalignment resulted in a small portion of the light coupling into higher-order modes, which were directly reflected. As the fundamental and higher-order modes propagated, they accumulated a differential phase. Subsequently, in a second cavity, these light fields interact with each other and are measured using a homodyne detection setup.

This chapter is structured as follows: Section 4.1 introduces the physical picture. Section 4.2 describes a preliminary investigation of weak coupling in a single-cavity configuration. Section 4.3 demonstrates hyperloss in a two-cavity setup, followed by a discussion of their implications for quantum networks.

The project resulted from a close collaboration with colleagues from my working group. I was responsible for project coordination and planning, while both M. Sc. Stephan Grebien and I carried out the experimental work. Stephan Grebien handled the data analysis, and Dr. Mikhail Korobko contributed the theoretical analysis of the effect.

4.1 The Physical Picture of Hyperloss

The origin of hyperloss can be illustrated using a simple optical network consisting of two strongly overcoupled cavities, each representing one part of the full experiment. A laser field connects the two cavities, and a phase-sensitive detector analyses the resulting interference. To give an introduction to the underlying principle, we first focus on a single cavity, as shown in the left panel of Figure 4.2. In practice, small mode matching imperfections lead to spatial-mode mixing (SMM), even when the cavity's resonant mode is carefully optimized to match the laser's fundamental TEM_{00} mode. The fraction of light that is not mode matched does not enter the cavity; instead, it is directly reflected and acquires an additional phase shift. As a result, two fields emerge: the directly reflected, slightly displaced field (orange mode) and the field leaking out of the cavity (blue mode). These two fields interfere and form a superposition of the fundamental mode (FM) and one or more higher-order modes (HOM), illustrated as the green mode. The right panel of Figure 4.2 illustrates this effect in terms of Gaussian beam profiles along the optical x-axis.

An alternative but equivalent description uses a beam-splitter model. A displaced field enters one input port of the beam splitter, while a fundamental mode enters the other. Their interference produces a field containing higher-order spatial modes.

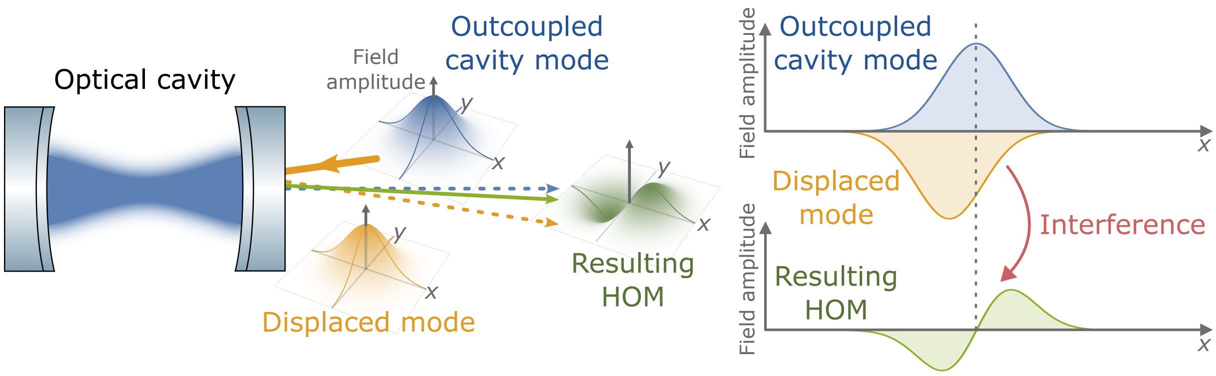

Figure 4.2: *Schematic illustration of mode mismatch between the cavity mode and a misaligned (displaced) incoming laser field. The fundamental-mode component of the incident field couples into the cavity mode, while the remaining part is directly reflected and acquires an additional phase shift. The interference between these two fields produces higher-order spatial modes. A three-dimensional illustration is presented in the left panel, whereas the right panel highlights the field amplitude along a single transverse direction. For clarity, the illustration assumes equal amplitudes for the two fields and shows only one resulting higher-order mode. In practice, stronger mode mismatch would generate multiple higher-order modes. The figure was adapted from an illustration by Dr. Korobko.*

To further formalize this interaction and to describe how multiple cavities contribute to hyperloss, it is useful to change to the eigenbasis of the first resonator. In this basis, the incoming beam is represented as a superposition of the fundamental mode and a higher-order mode that is intentionally designed to be off-resonance. Consequently, the first cavity acts as a mode-splitting element between the fundamental and higher-order spatial modes. When the light interacts with a second cavity, part of the higher-order mode is converted back into the fundamental mode. The resulting field is then detected with a phase-sensitive detector, which measures the quantum correlations in the same spatial mode as its reference beam, namely the fundamental mode.

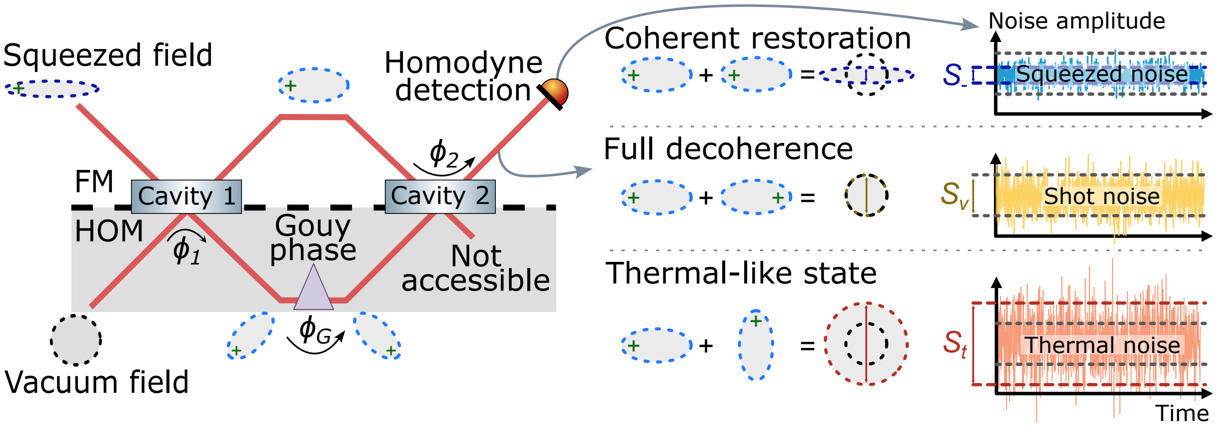

Figure 4.3: *Schematic of coupling between fundamental and higher-order modes utilizing squeezed light. Left panel: A simple two-cavity network can be associated with an effective Mach-Zehnder interferometer. Presented is a schematic divided into two parts: the upper half displays the FM progression, and the lower half the HOM progression. The blue dotted ellipses represent a squeezed field in the X and Y phase-space quadratures, with one quadrature squeezed and the other anti-squeezed. Green crosses illustrate the progression of a specific field amplitude. At the first cavity, squeezing in the FM couples to the HOM and acquires a relative phase ϕ_1. Free space propagation further rotates the HOM in phase-space due to the Gouy phase ϕ_G. Coupling into the second cavity adds a third phase ϕ_2. This results in a phase delay between FM and HOM. The noise level can be measured along one quadrature at the homodyne detector. Right panel: Three cases are presented. First, perfectly aligned ellipses with squeezing fully coherently restored. Second, ellipses are rotated by exactly π relative to each other. Correlations are canceled completely and the measured state's noise level is equal to the shot-noise level. Third, at a relative phase of $^{\pi}/_{2}$ the higher-order mode anti-squeezing couples to the squeezed quadrature and produces a thermal-like state. The choice to represent this as a thermal state is for illustrative purposes only. This schematic is adapted from a figure by Dr. Korobko.*

In the following, a simplified two-cavity quantum-enhanced network that utilizes squeezed light is presented. For this purpose, a schematic diagram is shown in the left panel of Figure 4.3. In analogy to a Mach–Zehnder interferometer, the cavities can be interpreted as effective beam splitters. This analogy allows the interferometer to be divided into two paths: the upper path corresponds to the fundamental mode, while the grey-shaded lower path represents the higher-order mode. At the first beam splitter (cavity 1), the fundamental and higher-order modes become entangled. At the second beam splitter (cavity 2), these two entangled paths interfere and the resulting field is detected with a homodyne detector. The blue dotted ellipses depict the squeezed field in phase space, with one quadrature squeezed and the orthogonal quadrature anti-squeezed. Green crosses illustrate how the phase of the state evolves. Three different cases can be distinguished:

Coherent restoration: The differential phase between the two paths is zero, such that the ellipses are perfectly aligned. In this case, the squeezing variance is coherently restored and, under the condition of equal mismatches at both cavities, no observable effect of mode mismatch remains.

Full decoherence: A differential phase of π cancels the quantum correlations completely, resulting in no measurable squeezing; the homodyne detector observes shot noise. This situation likewise assumes equal mismatch contributions from both cavities.

Thermal-like state: A differential phase of $\pi/2$ leads to the anti-squeezed quadrature of the higher-order mode coupling into the squeezed quadrature of the fundamental mode (or vice versa). This produces a fully thermal-like state, with the homodyne detector output exceeding the shot-noise level.

The central aspect is the differential phase that a single fundamental mode and a single higher-order mode acquire while propagating through the network. This differential phase determines whether the interference is constructive or destructive and thereby influences the extent of hyperloss. To analyse this, we first consider the phase evolution of an individual mode. Due to the nature of Gaussian beam propagation, the accumulated Gouy phase ϕ_G depends on the mode order [95]. In addition, the cavity is designed to be resonant only for the fundamental mode, while all other modes are reflected. As a consequence, the different modes acquire distinct phase shifts (ϕ_1 and ϕ_2). Together, these contributions form the differential phase that lies at the heart of the observed effect. Since the underlying mechanism originates from imperfect spatial mode matching (SMM) at the first cavity, the process can also be interpreted as a phase-dependent form of SMM. The situation becomes even more complex when additional higher-order modes generated upon reflection from the cavity are taken into account.

We distinguish between *hot* and *cold* phase-dependent SMM, defined by the input state injected into the network:

Hot SMM occurs when the initial beam incident on the first cavity is in a (pure) quantum-correlated state, in our case a squeezed state. In this regime, the coupling of the spatial modes generates an entangled field between the FM and HOM. As a result, the measurement of one mode yields a mixed, thermal-like state. This is the regime considered in the preceding section.

Cold SMM occurs when a coherent light field is incident on the first cavity. In this case, the effect manifests as a direct, phase-dependent power loss in the FM and is bounded by a maximum loss of 100 %. The effective loss is defined by

$$\lambda_{\mathrm{smm}} \equiv 1 - \frac{P_{\mathrm{out}}}{P_{\mathrm{in}}} = k_1^2 + k_2^2 + 2k_1k_2\cos\phi \tag{4.1}$$

$$\overset{k_1=k_2}{=} 2k^2\left(1+\cos\phi\right), \tag{4.2}$$

with $P_{\mathrm{in,out}}$ as the average measured optical powers of the input and output light fields, k quantifies the misalignment strength at both cavities assumed equal, and ϕ is the accumulated differential phase between the two modes. The heart of the cold phase-dependent SMM can be observed here: mismatch loss λ_{smm} cannot be modeled as two independent sources of loss, which would yield $\lambda_{\mathrm{smm}} = 1 - 2k^2$. Instead, the interaction between the two coupled modes may either amplify or diminish the evident loss, depending on the relative phase ϕ. For instance, a beam reflected sequentially from two optical cavities, each exhibiting a mode mismatch of approximately $k^2 = 8\,\%$, would typically be considered to incur an overall loss of roughly 15 %, alias the baseline. In the cold phase-dependent SMM case the total loss varies between 0 % ($\phi = \pi$) and approx 30 % ($\phi = 0$), as shown in Figure 4.4.

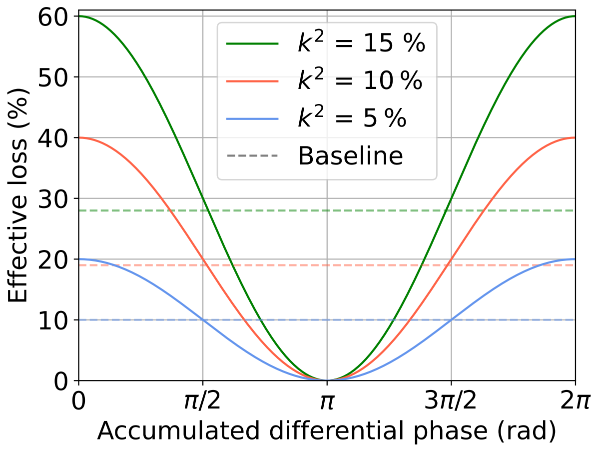

Figure 4.4: *Simulation of phase-dependent cold SMM for different mismatch factors (solid lines). The baseline represents a simple loss assumption (dashed line).*

However, in the hot phase-dependent SMM scenario, the effect becomes even more dramatic due to the involvement of quantum-correlated light. Higher squeeze factors, which correspond to a greater quantum advantage [76], are limited by quantum decoherence, typically caused by conventional optical loss. Therefore, we first examine conventional loss. As formalized in Section 1.3.3, the mechanism can be described by a beam-splitter that cross-couples the squeezed state with vacuum fluctuations, $\Delta^2\hat{X}_{\text{vac}}(\Omega) = 1$, thereby reducing the squeeze factor:

$$\Delta^2\hat{X}_{\text{meas}}(\Omega) = (1-\lambda_{\text{bs}})\Delta^2\hat{X}_{\text{in}}(\Omega) + \lambda_{\text{bs}}\Delta^2\hat{X}_{\text{vac}}(\Omega), \tag{4.3}$$

where $\Delta^2\hat{X}_{\text{in}}(\Omega)$ and $\Delta^2\hat{X}_{\text{meas}}(\Omega)$ denote the uncertainties of the initial and measured (decohered) state at a Fourier frequency Ω. The parameter λ_{bs} represents the power loss, modeled as the power transmissivity of the beam splitter.

Hot SMM has a stronger impact on $\Delta^2\hat{X}_{\text{meas}}(\Omega)$ than conventional loss, as it can couple anti-squeezed uncertainty into the measured uncertainty in addition to vacuum fluctuation. Analogous to cold SMM, this occurs because a portion of the squeezed field is reflected into the HOM at the first cavity (see Figure 4.3) and couples back into the FM at the second mixing interface with a differential phase. Depending on the accumulated phase, the anti-squeezed quadrature may couple into the squeezed quadrature of the fundamental field, which results in significant decoherence. The total detected noise can be expressed as:

$$\Delta^2\hat{X}_{\text{meas}}(\Omega) = (1-\lambda_{\text{smm}})\Delta^2\hat{X}_{\text{in}}(\Omega) + \lambda_{\text{smm}}\Delta^2\hat{X}_{\text{vac}}(\Omega) + T(\Omega), \tag{4.4}$$

where $T(\Omega) = k_1^2 k_2^2 e^{2r_s}$ originates from the projection of the anti-squeezed variance of the higher-order mode onto the fundamental mode at the second mixing interface. This term is proportional to the initial anti-squeezing and the phase mismatch ϕ, assuming equal squeezing r_s and anti-squeezing r_a parameters. For the sake of completeness, the full derivation yields

$$\begin{aligned}\Delta^2\hat{X}_{\text{meas}}(\Omega) = (&\cos k_2 \sin k_1 + \cos k_1 \cos\phi \sin k_2)^2 + \\ &e^{-2r_s}(\cos k_1 \cos k_2 - \cos\phi \sin k_1 \sin k_2)^2 + \cos^2 k_1 \sin^2 k_2 \sin^2\phi + \\ &e^{2r_a}\sin^2 k_1 \sin^2 k_2 \sin^2\phi\end{aligned} \tag{4.5}$$

which is illustrated in Figure 4.5. The left panel of Figure 4.5 presents the phase dependence between the FM and HOM with an equal mismatch $k_{1,2}^2 = 8\,\%$ at each cavity for different initial squeezing values, reaching hyperloss (also referred to as a thermal-like state) at $\phi = \pi/2$, $3\pi/2$ and a recovery state (which we refer to as coherent restoration) at π. Due to the initial mode mismatch, the squeezed states recover only relative to the baseline. The baseline represents a simple estimate of the mismatch-induced loss, considering only conventional optical loss, and can be calculated using Equation 4.3.

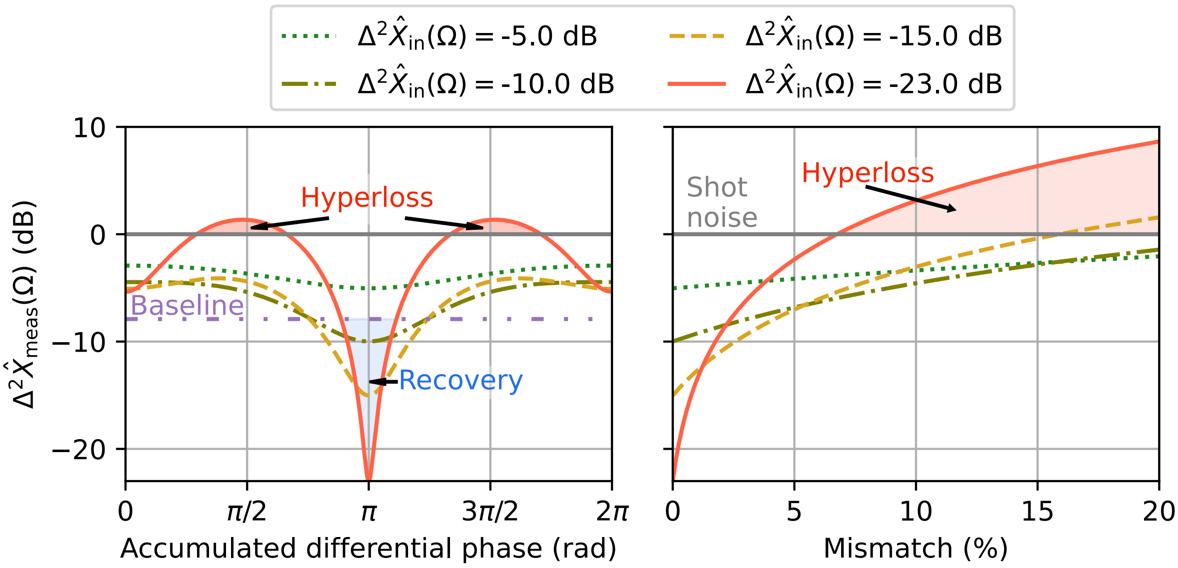

Figure 4.5: *Measured state as a function of differential phase (left panel) and mode mismatch (right panel) for various initial squeezing levels. In the left panel, a thermal-like state of approximately 1.4 dB is obtained for an initial squeezing of −23 dB. The baseline is calculated for* $\hat{X}_{in}(\Omega) = -23$ *dB.*

The qualitative regimes introduced above are complemented by their corresponding analytical expressions, which quantify the behavior as a function of the differential phase and mismatch:

Recovery regime: The appropriate phase relation between the modes restores the lost correlations and recovers the initial squeezing relative to the baseline. For $\phi = \pi$,one obtains $\Delta^2\hat{X}_{\text{meas}}(\Omega) = e^{-2r_s}$, which corresponds to the condition previously referred to as full coherent restoration.

Neutral regime: In this regime, the thermal contribution increases as the squeeze factor is reduced, up to the point where either the hyperloss or the recovery regime is reached. For example, for $\phi = 0$ one obtains $\Delta^2\hat{X}_{\text{meas}}(\Omega) = \sin^2 2k_1 + e^{-2r_s}\cos^2 2k_1$, which corresponds to the coherent restoration described earlier.

Hyperloss regime: This regime is reached when the state becomes significantly mixed (thermal-like), with the measured variance exceeding the shot-noise level for all quadratures; i.e. $\Delta^2\hat{X}_{\text{meas}}(\Omega) > 0$. For $\phi = \pi/2$, one finds $\Delta^2\hat{X}_{\text{meas}}(\Omega) = e^{-2r_s}\cos^4 k_1 + 2\cos^2 k_1 \sin^2 k_1 + e^{2r_a}\sin^4 k_1$ which corresponds to the hyperloss condition, previously referred to as a thermal-like state.

The right side of Figure 4.5 depicts the measured noise variance as a function of mismatch for different initial squeezing levels at a differential phase of $\pi/2$. This corresponds to the regime in which one quadrature of the field couples to a hot thermal bath. Two effects can be observed: first, an increase in the initial noise variance amplifies the impact of mismatch; second, increasing the mismatch can bring the system into the hyperloss regime for almost all initial noise variances. These results highlight the significance of the mismatch loss channel.

In summary, the core mechanism underlying SMM is the accumulated differential phase between the FM and HOM, which arises from insufficient mode matching to resonators within a quantum network. Two important cases can be distinguished: First, the hyperloss regime, in which the squeezed state is transformed into a thermal-like state. Second, the recovery regime, in which the lost correlations are fully restored and only the mode-matching loss remains relevant.

The physical framework developed above implies a set of measurable signatures, whose experimental verification is the focus of the following chapters. We concentrate on the observation of *hot* SMM, while *cold* SMM, being purely classical, serves as a reference measurement.

4.2 Preliminary Study With Weak Coupling

We begin by investigating the single-resonator configuration in more detail. Our underlying hypothesis was that *hot* SMM should already be observable in this setup, since the system provides two coupling interfaces with spatial-mode mismatch: the cavity itself and the local oscillator used for the homodyne detection. In this picture, the local oscillator takes the role of cavity 2 in Figure 4.3.

4.2.1 Experimental Realization

Figure 4.6 shows a schematic illustration of the experiment. This is split into two panels: the left panel shows a simplified version, and the right panel shows a more detailed one.

First, I explain the basic principle and focus on the left panel. A 1064 nm Nd:YAG laser by InnoLight model Mephisto is frequency doubled to 532 nm. The green light pumps a nonlinear cavity to produce a squeezed vacuum state via parametric down-conversion. An overview of the squeezing-cavity properties is provided in Table 4.1. The squeezed light is mode matched to cavity one (shown in green, properties can be seen in Table 4.1) by passing a custom Faraday isolator consisting of a $\lambda/2$-waveplate, $\lambda/4$-waveplate, and a polarizing beam splitter. An intentional 19 % misalignment was introduced using a set of mode matching lenses (highlighted in pink) for cavity one. For simplicity, we used the Laguerre–Gaussian (LG) mode with radial index 0 and azimuthal index 1 (LG_{01}), as Hermite–Gaussian (HG) modes introduce a spatial displacement over long optical paths that complicates the recombination of the FM and HOM. However, this protocol can also be implemented using Hermite–Gaussian modes. The cavity was designed to be resonant with the FM LG_{00}, meaning all other HOMs as LG_{01} are reflected. The length of cavity 1 can be stabilized at different resonance points (as shown in Figure 4.7). This is a crucial step in the experiment, since it allows us to adjust the differential phase between the FM and HOM, as described in the theory Section 1.1.1. Both modes were guided to a 50:50 beam splitter and subsequently measured using a homodyne setup with a local oscillator prepared in the LG_{00} mode, ensuring that the detection was performed in the fundamental mode. A self-built homodyne detector together with an Advantech PCIe-1840L data acquisition card was used to record the data.

Table 4.1: *Optical properties of the used cavities.*

	Squeezing Cavity	Cavity 1
Wavelength (nm)	1064	1064
Finesse	66	79
Free spectral range (GHz)	5.28	1.3
Linewidth (MHz)	80	16.5

For a detailed explanation, focusing on the corresponding mode matching, I refer to the right panel of Figure 4.6. The squeezed light co-propagates with a weak control field to ensure proper alignment of the experiment. However, this beam is too weak to align the full setup, so a brighter beam is required. To generate a bright control beam following the squeezed beam, a strong control field (orange) was overlapped with the weak control beam. This overlap was verified using a diagnostic mode cleaner, as shown in the diagnostic setup (framed in purple). As a result, a strong control beam with the same trajectory as the squeezed light is obtained.

The next step is to match this strong control field to the first cavity with the help of PD 2.

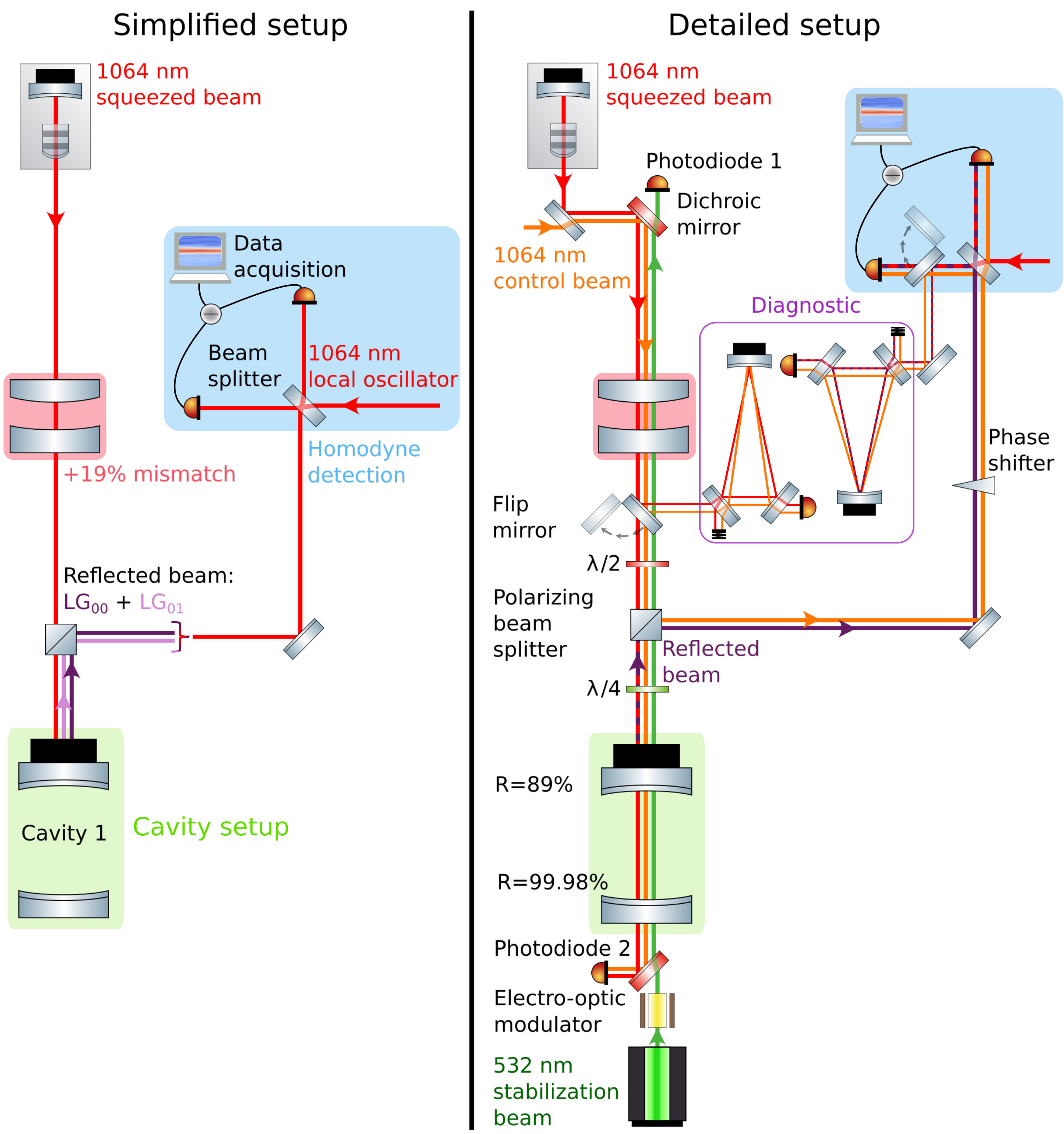

Figure 4.6: *Schematic diagram of the experimental setup. The simplified version is shown on the left, while a more detailed view is on the right. In the main text, we focus first on the left side for schematic explanation followed by a more detailed mode matching analysis using the right side. Squeezed light at 1064 nm was used to perform the experiment. An intentional 19 % misalignment was introduced using a set of mode matching lenses (highlighted in pink) for cavity one. For simplicity, we choose the* LG_{01} *mode; however, there is no issue with implementing this protocol using Hermite-Gaussian modes as well. The reflected fundamental mode,* LG_{00} *by design choice, and the higher-order mode,* LG_{01}*, propagate through free space and acquire a relative phase. For measurement, these modes were overlapped with a local oscillator at a 50:50 beam splitter and detected using a custom homodyne detector.*

A 532 nm auxiliary beam (green) and a custom Pound-Drever-Hall control scheme in transmission of cavity one was used to stabilize the cavity length using a frequency-stabilization scheme. The Airy distribution of the cavity was monitored with PD 1, as shown in Figure 4.7 and is discussed in the next paragraph. After this, the first cavity was kept off-resonance and the strong control beam was overlapped with the 1064 nm local oscillator at a 50:50 beam splitter with the help of the diagnostic mode cleaner. This procedure ensures a fully aligned setup.

Figure 4.7 presents the Airy distribution of the first cavity zoomed in around one Airy peak. Red traces show the 1064 nm Airy peak, which corresponds to the fundamental mode. Shown in green is the 532 nm Airy peak, which allows us to select the differential phase between FM and HOM through the cavity's phase response, as discussed in Section 1.1.1. The gray highlighted mode is used to stabilize the cavity and therefore the cavity phase response. One special case needs to be highlighted: $\Phi = \pi/2$, which corresponds to the cavity being doubly resonant for both fields.

The heart of this experiment is the differential phase between the FM and HOM. This can be adjusted through the phase acquired by detuning the first cavity from perfect resonance, as seen in Section 1.1.1. Other phases, such as the Gouy phase or the cavity coupling phases acting on different modes, were unknown. However, the combination of all tunable parameters allowed us to explore the full range of differential phases.

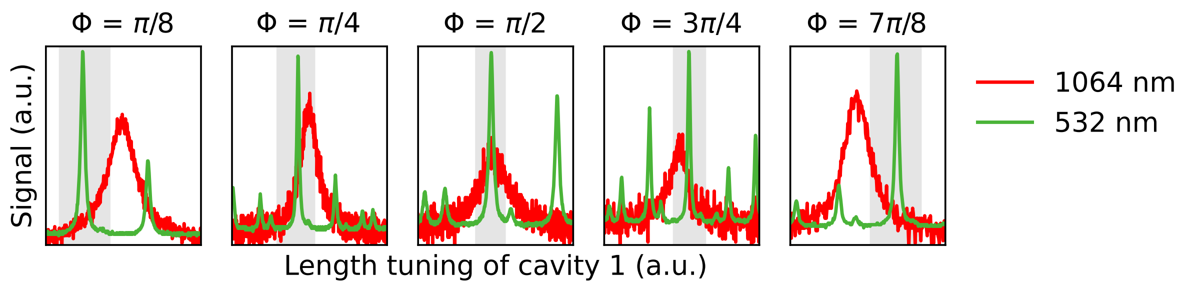

Figure 4.7: *Airy peaks of 1064 nm (monitored at PD 2) and 532 nm (monitored at PD 1) of cavity one are shown. We used the green laser as length stabilization beam for this cavity at different phases with respect to the 1064 nm resonance peak. For this purpose, various modes of 532 nm were optimized; those used for stabilization are highlighted in gray, while all other modes of the 532 nm light can be ignored, as they do not contribute to the experiment.*

4.2.2 Analysis and Result Presentation

Externally modifying the phase of the 1064 nm beam via a phase shifter allows us to measure the distribution shown in Figure 4.8. An evolution of the Airy distribution for different frequency stabilization points of cavity one is shown. Two important regimes can be identified. First, the so-called *off-resonance* case, which is defined by a near-perfect mode matching. Second, the *on-resonance* case, here the mismatch was introduced. The names *off-resonance* and *on-resonance* are defined by the Airy peak position of the 532 nm in relation to the 1064 nm resonance peak and can be identified in Figure 4.7. In this context, *off-resonance* is far from double resonance, whereas *on-resonance* refers to $\Phi = \pi/2$ and double resonance. It can be seen that the evolution from *off-resonance* to *on-resonance* introduces losses. This is evident from the reduction in the intensity of the main peaks and the growth of the HOM.

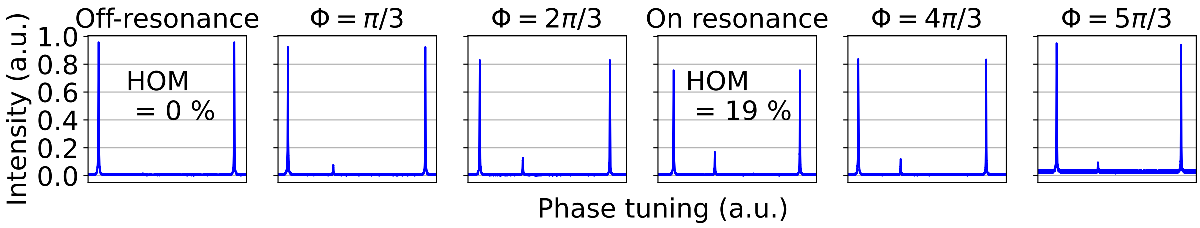

Figure 4.8: *Higher-order mode evolution of cavity 1 using PD 1 as monitoring source by tuning the cavity length can be seen.*

The above characterisation confirms how the intentional mismatch manifests itself in the spatial modes of the reflected field. With these regimes identified, we now investigate their effect on the quantum noise by analysing the squeezing and anti-squeezing variances.

Left panel of Figure 4.9 presents the normalized relative noise level as a function of length tuning of cavity one. The top panel shows the anti-squeezed variance (red dots), and the bottom panel shows the squeezed variance (blue dots). Both squeezing and anti-squeezing decrease when tuning onto resonance (gray highlighted area) and reach the baseline level.

The first indication that hot SMM is not observed comes from comparing the measured squeezing with the expectation for classical loss, calculated using Equation 4.3. For the given losses of 19 % and an initial squeezing of (-5.8 ± 0.5) dB, we expect a resulting squeezing level of (-4.5 ± 0.5) dBB, shown as the baseline (purple line).

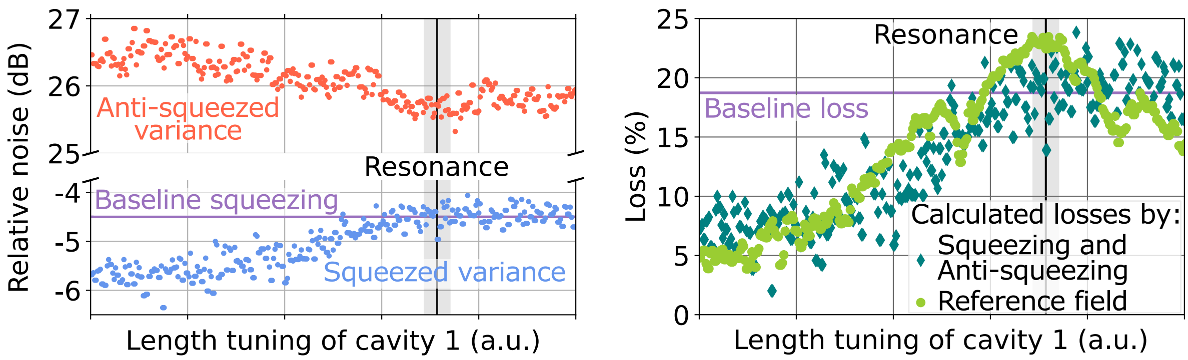

Figure 4.9: *(a) Measured squeezed and anti-squeezed variance tuning the length of cavity one. Both variances approaching the shot noise level, indicating classical loss. (b) Comparison of the losses once through the given squeezing and anti-squeezing variances, and an interference measurement, alias reference field or the cold SMM (more information given in the main text). Both measurements behave similarly, showing that the loss is only classical and not hot SMM.*

Right panel of Figure 4.9 visualizes the losses during the length tuning. The loss η_{QU} (dark green diamonds) was calculated from the measured squeezing and anti-squeezing values using Equation 3.8. The same procedure was repeated with the strong control beam instead of the squeezed field. Here, the interference between the control beam and the local oscillator was used to derive the corresponding loss η_{DC} (bright green dots), calculated from the relation

$$\eta_{\mathrm{DC}} = \left(1 - \frac{I_{\mathrm{measured}}}{I_{\mathrm{min}}}\right)^2. \tag{4.6}$$

Where I_{measured} is the measured interference over the full time and I_{min} the minimum of it, both normalized by dark counts. The dips are artifacts of the data acquisition system.

In summary, it can be said that hot SMM was not observed in the case of a single cavity. This is because the observed behavior of the squeezing variance when tuning the length of the first cavity can be explained by the classical loss theory of squeezing. Returning to the initial statement made at the beginning of this chapter that the second cavity in Figure 4.3 can be replaced by an LO, this assumption has been disproved. The physical picture behind this is the following: a mismatch at cavity 1 reflects a HOM together with the FM towards the homodyne detection setup. Since the local oscillator was chosen in the FM, the detector extracts only the information carried by the FM component. As a result, the mismatch introduced at cavity 1 appears purely as classical loss. In this configuration, the LO therefore provides a too weak coupling between the reflected FM and reflected HOM to reveal any quantum effect. In principle, choosing an LO with the same mode shape as the reflected field, that is, the same combination of FM and HOM, would improve the coupling strength and could potentially reveal quantum behavior. Instead of generating such a tailored LO, we chose to couple the reflected modes back into a single mode using a second cavity and to analyse the resulting field with the given LO.

4.3 Experimental Demonstration of Hyperloss

As shown in the previous section, the coupling with a local oscillator is too weak to reach the hyperloss regime. Therefore, in this section we analyze the coupling with a second cavity, resulting in a quantum network consisting of two cavities.

4.3.1 Schematic Demonstration of the Experiment

In this subsection, I provide a schematic overview of the two-cavity configuration used to investigate the stronger mode coupling required to reach the hyperloss regime. The aim is to outline the structure of the setup and to highlight how it extends the single-cavity arrangement discussed in the previous section, before moving on to the detailed alignment and measurement procedures.

In Figure 4.10 the schematic of the experimental setup is shown. I will not go into every detail here, as the setup is an extension of that shown in Figure 4.6, but I will focus only on the part from the first cavity onwards. More detailed explanations of the previous part can be found in Section 4.2.1.

Details for the squeezing cavity and for cavities one and two are summarized in Table 4.2.

Table 4.2: *Optical properties of the used cavities.*

	Squeezing Cavity	**Cavity 1**	**Cavity 2**
Wavelength (nm)	1064	1064	1064
Finesse	66	53.8	79
Free spectral range (GHz)	5.28	33.3	1.3
Linewidth (MHz)	80	618	16.5

A custom optical diode, consisting of a quarter waveplate, a half waveplate, and a polarizing beam splitter, was used to separate the reflected fundamental mode LG_{00} (pink line) and higher-order mode LG_{01} (violet line), with respect to the eigenbasis of cavity 1, from the entering light. The reflected beam was matched to a triangular cavity, cavity 2, by length stabilizing cavity one at double resonance ($\Phi = \pi/2$). The reason for using a triangular-shaped cavity was to minimize optical loss without using another custom optical diode or Faraday isolator, and to simplify handling. In principle, we see no problem in doing this with two Fabry-Perot-like cavities. Both modes were combined at cavity two, and the reflected quantum state was then measured via a homodyne detection system (highlighted blue) with a custom transimpedance amplifier stage and a 1064 nm local oscillator. With this alignment strategy we get a fully aligned setup and have control over each mode matching.

All cavities were designed to be resonant for the fundamental LG_{00} mode and anti-resonant for higher-order modes. A mismatch was introduced at cavity 1 using a pair of lenses such that $(8 \pm 1)\,\%$ of the light was coupled into a higher-order mode. The LG_{01} mode, highlighted in pink, was selected, while cavity 1 was stabilized off resonance (see Figure 4.8). However, this also means that the perfect mode matching is far from the double resonance. For simplicity, we used Laguerre-Gaussian modes, although the experiment can equally be performed using Hermite-Gaussian modes. To ensure that the field entering the second cavity was perfectly mode-matched to its LG_{00} eigenmode, we introduced a second set of lenses that compensated the initial $(8 \pm 1)\,\%$ mismatch.

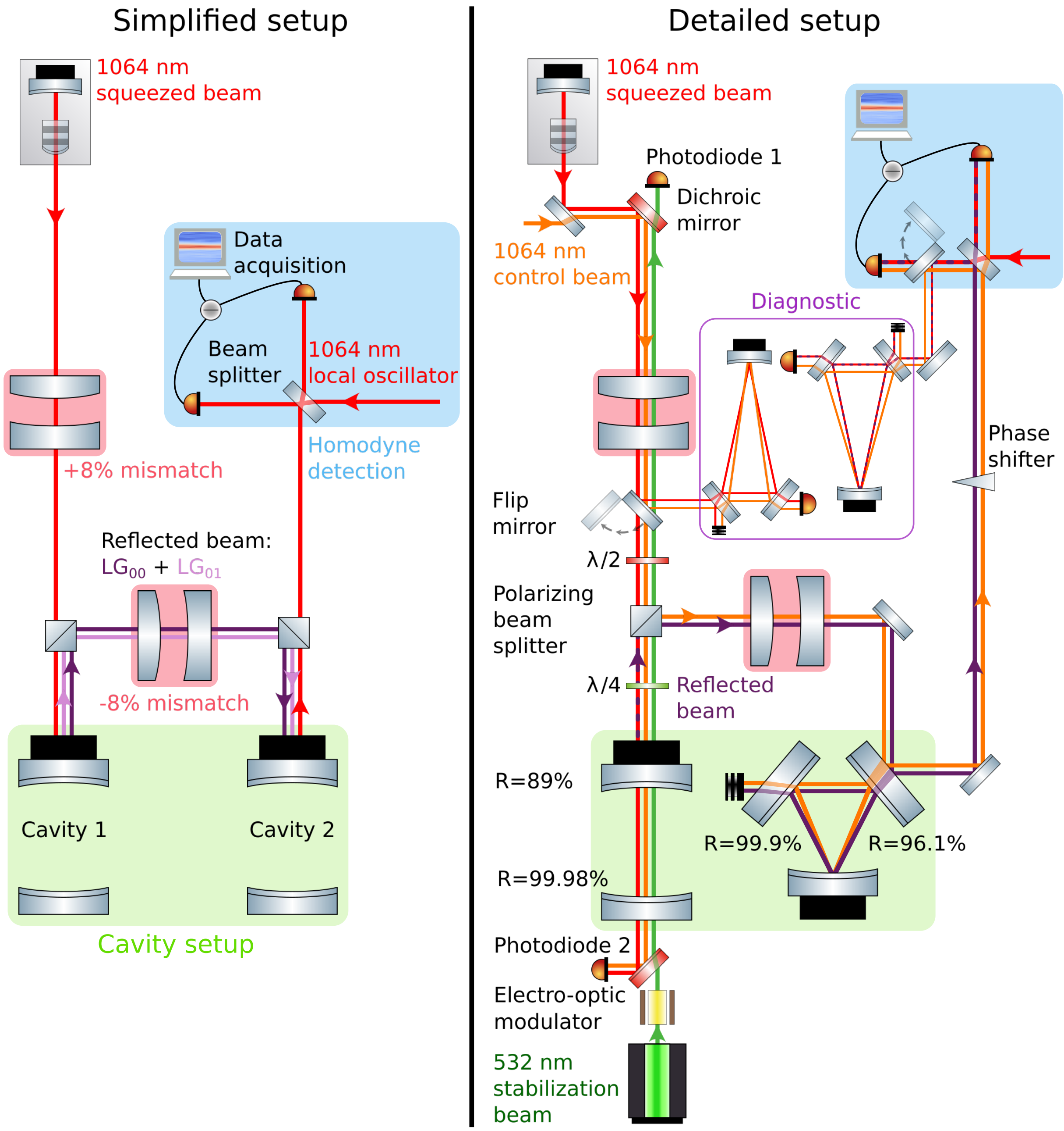

Figure 4.10: *Schematic description of the experimental setup for a small two-cavity network. Two sections are presented: a simple illustration on the left, and the detailed experiment on the right. The experiment was performed using squeezed light at 1064 nm. We introduced a $\pm 8\,\%$ mismatch with a set of lenses (highlighted in red) for cavity 1, which resulted in a combined reflection of Laguerre-Gauss modes (LG_{00} and LG_{01}). An additional set of lenses perfectly mode-matched the reflected and out-coupled light to cavity two, thereby compensating the initial mismatch and yielding a pure LG_{00} mode. Afterwards, it was overlapped with a local oscillator at a 50:50 beam-splitter and detected using a custom homodyne detector (highlighted in blue).*

The heart of this experiment is the differential phase between the FM and HOM. This can be adjusted via two methods: first, by detuning the first cavity from perfect resonance (using the green-beam stabilization), and second, by continuously tuning the second cavity to imprint a phase shift on the FM. Other phases like the Gouy phase and coupling phases of the cavities, acting on the different modes, were unknown. However, the combination of all tunable parameters allowed us to observe the full range of possible differential phases.

For the measurements, cavity one was length-stabilized at different points while the length of cavity 2 was tuned using a piezo actuator. The sampling rate of the local oscillator was significantly higher than that of cavity two, allowing the full phase information of the homodyne measurement could be obtained at a sampling point of cavity two. Our custom homodyne detector has two output ports for the DC and AC signals (the DC signal is high-pass filtered). Both outputs were recorded using an acquisition card, made by ADVANTECH model PCIe-1840L, with a sampling rate of 80 MHz and an anti-aliasing filter at 20 MHz. The DC port was used to record the beat between the weak reference beam and the local oscillator, and the AC port for recording the squeezed light field. It should be noted that the DC port was low-pass filtered to remove noise from the squeezed state, which was not phase synchronized to the DC reference.

4.3.2 Results

We used full-state tomography, that is, homodyne measurements over the full range of local-oscillator phases, to record the noise variance as a function of measurement frequency. The result is shown in Figure 4.11. Each column describes a different regime, and we switch the regime by changing the differential phase between the fundamental and higher-order mode. By selecting an alternative stabilization point at the first cavity, the system acquires a different initial differential phase between the modes, which is subsequently adjusted at the second cavity. The resulting phase, which arises from the combination of the initial phase and the applied tuning, is referred to as the differential phase ($\Delta\phi_1$ and $\Delta\phi_2$). This distinction is defined as regime one and regime two, as the scan rate of the second cavity and the accumulated propagation phase remains the same. On the left side, the hyperloss regime is presented, and on the right side, the recovery regime. This separation between the two regimes is important because one adds additional loss to the system, while the other reduces it.

At the same time, we recorded the cold SMM by measuring the power loss of the weak control beam, obtained from the beat signal between the weak control field and the local oscillator. This measurement, shown in the top row, provides an estimate of the expected classical losses, which vary between approximately 65 % and 40 %.

In the second row on the left, we show the hot SMM, illustrating the transition of a quantum state (orange points) into a thermal-like state (red points). We observe a total loss of the (5.8 ± 0.5) dB squeezed field *below* the shot noise level (gray line) and its transformation into a thermal-like state with approximately (1.4 ± 0.5) dB (red dots) *above* the shot-noise level. This behavior directly reproduces the physical picture described in Section 4.1. Crucially, the cold SMM (top row) cannot account for the observed decoherence: using the measured cold losses to calculate the expected squeezing variance (Appendix A.5) does not reproduce the behavior observed in the hot case. This confirms the genuinely quantum nature of the hyperloss and highlights the fundamental difference between the hot and cold SMM.

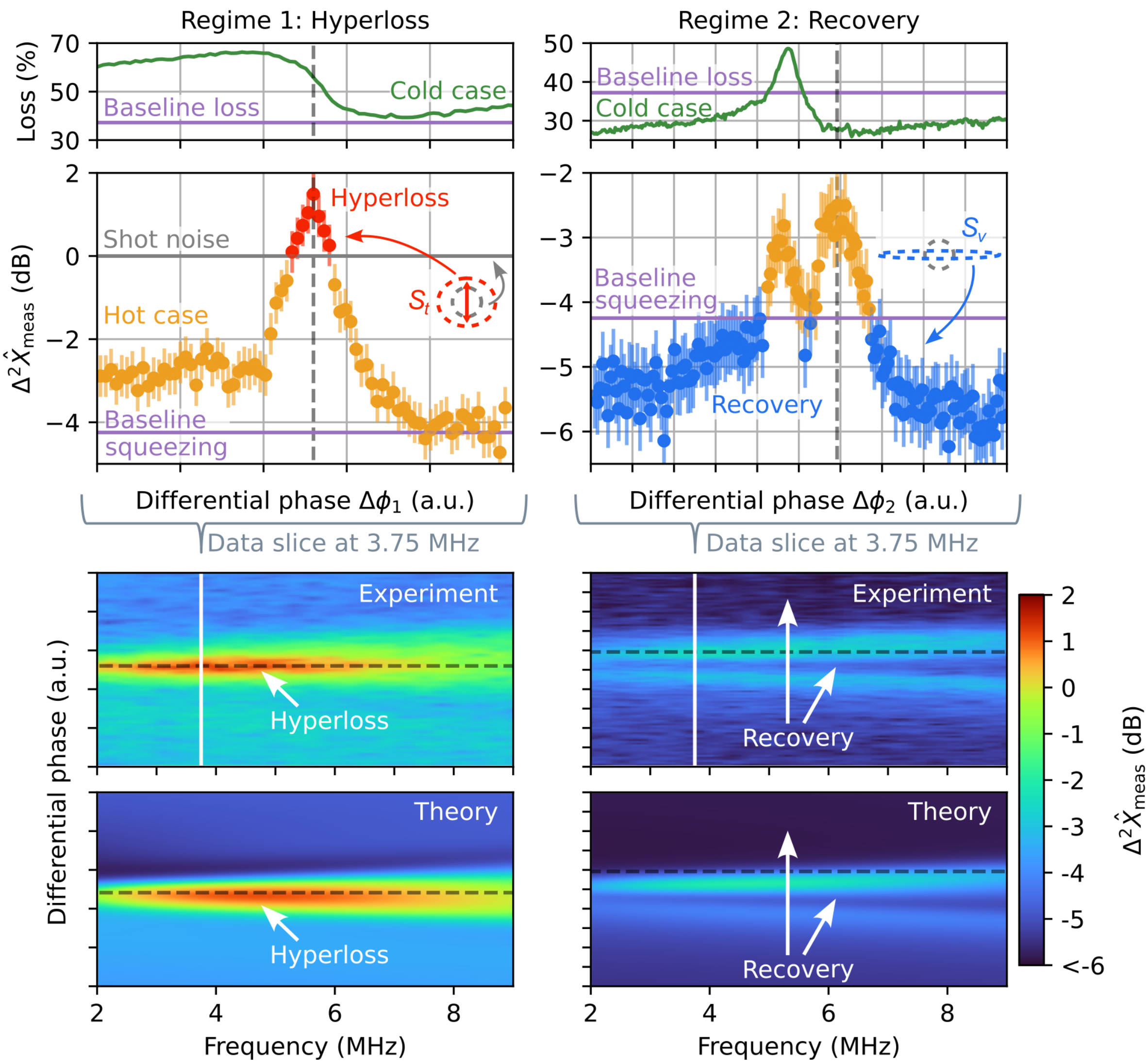

Figure 4.11: *Splitting the figure in two columns, left side describes the hyperloss regime and the right side the recovery regime. The differential phase decides in which regime the system operates. Top row: cold SMM effect as power loss on the coherent field as a function of the differential phase between fundamental mode and higher-order mode. In violet the loss level as treating the mode mismatch as direct optical loss is shown, we call this "Baseline loss". The second row: the minimal measured quantum variance (squeezed field) versus the differential phase is shown. A thermal-like state with around (1.4 ± 0.5) dB noise above the shot noise level was reached, this is the hyperloss, because all squeezing is lost. Choosing a different differential phase, allows to recover up to 5.2 dB of initial 8 dB squeezing, seen as the noise drops below the baseline squeezing (applying the baseline loss on the initial squeezing value), meaning the 15 % mismatch acts like approximately 2.8 %. The third row: shows a spectrogram of the full data set of the minimal noise variance versus the frequency and the differential phase. Here, we chose a slice at 3.75 MHz (white line) for the first and second rows. Bottom row: presents a theoretical simulation with the use of independently measured parameters from the setup, the only fitting parameter was the Gouy phase, leading to a similar behavior as measured. Dotted gray lines serve as guidelines.*

The opposite behavior is shown on the right side of the second row in blue dots. By carefully adjusting the differential phase, the system enters the recovery regime. In this regime, up to

12 % of the correlations lost due to the introduced mismatch are recovered relative to the baseline squeezing, as explained in Section 4.1.

The third and fourth rows present a spectrogram of the observed noise variance as a function of the measurement frequency and the tuning of the second cavity, i.e., the differential phase. This representation illustrates the frequency dependence of the SMM. Importantly, this behavior can be tuned by adjusting experimental parameters, allowing access to any desired frequency range. A comparison between the experimental data (third row) and theoretical simulations (fourth row) shows strong qualitative agreement, demonstrating a solid understanding of the underlying physics. A detailed description of the theoretical model can be found in our paper [94].

Cavity 1 provides five distinct frequency stabilization points, shown in Figure 4.7. Stabilizing the cavity at each of these points generates a different initial phase, which in combination with the second cavity yields five differential phases $\Delta\phi_1$ to $\Delta\phi_5$. These phases give rise to five distinct operational regimes, illustrated in Figure 4.12. Five distinct manifestations of mode mismatch are covered by these regimes, ranging from strongly mixed states to near-coherent recovery.

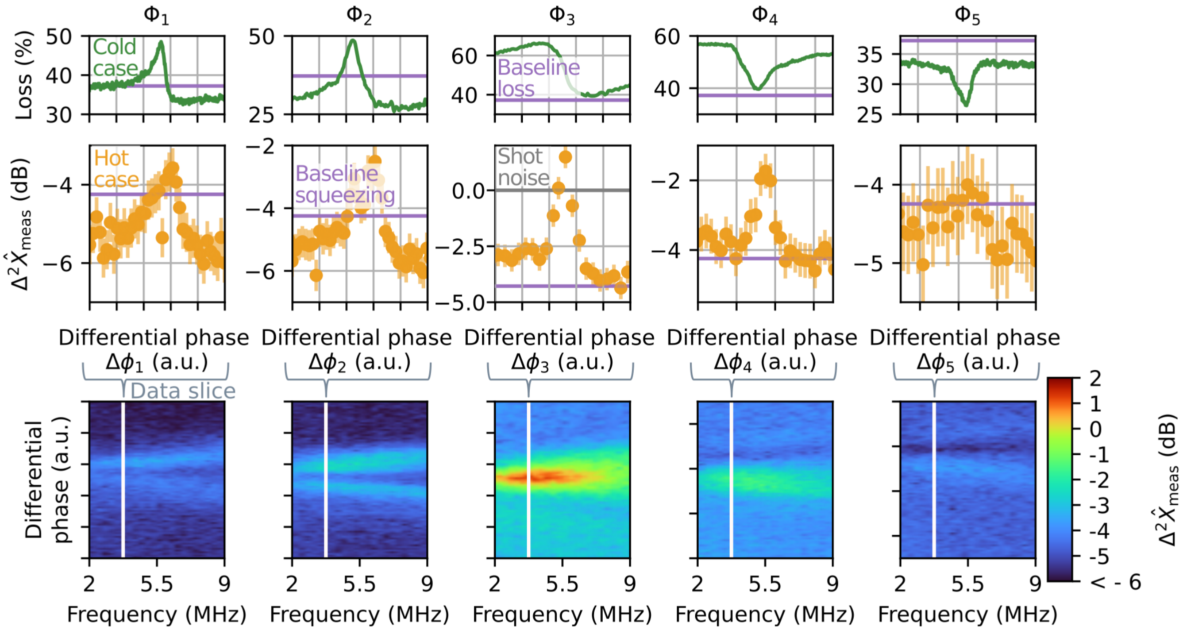

Figure 4.12: *Evolution of hyperloss as a function of five different length stabilization points of the first cavity; the maximum is reached at Φ_3. The top row depicts the cold SMM, the middle row a slice at 3.75MHz, and the bottom row the spectrogram. For clarity of presentation, only every fourth data point is shown in the middle row.*

The top row shows the corresponding cold SMM, derived from the beat between the weak control beam and the local oscillator. Presented in the second row are the hot SMM, displaying both strongly thermal-like transitions and coherent recovery relative to the baselines. Among these regimes, Φ_3 corresponds to the maximal thermal-like state, while Φ_2 shows the strongest recovery. The remaining regimes interpolate between these two extremes.

In the third row, a spectrogram of the noise variance is shown, with the white line marking the frequency (3.75 MHz) at which the cold and hot SMM slices above were taken.

Traditional Squeezing Zero-Span Variance Measurement

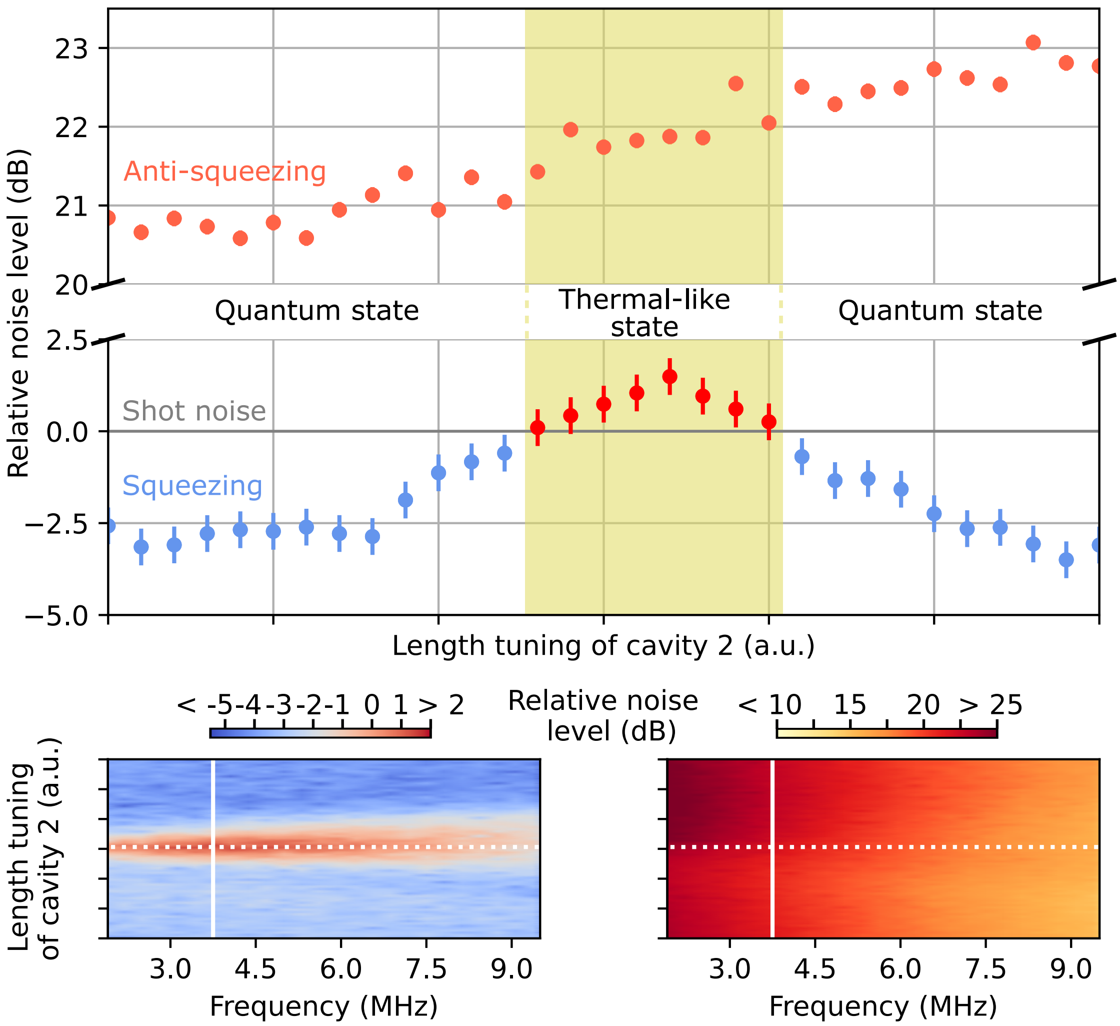

Figure 4.13: *Top image: Illustrates the transfer of a quantum state to a thermal-like state and back by tuning the length of cavity 2 at a measurement frequency of 3.75 MHz for the hyperloss regime (Φ_3). The quantum states are represented by anti-squeezing (light red), squeezing (blue) and the thermal-like (bright red) state is highlighted in yellow. Bottom left: Spectrogram of squeezing. The vertical white line indicates the point of the slice corresponding to the top image, while the dashed horizontal white line marks the position of cavity 2 with the most hyperloss. Bottom right: Spectrogram of anti-squeezing.*

To further investigate the hot SMM, Figure 4.13 provides a detailed zero-span analysis of the squeezing and anti-squeezing signals. The bottom row shows spectrograms of squeezing (left) and anti-squeezing (right) as a function of the measurement frequency, ranging from 2.5 MHz to 9.25 MHz, and the tuning range of cavity two. A slice at 3.75 MHz is shown in the top panel. Tuning the length of cavity two reveals the evolution of the minimum-noise state from quantum to thermal and back. Quantum states are distinguished by anti-squeezing (light red dots, top half) and squeezing (blue dots, bottom half), with the thermal state highlighted in yellow. A clear transfer from approximately (2.5 ± 0.5) dB *below* the shot noise level to approximately (1.4 ± 0.5) dB *above* the shot noise level and back can be observed, with red dots indicating the thermal-like measurement points. At this point, it is important to note that the uncertainties are dominated by the evaluation procedure, as discussed in Section 4.3.3. Note that this figure shows a zoomed-in section of the data presented in the previous Figure 4.11. This agrees with the analytical simulation in Figure 4.5. Meanwhile, anti-squeezing increases throughout the full tuning-length range.

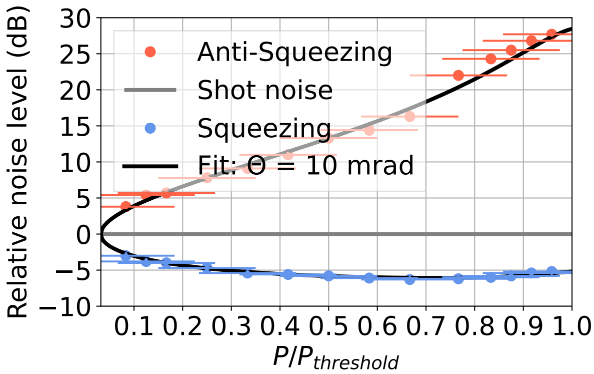

Figure 4.14: *Phase noise estimation.*

An increase in anti-squeezing and a decrease in squeezing directly indicate non-classical behavior. In Figure 1.12 the effect of classical loss on squeezed light was simulated, using the analytical Equation 1.48, detailed explanation can be found in the theory Chapter 1.3.3. For the sake of completeness, we also checked the phase noise of the source generating the SMM, as shown in Figure 4.14. In this measurement, both cavities were set to off-resonance, and squeezing (blue dots) and anti-squeezing (red dots) were measured at different pump powers relative to the threshold power $P_{\text{thr}} = (120 \pm 12)$ mW of the squeezer resonator. The uncertainty is given as 10 % based on the power meter OPHIR model Nova II. Our results are verified by theory using the analytical Equation 1.46, leading to a phase noise of (10 ± 1) mrad. This is comparable to what other experiments achieved that were using similarly complex quantum networks [96]. Taken together, these results demonstrate the hyperloss effect.

4.3.3 Classical Calibration Analysis

We have estimated our classical loss contribution; the results can be seen in Table 4.3. Most components are specified by the manufacturer, e.g., the general propagation loss towards the homodyne detection. This is relatively minor due to the use of high-quality mirrors ($R \geq 99\,\%$) and is provided by the manufacturer LASEROPTIK. The same applies to all other common components such as Faraday isolators, lenses, photodiodes, and dichroic beam splitter.

We defined a group of optical components, referred to as Set 1, because these elements could not be distinguished or measured individually. This set was measured as a single component using a power meter, and the individual losses were estimated accordingly. The accuracy of these estimations is limited by the 10 % measurement precision of the power meter OPHIR model Nova II.

The escape efficiency of the squeezed light source is given by $\frac{T}{T+L}$, where T is the transmissivity of the coupling mirror and L is the sum of all round-trip losses. These include scattering and absorption losses, as well as residual transmission through the crystal's imperfectly reflecting rear face. The manufacturer provided the transmissivity of the coupling mirror and the crystal characteristics, which were then used to determine the escape efficiency and convert it to the

Table 4.3: *Overview of all optical losses*

Source	Loss (%)
Propagation loss	1
Faraday isolator	2.3
Lenses	0.3
DBS front squeezer	0.1
DBS front cavity one	0.5
Waveplate	0.2
Set 1 measured: *PBS, $\lambda/4$-waveplate, Mirror, Cavity 1*	16.3 ± 10.0
Intracavity on-resonance	0.3
Intracavity off-resonance	1.1
Escape efficiency as loss of the squeezer	1 ± 0.1
Quantum efficiency of photodiodes	0.5
Visibility	2 ± 0.2
Phase noise equivalent	$(0 \text{ to } 4) \pm 0.1$
Estimated losses	$(26.3 \text{ to } 30.3) \pm 10.4$

loss $(\eta - 1)$.

Interference measurements were used to analyze the overlap between the local oscillator and the squeezed light field. For this purpose we used the well aligned control beam, instead of the squeezed beam and measured its interference with the local oscillator at the beamsplitter of the balanced homodyne detector. Quantification was done by using the visibility as given by Equation 1.56.

Note that the limit on the squeezing value we calculated using the classical loss values cannot be directly compared to the (measured) squeezing values, as the conditions were slightly different for each measurement, specifically in terms of phase matching temperature, pump power, and data evaluation. Since phase matching and pump power influence the highest observable squeezing as described in Section 1.2.2 and 1.3.3, we always aimed to obtain the maximum squeezing and anti-squeezing values. Estimating the introduced loss for cavity one is not trivial, since PD 2 was sensitive to the individual modes differently depending on the beam position.

Data Evaluation and Choice of the Digital Filter

Data were acquired using a data acquisition card and subsequently post-processed with digital filters. The AC and DC channel signals were divided into time bins i_{bins}, with each time bin containing 51.2 M samples.

Starting with the analysis of the DC signal (beat between the weak control beam and the local oscillator): for each time bin, we extracted the corresponding amplitude $A[i_{\text{bins}}]$ from the recorded trace. To remove slow drifts and offsets, we determined the maximum and minimum value of the signal within each bin and defined a cleaned amplitude

$$A[i_{\text{bins}}]_{\text{clean}} = A[i_{\text{bins}}]_{\text{max}} - A[i_{\text{bins}}]_{\text{min}}. \tag{4.7}$$

This corresponds to extracting the peak-to-peak amplitude within each time bin. The corresponding output power was then obtained as

$$P[i_{\text{bins}}]_{\text{out}} = A[i_{\text{bins}}]^2_{\text{clean}} \tag{4.8}$$

Applying the same procedure to the off-resonance case yielded the reference power $P[i_{\text{bins}}]_{\text{in}}$. From this, the *cold* spatial mode mixing was calculated using Formula 4.1. The AC signal was used to estimate the *hot* SMM. A spectrogram was computed using the `scipy.signal.spectrogram` function from the 'scipy' Python package (Python version 3.8.8 and 'scipy' version 1.6.2), with the parameters listed in Table 4.4.

Table 4.4: *Parameters used for the `scipy.signal.spectrogram` function.*

Parameter	Value
Sampling frequency (`fs`)	80,000,000
Segment length (`nperseg`)	256
Overlap between segments (`noverlap`)	128
Window type (`window`)	Tukey, shape parameter 0.25

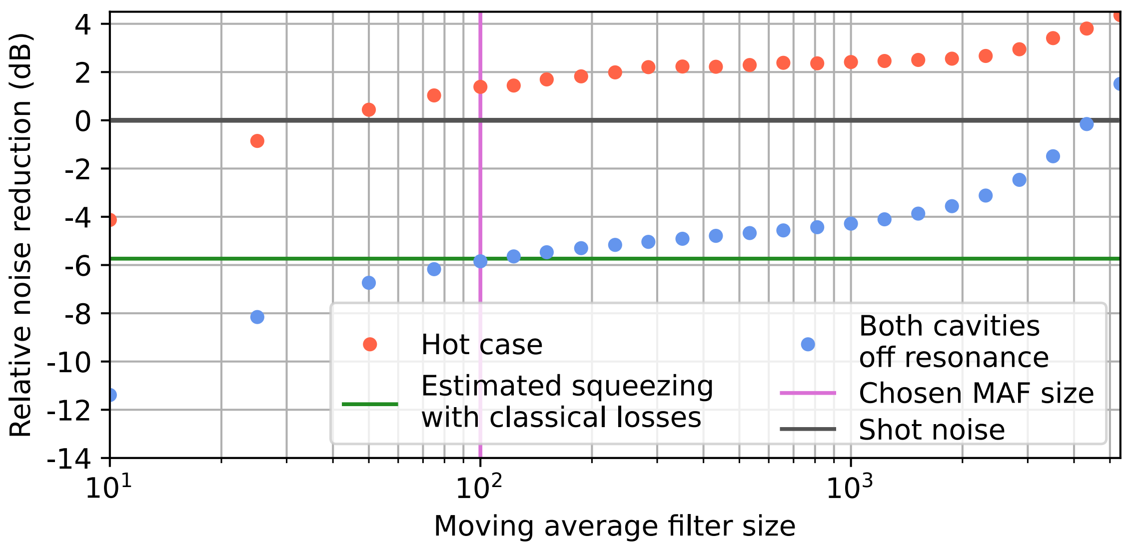

Figure 4.15: *Squeezing as a function of the moving average filter from our spectrogram data at 3.125 MHz (red dots) for the strongest coupling and a reference case with both cavities off-resonance (blue dots). Draft image by M. Sc. Grebien; revised and adapted for this work by the author.*

To reduce statistical noise introduced by the power estimation, the spectrogram was smoothed using a moving average filter (MAF) with a size of 100. Choosing the MAF size has a significant impact on the result, either leading to overestimation or underestimation, as shown in Figure 4.15. Squeezing as a function of MAF size is shown for both the hyperloss regime and the reference case. Two counteracting effects influenced the observed squeezing. First, a small systematic error in the power calculation, arising from the peak-to-peak amplitude extraction described above, led to a slight overestimation of the squeezing level. Second, the moving-average filter applied to the time-series phase angle introduced excessive temporal smoothing, which in turn underestimated the squeezing by averaging out fast phase fluctuations. In other words, a small MAF size results in a larger inaccuracy in power estimation but a smaller phase angle, and vice versa.

Estimating the expected squeezing level from the given classical loss (green line) with the reference case offers a reasonable basis for selecting an appropriate MAF size. Figure 4.16 shows the evolution of the moving average filter size as spectrograms of the hyperloss regime, given as a function of the measurement frequency and the tuning of cavity two. Three regions can be identified:

MAF $\leq$ 100: This range largely overestimates squeezing.

MAF between 100 and 1000: The overestimation steadily decreases until squeezing becomes underestimated.

MAF $\geq$ 1000: Artifacts appear due to averaging over large phase variations combined with a drifting phase of the squeezed state, since the phase was not stabilized to the local oscillator.

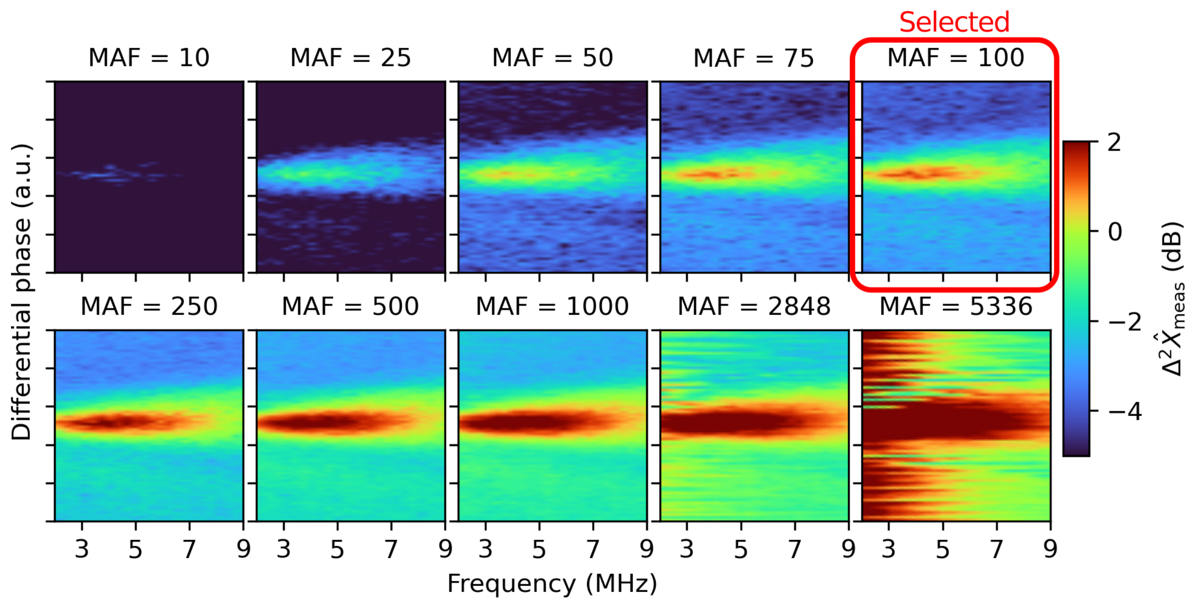

Figure 4.16: *This figure shows squeezing spectrograms for different moving average filter sizes. Further details are explained in the text. To improve the visibility of the color gradient, the color bar was normalized to 30 %.*

4.3.4 Simulation of a Quantum Network

To examine the impact of mode mismatch along a single path within a large-scale quantum network, such as gravitational-wave detectors or continuous-variable cluster-state quantum computers (CVQC), we extend the basic model from the previous chapter, as shown in Figure 4.17(a). Consider a series of mixing components, each described by the coupling strength k_i and differential phase ϕ_i, assuming equal coupling strength $k_i = k$ and equal phase shifts $\phi_i = \phi$ for simplicity. In a real network, these parameters can vary at each node and the system becomes much more complex to simulate. This simplified model is intended to provide an initial intuitive impression. A comprehensive model is still required to predict precise numerical results.

Figure 4.17(b) shows the expected squeezing level as a function of the overall differential phase shift for two different mode mismatch values.

Case one describes a 1 % mismatch per node. After 10 nodes, the mismatches result in 10.2 dB below shot noise, shown as horizontal blue line. This level is sufficient for a fault tolerance level of 10 dB below the shot noise, in CVQC. However, when hot SMM effects are taken into account, as shown as dashed blue lines, this leads to 55 % of the system being insufficient for the fault tolerance. At the same time, careful optimization of the phase can achieve fault threshold with squeezing values around 15 dB, which are not initially expected, and is in the same level range as the initial squeezing.

In the second case, assuming 2 % mismatch per node, the incoherent model predicts insufficient squeezing with respect to the fault tolerance. However, by optimizing the differential phase, the system can recover enough squeezing to reach the tolerance, which in this scenario is achieved in approximately 25 % of the cases.

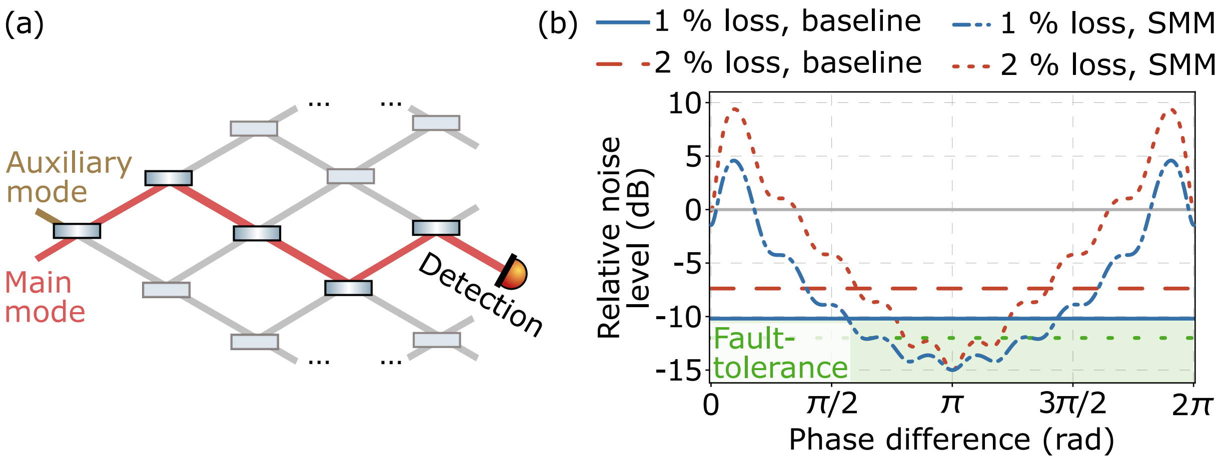

Figure 4.17: *Left side illustrates a simplified setup of the quantum network with multiple mixing components, each experiencing SMM at every node. Right side displays the relative noise level as a function of the overall differential phase for two cases: case one assumes a 1 % loss at each node (blue), while case two assumes a 2 % loss (red). The simulation is simplified by assuming equal coupling strength and phase shift at each component and simulating 10 nodes. Additionally, a tolerance of -10 dB for CVQC is implemented (green area); any squeezing above this tolerance is not considered useful for computation, thereby limiting the operational phase range. In case one, the incoherent loss model predicts sufficient squeezing for fault tolerance (blue baseline). In contrast, case two does not allow fault tolerance (red baseline). Considering hot SMM effects reveals a significant fraction of insufficient squeezing in both cases. However, by optimizing the differential phase, a fault tolerance network for both cases can be achieved. Image originally created by Dr. Korobko and adapted for the present work.*

4.4 Conclusion and Outlook

The work presented in this chapter provides the first experimental demonstration of hyperloss. This is a decoherence mechanism that arises from spatial mode mixing in squeezed light experiments. In contrast to conventional optical loss, which couples the squeezed field to vacuum fluctuations, hyperloss can drive the state into a thermal-like regime and thereby remove all quantum advantage. At the same time, the nature of spatial mode mixing offers a potential solution for hyperloss. It appears only for specific differential phases between the fundamental and higher-order modes, which are generated by mismatched cavities. For other differential phase settings, the effect of mode mismatch becomes very small and the influence of this loss channel on the squeezed field is strongly reduced. This identified the differential phase as the central parameter of spatial mode mixing.

For future experiments, this means that the optical design must explicitly consider the differential phase. Possible strategies include adjusting optical path lengths to compensate accumulated Gouy phase, adding auxiliary cavities to control the model phase, or preparing squeezed higher-order modes to reduce the sensitivity to mode mismatch [92]. Thermal effects, such as thermally induced lensing, can also modify the model phase over time. In such situations, active control using adaptive optics may be required [97].

Spatial mode mixing is therefore relevant for any quantum-correlated network that relies on strongly squeezed light. Although originally theorized for gravitational-wave detectors [91], our results indicate that the same mechanism may contribute to the currently unexplained losses observed in gravitational-wave observatories [96]. This effect is also expected in several other photonic platforms, such as Gottesman–Kitaev–Preskill (GKP) states and modern error-correction schemes [98, 99, 100, 101], as well as in large-scale interferometers [102].

In this work, for simplicity we deliberately introduced only one specific higher-order mode. However, in real experiments, each interface typically introduces an independent set of modes with varying coupling strengths. This complexity complicates the design of hyperloss-immune systems, but the fundamental concept remains unchanged: hyperloss can be managed by controlling the differential phases between the modes. An alternative approach would be to detect higher-order modes individually and attempt to reverse the mixing. This approach is, however, difficult to implement because it would require a large number of detectors and optical paths. For this reason, most experiments focus on phase-engineering techniques such as Gouy-phase control or cavity detuning rather than explicit multimode detection.

Chapter 5

Concluding Remarks and Future Directions

5.1 Summary and Conclusion

Future generations of gravitational-wave observatories aim for significantly higher sensitivity, and thus a larger detection range, than current detectors. Achieving this requires substantial improvements in overall detector performance. Prominent noise sources include thermal noise in the mirror coatings, arising from thermally driven microscopic motion, and quantum noise caused by fluctuations in the photon number. Thermal noise can be mitigated by cryogenic operation of the mirrors, which necessitates new coating materials and therefore new operating wavelengths. Wavelengths in the 2 µm region are considered promising in this context. Operating at such wavelengths requires the development of new technologies, including low-noise, high-power laser systems and audio-band squeezed-light sources for quantum-noise reduction.

This thesis evaluates and optimizes technologies based on 2128 nm, one of the most promising candidates for future cryogenic GWOs, and is structured around three main goals. First, a laser generating up to 20 W at a wavelength of 2128 nm with high mode purity and low laser noise was demonstrated. This was achieved using a degenerate optical parametric oscillator pumped by a 1064 nm high-power laser, whose setup is similar to the configuration used during LIGO's third observation run. Moreover, it was found that the technical noise level of the converted light can be reduced by a factor of two compared to the noise of the pump laser, revealing a previously unreported noise reduction mechanism in this nonlinear conversion process. Second, a shot-noise reduction of more than 3.3 dB in the audio band at 15 kHz was achieved. It was also shown that the dark noise of the corresponding photodiodes can be reduced by more than 15 dB when cooled, although this improvement comes at the cost of reduced quantum efficiency. The self-built Faraday isolator achieved a transmission of 89 % and isolation of 33 dB. Third, it was demonstrated that higher-order spatial modes reflected by an insufficiently mode-matched cavity can couple into the fundamental mode, a general, wavelength-independent effect in squeezed-light systems that can potentially transform the squeezed state into a thermally dominated one and thereby add excess noise. This effect can, however, be mitigated by optimizing the relative phase of the fields.

The experimental performance achieved in this work is ultimately limited by several fundamental and technical constraints. In the high-power laser system, the achievable conversion efficiency is limited by thermal effects in the cavity, which reduce the cavity's frequency stability and thereby restrict the conversion power at a given pump level. For the detection of squeezed states, the quantum efficiency of the photodiodes constitutes an intrinsic limitation. Additional constraints arise from the relatively high dark-noise level of the detection system, primarily originating from the signal analyzer and the homodyne detector, as well as from imperfect spatial mode overlap between the local oscillator and the squeezed field. This overlap can be further affected by the stability of the OPO cavity's degeneracy condition.

Other implementations in the 2 µm region have also seen substantial progress, which provides important context for the results of this work. These advances are complementary rather than competing: for example, systems operating around 1990 nm have achieved shot-noise suppression at lower frequencies, and first high-power prototype sources have been demonstrated, although their performance is currently limited by beam quality, a constraint that does not affect the configuration investigated here. These results therefore fill a gap within the broader 2 µm research landscape, where different wavelengths address different technological constraints. In parallel, a photodiode design concept emerging from semiconductor research predicts quantum efficiencies well above 95 % at wavelengths around 2 µm.

In the broader context of 2 µm platforms, these results represent important steps toward establishing 2128 nm as a promising operating wavelength for future cryogenic GWOs. They provide a foundation for further development of key technologies, including low-noise high-power laser systems, squeezed-light sources, advanced photodetectors, Faraday isolators, and quantum-network architectures based on squeezed states.

5.2 Outlook

Despite the progress achieved in this thesis towards establishing 2128 nm light as a primary wavelength for future cryogenic gravitational-wave observatories, several key technological challenges remain. One major challenge is the realization of a high-power laser source that meets requirements of more than 100 W output power while simultaneously fulfilling stringent constraints on beam quality, stability, and laser noise. Current technologies are limited either by insufficient spatial beam quality, inadequate output power, or laser noise. Another key challenge is the generation and detection of squeezed light at frequencies below 100 Hz, where technical noise sources dominate. This task is further constrained by the limited performance of existing photodetectors at 2 µm, particularly in terms of quantum efficiency and dark noise. In addition, wavelength-independent limitations arise from coupling between different optical modes in squeezed-light–based quantum systems. In particular, mode-mismatch-induced coupling between higher-order and fundamental spatial modes remains insufficiently understood in complex quantum networks and requires further investigation.

To address the aforementioned challenges, several improvements and extensions to the current experimental setup and methodology can be envisioned. For the high-power laser system, a comprehensive redesign of the cavity configuration, including mirror reflectivities, intracavity beam waist, and potentially the nonlinear crystal, could enable significantly higher output power. In addition, improved thermal stabilization of the crystal, for example through enhanced heat sinking or additional Peltier elements, would allow for more precise temperature control than achieved in the present setup. For squeezed-light detection, reducing the dark-noise contribution of the detection chain by further optimizing the spectrum analyzer and the homodyne detector would enable the observation of squeezing at frequencies below 100 Hz. Achieving higher levels of squeezing will require photodiodes with improved semiconductor structures, such as GaInAs/AlInAs-based devices, which have already demonstrated quantum efficiencies of up to 95 %. An alternative approach employs second-harmonic generation of the 2128 nm field to obtain 1064 nm light, where high-quantum-efficiency photodiodes are readily available for squeezing measurements. Alternatively, the squeezed field can be amplified prior to detection, as demonstrated in [103]. Long-term stabilization of the degenerate operating point of the optical parametric oscillator is essential, as it is highly sensitive to environmental perturbations such as temperature fluctuations, humidity, airflow, and optical back reflections. These effects may drive the system away from degeneracy. A promising approach is the use of a 1064 nm reference derived via second-harmonic generation, which can be locked to the pump field for stabilization. Alternative approaches include locking to narrow gas-absorption features; however, no suitable transition at 2128 nm is currently known. Further improvements can be achieved through enhanced environmental shielding, a low-loss Faraday isolator at 2128 nm, and tighter laboratory environmental control. Finally, constructing a quantum network consisting of more than two cavities, as presented in this work, to study mode coupling presents substantial experimental challenges. Each cavity must be precisely controlled, the Gouy phase along the propagation path must be carefully managed, and optical losses must be minimized to maintain measurable levels of squeezing.

If the aforementioned improvements are implemented, a fully operational high-power 2128 nm laser system together with a stable source of strongly squeezed light could be deployed in test facilities such as ETpathfinder [12]. This would allow the verification of expected sensitivity improvements and enable investigations of long-term performance under realistic interferometer conditions. In parallel, further experiments on large-scale optical quantum networks would make it possible to develop a comprehensive theoretical model of mode coupling and quantum-state propagation in multi-cavity networks. This model could then be transferred to and experimentally validated in emerging large-scale optical networks.

The technological developments presented here extend far beyond the field of GWOs. Stable, low-noise, high-power laser sources at 2 μm are of great relevance for material studies, including coating investigations and absorption measurements, as well as for advanced spectroscopic techniques and biological sensing. Furthermore, optical clocks increasingly rely on ultra-low-noise laser systems, and there are proposed clock architectures that are designed to operate at wavelengths around 2 μm. The results of this work may therefore support the development of next-generation frequency standards. In addition, the availability of high-performance laser and squeezing technologies in this wavelength regime opens new possibilities for fundamental research in opto-mechanical systems and quantum communication in a previously unexplored spectral window.

Chapter A

Appendix

A.1 Hitchhiker's Guide to a Degenerate State in an OPO

A degenerate optical parametric oscillator can be operated for various purposes. The degenerate state plays a central role in its use as a laser. In the following, I provide several hints as well as practical tips and tricks that helped us to reliably identify the degenerate state and maintain stable operation.

Finding the Degenerate State

In my experience, there were two reliable methods for identifying the degenerate state.

Temperature tuning: Our crystal was temperature-stabilized using two Peltier elements: a larger Peltier element for the main crystal body and a smaller one for the curved surface (see Figure 2.2). The temperature of the main body (T_1) played a decisive role in locating the degenerate point. The simplest approach was to set both temperatures to the same value ($T_1 = T_2$). We found that this only worked reliably when the system was tuned from higher to lower temperatures; when tuning in the opposite direction, the degenerate state was often missed.

Mechanical impulse: If the temperature is already set and the degenerate state has been observed at least once, a useful trick is to apply a slight mechanical impulse to the optical table; varying the position of this impulse can sometimes help. Another option is to apply an electrical impulse to the cavity piezo, although in my case this method was generally less effective.

Maintaining the Degenerate State

After finding the degenerate state, it can happen that external influences cause it to be lost again. Here is my list of potential sources of interference and how I fixed them, as well as methods to make the degenerate state more robust.

Temperature tuning: As discussed above, setting $T_1 = T_2$ makes it straightforward to find the degenerate state. Once the degeneracy has been located, however, T_2 becomes the more critical parameter, as it increases the stability of the degenerate state in addition to its other functions. In my setup, T_2 was typically set significantly below T_1.

Mechanical impulse: During alignment work, it is sometimes essential to maintain the degenerate state. I observed that pushing the mirror mounts can easily disrupt the degeneracy. My approach was either to push very gently while keeping the pushing hand in as much contact as possible with the optical table, or, more time-consuming but sometimes necessary, to push and then re-establish the degenerate state afterward. Occasionally one adjustment led to another...

Enclosing the table: For critical measurements, it was important to enclose the optical table as completely as possible to prevent air fluctuations or temperature changes from affecting the cavity.

Lab conditions: As implied above, stable room conditions are crucial. This includes maintaining a constant temperature and, ideally, minimizing air currents and other environmental noise sources. In my experience, temperature variations and air currents were the most disruptive factors.

Reflections: Unwanted back-reflections caused by insufficient AR coatings can couple back into the cavity and affect its stability. In particular, they can shift the bistable state (see Source [104, 105]), thereby altering the phase of the light field. More generally, they can also destroy the degeneracy altogether. What helped in my case was using high-quality AR-coated optics, integrating a Faraday isolator into the system, and slightly tilting certain optics so that any residual back-reflection does not directly re-enter the DOPO.

Clarification of the Wavelength Used

In this thesis, the focus is primarily on platforms operating at a wavelength of 2128 nm. But this value is rounded: the datasheet indicates that the pump laser operates at 1064.x nm [106], which the gravitational-wave community traditionally refers to simply as 1064 nm. When the actual pump wavelength is doubled, the resulting value lies between 2128 nm and 2129 nm; more precisely, it is closer to 2129 nm. In this work, however, the pump wavelength was not checked or verified in detail. Moreover, multiple pump lasers from the same company and model were used across the different experiments, so that the effective pump wavelength could differ between setups. Therefore, and also for historical reasons, I decided to use 2128 nm throughout.

A.2 Hamiltonian Analysis of Noise Conversion in a DOPO

The following is a quantum mechanical analysis of noise conversion, calculated by Dr. Mikhael Korobko and included in my thesis for the sake of completeness. This derivation can also be found in our paper [34]. In this appendix, Dr. Mikhael Korobko calculates the conversion efficiency, noise contributions, and the noise transfer factor for the RIN, according to Equation 2.1. Starting with the Hamiltonian for a cavity containing a nonlinear crystal and two intra-cavity fields, signal $\hat{s}$ and pump $\hat{p}$, [107], assuming perfectly matched input and cavity modes and zero loss:

$$\begin{aligned}\mathcal{H} =&\hbar\omega_s\hat{s}^\dagger\hat{s} + \hbar\omega_p\hat{p}^\dagger\hat{p} + i\hbar\chi\left(\hat{p}^\dagger\hat{s}^2 - h.c.\right) + \\ &i\hbar\sqrt{2\gamma_s}\int_{-\infty}^{\infty}\left(\hat{s}^\dagger(\omega)\hat{s}_{\text{in}}(\omega) - h.c.\right)d\omega + \\ &i\hbar\sqrt{2\gamma_p}\int_{-\infty}^{\infty}\left(\hat{p}^\dagger(\omega)\hat{p}_{\text{in}}(\omega) - h.c.\right)d\omega,\end{aligned} \tag{A.1}$$

where $\omega_{s,p}$ is the angular frequency of the respective light field, $\gamma_{s,p}$ is the coupling rate of the cavity for the corresponding light field $\hat{s}_{\text{in}}$, $\hat{p}_{\text{in}}$, and χ denotes the second-order nonlinear coefficient of the crystal. The Heisenberg equations of motion are given by

$$\dot{\hat{s}} = -\gamma_s\hat{s} + \sqrt{2\gamma_s}\hat{s}_{\text{in}} - 2\chi\hat{s}^\dagger\hat{p}, \tag{A.2}$$

$$\dot{\hat{p}} = -\gamma_p\hat{p} + \sqrt{2\gamma_p}\hat{p}_{\text{in}} + \chi\hat{s}^2, \tag{A.3}$$

$$\hat{s}_{\text{out}} = -\hat{s}_{\text{in}} + \sqrt{2\gamma_s}\hat{s}. \tag{A.4}$$

We can linearize these equations by considering small fluctuations around the average amplitude: $\hat{s} = S + \hat{\varsigma}$, $\hat{p} = P + \hat{\rho}$, $\hat{\varsigma} \ll S$, $\hat{\rho} \ll P$.

A.2.1 Calculating Average Power

The average power is determined using the steady-state approximation, which is valid in our application due to the absence of instabilities or chaotic behavior

$$0 = -\gamma_s S + \sqrt{2\gamma_s}S_{\text{in}} - 2\chi S^* P, \tag{A.5}$$

$$0 = -\gamma_p P + \sqrt{2\gamma_p}P_{\text{in}} + \chi S^2, \tag{A.6}$$

$$S_{\text{out}} = -S_{\text{in}} + \sqrt{2\gamma_s}S. \tag{A.7}$$

Solving these equations for P and substituting the result into the equation for S yields:

$$P = \sqrt{\frac{2}{\gamma_p}}P_{\text{in}} + \frac{\chi}{\gamma_p}S^2, \tag{A.8}$$

$$0 = -\gamma_s S + \sqrt{2\gamma_s}S_{\text{in}} - 2\chi\sqrt{\frac{2}{\gamma_p}}S^* P_{\text{in}} - \frac{(\chi)^2}{\gamma_p}S^* S^2. \tag{A.9}$$

Applied to our experiment, which operates without an input field $S_{\text{in}} = 0$, the average signal power is defined as:

$$I_s = \frac{\hbar\omega_s}{2}S^* S = \frac{\hbar\omega_s\gamma_p}{(\chi)^2}\left(-\gamma_s - 2\chi\sqrt{\frac{2}{\gamma_p}}\frac{S^*}{S}P_{\text{in}}\right). \tag{A.10}$$

We choose the phases of the fields such that the power is positive, taking P_{in} to be real and write $S = |S|e^{i\phi}$ with $\phi = \pi/2$. With this, we can determine the condition for the threshold amplitude P_{th} and the corresponding threshold power I_{th}, defined at $I_s = 0$:

$$P_{\text{th}} = \frac{\gamma_s\sqrt{\gamma_p}}{2\sqrt{2}\chi}, \quad I_{\text{th}} = \frac{\hbar\omega_s\gamma_s^2\gamma_p}{8\chi^2} \tag{A.11}$$

The equation for the output signal power (using $S_{\text{out}} = \sqrt{2\gamma_s}S$) can be written as:

$$I_{\text{s,out}} = 2\hbar\omega_s P_{\text{th}}^2\left(\frac{P_{\text{in}}}{P_{\text{th}}} - 1\right) = 4I_{\text{th}}\left(\sqrt{\frac{I_{\text{in}}}{I_{\text{th}}}} - 1\right). \tag{A.12}$$

Conversion efficiency is defined as the ratio of the two powers:

$$\eta = \frac{I_{\text{s,out}}}{I_{\text{in}}} = 4\frac{I_{\text{th}}}{I_{\text{in}}}\left(\sqrt{\frac{I_{\text{in}}}{I_{\text{th}}}} - 1\right). \tag{A.13}$$

It reaches its maximum at $I_{\text{in}} = 4I_{\text{th}}$. In the idealized situation considered here, without losses and with perfect phase matching, the conversion efficiency reaches unity.

A.2.2 Analysis of Relative Intensity Noise

To compute the noise behavior of the system, we linearize the equations of motion, keeping only the terms linear in noise:

$$\hat{\rho} = \sqrt{\frac{2}{\gamma_p}}\hat{\rho}_{\text{in}} - \frac{2\chi}{\gamma_p}S\hat{\varsigma}, \tag{A.14}$$

$$\begin{aligned} 0 = &- \frac{2\chi^2}{\gamma_b}S^2\left(\hat{\varsigma}^\dagger + 2\hat{\varsigma}\right) + 2\chi\sqrt{\frac{2}{\gamma_b}}\left(S\hat{\rho} + P\hat{\varsigma}^\dagger\right) \\ &- \gamma_a\hat{\varsigma} + \sqrt{2\gamma_a}\hat{\varsigma}_{\text{in}}. \end{aligned} \tag{A.15}$$

We define the amplitude and phase quadrature amplitudes as

$$\hat{\varsigma}_a = \frac{\hat{\varsigma} + \hat{\varsigma}^\dagger}{\sqrt{2}}, \quad \hat{\varsigma}_p = \frac{\hat{\varsigma} - \hat{\varsigma}^\dagger}{i\sqrt{2}}. \tag{A.16}$$

The factor $\sqrt{2}$ normalizes the respective ground-state variances of a one-sided spectrum to unity. The solutions for the intra-cavity fields read:

$$\hat{\varsigma}_a = \hat{\varsigma}_{\text{in,a}}\frac{P_{\text{th}}}{\sqrt{2\gamma_p}\left(P_{\text{in}} - P_{\text{th}}\right)} + \hat{\rho}_{\text{in,a}}\frac{\sqrt{P_{\text{th}}}}{\sqrt{\gamma_s\left(P_{\text{in}} - P_{\text{th}}\right)}} \tag{A.17}$$

$$\hat{\varsigma}_p = \hat{\varsigma}_{\text{in,p}}\frac{P_{\text{th}}}{\sqrt{2\gamma_p}P_{\text{in}}} + \hat{\rho}_{\text{in,p}}\frac{\sqrt{P_{\text{th}}\left(P_{\text{in}} - P_{\text{th}}\right)}}{\sqrt{\gamma_s}P_{\text{in}}}. \tag{A.18}$$

Using the input–output relations, we obtain the noise at the cavity output:

$$\hat{\varsigma}_{\text{out,a}} = -\hat{\varsigma}_{\text{in,a}}\frac{P_{\text{in}} - 2P_{\text{th}}}{P_{\text{in}} - P_{\text{th}}} + \hat{\rho}_{\text{in,a}}\frac{\sqrt{2P_{\text{th}}}}{\sqrt{\left(P_{\text{in}} - P_{\text{th}}\right)}} \tag{A.19}$$

$$\hat{\varsigma}_{\text{out,p}} = -\hat{\varsigma}_{\text{in,p}}\frac{P_{\text{in}} - P_{\text{th}}}{P_{\text{in}}} + \hat{\rho}_{\text{in,p}}\frac{\sqrt{2P_{\text{th}}\left(P_{\text{in}} - P_{\text{th}}\right)}}{P_{\text{in}}}. \tag{A.20}$$

We can finally compute the single-sided spectral densities of the noise at Fourier frequencies close to zero:

$$\mathcal{S}^{\mathrm{a}}_{\hat{\varsigma},\mathrm{out}} = \mathcal{S}^{\mathrm{a}}_{\hat{\varsigma},\mathrm{in}} \frac{\left(P_{\mathrm{in}} - 2P_{\mathrm{th}}\right)^2}{\left(P_{\mathrm{in}} - P_{\mathrm{th}}\right)^2} + \mathcal{S}^{\mathrm{a}}_{\hat{\rho},\mathrm{in}} \frac{2P_{\mathrm{th}}}{\left(P_{\mathrm{in}} - P_{\mathrm{th}}\right)}, \tag{A.21}$$

$$\mathcal{S}^{\mathrm{p}}_{\hat{\varsigma},\mathrm{out}} = \mathcal{S}^{\mathrm{p}}_{\hat{\varsigma},\mathrm{in}} \frac{\left(P_{\mathrm{in}} - P_{\mathrm{th}}\right)^2}{P_{\mathrm{in}}^2} + \mathcal{S}^{\mathrm{p}}_{\hat{\rho},\mathrm{in}} \frac{2P_{\mathrm{th}}\left(P_{\mathrm{in}} - P_{\mathrm{th}}\right)}{P_{\mathrm{in}}^2}. \tag{A.22}$$

In the relevant case under consideration, the signal input is in the ground state, whereas the pump field exhibits quantum and technical (and thermal) excitations:

$$\mathcal{S}^{\mathrm{a}}_{\hat{\varsigma},\mathrm{in}} = \mathcal{S}^{\mathrm{p}}_{\hat{\varsigma},\mathrm{in}} = 1, \tag{A.23}$$

$$\mathcal{S}^{\mathrm{a}}_{\hat{\rho},\mathrm{in}} = 1 + \mathcal{S}^{\mathrm{a}}_{\hat{\rho},\mathrm{tech}}, \tag{A.24}$$

$$\mathcal{S}^{\mathrm{p}}_{\hat{\rho},\mathrm{in}} = 1 + \mathcal{S}^{\mathrm{p}}_{\hat{\rho},\mathrm{tech}}, \tag{A.25}$$

where $\mathcal{S}^{\mathrm{a}}_{\hat{\rho},\mathrm{in}}$ and $\mathcal{S}^{\mathrm{p}}_{\hat{\rho},\mathrm{in}}$ denote the spectral densities of amplitude and phase technical noise, respectively. With these definitions Equation A.21 can be rewritten in a more compact form:

$$\mathcal{S}^{\mathrm{a}}_{\hat{\varsigma},\mathrm{out}} = 1 + \frac{P_{\mathrm{th}}^2}{\left(P_{\mathrm{in}} - P_{\mathrm{th}}\right)^2} + \frac{2P_{\mathrm{th}}}{\left(P_{\mathrm{in}} - P_{\mathrm{th}}\right)} \mathcal{S}^{\mathrm{a}}_{\hat{\rho},\mathrm{tech}}, \tag{A.26}$$

$$\mathcal{S}^{\mathrm{p}}_{\hat{\varsigma},\mathrm{out}} = 1 - \frac{P_{\mathrm{th}}^2}{P_{\mathrm{in}}^2} + \frac{2P_{\mathrm{th}}\left(P_{\mathrm{in}} - P_{\mathrm{th}}\right)}{P_{\mathrm{in}}^2} \mathcal{S}^{\mathrm{p}}_{\hat{\rho},\mathrm{tech}}. \tag{A.27}$$

In the first two terms of these expressions, we observe the well-known behavior of strong amplitude anti-squeezing and phase squeezing for pump powers close to threshold, both of which rapidly approach the shot-noise level far above threshold. At the same time, the pump amplitude noise $\mathcal{S}^{\mathrm{a}}_{\hat{\rho},\mathrm{tech}}$ is amplified near threshold and strongly suppressed far above it. Ultimately, regardless of the magnitude of the classical contributions $\mathcal{S}^{\mathrm{a}}_{\hat{\rho},\mathrm{tech}}, \mathcal{S}^{\mathrm{p}}_{\hat{\rho},\mathrm{tech}}$, both are suppressed down to the shot-noise level. Far above threshold, the output field approaches a coherent state, and no squeezing is observed.
To compute the RIN, we define the noise $\hat{n}_{\mathrm{s,out}}$ on the output signal power $I_{\mathrm{s,out}}$:

$$\hat{n}_{\mathrm{s,out}} = \hbar\omega_s S_{\mathrm{out}} \hat{\varsigma}_{\mathrm{out,a}} = \sqrt{2\hbar\omega_s I_{\mathrm{s,out}}}\,\hat{\varsigma}_{\mathrm{out,a}}, \tag{A.28}$$

from which the RIN follows as

$$\mathrm{RIN}_{\mathrm{out}} = \frac{n_{\mathrm{s,out}}}{I_{\mathrm{s,out}}} = \frac{\sqrt{2\hbar\omega_s}}{\sqrt{I_{\mathrm{s,out}}}} \hat{\varsigma}_{\mathrm{out,a}}. \tag{A.29}$$

In the following, we restrict ourselves to the regime of large technical noise, $\mathcal{S}^{\mathrm{a}}_{\hat{\rho},\mathrm{tech}} \gg 1$, which allows us to neglect the contribution from quantum noise. This yields the spectral density of the output noise $\hat{n}_{\mathrm{s,out}}$:

$$\begin{aligned}
\frac{\mathcal{S}_{n,\mathrm{out}}}{I_{\mathrm{s,out}}^2} &= \frac{2\hbar\omega_s}{I_{\mathrm{s,out}}} \mathcal{S}^{\mathrm{a}}_{\hat{\varsigma},\mathrm{out}} \\
&= \frac{2\hbar\omega_s}{I_{\mathrm{s,out}}} \frac{2P_{\mathrm{th}}}{\left(P_{\mathrm{in}} - P_{\mathrm{th}}\right)} \mathcal{S}^{\mathrm{a}}_{\hat{\rho},\mathrm{tech}} \\
&= \frac{2\hbar\omega_s}{I_{\mathrm{s,out}}} \frac{2\sqrt{I_{\mathrm{th}}}}{\left(\sqrt{I_{\mathrm{in}}} - \sqrt{I_{\mathrm{th}}}\right)} \frac{\mathcal{S}_{n,\mathrm{in}}}{2\hbar\omega_p I_{\mathrm{in}}} \\
&= \frac{I_{\mathrm{in}}}{I_{\mathrm{s,out}}} \frac{\sqrt{I_{\mathrm{th}}}}{\sqrt{I_{\mathrm{in}}} - \sqrt{I_{\mathrm{th}}}} \frac{\mathcal{S}_{n,\mathrm{in}}}{I_{\mathrm{in}}^2},
\end{aligned} \tag{A.30}$$

where the spectral density of the technical input noise on the pump power is defined as $\mathcal{S}_{n,\text{in}} = 2\hbar\omega_p I_\text{in}\mathcal{S}^{\text{a}}_{\hat{\rho},\text{tech}}$. We define the noise transfer factor $\mathcal{N}$:

$$\frac{\mathcal{S}_{n,\text{out}}}{I^2_{\text{s,out}}} = \mathcal{N}^2 \frac{\mathcal{S}_{n,\text{in}}}{I^2_{\text{in}}} \tag{A.31}$$

Using this definition together with Equation A.12, we obtain the noise transfer factor (corresponding to Equation 2.5 in the main text):

$$\mathcal{N} = \sqrt{\frac{I_\text{in}}{I_{s,out}} \frac{\sqrt{I_\text{th}}}{\sqrt{I_\text{in}} - \sqrt{I_\text{th}}}} = \frac{1}{2} \frac{\sqrt{I_\text{in}}}{\sqrt{I_\text{in}} - \sqrt{I_\text{th}}}. \tag{A.32}$$

A degenerate optical parametric oscillator pumped far above threshold generates an output field (at twice the wavelength) whose RIN is reduced by a factor of two. Importantly, while the absolute noise is suppressed arbitrarily strongly in the limit of large pump powers, the RIN itself is not: its suppression saturates at a factor of 2.

A.3 High-Power Laser Comparison

Table A.1 lists the high-power laser systems considered in this work, together with their key parameters. Some data in the literature are incomplete; the author compiled the table to the best of his knowledge.

Table A.1: *Comparison of high-power lasers in the 2 μm range.*

Index	Method	Wavelength (nm)	Power (W)	M^2	Year	Source
Nonlinear Conversion						
0	DOPO	2128	29	-	2025	this work
1	OPO	2000	20	8–16	2000	[20]
Active Gain Medium						
2	Tm:YAG	2020	77.1	-	2013	[108]
3	Ho:YVO_4	2052	3.9	1.09	2014	[109]
4	Ho:$LuLiF_4$	2053	5.4	1.1	2010	[110]
5	Tm:YAG	2070	115	15	2013	[108]
6	Ho:YAG	2090	38	1.48	2015	[111]
7	Ho:YAG	2097	13.4	1.09	2021	[112]
8	Ho:YAG	2097	65	1.3	2017	[113]
9	Ho:YAP	2117	107	2.9	2020	[114]
Thin-Disk Lasers						
10	Tm:YAG	2014	24	11.7	2018	[115]
11	Ho:YLF	2051	26.5	1.1	2025	[116]
12	Ho:YAG	2090	15	2	2011	[117]
13	Ho:YAG	2090	112	1.1	2021	[118]
14	Ho:YAG	2095	50	5.3	2018	[115]
Fiber Lasers						
15	Tm:MOPA	1930	327.5	-	2016	[119]
16	Tm:oscillator	1940	185	-	2024	[120]
17	Tm:MOPA	1940	273	1.2	2024	[121]
18	Tm:oscillator	1940	400	1.1	2007	[122]
19	Tm:MOPA	1941	790	2.7	2018	[123]
20	Tm:MOPA	1943	920	1.18	2023	[124]
21	Tm:oscillator	1950	170	1.01	2015	[125]
22	Tm:MOPA	1950	1100	1.1	2021	[126]
23	Tm:MOPA	1965	255	-	2015	[127]
24	Tm:MOPA	1970	102	-	2013	[128]
25	Tm:MOPA	1970	255	-	2015	[127]
26	Tm:oscillator	1970	567	2.6	2016	[129]
27	Tm:MOPA	1980	270	-	2015	[127]
28	Tm:MOPA	1981	530	1.3	2020	[130]
29	Tm:MOPA	1990	265	-	2015	[127]

Continued on next page

Index	Method	Wavelength (nm)	Power (W)	M^2	Year	Source
30	Tm:MOPA	2000	260	-	2015	[127]
31	Tm:oscillator	2000	226	2.2	2008	[131]
32	Tm:MOPA	2000	253	2	2015	[132]
33	Tm:MOPA	2001	210	-	2014	[133]
34	Tm:oscillator	2004	15.2	-	2019	[134]
35	Tm:oscillator	2009	15.8	-	2019	[134]
36	Tm:oscillator	2013	16.2	-	2019	[134]
37	TmHo:oscillator	2015	38.3	-	2020	[135]
38	Tm:oscillator	2019	137	1.21	2012	[136]
39	Tm:oscillator	2022	20.9	-	2019	[134]
40	Tm:oscillator	2025	22.6	-	2019	[134]
41	Tm:MOPA	2034	441	1.2	2024	[121]
42	Tm:oscillator	2036	24.4	-	2019	[134]
43	TmHo:oscillator	2036	60.7	-	2020	[135]
44	Tm:MOPA	2036	937	-	2024	[137]
45	Tm:oscillator	2040	300	-	2009	[138]
46	Tm:MOPA	2040	608	1.05	2009	[139]
47	Tm:oscillator	2040	885	-	2009	[138]
48	TmHo:oscillator	2050	181	-	2020	[140]
49	Tm:MOPA	2050	205	-	2021	[141]
50	TmHo:oscillator	2085	34.5	-	2020	[135]
51	TmHo:oscillator	2090	29.6	-	2020	[135]
52	Tm:oscillator	2090	193	-	2024	[120]
53	TmHo:oscillator	2090	195	1.08	2021	[142]
54	TmHo:oscillator	2095	23.5	-	2020	[135]
55	TmHo:oscillator	2100	262	1.15	2022	[143]
56	TmHo:oscillator	2103	20.6	-	2020	[135]
57	TmHo:oscillator	2105	37.7	-	2020	[135]
58	TmHo:oscillator	2105	83	1.5	2007	[144]
59	Ho:MOPA	2106	265	-	2014	[145]
60	TmHo:oscillator	2114	30.1	-	2020	[135]
61	Ho:oscillator	2120	62	1.2	2022	[146]
62	Ho:oscillator	2120	90	-	2020	[147]
63	Tm:oscillator	2120	132	-	2024	[120]
64	Ho:oscillator	2125	140	1.4	2013	[148]

A.4 Homodyne Detector Circuit Diagrams

In this appendix, the circuit diagrams of the homodyne detector employed in this study are presented. The schematic was developed during my Master's thesis and subsequently optimized for low-frequency operation within the scope of the current work.

This circuit board is notable because it provides a variable reverse bias for each photodiode (Figure A.1), enabling the optimization of dark noise. The schematic of the current subtraction stage is shown in Figure A.2, illustrating that no amplification stage is included in the DC path. The components used are listed in Table A.2, excluding those of the AC path, as this signal was dominated by noise and was therefore not utilized.

Table A.2: *List of key components highlighted in the circuit schematic.*

Part-number	D3	N1 = N2	P3 = P4	N3	C9	R3
Device	1N4007	OP177	100 kΩ	AD797	6.8 pF	5.11 kΩ

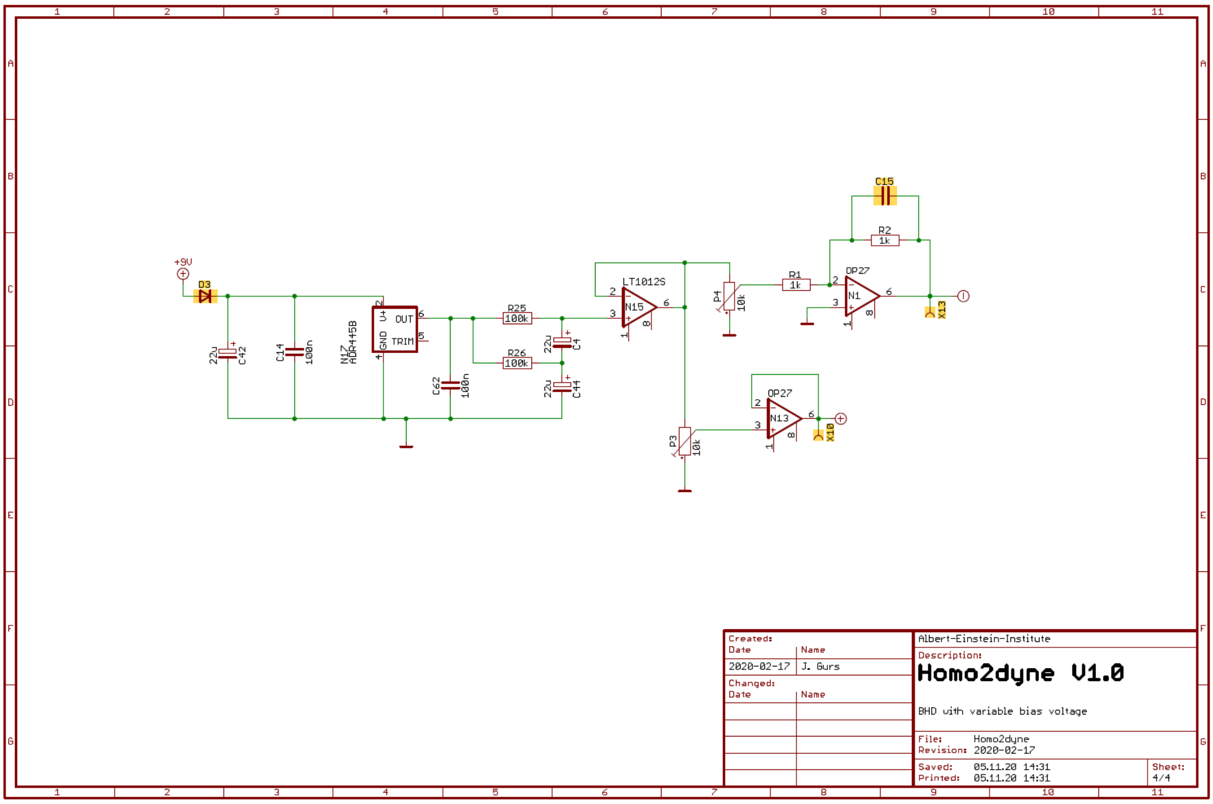

Figure A.1: *Shown here is the circuit diagram used to adjust the photodiode reverse bias in the homodyne detector.*

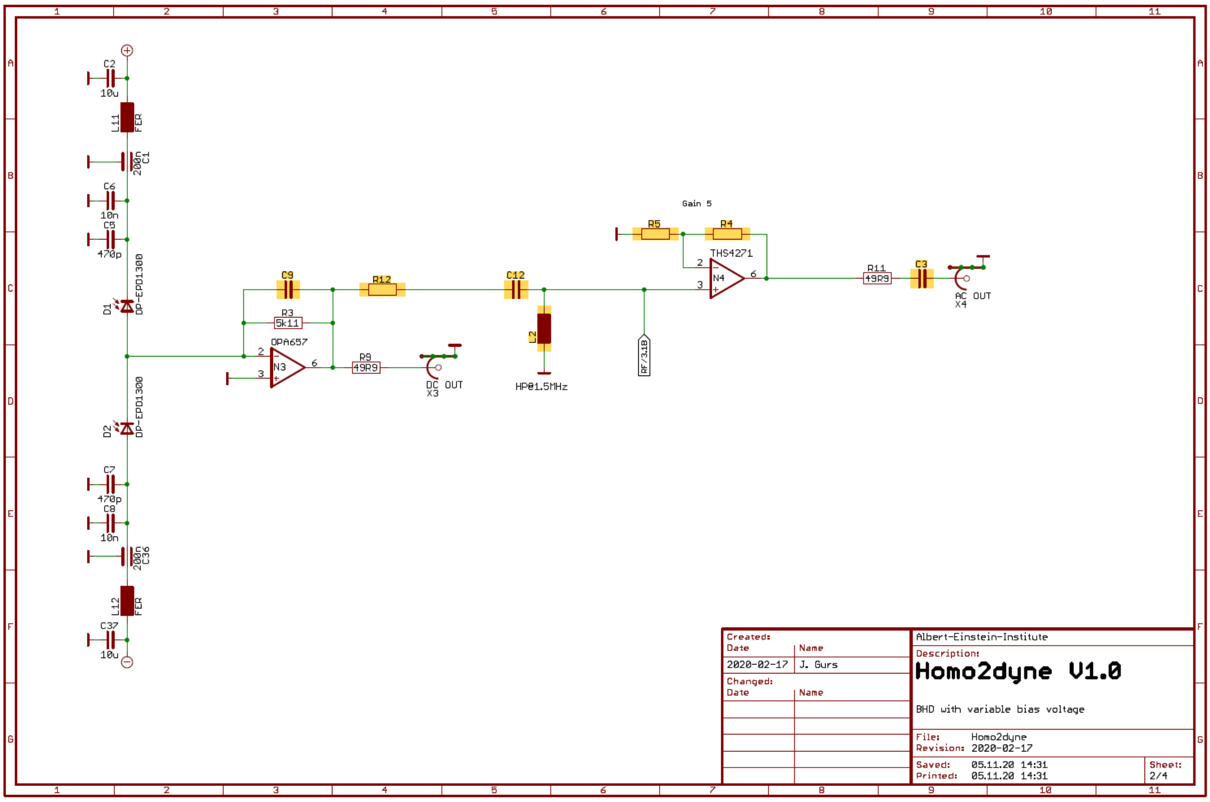

Figure A.2: *The diagram depicts the circuitry employed for the subtraction of the photodiode currents in the homodyne detector.*

A.5 Additional Information for Hyperloss

The figure below is an expanded version of Figure 4.11. In this representation, the expected squeezing variance was calculated from the beat between the weak control beam and the local oscillator (referred to as cold case) using Equation 3.8. The resulting values were then plotted together with the measured squeezing (referred to as hot case). It can be observed that the calculated squeezing variance follows a similar trend as the measured squeezing variance, with the important distinction that it does not enter the hyperloss regime (as shown in the left panel). In the right-hand panel, the calculated squeezing exhibits only a single peak, whereas the measured squeezing variance shows two. This difference is inherent to the physical nature of spatial mode mixing.

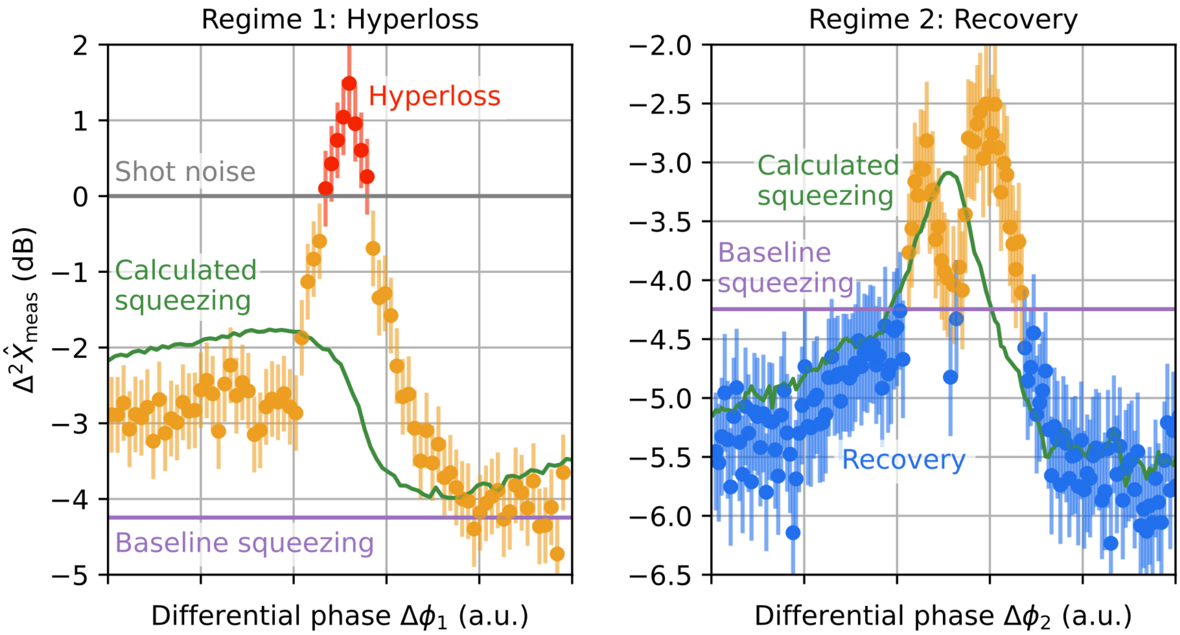

Figure A.3: *Comparison between the calculated squeezing variance arising from the beat between a weak control beam (cold case) and the measured squeezing variance in the hot case.*

Chapter B

List of Abbreviations

Abbreviation	Meaning
AGM	Active gain medium
aLIGO	Advanced Laser Interferometer Gravitational-Wave Observatory
AOI	Angle of incidence
AR	Anti-reflection
AVG	Average
BS	Beam splitter
CVQC	Cluster-state quantum computers
DAQ	Data acquisition system
DE	Detection efficiency
DFG	Difference-frequency generation
DPDC	Degenerate parametric down-conversion
DOPO	Degenerate optical parametric oscillation
DBS	Dichroic beam splitter
EOM	Electro-optic modulator
ET	Einstein Telescope
FI	Faraday isolator
FR	Faraday rotator
FSR	Free spectral range
FM	Fundamental mode
FWHM	Full width at half maximum
GWO	Gravitational-wave observatory
HOM	Higher-order modes
HR	High-reflective
KAGRA	Kamioka Gravitational Wave Detector
LG	Laguerre-Gauss mode
LIGO	Laser Interferometer Gravitational-Wave Observatory
LO	Local oscillator
LVK	LIGO-Virgo-KAGRA
MAF	Moving average filter
NLC	Nonlinear conversion

Continued on next page

Abbreviation	**Meaning**
NPRO	Non-planar ring oscillator
OPO	Optical parametric oscillator
PBS	Polarizing beam splitter
PD	Photodiode
PDC	Parametric down-conversion
PPKTP	Periodically poled potassium titanyl phosphate
PM	Power meter
PHD	Pound–Drever–Hall
PRM	Power recycling mirror
QE	Quantum efficiency
RBW	Resolution bandwidth
RIN	Relative intensity noise
SA	Signal Analyzer
SFG	Sum-frequency generation
SHG	Second-harmonic generation
SMM	Spatial mode mixing
SNR	Signal to noise ratio
SRM	Signal recycling mirror
TDL	Thin-disk laser
TEM	Transverse electromagnetic mode
PVC	Polyvinyl chloride
VBW	Video bandwidth
s/p-polarization	Polarization perpendicular/parallel to the beam plane

Chapter C

List of Figures

Chapter D

List of Tables

Chapter E

Bibliography

[1] Nobel Prize Outreach, "The Nobel Prize in Physics 2017." URL: https://www.nobelprize.org/prizes/physics/2017/summary/ [Accessed 02-03-2026].

[2] M. Pitkin, S. Reid, S. Rowan, and J. Hough, "Gravitational Wave Detection by Interferometry (Ground and Space)," *Living Reviews in Relativity*, vol. 14, p. 5, jul 2011. doi:10.12942/lrr-2011-5.

[3] "pyGWINC." https://git.ligo.org/gwinc/pygwinc. [Accessed 08-06-2026].

[4] J. Steinlechner, I. W. Martin, A. S. Bell, J. Hough, M. Fletcher, P. G. Murray, R. Robie, S. Rowan, and R. Schnabel, "Silicon-Based Optical Mirror Coatings for Ultrahigh Precision Metrology and Sensing," *Physical Review Letters*, vol. 120, p. 263602, jun 2018. doi:10.1103/PhysRevLett.120.263602.

[5] R. X. Adhikari and et al., "A cryogenic silicon interferometer for gravitational-wave detection," *Classical and Quantum Gravity*, vol. 37, jul 2020. doi:10.1088/1361-6382/ab9143.

[6] D. Reitze, R. X. Adhikari, S. Ballmer, B. Barish, L. Barsotti, G. Billingsley, D. A. Brown, Y. Chen, D. Coyne, R. Eisenstein, M. Evans, P. Fritschel, E. D. Hall, A. Lazzarini, G. Lovelace, J. Read, B. S. Sathyaprakash, D. Shoemaker, J. Smith, C. Torrie, S. Vitale, R. Weiss, C. Wipf, and M. Zucker, "Cosmic Explorer: The U.S. Contribution to Gravitational-Wave Astronomy beyond LIGO," jul 2019. arXiv: https://arxiv.org/abs/1907.04833.

[7] ET Steering Committee Editorial, "Design Report Update 2020 for the Einstein Telescope," September 2020. URL: https://www.einsteintelescope-emr.eu/wp-content/uploads/2024/05/ET-0007B-20_ETDesignReportUpdate2020.pdf [Accessed 04-03-2026].

[8] G. L. Mansell, T. G. McRae, P. A. Altin, M. J. Yap, R. L. Ward, B. J. Slagmolen, D. A. Shaddock, and D. E. McClelland, "Observation of Squeezed Light in the 2 μm Region," *Physical Review Letters*, vol. 120, p. 203603, may 2018. doi:10.1103/PhysRevLett.120.203603.

[9] I. Snetkov and A. Yakovlev, "Faraday isolator based on crystalline silicon for 2-µm laser radiation," *Opt. Lett.*, vol. 47, pp. 1895–1898, apr 2022. doi:10.1364/OL.452218.

[10] M. J. Yap, D. W. Gould, T. G. McRae, P. A. Altin, N. Kijbunchoo, G. L. Mansell, R. L. Ward, D. A. Shaddock, B. J. J. Slagmolen, and D. E. McClelland, "Squeezed vacuum phase control at 2 μm," *Optics Letters*, vol. 44, p. 5386, nov 2019. doi:10.1364/ol.44.005386.

[11] C. Darsow-Fromm, J. Gurs, R. Schnabel, S. Steinlechner, S. Steinlechner, and S. Steinlechner, "Squeezed light at 2128 nm for future gravitational-wave observatories," *Optics Letters*, vol. 46, pp. 5850–5853, dec 2021. doi:10.1364/OL.433878.

[12] ETpathfinder Team, "ETpathfinder Design Report," jan 2020. URL: https://www.etpathfinder.eu/wp-content/uploads/2020/03/ETpathfinder-Design-Report.pdf [Accessed 22-04-2026].

[13] N. Bode, J. Briggs, X. Chen, M. Frede, P. Fritschel, M. Fyffe, E. Gustafson, M. Heintze, P. King, J. Liu, J. Oberling, R. L. Savage, A. Spencer, and B. Willke, "Advanced LIGO Laser Systems for O3 and Future Observation Runs," *Galaxies*, vol. 8, dec 2020. doi:10.3390/galaxies8040084.

[14] M. Evans, L. Barsotti, P. Kwee, J. Harms, and H. Miao, "Realistic filter cavities for advanced gravitational wave detectors," *Phys. Rev. D*, vol. 88, p. 022002, jul 2013. doi:10.1103/PhysRevD.88.022002.

[15] N. Ismail, C. C. Kores, D. Geskus, and M. Pollnau, "Fabry-Pérot resonator: spectral line shapes, generic and related Airy distributions, linewidths, finesses, and performance at low or frequency-dependent reflectivity," *Opt. Express*, vol. 24, pp. 16366–16389, jul 2016. doi:10.1364/OE.24.016366.

[16] M. Gmelch and S. Reineke, *Durchblick in Optik: Mit Phänomenen, Formeln und Fragen zum Verständnis*. Berlin, Heidelberg: Springer Spektrum, 2019. doi:10.1007/978-3-662-58939-7.

[17] R. W. Boyd, *Nonlinear Optics*. Elsevier, 2 ed., 2003. ISBN: 9780080479750.

[18] H.-A. Bachor and T. C. Ralph, *A Guide to Experiments in Quantum Optics*, vol. 53. 2019. ISBN: 9788578110796.

[19] L.-A. Wu, M. Xiao, and H. J. Kimble, "Squeezed states of light from an optical parametric oscillator," *J. Opt. Soc. Am. B*, vol. 4, pp. 1465–1475, oct 1987. doi:10.1364/JOSAB.4.001465.

[20] R. F. Wu, P. B. Phua, K. S. Lai, Y. L. Lim, E. Lau, A. Chng, C. Bonnin, and D. Lupinski, "Compact 21-W 2-μm intracavity optical parametric oscillator," *Optics Letters*, vol. 25, pp. 1460–1462, oct 2000. doi:10.1364/OL.25.001460.

[21] G. Arisholm, E. Lippert, G. Rustad, and K. Stenersen, "Efficient conversion from 1 to 2 μm by a KTP-based ring optical parametric oscillator," *Optics Letters*, vol. 27, pp. 1336–1338, aug 2002. doi:10.1364/OL.27.001336.

[22] C. R. Phillips, J. S. Pelc, and M. M. Fejer, "Continuous wave monolithic quasi-phase-matched optical parametric oscillator in periodically poled lithium niobate," *Optics Letters*, vol. 36, pp. 2973–2975, aug 2011. doi:10.1364/OL.36.002973.

[23] C. Darsow-Fromm, M. Schröder, J. Gurs, R. Schnabel, and S. Steinlechner, "Highly-efficient generation of coherent light at 2128 nm via degenerate optical-parametric oscillation," *Optics Letters*, vol. 45, pp. 6194–6197, aug 2020. doi:10.1364/OL.405396.

[24] B. Tohermes, *Generation and fiber-based distribution of high-bandwidth entanglement for continuous variable quantum key distribution*. Phd dissertation, Universität Hamburg, 2025. URL: https://ediss.sub.uni-hamburg.de/handle/ediss/11982 [Accessed 06-03-2026].

[25] C. C. Gerry and P. L. Knight, *Introductory Quantum Optics*. Cambridge University Press, 2004. ISBN: 9780521527354.

[26] R. Schnabel, "Squeezed states of light and their applications in laser interferometers," *Physics Reports*, vol. 684, pp. 1–51, apr 2017. doi:10.1016/j.physrep.2017.04.001.

[27] A. Scönbeck, F. Thies, and R. Schnabel, "13 dB squeezed vacuum states at 1550 nm from 12 mW external pump power at 775 nm," *Optics Letters*, vol. 43, p. 110, jan 2018. doi:10.1364/OL.43.000110.

[28] LIGO Scientific Collaboration and Virgo Collaboration and KAGRA Collaboration, "The LSC Instrument Science White Paper (2025 edition)," Tech. Rep. T2400407–v1, LIGO Scientific Collaboration, California Institute of Technology & Massachusetts Institute of Technology. URL: `https://dcc.ligo.org/DocDB/0197/T2400407/001/Instrument_Science_White_Paper_2025_v1.pdf`.

[29] A. Boudkhil, A. Ouzzani, and B. Soudini, "Analysis of Fundamental Photodetection Noises and Evaluation of PIN and APD Photodiodes Performances using an Optical High Debit Transmission Chain Simulated by Optisystem," *International Journal of Computer Applications*, vol. 115, pp. 21–29, apr 2015. doi:10.5120/20252-2620.

[30] Thorlabs Inc., "Spec sheet photodiode: FDG50." `https://media.thorlabs.com/globalassets/items/f/fd/fdg/fdg50/24704-s01.pdf?v=0116113132`, 2026. [Accessed 09-06-2026].

[31] S. Ghosh, K. Fu, F. Kargar, S. Rumyantsev, Y. Zhao, and A. A. Balandin, "Low-frequency noise characteristics of GaN vertical PIN diodes—Effects of design, current, and temperature," *Applied Physics Letters*, vol. 119, p. 243505, dec 2021. doi:10.1063/5.0075498.

[32] R. C. Eckardt, C. D. Nabors, W. J. Kozlovsky, and R. L. Byer, "Optical parametric oscillator frequency tuning and control," *J. Opt. Soc. Am. B*, vol. 8, pp. 646–667, mar 1991. doi:10.1364/JOSAB.8.000646.

[33] C. D. Nabors, S. T. Yang, T. Day, and R. L. Byer, "Coherence properties of a doubly resonant monolithic optical parametric oscillator," *J. Opt. Soc. Am. B*, vol. 7, pp. 815–820, may 1990. doi:10.1364/JOSAB.7.000815.

[34] J. Gurs, M. Korobko, C. Darsow-Fromm, S. Steinlechner, and R. Schnabel, "Coherent noise suppression at high-efficiency wavelength doubling for high-precision experiments," *Optics and Laser Technology*, vol. 183, p. 112179, may 2025. doi:10.1016/j.optlastec.2024.112179.

[35] J. Gurs, N. Bode, C. Darsow-Fromm, H. Vahlbruch, P. Gewecke, S. Steinlechner, B. Willke, and R. Schnabel, "Conversion of 30 W laser light at 1064 nm to 20 W at 2128 nm and comparison of relative power noise," *Classical and Quantum Gravity*, vol. 41, p. 245008, nov 2024. doi:10.1088/1361-6382/ad8f8b.

[36] A. Schönbeck, *Compact squeezed-light source at 1550 nm*. PhD thesis, Universität Hamburg, 2018. URL: `https://ediss.sub.uni-hamburg.de/handle/ediss/7811` [Accessed 06-03-2026].

[37] R. W. P. Drever, J. L. Hall, F. V. Kowalski, J. Hough, G. M. Ford, A. J. Munley, and H. Ward, "Laser phase and frequency stabilization using an optical resonator," *Applied Physics B*, vol. 31, pp. 97–105, jun 1983. doi:10.1007/BF00702605.

[38] E. D. Black, "An introduction to Pound–Drever–Hall laser frequency stabilization," *American Journal of Physics*, vol. 69, p. 79, jan 2001. doi:10.1119/1.1286663.

[39] M. Hagemann, *Development of a Tunable and Compact Source of Squeezed States of Light*. PhD thesis, Universität Hamburg, 2024. URL: `https://ediss.sub.uni-hamburg.de/handle/ediss/10969` [Accessed 06-03-2026].

[40] C. Darsow-Fromm, *Squeezed light at 2128 nm for future gravitational-wave observatories*. PhD thesis, Universität Hamburg, 2022. URL: `https://ediss.sub.uni-hamburg.de/handle/ediss/9877` [Accessed 04-03-2026].

[41] G. Breitenbach, S. Schiller, and J. Mlynek, "81% Conversion efficiency in frequency-stable continuous-wave parametric oscillation," *J. Opt. Soc. Am. B*, vol. 12, pp. 2095–2101, nov 1995. doi:10.1364/JOSAB.12.002095.

[42] M. Martinelli, K. S. Zhang, T. Coudreau, A. Maître, and C. Fabre, "Ultra-low threshold CW triply resonant OPO in the near infrared using periodically poled lithium niobate," *Journal of Optics A: Pure and Applied Optics*, vol. 3, p. 300, jul 2001. doi:10.1088/1464-4258/3/4/312.

[43] S. Brosnan and R. Byer, "Optical parametric oscillator threshold and linewidth studies," *IEEE Journal of Quantum Electronics*, vol. 15, pp. 415–431, jun 1979. doi:10.1109/JQE.1979.1070027.

[44] S. Schiller, K. Schneider, and J. Mlynek, "Theory of an optical parametric oscillator with resonant pump and signal," *J. Opt. Soc. Am. B*, vol. 16, pp. 1512–1524, sep 1999. doi:10.1364/JOSAB.16.001512.

[45] C. Darsow-Fromm, L. Dekant, S. Grebien, M. Schröder, R. Schnabel, and S. Steinlechner, "NQontrol: An open-source platform for digital control-loops in quantum-optical experiments," *Review of Scientific Instruments*, vol. 91, p. 035114, mar 2020. doi:10.1063/1.5135873.

[46] Reicol Crystal, "Raicol Crystals, ppKTP Crystal." `https://raicol.com/product/quantum-components/ppktp`. [Accessed 23-09-2025].

[47] F. Thies, N. Bode, P. Oppermann, M. Frede, B. Schulz, and B. Willke, "Nd:YVO4 high-power master oscillator power amplifier laser system for second-generation gravitational wave detectors," *Opt. Lett.*, vol. 44, pp. 719–722, feb 2019. doi:10.1364/OL.44.000719.

[48] Varian and Agilent, "Preliminary Performance Data: UV-VIS-NIR Cary 4000, 5000, 6000i Spectrophotometers," 2004. `https://www.agilent.com/cs/library/brochures/5990-7786EN_Cary-4000-5000-6000i-UV-Vis-NIR_Brochure.pdf` [Accessed 05-03-2026].

[49] Thorlabs, "Thorlabs Beam Beam Analyzing Software: BP209-VIS(/M), BP209IR1(/M), and BP209-IR2(/M) with M2MS(-AL) Operating Manual," 2023. URL: `https://www.thorlabs.com/newgrouppage9.cfm?objectgroup_ID=804` [Accessed 05-03-2026].

[50] J. Petermann, C. Darsow-Fromm, and S. Steinlechner, "las-nq / openqlab · gitlab." URL: `https://gitlab.rrz.uni-hamburg.de/las-nq/openqlab` [Accessed 06-03-2026].

[51] T. Braunschweig, "FTIR Spectrometers." `https://www.tu-braunschweig.de/index.php?eID=dumpFile&t=f&f=47858&token=5af4dc0f42aa0263a44ba4fb97cdba007321db4c`. [Accessed 06-10-2025].

[52] A. V. Smith, J. J. Smith, and B. T. Do, "Thermo-optic and thermal expansion coefficients of RTP and KTP crystals over 300-350 K," jul 2016. arXiv: `https://arxiv.org/abs/1607.03964`.

[53] J. A. Giordmaine and R. C. Miller, "Tunable Coherent Parametric Oscillation in $LiNbO_3$ at Optical Frequencies," *Phys. Rev. Lett.*, vol. 14, pp. 973–976, jun 1965. doi:10.1103/PhysRevLett.14.973.

[54] TKS, "NTC Thermistor TTS Series." https://www.datasheet.live/pdfviewer?url=https%3A%2F%2Fpdf.datasheet.live%2Ffd9baed1%2Fthinking.com.tw%2FTTS1A103F34D3RY.pdf. [Accessed 06-10-2025].

[55] Ophir, "3A-QUAD BeamTrack Broadband Laser Position Sensor." https://www.ophiropt.com/de/f/3a-quad-laser-position-sensor. [Accessed 06-10-2025].

[56] J. Steinlechner, *Optical Absorption Measurements for Third Generation Gravitational Wave Detectors*. PhD thesis, Gottfried Wilhelm Leibniz Universität Hannover, 2013. doi:10.15488/8175.

[57] N. Lastzka, *Numerical modelling of classical and quantum effects in non-linear optical systems*. PhD thesis, Gottfried Wilhelm Leibniz Universität Hannover, 2010. doi:10.15488/7447.

[58] R. Paschotta, "Noise in Laser Technology," *Optik & Photonik*, vol. 5, pp. 55–57, apr 2010. doi:10.1002/opph.201190083.

[59] M. Hagemann, J. Zander, A. Schönbeck, and R. Schnabel, "10-dB squeeze laser tuneable over half a nanometer around 1550 nm," *Opt. Express*, vol. 32, pp. 7954–7958, feb 2024. doi:10.1364/OE.507573.

[60] T. Meier, *High-Power CW Green Lasers for Optical Metrology and Their Joint Benefit in Particle Physics Experiments*. PhD thesis, Gottfried Wilhelm Leibniz Universität Hannover, 2011. doi:10.15488/7701.

[61] N. Bode, *Characterization, Stabilization and Coherent Combination of High Power Laser Beams for Gravitational Wave Detectors*. PhD thesis, Gottfried Wilhelm Leibniz Universität Hannover, 2023. doi:10.15488/13693.

[62] H. Vahlbruch, F. Meylahn, and B. Willke, "Characterization of non-planar ring oscillators at a wavelength of 1064 nm for high precision metrology," *Review of Scientific Instruments*, vol. 96, p. 113001, nov 2025. doi:10.1063/5.0298918.

[63] H. Grote, K. Danzmann, K. L. Dooley, R. Schnabel, J. Slutsky, and H. Vahlbruch, "First Long-Term Application of Squeezed States of Light in a Gravitational-Wave Observatory," *Physical Review Letters*, vol. 110, p. 181101, may 2013. doi:10.1103/PhysRevLett.110.181101.

[64] F. Acernese and et al., "Increasing the Astrophysical Reach of the Advanced Virgo Detector via the Application of Squeezed Vacuum States of Light," *Physical Review Letters*, vol. 123, p. 231108, dec 2019. doi:10.1103/PhysRevLett.123.231108.

[65] M. Tse and et al., "Quantum-Enhanced Advanced LIGO Detectors in the Era of Gravitational-Wave Astronomy," *Physical Review Letters*, vol. 123, p. 231107, dec 2019. doi:10.1103/PhysRevLett.123.231107.

[66] J. Gurs, N. Sültmann, C. Darsow-Fromm, S. Steinlechner, and R. Schnabel, "Photodiode quantum efficiency for 2-μm light in the signal band of gravitational wave detectors," *Comptes Rendus. Physique*, vol. 27, pp. 41–48, jan 2026. doi:10.5802/crphys.269.

[67] K. J. Carothers, R. A. Norwood, and J. Pyun, "High Verdet Constant Materials for Magneto-Optical Faraday Rotation: A Review," *Chemistry of Materials*, vol. 34, pp. 2531–2544, mar 2022. doi:10.1021/acs.chemmater.2c00158.

[68] RefractiveIndex.INFO, "Refractive Index Database: CDGM H-FK61." https://refractiveindex.info/?shelf=specs&;book=CDGM-optical&page=H-FK61, 2026. [Accessed 03-02-2026].

[69] C. Semprebon, *Wetting on Anisotropically Patterned and Rough Surfaces*. PhD thesis, Università degli Studi di Padova, 2009. URL: https://hdl.handle.net/20.500.14242/109446 [Accessed 06-03-2026].

[70] Coherent Inc., "MAKROS Optomechanical Components – Datasheet." https://www.coherent.com/resources/datasheet/components-and-accessories/makros-ds.pdf, 2026. [Accessed 03-02-2026].

[71] Agiltron Inc., "Free Space 2000 nm Isolator – Datasheet." https://agiltron.com/dlc/specs/Free%20Space%202000nm%20isolator.pdf, 2026. [Accessed 03-02-2026].

[72] Thorlabs Inc., "IR Free-Space Optical Isolators (1110–2100 nm)." https://www.thorlabs.com/ir-free-space-isolators-1110---2100-nm?tabName=Overview, 2026. [Accessed 03-02-2026].

[73] E. Genin, M. Mantovani, G. Pillant, C. D. Rossi, L. Pinard, C. Michel, M. Gosselin, and J. Casanueva, "Vacuum-compatible low-loss Faraday isolator for efficient squeezed-light injection in laser-interferometer-based gravitational-wave detectors," *Appl. Opt.*, vol. 57, pp. 9705–9713, nov 2018. doi:10.1364/AO.57.009705.

[74] S. M. Sze and K. K. Ng, *Physics of Semiconductor Devices*. Wiley-Interscience, 3rd ed., 2007. doi:10.1002/0470068329.

[75] Thorlabs, "Thorlabs FD05D." https://www.thorlabs.com/item/FD05D. [Accessed 29-12-2025].

[76] H. Vahlbruch, M. Mehmet, K. Danzmann, and R. Schnabel, "Detection of 15 dB Squeezed States of Light and their Application for the Absolute Calibration of Photoelectric Quantum Efficiency," *Phys. Rev. Lett.*, vol. 117, p. 110801, sep 2016. doi:10.1103/PhysRevLett.117.110801.

[77] F. Meylahn, B. Willke, and H. Vahlbruch, "Squeezed States of Light for Future Gravitational Wave Detectors at a Wavelength of 1550 nm," *Phys. Rev. Lett.*, vol. 129, p. 121103, sep 2022. doi:10.1103/PhysRevLett.129.121103.

[78] T. J. Kuhlbusch, M. Zeoli, R. Joppe, C. Collette, T. Hebbeker, J. V. van Heijningen, and A. Stahl, "Characterizing 1550 nm optical components down to 8 K," *Cryogenics*, vol. 142, p. 103895, sep 2024. doi:10.1016/j.cryogenics.2024.103895.

[79] J. M. Liu, *Photonic devices*. Los Angeles: Cambridge University Press, 2005. doi:10.1017/CBO9780511614255.

[80] A. Devices, "AD797 a Ultralow Distortion, Ultralow Noise Op Amp," URL: https://www.analog.com/media/en/technical-documentation/data-sheets/ad797.pdf [Accessed 04-03-2026].

[81] N. Qian, "On the momentum term in gradient descent learning algorithms," *Neural Networks*, vol. 12, pp. 145–151, jan 1999. doi:10.1016/S0893-6080(98)00116-6.

[82] D. K. Gaskill, N. Bottka, L. Aina, and M. Mattingly, "Band-gap determination by photoreflectance of InGaAs and InAlAs lattice matched to InP," *Applied Physics Letters*, vol. 56, pp. 1269–1271, mar 1990. doi:10.1063/1.102533.

[83] A. Rogalski, "Third-generation infrared photodetector arrays," *Journal of Applied Physics*, vol. 105, p. 091101, may 2009. doi:10.1063/1.3099572.

[84] A. J. Moseley, M. D. Scott, A. H. Moore, and R. H. Wallis, "High-efficiency, low-leakage MOCVD grown GaInAs/AlInAs heterojunction photodiodes for detection to 2.4 μm," *Electronics Letters*, vol. 22, pp. 1206–1207, oct 1986. doi:10.1049/el:19860826.

[85] R. Kochanov, I. Gordon, L. Rothman, P. Wcisło, C. Hill, and J. Wilzewski, "HITRAN Application Programming Interface (HAPI): A comprehensive approach to working with spectroscopic data," *Journal of Quantitative Spectroscopy and Radiative Transfer*, vol. 177, pp. 15–30, jul 2016. XVIIIth Symposium on High Resolution Molecular Spectroscopy (HighRus-2015), Tomsk, Russia; doi:10.1016/j.jqsrt.2016.03.005.

[86] L. Lechevallier, S. Vasilchenko, R. Grilli, D. Mondelain, D. Romanini, and A. Campargue, "The water vapour self-continuum absorption in the infrared atmospheric windows: new laser measurements near 3.3 and 2.0 μm," *Atmospheric Measurement Techniques*, vol. 11, pp. 2159–2171, apr 2018. doi:10.5194/amt-11-2159-2018.

[87] A. Savitzky and M. J. E. Golay, "Smoothing and Differentiation of Data by Simplified Least Squares Procedures," *Analytical Chemistry*, vol. 36, pp. 1627–1639, jul 1964. doi:10.1021/ac60214a047.

[88] LAYERTEC GmbH, "Ho:YAG and Tm:YAG Lasers (2010 nm, 2100 nm) – Selection of Optical Components and Coatings." `https://www.layertec.de/en/coatings/common-laser-types/Ho-YAG-laser-coatings/`, 2026. [Accessed 29-01-2026].

[89] Laseroptik GmbH, "NIR 1101–2500 nm coatings." `https://www.laseroptik.com/en/coatings/ranges/nir-1101-2500-nm`, 2026. [Accessed 29-01-2026].

[90] P. Hariharan, *Optical Interferometry*. San Diego, CA, USA: Academic Press, 2003. doi:10.1016/B978-0-12-311630-7.X5000-X.

[91] D. Toeyrae, D. D. Brown, M. Davis, S. Song, A. Wormald, J. Harms, H. Miao, and A. Freise, "Multi-spatial-mode effects in squeezed-light-enhanced interferometric gravitational wave detectors," *Phys. Rev. D*, vol. 96, p. 022006, jul 2017. doi:10.1103/PhysRevD.96.022006.

[92] S. Steinlechner, N.-O. Rohweder, M. Korobko, D. Töyrä, A. Freise, and R. Schnabel, "Mitigating Mode-Matching Loss in Nonclassical Laser Interferometry," *Phys. Rev. Lett.*, vol. 121, p. 263602, dec 2018. doi:10.1103/PhysRevLett.121.263602.

[93] L. McCuller, S. E. Dwyer, A. C. Green, H. Yu, K. Kuns, L. Barsotti, C. D. Blair, D. D. Brown, A. Effler, and et al., "Ligo's quantum response to squeezed states," *Phys. Rev. D*, vol. 104, p. 062006, sep 2021. doi:10.1103/PhysRevD.104.062006.

[94] J. Gurs, S. Grebie, R. Schnabel, and M. Korobko, "Hyperloss from coherent spatial-mode mixing in quantum-correlated networks," *Nat. Commun.*, vol. 17, jul 2026. doi:10.1038/s41467-026-75899-5.

[95] S. Feng and H. G. Winful, "Physical origin of the Gouy phase shift," *Opt. Lett.*, vol. 26, pp. 485–487, apr 2001. doi:10.1364/OL.26.000485.

[96] D. Ganapathy and et al., "Broadband Quantum Enhancement of the LIGO Detectors with Frequency-Dependent Squeezing," *Phys. Rev. X*, vol. 13, p. 041021, oct 2023. doi:10.1103/PhysRevX.13.041021.

[97] A. W. Goodwin-Jones, R. Cabrita, M. Korobko, M. V. Beuzekom, D. D. Brown, V. Fafone, J. V. Heijningen, A. Rocchi, M. G. Schiworski, and M. Tacca, "Transverse mode control in quantum enhanced interferometers: a review and recommendations for a new generation," *Optica*, vol. 11, pp. 273–290, feb 2024. doi:10.1364/OPTICA.511924.

[98] N. C. Menicucci, “Fault-Tolerant Measurement-Based Quantum Computing with Continuous-Variable Cluster States,” *Physical Review Letters*, vol. 112, p. 120504, mar 2014. doi:10.1103/PhysRevLett.112.120504.

[99] B. W. Walshe, L. J. Mensen, B. Q. Baragiola, and N. C. Menicucci, “Robust Fault Tolerance for Continuous-Variable Cluster States with Excess Antisqueezing,” *Physical Review A*, vol. 100, p. 010301, jul 2019. doi:10.1103/PhysRevA.100.010301.

[100] K. Fukui and S. Takeda, “Building a large-scale quantum computer with continuous-variable optical technologies,” *Journal of Physics B: Atomic, Molecular and Optical Physics*, vol. 55, p. 012001, feb 2022. doi:10.1088/1361-6455/ac489c.

[101] K. Fukui, “High-Threshold Fault-Tolerant Quantum Computation with the Gottesman-Kitaev-Preskill Qubit under Noise in an Optical Setup,” *Physical Review A*, vol. 107, p. 052414, may 2023. doi:10.1103/PhysRevA.107.052414.

[102] V. B. Braginsky, M. L. Gorodetsky, and S. P. Vyatchanin, “Thermo-refractive noise in gravitational wave antennae,” *Physics Letters A*, vol. 271, pp. 303–307, jul 2000. doi:10.1016/S0375-9601(00)00389-3.

[103] K. M. Kwan, T. G. McRae, J. Qin, D. W. Gould, S. S. Y. Chua, J. Junker, R. Iden, V. B. Adya, M. J. Yap, B. J. J. Slagmolen, D. E. McClelland, and R. L. Ward, “Loss-Tolerant Detection of Squeezed States in the 2 μm Region,” *Phys. Rev. Lett.*, vol. 136, p. 123601, mar 2026. doi:10.1103/s61z-fcyp.

[104] L. A. Lugiato, C. Oldano, C. Fabre, *et al.*, “Bistability, self-pulsing and chaos in optical parametric oscillators,” *Il Nuovo Cimento D*, vol. 10, pp. 959–977, aug 1988. doi:10.1007/BF02450197.

[105] M. D. Reid and B. Yurke, “Effect of bistability and superpositions on quantum statistics in degenerate parametric oscillation,” *Phys. Rev. A*, vol. 46, pp. 4131–4137, oct 1992. doi:10.1103/PhysRevA.46.4131.

[106] Coherent Corp., “Mephisto / Mephisto S: Ultra-Narrow Linewidth CW DPSS Laser Datasheet,” 2024. Datasheet, URL: https://www.coherent.com/content/dam/coherent/site/en/resources/datasheet/lasers/mephisto-mephisto-s-ds.pdf [Accessed 03-05-2026].

[107] P. D. Drummond and Z. Ficek, eds., *Quantum Squeezing*. Springer Series on Atomic, Optical, and Plasma Physics, Berlin, Heidelberg: Springer Science & Business Media, 2004. doi:10.1007/978-3-662-09645-1.

[108] C. Wang, S. Du, Y. Niu, Z. Wang, C. Zhang, Q. Bian, C. Guo, J. Xu, Y. Bo, Q. Peng, D. Cui, J. Zhang, W. Lei, and Z. Xu, “Wavelength switchable high-power diode-side-pumped rod tm:yag laser around 2μm,” *Opt. Express*, vol. 21, pp. 7156–7161, mar 2013. doi:10.1364/OE.21.007156.

[109] L. Han, B. Yao, X. Duan, S. Li, T. Dai, Y. Ju, and Y. Wang, “Experimental study of continuous-wave and Q-switched laser performances of Ho:YVO4 crystal,” *Chin. Opt. Lett.*, vol. 12, p. 081401, aug 2014. URL: https://opg.optica.org/col/abstract.cfm?URI=col-12-8-081401 [Accessed 06-03-2026].

[110] J. W. Kim, J. I. Mackenzie, D. Parisi, S. Veronesi, M. Tonelli, and W. A. Clarkson, “Efficient in-band pumped Ho:LuLiF$_4$ 2 μm laser,” *Opt. Lett.*, vol. 35, pp. 420–422, feb 2010. doi:10.1364/OL.35.000420.

[111] E. Ji, Q. Liu, Z. Hu, P. Yan, and M. Gong, “High-power, high-energy Ho:YAG oscillator pumped by a Tm-doped fiber laser,” *Chinese Optics Letters*, vol. 13, p. 121402, dec 2015. doi:10.3788/COL201513.121402.

[112] J. Kwiatkowski and J. Sotor, "Laser wavelength shift and dual-wavelength generation in continuous-wave operation of Ho:YAG laser pumped by thulium-doped fiber laser," *Optics and Laser Technology*, vol. 146, p. 107544, feb 2022. doi:10.1016/j.optlastec.2021.107544.

[113] M. Ganija, A. Hemming, N. Simakov, K. Boyd, J. Haub, P. Veitch, and J. Munch, "High power cryogenic ho:yag laser," *Opt. Express*, vol. 25, pp. 31889–31895, dec 2017. doi:10.1364/OE.25.031889.

[114] J. Tang, E. Li, F. Wang, W. Yao, C. Shen, and D. Shen, "High Power Ho:YAP Laser With 107 W of Output Power at 2117 nm," *IEEE Photonics Journal*, vol. 12, pp. 1–7, jan 2020. doi:10.1109/JPHOT.2020.2968745.

[115] J. Zhang, F. Schulze, K. F. Mak, V. Pervak, D. Bauer, D. Sutter, and O. Pronin, "High-Power, High-Efficiency Tm:YAG and Ho:YAG Thin-Disk Lasers," *Laser & Photonics Reviews*, vol. 12, p. 1700273, jan 2018. doi:10.1002/lpor.201700273.

[116] B. Lei, L. Zhang, S. Yang, S. Yao, Y. Cheng, G. Sun, Y. Wang, X. Xie, W. Zhao, H. Lin, and Y. Fu, "Near diffraction-limited in-band pumped Ho:YLF composite thin disk laser at 2 μm," *Opt. Express*, vol. 33, pp. 7569–7578, feb 2025. doi:10.1364/OE.553246.

[117] G. Renz, P. Mahnke, J. Speiser, and A. Giesen, "2 µm Ho:YAG Thin Disk Laser," in *Advances in Optical Materials*, p. AWA24, Optica Publishing Group, feb 2011. doi:10.1364/ASSP.2011.AWA24.

[118] S. Tomilov, M. Hoffmann, Y. Wang, and C. J. Saraceno, "Moving towards high-power thin-disk lasers in the 2 µm wavelength range," *Journal of Physics: Photonics*, vol. 3, p. 022002, feb 2021. doi:10.1088/2515-7647/abdd81.

[119] K. Yin, R. Zhu, B. Zhang, G. Liu, P. Zhou, and J. Hou, "300 W-level, wavelength-widely-tunable, all-fiber integrated thulium-doped fiber laser," *Opt. Express*, vol. 24, pp. 11085–11090, may 2016. doi:10.1364/OE.24.011085.

[120] C. Louot, F. Sanson, A. Motard, T. Ibach, I. Manek-Hönninger, A. Berrou, N. Dalloz, T. Robin, B. Cadier, and A. Hildenbrand-Dhollande, "Emission Wavelength Limits of a Continuous-Wave Thulium-Doped Fiber Laser Source Operating at 1.94 µm, 2.09 µm or 2.12 µm," *Photonics*, vol. 11, mar 2024. doi:10.3390/photonics11030246.

[121] M. Michalska, P. Honzatko, P. Grzes, M. Kamradek, O. Podrazky, I. Kasik, and J. Swiderski, "Thulium-Doped 1940- and 2034-nm Fiber Amplifiers: Towards Highly Efficient, High-Power All-Fiber Laser Systems," *Journal of Lightwave Technology*, vol. 42, pp. 339–346, aug 2024. doi:10.1109/JLT.2023.3301397.

[122] M. Meleshkevich, N. Platonov, D. Gapontsev, A. Drozhzhin, V. Sergeev, and V. Gapontsev, "415W Single-Mode CW Thulium Fiber Laser in all-fiber format," in *CLEO: Europe and IQEC 2007 Conference Digest*, p. CP2_3, Optica Publishing Group, 2007. URL: `https://opg.optica.org/abstract.cfm?URI=CLEO_Europe-2007-CP2_3` [Accessed 06-03-2026].

[123] W. Yao, C. Shen, Z. Shao, J. Wang, F. Wang, Y. Zhao, and D. Shen, "790 W incoherent beam combination of a Tm-doped fiber laser at 1941 nm using a 3×1 signal combiner," *Appl. Opt.*, vol. 57, pp. 5574–5577, jul 2018. doi:10.1364/AO.57.005574.

[124] C. Ren, Y. Shen, Y. Zheng, Y. Mao, F. Wang, D. Shen, and H. Zhu, "Widely-tunable all-fiber Tm doped MOPA with > 1 kW of output power," *Opt. Express*, vol. 31, pp. 22733–22739, jul 2023. doi:10.1364/OE.494015.

[125] N. Simakov, A. V. Hemming, A. Carter, K. Farley, A. Davidson, N. Carmody, M. Hughes, J. M. O. Daniel, L. Corena, D. Stepanov, and J. Haub, "Design and experimental demonstration of a large pedestal thulium-doped fibre," *Opt. Express*, vol. 23, pp. 3126–3133, feb 2015. doi:10.1364/OE.23.003126.

[126] B. M. Anderson, J. Solomon, and A. Flores, "1.1 kW, beam-combinable thulium doped all-fiber amplifier," in *Fiber Lasers XVIII: Technology and Systems* (M. N. Zervas, ed.), vol. 11665, p. 116650B, International Society for Optics and Photonics, SPIE, mar 2021. doi:10.1117/12.2576209.

[127] X. Wang, X. Jin, P. Zhou, X. Wang, H. Xiao, and Z. Liu, "High power, widely tunable, narrowband superfluorescent source at 2 μm based on a monolithic Tm-doped fiber amplifier," *Opt. Express*, vol. 23, pp. 3382–3389, feb 2015. doi:10.1364/OE.23.003382.

[128] X. Wang, P. Zhou, X. Wang, H. Xiao, and L. Si, "102 W monolithic single frequency Tm-doped fiber MOPA," *Opt. Express*, vol. 21, pp. 32386–32392, dec 2013. doi:10.1364/OE.21.032386.

[129] T. Walbaum, M. Heinzig, T. Schreiber, R. Eberhardt, and A. Tünnermann, "Monolithic thulium fiber laser with 567 W output power at 1970 nm," *Opt. Lett.*, vol. 41, pp. 2632–2635, jun 2016. doi:10.1364/OL.41.002632.

[130] L. Yin-Zi, X. Ying-Bing, L. Lei, W. Yi-Bo, P. Jing-Gang, L. Hai-Qing, D. Neng-Li, and L. Jin-Yan, "530 W all-fiber continuous-wave Tm-doped fiber laser," *Acta Physica Sinica*, vol. 69, pp. 184209–1–184209–7, jan 2020. doi:10.7498/aps.69.20200466.

[131] A. Hemming, S. Bennetts, A. Davidson, N. Carmody, and D. G. Lancaster, "A 226W high power Tm fibre laser," in *OECC/ACOFT 2008 - Joint Conference of the Opto-Electronics and Communications Conference and the Australian Conference on Optical Fibre Technology*, pp. 1–2, aug 2008. doi:10.1109/OECCACOFT.2008.4610435.

[132] L. Shah, R. A. Sims, P. Kadwani, C. C. Willis, J. B. Bradford, A. Sincore, and M. Richardson, "High-power spectral beam combining of linearly polarized Tm:fiber lasers," *Appl. Opt.*, vol. 54, pp. 757–762, feb 2015. doi:10.1364/AO.54.000757.

[133] J. Liu, H. Shi, K. Liu, Y. Hou, and P. Wang, "210 W single-frequency, single-polarization, thulium-doped all-fiber MOPA," *Opt. Express*, vol. 22, pp. 13572–13578, jun 2014. doi:10.1364/OE.22.013572.

[134] N. J. Ramírez-Martínez, M. N. nez Velázquez, A. A. Umnikov, and J. K. Sahu, "Highly efficient thulium-doped high-power laser fibers fabricated by MCVD," *Opt. Express*, vol. 27, pp. 196–201, jan 2019. doi:10.1364/OE.27.000196.

[135] N. J. Ramírez-Martínez, M. N. nez Velázquez, and J. K. Sahu, "Study on the dopant concentration ratio in thulium-holmium doped silica fibers for lasing at 2.1µm," *Opt. Express*, vol. 28, pp. 24961–24967, aug 2020. doi:10.1364/OE.397855.

[136] Y. Tang, C. Huang, S. Wang, H. Li, and J. Xu, "High-power narrow-bandwidth thulium fiber laser with an all-fiber cavity," *Opt. Express*, vol. 20, pp. 17539–17544, jul 2012. doi:10.1364/OE.20.017539.

[137] C. Romano, D. Panitzek, D. Lorenz, P. Forster, M. Eichhorn, and C. Kieleck, "High-power thulium-doped fiber MOPA emitting at 2036 nm," jan 2024. doi:10.1109/jlt.2023.3310121.

[138] P. F. Moulton, G. A. Rines, E. V. Slobodtchikov, K. F. Wall, G. Frith, B. Samson, and A. L. G. Carter, "Tm-Doped Fiber Lasers: Fundamentals and Power Scaling," *IEEE Journal of Selected Topics in Quantum Electronics*, vol. 15, pp. 85–92, jan 2009. doi:10.1109/JSTQE.2008.2010719.

[139] G. D. Goodno, L. D. Book, and J. E. Rothenberg, "Low-phase-noise, single-frequency, single-mode 608 W thulium fiber amplifier," *Opt. Lett.*, vol. 34, pp. 1204–1206, apr 2009. doi:10.1364/OL.34.001204.

[140] P. Forster, C. Romano, C. Kieleck, and M. Eichhorn, "Advances in two-micron lasers for nonlinear conversion into the mid-IR," apr 2020. doi:10.1117/12.2560169.

[141] J. S. Shin, Y.-H. Cha, B. J. Chun, D.-Y. Jeong, and H. Park, "200-W Continuous-wave Thulium-doped All-fiber Laser at 2050 nm," *Current Optics and Photonics*, vol. 5, pp. 306–310, jun 2021. doi:10.3807/COPP.2021.5.3.306.

[142] A. Motard, C. Louot, T. Robin, B. Cadier, I. Manek-Hönninger, N. Dalloz, and A. Hildenbrand-Dhollande, "Diffraction limited 195-W continuous wave laser emission at 2.09 μm from a Tm^{3+}, Ho^{3+}-codoped single-oscillator monolithic fiber laser," *Opt. Express*, vol. 29, pp. 6599–6607, mar 2021. doi:10.1364/OE.416443.

[143] P. Forster, C. Romano, J. Schneider, M. Eichhorn, and C. Kieleck, "High-power continuous-wave Tm^{3+}:Ho^{3+}-codoped fiber laser operation from 2.1 μm to 2.2 μm," *Opt. Lett.*, vol. 47, pp. 2542–2545, may 2022. doi:10.1364/OL.458921.

[144] S. D. Jackson, A. Sabella, A. Hemming, S. Bennetts, and D. G. Lancaster, "High-power 83 W holmium-doped silica fiber laser operating with high beam quality," *Opt. Lett.*, vol. 32, pp. 241–243, feb 2007. doi:10.1364/OL.32.000241.

[145] A. Hemming, N. Simakov, A. Davidson, M. Oermann, L. Corena, D. Stepanov, N. Carmody, J. Haub, R. Swain, and A. Carter, "Development of high power holmium-doped fibre amplifiers," in *Fiber Lasers XI: Technology, Systems, and Applications* (S. Ramachandran, ed.), vol. 8961 of *Proceedings of SPIE*, p. 89611A, SPIE, mar 2014. doi:10.1117/12.2042963.

[146] B. Beaumont, P. Bourdon, A. Barnini, L. Kervella, T. Robin, and J. L. Gouët, "High Efficiency Holmium-Doped Triple-Clad Fiber Laser at 2120 nm," *Journal of Lightwave Technology*, vol. 40, pp. 6480–6485, oct 2022. doi:10.1109/JLT.2022.3196807.

[147] J. L. Gouët, F. Gustave, P. Bourdon, T. Robin, A. Laurent, and B. Cadier, "Realization and simulation of high-power holmium doped fiber lasers for long-range transmission," *Opt. Express*, vol. 28, pp. 22307–22320, jul 2020. doi:10.1364/OE.394011.

[148] A. Hemming, S. Bennetts, N. Simakov, A. Davidson, J. Haub, and A. Carter, "High power operation of cladding pumped holmium-doped silica fibre lasers," *Opt. Express*, vol. 21, pp. 4560–4566, feb 2013. doi:10.1364/OE.21.004560.

Chapter F

Publications

The results presented in this work are summarized in the following publications, sorted by publication date:

High-power laser: J. Gurs, N. Bode, C. Darsow-Fromm, H. Vahlbruch, P. Gewecke, S. Steinlechner, B. Willke, and R. Schnabel, "Conversion of 30 W laser light at 1064 nm to 20 W at 2128 nm and comparison of relative power noise", Classical and Quantum Gravity, Vol. 41, 2024, doi: 10.1088/1361-6382/ad8f8b.

Technical noise conversion: J. Gurs, M. Korobko, C. Darsow-Fromm, S. Steinlechner, and R. Schnabel, "Coherent noise suppression at high-efficiency wavelength doubling for high-precision experiments", Optics and Laser Technology, Vol. 183, 2025, doi: 10.1016/j.optlastec.2024.112179.

Photodiode cooling: J. Gurs, N. Sültmann, C. Darsow-Fromm, S. Steinlechner, and R. Schnabel, "Photodiode quantum efficiency for 2 µm light in the signal band of gravitational wave detectors", Comptes Rendus. Physique, Vol. 27, 2026, doi: 10.5802/crphys.269.

Hyperloss: J. Gurs, S. Grebie, R. Schnabel, and M. Korobko, "Hyperloss from coherent spatial-mode mixing in quantum-correlated networks", Nature Communications, Vol. 17, 2026, doi: 10.1038/s41467-026-75899-5

During this work, I undertook a research stay at LIGO Hanford, where I built a second harmonic generator. Through combined effort with other researchers, an internal LIGO document was created as a blueprint for their SHGs. This document can be found as LIGO Document T2500031-v1, authored by Julian Gurs, Camilla Compton, Sheila Dwyer, Kar Meng Kwan, Terry McRae, Nutsinee Kijbunchoo, and Daniel Sigg (authors listed in no particular order).

Fundamental findings that influenced this work were discovered during my Master's thesis and published in the following papers:

Low-power laser: C. Darsow-Fromm, M. Schröder, J. Gurs, R. Schnabel, and S. Steinlechner, "Highly efficient generation of coherent light at 2128 nm via degenerate optical-parametric oscillation", Optics Letters, Vol. 45, 2020, doi: 10.1364/OL.405396.

High frequency squeezing: C. Darsow-Fromm, J. Gurs, R. Schnabel, S. Steinlechner, S. Steinlechner, and S. Steinlechner, "Squeezed light at 2128 nm for future gravitational-wave observatories", Optics Letters, Vol. 46, 2021, doi: 10.1364/OL.433878.

As part of the LIGO-Virgo-KAGRA (LVK) collaboration, I co-authored the publications listed below, ordered by publication date.

- LVK collaboration, "Model-based Cross-correlation Search for Gravitational Waves from the Low-mass X-Ray Binary Scorpius X-1 in LIGO O3 Data", The Astrophysical Journal Letters, Vol. 941, 2022, doi: 10.3847/2041-8213/aca1b0.
- LVK collaboration, "Open Data from the Third Observing Run of LIGO, Virgo, KAGRA, and GEO", The Astrophysical Journal, Vol. 267, 2023, doi: 10.3847/1538-4365/acdc9f.
- LVK collaboration, "Search for subsolar-mass black hole binaries in the second part of Advanced LIGO's and Advanced Virgo's third observing run", Monthly Notices of the Royal Astronomical Society, Vol. 524, 2024, doi: 10.1093/mnras/stad588.
- LVK collaboration, "Search for Gravitational-lensing Signatures in the Full Third Observing Run of the LIGO–Virgo Network", The Astrophysical Journal, Vol. 970, 2024, doi: 10.3847/1538-4357/ad3e83.
- LVK collaboration, "Observation of Gravitational Waves from the Coalescence of a 2.5–4.5 M Compact Object and a Neutron Star", The Astrophysical Journal, Vol. 970, 2024, doi: 10.3847/2041-8213/ad5beb.
- LVK collaboration, "Ultralight vector dark matter search using data from the KAGRA O3GK run", Physical Review D, Vol. 110, 2024, doi: 10.1103/PhysRevD.110.042001.
- LVK collaboration, "Search for Eccentric Black Hole Coalescences during the Third Observing Run of LIGO and Virgo", The Astrophysical Journal, Vol. 973, 2024, doi: 10.3847/1538-4357/ad65ce.
- LVK collaboration, "A Search Using GEO600 for Gravitational Waves Coincident with Fast Radio Bursts from SGR 1935+2154", The Astrophysical Journal, Vol. 977, 2024, doi: 10.3847/1538-4357/ad8de0.
- LVK collaboration, "GW250114: Testing Hawking's Area Law and the Kerr Nature of Black Holes", Physical Review Letters, Vol. 135, 2025, doi: 10.1103/kw5g-d732.
- LVK collaboration, "Swift-BAT GUANO Follow-up of Gravitational-wave Triggers in the Third LIGO–Virgo–KAGRA Observing Run", The Astrophysical Journal, Vol. 980, 2025, doi: 10.3847/1538-4357/ad9749.
- LVK collaboration, "Advanced LIGO detector performance in the fourth observing run", Physical Review D, Vol. 111, 2025, doi: 10.1103/PhysRevD.111.062002.
- LVK collaboration, "Search for Continuous Gravitational Waves from Known Pulsars in the First Part of the Fourth LIGO-Virgo-KAGRA Observing Run", The Astrophysical Journal, Vol. 983, 2025, doi: 10.3847/1538-4357/adb3a0.
- LVK collaboration, "Search for Gravitational Waves Emitted from SN 2023ixf", The Astrophysical Journal, Vol. 985, 2025, doi: 10.3847/1538-4357/adc681.
- LVK collaboration, "Open Data from LIGO, Virgo, and KAGRA through the First Part of the Fourth Observing Run", arXiv: 2508.18079, 2025.
- LVK collaboration, "GWTC-4.0: Population Properties of Merging Compact Binaries", arXiv: 2508.18083, 2025.

- LVK collaboration, "GWTC-4.0: Updating the Gravitational-Wave Transient Catalog with Observations from the First Part of the Fourth LIGO-Virgo-KAGRA Observing Run", arXiv: 2508.18082, 2025.
- LVK collaboration, "GWTC-4.0: Methods for Identifying and Characterizing Gravitational-wave Transients", arXiv: 2508.18081, 2025.
- LVK collaboration, "Upper Limits on the Isotropic Gravitational-Wave Background from the first part of LIGO, Virgo, and KAGRA's fourth Observing Run", Physical Review D, accepted, 2025, doi: 10.1103/wq57-sjt2.
- LVK collaboration, "Improving cosmological reach of a gravitational wave observatory using Deep Loop Shaping", Science, Vol. 389, 2025, doi: 10.1126/science.adw1291.
- LVK collaboration, "GWTC-4.0: Constraints on the Cosmic Expansion Rate and Modified Gravitational-wave Propagation", arXiv: 2509.04348, 2025.
- LVK collaboration, "Directed searches for gravitational waves from ultralight vector boson clouds around merger remnant and galactic black holes during the first part of the fourth LIGO-Virgo-KAGRA observing run", arXiv: 2509.07352, 2025.
- LVK collaboration, "GW250114: Testing Hawking's Area Law and the Kerr Nature of Black Holes", Physical Review Letters, Vol. 135, 2025, doi: 10.1103/kw5g-d732.
- LVK collaboration, "Directional Search for Persistent Gravitational Waves: Results from the First Part of LIGO-Virgo-KAGRA's Fourth Observing Run", arXiv: 2510.17487, 2025.
- LVK collaboration, "Cosmological and High Energy Physics implications from gravitational-wave background searches in LIGO-Virgo-KAGRA's O1-O4a runs", arXiv: 2510.26848, 2025.
- LVK collaboration, "Direct multi-model dark-matter search with gravitational-wave interferometers using data from the first part of the fourth LIGO-Virgo-KAGRA observing run", arXiv: 2510.27022, 2025.
- LVK collaboration, "GW231123: A Binary Black Hole Merger with Total Mass 190–265 M", The Astrophysical Journal Letters, Vol. 993, 2025, doi: 10.3847/2041-8213/ae0c9c.
- LVK collaboration, "GW241011 and GW241110: Exploring Binary Formation and Fundamental Physics with Asymmetric, High-spin Black Hole Coalescences", The Astrophysical Journal Letters, Vol. 993, 2025, doi: 10.3847/2041-8213/ae0d54.
- LVK collaboration, "All-sky search for short gravitational-wave bursts in the first part of the fourth LIGO-Virgo-KAGRA observing run", Physical Review D, Vol. 112, 2025, doi: 10.1103/-wjdz-jdby.
- LVK collaboration, "All-sky search for continuous gravitational-wave signals from unknown neutron stars in binary systems in the first part of the fourth LIGO-Virgo-KAGRA observing run", arXiv: 2511.16863, 2025.
- LVK collaboration, "Search for planetary-mass ultra-compact binaries using data from the first part of the LIGO-Virgo-KAGRA fourth observing run", Physical Review D, accepted, 2025, doi: 10.1103/s551-7pch.
- LVK collaboration, "GWTC-4.0: An Introduction to Version 4.0 of the Gravitational-Wave Transient Catalog", The Astrophysical Journal Letters, Vol. 995, 2025, doi: 10.3847/2041-8213/ae0c06.

- LVK collaboration, "GWTC-4.0: Searches for Gravitational-Wave Lensing Signatures", arXiv: 2512.16347, 2025.
- LVK collaboration, "Constraints on gravitational waves from the 2024 Vela pulsar glitch", arXiv: 2512.17990, 2025.
- LVK collaboration, Black Hole Spectroscopy and Tests of General Relativity with GW250114", Physical Review Letter, Vol. 136, 2026, doi: 10.1103/6c61-fm1n.
- LVK collaboration, "All-sky Searches for Continuous Gravitational Waves from Isolated Neutron Stars in the Data from the First Part of the Fourth LIGO-Virgo-KAGRA Observing Run", arXiv: 2603.14168, 2026.
- LVK collaboration, "GWTC-4.0: Tests of General Relativity. I. Overview and General Tests", arXiv: 2603.19019, 2026.
- LVK collaboration, "All-sky search for long-duration gravitational-wave transients in the first part of the fourth LIGO-Virgo-KAGRA Observing run", Physical Review D, Vol. 113, 2026, doi: 10.1103/83j3-pgk1.
- LVK collaboration, "GWTC-4.0: Tests of General Relativity. II. Parameterized Tests", arXiv: 2603.19020, 2026.
- LVK collaboration, "GWTC-4.0: Tests of General Relativity. III. Tests of the Remnants", arXiv: 2603.19021, 2026.
- LVK collaboration, "Searches for Continuous Gravitational Waves from Supernova Remnants in the first part of the LIGO-Virgo-KAGRA Fourth Observing run", arXiv: 2603.25808, 2026.
- LVK collaboration, "Narrowband searches for continuous gravitational waves from known pulsars in the first two parts of the fourth LIGO-Virgo-KAGRA observing run", arXiv: 2603.25938, 2026.
- LVK collaboration, "Searches for Binary Mergers with Sub-solar Mass Components in Data from the First Part of LIGO-Virgo-KAGRA's Fourth Observing Run", arXiv: 2605.05444, 2026.
- LVK collaboration, "GW240925 and GW250207: Astrophysical calibration of gravitational wave detectors", Physical Review Letters, accepted, 2026, doi: 10.1103/gzrj-mwv3.
- LVK collaboration and IceCube Collaboration, "Deep Search for Joint Sources of Gravitational Waves and High-energy Neutrinos with IceCube during the Third Observing Run of LIGO and Virgo", The Astrophysical Journal, Vol. 1003, 2026, doi: 10.3847/1538-4357/ae4e1b.

Chapter G

Acknowledgements

Eine Doktorarbeit wird oft als die Arbeit eines einzelnen Menschen gesehen, obwohl im Hintergrund sehr viele dazu beigetragen haben. Deswegen möchte ich mich an dieser Stelle ganz herzlich bei all den Menschen bedanken, die mich auf dem Weg bis hierher begleitet und unterstützt haben.

Als Allererstes fällt mir Roman Schnabel ein, für seine Unterstützung, das Vertrauen und die Möglichkeit, mich kreativ in den vielen schönen Experimenten auszuleben. Außerdem Sebastian Steinlechner, der eine Mentorenrolle für mich einnahm und in den 2 µm-Meetings als sehr kluge Stimme aus dem Ether auftauchte, um meine gelegentliche Verwirrung in Verständnis zu verwandeln. Zudem meinem Vorgänger Chris, der immer ein offenes Ohr hatte und auch mit seiner Expertise geholfen hat.

Abgesehen davon gibt es viele andere tolle Menschen, bei denen ich mich bedanken möchte. Angefangen bei allen, mit denen ich gemeinsam Experimente durchgeführt und veröffentlicht habe. Neben den bereits Genannten möchte ich stellvertretend für viele weitere Pascal, Stephan, Misha, Nils und auch das Team aus Hannover nennen. Zudem danke ich der Arbeitsgruppe für die vielen schönen und spaßigen Arbeitstage, an denen wir spannende Physik gemacht, aber auch Grillabende veranstaltet, Klask-Wettkämpfe ausgetragen, Volleyball gespielt oder einfach miteinander geschnackt haben.

Gerne möchte ich mich auch bei allen Personen bedanken, die zur Verbesserung der Dissertation beigetragen haben. Namentlich zu erwähnen sind: Bene, Chris, Jan, Jonas, Leif, Misha und Niels.

Für das Ertragen meiner Stimmung, je nachdem, wie ein Messtag ausfiel, danke ich meiner besten Freundin und nun auch Ehefrau Steffi, die nicht nur moralische Unterstützung geleistet hat, sondern auch dafür gesorgt hat, dass sich mein Leben nicht nur im Labor abgespielt hat. Und das Ganze schon seit über 10 Jahren! Des Weiteren danke ich meiner Mom Sabrina und meinem Dad Steffen für die lange Unterstützung und das Vertrauen in mich. Abschließend möchte ich noch meinem Opa danken, der den Grundstein für diesen Weg gelegt hat.

Es gibt noch so viel mehr Menschen, die ich hier nennen könnte. Seht es mir bitte nach, wenn ich euch hier nicht explizit nenne, aber ich hoffe, ihr wisst trotzdem, dass ihr gemeint seid.

Zum Abschluss bleibt mir nur noch zu sagen:

„Macht's gut und danke für den vielen Fisch!"

- Douglas Adams

Chapter H

List of Used Software

A variety of software and digital tools were used in the production of this thesis. The following list provides an overview of these tools and their purposes.

Visualization Schematic illustrations were created using Inkscape version 1.4.2, together with the ComponentLibrary illustration database by Alexander Franzen, which is gratefully acknowledged. Matplotlib version 3.9.2 was used for all plots. Autodesk Inventor Professional 2025 was used to create mechanical drawings, and EAGLE6 was used for circuit diagrams. Photographs were taken with an iPhone 8 Plus or iPhone 15.

Data analysis and simulation Simulations of beam propagation and cavity behavior were carried out using Finesse by the Finesse team, JamMt by Ian MacMillan, and Linear Cavity Simulator by Sebastian Steinlechner. Additional calculations were performed with Python version 3.12.7 and various scientific packages. In specific cases, these are described in more detail in the thesis. These computations were performed using JupyterLab version 4.2.5.

Text processing and organization This work was created using LaTeX; to be precise, TeXstudio was used. Literature such as books, data sheets, and publications was organized in Mendeley, and the resulting bibliography was further refined manually.

Linguistic assistance For linguistic refinement (including spelling, grammar, and stylistic improvements), digital services such as DeepL, UHHGPT, QuillBot, and LEO dictionaries were used. These tools were employed solely for language-related assistance. All scientific content, including derivations, analyses, and interpretations, was developed exclusively by the author.

Chapter I

Eidesstattliche Versicherung

Eidesstattliche Versicherung Hiermit versichere ich an Eides statt, die vorliegende Dissertationsschrift selbst verfasst und keine anderen als die angegebenen Hilfsmittel und Quellen benutzt zu haben.

Sofern im Zuge der Erstellung der vorliegenden Dissertationsschrift generative Künstliche Intelligenz (gKI) basierte elektronische Hilfsmittel verwendet wurden, versichere ich, dass meine eigene Leistung im Vordergrund stand und dass eine vollständige Dokumentation aller verwendeten Hilfsmittel gemäß der Guten wissenschaftlichen Praxis vorliegt. Ich trage die Verantwortung für eventuell durch die gKI generierte fehlerhafte oder verzerrte Inhalte, fehlerhafte Referenzen, Verstöße gegen das Datenschutz- und Urheberrecht oder Plagiate.

Hamburg, den 12.06.2026 Unterschrift